

ABSTRACT

Obesity and urinary incontinence represent health problem affecting a large part of the population worldwide. Nowadays, bariatric surgery and the artificial urinary sphincter placement are respectively the most common treatments for the diseases with a high percentage of complications and failures. Such surgical treatments are respectively evaluated only by clinical and surgical basis only. For a better understanding of the processes involved to the related treatments, a biomechanical analysis of such biological structures in pre- and post-surgical conformation is required. At this purpose, both experimental tests and computational models are made, describing the mechanical behaviour of the related tissues and structures.

In general, laparoscopic bariatric surgical procedures are effective, but are often associated with major complications. A novel endoscopic gastric banding technique is here proposed, focusing on the design of clips involved to applying the gastric band into the stomach wall. The strength of such clips is then tested by means of FEM analyses proving the safety of their structures.

The action induced by artificial sphincteric devices to provide urinary continence is related to the problem of evaluating the interaction between the occlusive cuff and the urethral duct. To access this investigation a suitable experimental setup is designed and realized. At first an experimental test bench is made. Then an acquisition system is realized, composed of an electronic circuit based on Arduino M0 PRO board connected to 4 pressure sensors and a PC user interface programmed in LabVIEW.

AKNOWLEDGEMENTS

Starting to write this thesis would not have been possible without the support of a few very special people in my life. I would like to show my gratitude to the following:

- *My father Andrea and my mother Rita, for always just wanting all the best for me. Your love and your believing in me was always perceived and gave me the energy to be a stronger person. I can never thank you enough to make your children the main priority in your life. Whatever I have done in life, I have done also to make you proud.*
- *My sister Luisa and my girlfriend Marta, for the huge support, the special love and for always believing in me.*
- *My special friends Alessandro and Gianluca, my brothers, for always being my second shoulders and giving the strength to overcome difficult moments.*
- *My grandmother Marisa, my second mother, for all the love and the special support given in this path.*
- *My friend Livio, for all the conversations had together and advices given.*

I would like to express my gratitude and sincere appreciation to Prof. Emanuele Luigi Carniel, professor of Mechanics of Biological Structures, School of Engineering of University of Padova, for suggesting the topic of this work and for giving me the opportunity to work under his supervision.

April 11, 2017

Luca Barp

INDEX

INTRODUCTION	1
CHAPTER 1	9
CLINICAL PROBLEMS: SURGICAL SOLUTION FOR THE TREATMENT OF OBESITY AND URINARY INCONTINENCE	9
1.1 OBESITY.....	9
1.1.1 ANATOMY OF THE GASTROINTESTINAL TRACT	11
THE STOMACH.....	12
THE SMALL INTESTINE	19
1.1.2 BARIATRIC SURGERY	21
LAPAROSCOPIC ROUX-EN-Y GASTRIC BYPASS	22
LAPAROSCOPIC VERTICAL SLEEVE GASTRECTOMY.....	24
LAPAROSCOPIC ADJUSTABLE GASTRIC BANDING	25
BILIOPANCREATIC DIVERSION WITH DUODENAL SWITCH	26
COMPLICATIONS AND LONG TERM RISK OF DEATH	27
ENDOSCOPIC BARIATRIC TREATMENTS	28
1.2 URINARY INCONTINENCE.....	31
1.2.1 CHRONIC URINANRY INCONTINENCE	32
STRESS URINARY INCONTINENCE.....	32
URGE URINARY INCONTINENCE	33
MIXED URINARY INCONTINENCE	33
OVERFLOW URINARY INCONTINENCE.....	33
FUNCTIONAL URINARY INCONTINENCE	34
CONTINUOUS URINARY INCONTINENCE.....	34
ANATOMY OF THE LOWER URINARY TRACT	34
THE URINARY BLADDER.....	36
THE MALE URETHRA.....	39
THE FEMALE URETHRA.....	47
SURGERY SOLUTIONS FOR THE TREATMENT OF URINARY INCONTINENCE	49
URETHRAL SLINGS	49
COLPOSUSPENSION.....	52
URETHRAL BULKING AGENTS.....	53
ARTIFICIAL URINARY SFINCTERS.....	54

CHAPTER 2	61
EXPERIMENTAL AND COMPUTATIONAL METHODS FOR THE INVESTIGATION OF STOMACH MECHANICS.....	61
2.1 EXPERIMENTAL TESTS.....	62
2.1.1 EXPERIMENTAL INVESTIGATION OF THE STOMACH WALL TISSUES MECHANICS...	62
2.1.2 STRUCTURAL TESTS IN PRE- AND POST-SURGICAL CONFIGURATION OF THE STOMACH.....	65
2.2 STOMACH TISSUE MECHANICS.....	70
2.3 COMPUTATIONAL MODEL.....	74
2.3.1 CONSTITUTIVE MODEL OF THE STOMACH TISSUES.....	76
2.3.2 COMPUTATIONAL ANALYSIS OF THE GASTRIC BANDING	79
2.3.3 NUMERICAL ANALYSIS	82
2.4 RESULTS	82
2.4 DISCUSSION	86
CHAPTER 3	91
EXPERIMENTAL AND COMPUTATIONAL METHODS FOR THE INVESTIGATION OF URETHRAL MECHANICS	91
3.1 EXPERIMENTAL TESTS.....	92
3.1.1 MECHANICAL TESTS OF URETHRAL TISSUES	94
3.1.2 MECHANICAL TESTS OF URETHRAL STRUCTURE.....	96
3.2 PRELIMINARY MODEL FORMULATIONS.....	98
3.2.1 ANALYSIS OF TENSILE TESTS ON TISSUE SPECIMENS	98
3.2.2 ANALYSIS OF INFLATION TESTS ON URETHRAL SAMPLES	99
3.3 URETHRAL MECHANICS	100
3.3.1 TISSUE MECHANICS OF URETHRA.....	100
3.3.2 STRUCTURAL MECHANICS OF THE URETHRA.....	102
3.4 COMPUTATIONAL MODELS OF THE URETHRA	103
3.4.1 2D FEM MODEL DEFINITION	103
3.4.2 3D FEM MODEL DEFINITION	106
3.4.3 CONSTITUTIVE FORMULATION	109
3.5 RESULTS OF NUMERICAL ANALYSES	111
3.5.1 2D NUMERICAL ANALYSES RESULTS	111
3.5.2 3D NUMERICAL ANALYSES RESULTS	115
3.6 DISCUSSION	124

CHAPTER 4	129
COMPUTATIONAL INVESTIGATION OF THE DEVICES FOR AN INNOVATIVE APPROACH TO BARIATRIC SURGERY	129
4.1 ENDOSCOPIC GASTRIC BANDING TECHNIQUE.....	130
4.2 DESIGN OF THE CLIPS.....	132
4.2.1 AN OPTIMIZED GEOMETRICAL MODEL OF THE CLIPS	133
4.2.2 3D CAD MODELLING OF THE CLIPS	135
4.2.3 THE MATERIAL	137
4.3 COMPUTATIONAL MODELS OF THE CLIPS	138
4.3.1 MODELS DISCRETIZATION	138
4.3.2 LOAD BOUNDARY CONDITIONS SETUP	141
4.4 RESULTS	143
4.4.1 FIRST RESULTS OF BASIC M1 AND M2 MODELS.....	143
4.4.2 FIRST M1 AND M2 RESULTS COMPARISON AND DISCUSSION.....	146
4.4.3 M2 TYPE A FURTHER RESULTS	147
4.5 SAFETY OF THE CLIPS	153
4.5.1 PROOF OF YIELD STRENGTH.....	153
4.5.2 FATIGUE STRENGTH	155
4.6 DISCUSSION	159
CHAPTER 5	161
EXPERIMENTAL SET UP FOR THE ANALYSIS OF THE FUNCTIONALITY OF ARTIFICIAL URINARY SPHINCTERS	161
5.1 EXPERIMENTAL TEST DESIGN	162
5.1 EXPERIMENTAL TEST BENCH	163
5.2 URETHRAL OCCLUSION DEVICE	165
5.3 DATA ACQUISITION SYSTEM	167
5.3.1 ARDUINO BASED SENSOR-INSTRUMENTATION	167
5.3.2 ARDUINOUI: LABVIEW-BASED USER INTERFACE.....	170
5.4 SET UP AND CALIBRATION	173
5.4.1 THE CALIBRATION PROCEDURE	175
CONCLUSIONS	177
APPENDIX.....	185
A.1 PIG STOMACH HISTOLOGY	185

A.2 HORSE URETHRA HISTOLOGY	186
A.3 TECHNICAL DATA OF THE PRESSURE SENSORS	189
A.4 ARDUINO SOFTWARE	192
A.5 LABVIEW USER INTERFACE SOFTWARE	193
REFERENCES	199
<i>WEB SITES CONSULTED:</i>	202

INTRODUCTION

The technological progress of this era has led to a general improvement of the life quality and this may be considered not only due to all fundamental results and discoveries reached in specific science fields but mostly due to an important integration of different knowledges, such as mechanics, electronics, biology, surgery, physiology and more over. This fact led to an overall growth of new interdisciplinary professionals and knowledge fields, such as the bioengineering.

These epistemological considerations are reminiscent of James Clark Maxwell's, a greater supporter of the knowledge's fellowship, about his point of view on the "cross-fertilization of sciences": *"Whatever it may be said about the importance of aiming at a depth rather than breadth of our studies, and it may be strong in the present time the demand for skilled people, there will always work not only for those who build special sciences and on them they write monographs, but also for those that disclose communications between different groups of knowledges to facilitate an healthy interaction between them. And in a university, we are particularly required to take into account not only the unity of the science itself, but also the fellowship of those who work in science"* [G. Peruzzi, 2010].

However, the specific contribute of bioengineers to the improvement of the quality of life may be linked to an evolution of the specific treatments of people diseases by means of the introduction of a strong engineering point of view in all medical problems which until now was evaluated exclusively by a surgical and clinical basis.

Consequences are relevant not only in health but also in terms of social and economic fields, especially when diseases involve a large part of the world population.

This thesis is an example of how an engineering approach to clinical problems may improve not only the health of patients but also socio-economic conditions of the

population. In fact, this work aims to be a contribution to improving the treatments of *obesity* and *urinary incontinence* diseases, two big challenges which involves some hundreds of millions of people worldwide confirming the strong social and economic impacts [Flegal et al., 2012; Knai et al., 2007; Griebling et al., 2014; Brandes et al., 2014].

The 20th century was subjected to an extreme increase in population prevalence of *obesity*. Despite recent surveys suggest that the increase in prevalence previously observed may not be continuing at a similar rate, there are no indications that the prevalence of obesity is declining. However, in 2009-2010, the prevalence of obesity was 35.5% among adult men and 35.8% among adult women in USA [Flegal et al., 2012]. European populations are also largely affected by obesity conditions [Knai et al., 2007] and overweight and obesity are also diffused among child population [Huston et al., 2009]. The most important long-term consequence of childhood obesity is its persistence into adulthood, with all the associated health risks. The economic costs of obesity have been assessed in several developed countries and are in the range 2-7% of total health care costs, as shown in table 1.

Country	Year	BMI	Estimated direct costs	National health care costs
Australia	1989–1990	>30	A\$ 464 million	>2%
France	1992	≥27	FF 12000 million	2%
Netherlands	1981–1989	>25	NLG 1000 million	4%
USA	1994	>29	US\$ 45800 million	6.8%

Table 1 - Economic costs estimation of obesity by the World Health Organization (2000).

These are conservative estimates based on variable criteria but clearly indicate that obesity represents one of the largest items of expenditure in national health care budgets [WHO, 2000]. This highlights the importance of preventing weight gain throughout adult life. The treatments of obesity that today ensure reliability results in terms of weight loss are those of bariatric surgery. Nowadays, bariatric

procedures that ensure effectively long term results consist in laparoscopic techniques, such as the gastric banding, the sleeve gastrectomy and the gastric bypass. Despite patients who undergo bariatric surgery are likely healthier than severely obese others, early and late rates of adverse events associated with bariatric surgery remain problematically high. Perioperative and postoperative risks include infection, respiratory failure, acute kidney injury and death, mainly due to the invasiveness of the procedures. There is consequently a need for less-invasive weight loss interventions to bridge the current gap in our management approach to obesity and also to improve access. Emerging endoscopic technologies can reproduce some of the anatomic alterations created during bariatric surgery and are proving to be effective treatments for obesity in selected patients. They additionally offer the potential advantages of reduced invasiveness, reversibility, repeatability, and cost-effectiveness.

The specific bariatric procedure and the post-surgical conformation of the operated gastrointestinal organs are usually defined on clinical basis only, considering calories intake requirement and surgical parameters. Further physiological and mechanical processes should be considered, as the physio-mechanical functionality of the gastrointestinal organs and the relationship between food intake, mechanical stimulation of gastrointestinal wall, adsorbing capacity and feeling of satiety. Methods and procedures of bariatric surgery should be consequently defined by integrating competences in the areas of surgery, physiology and biomechanics. Considering the specific bariatric procedure, computational models of the gastrointestinal tract can be developed and applied to quantitatively investigate the mechanical stimulation of the gastrointestinal wall because of food intake. Physiological investigations can be performed to identify quantitative relationships between mechanical stimulation of the gastrointestinal wall, adsorption capacity and feeling of satiety. Depending on the mentioned parameters, an optimized bariatric procedure can be identified for the specific patient.

Regarding *urinary incontinence*, it is a well-known fact that it is highly prevalent in older adults and that the prevalence increases with age [Griebing, 2014]. Urinary incontinence affects almost half of middle-aged and older women and is associated with substantial medical and psychological morbidity and diminished quality of life [Subak et al., 2014]. There is a significant difference between the urinary incontinence rates of elderly people living in the community and those residing in nursing homes as well as those admitted to the hospital. The exact prevalence rate varies according to many factors including the population studied, the definition of urinary incontinence used in the survey, and how the survey is conducted. For community-dwelling elders who are older than 60 years old, the prevalence of urinary incontinence ranges from 15 to 35 %. The rate is twice that for women than men. The prevalence of incontinence in patients two weeks after admission to nursing homes is revealed at a rate of 39 % and that of patients who permanent are residing there is estimated at 50 % [Griebing, 2014]. Urinary incontinence is estimated to affect up to 19 % of men, with 10 % of cases further stratified as stress urinary incontinence. Although multiple etiologies exist for man incontinence, prostatectomy remains the most common iatrogenic etiology with published rates ranging from 2 to 43 % [Brandes et al., 2014]. While curative for the majority of men who requires it, the urinary and sexual dysfunction associated with a radical prostatectomy can have deleterious effects on a patient's quality of life. Specifically, *post-prostatectomy incontinence* has been shown to negatively impact quality of life even in those patients with minimal incontinence. After removal of the post-operative catheter, nearly all patients will experience at least transient stress urinary incontinence. Additional factors that have been shown to be associated with post-prostatectomy include patient age, body mass index (BMI), baseline urinary function, prior prostate procedures, surgeon experience, nerve sparing technique and post-op bladder neck contractures, among others [Brandes et al., 2014]. Given the prevalence and treatable nature of the condition, stress urinary incontinence remains an important topic with significant implications on quality of life issues. Furthermore, the cost of treatments of

urinary incontinence are substantial, accounting for over \$20 billion per year in the United States, with a majority attributed to resources used for incontinence management or routine care that patients pay out-of-pocket for absorbent pads, protection, and laundry. Annual cost estimates vary widely between \$50 and \$1000 per person per year and increase with the severity of urinary incontinence [Subak et al., 2014], confirming the high social-economic impact of urinary incontinence, as well as the obesity problem.

Nowadays, clinical treatments of incontinence consist of conservative procedures and surgical procedures. Despite some recent studies showed the cost effectiveness of the surgical rather than conservative techniques at 1 year [Richardson et al.,2014], their reliability and durability should be investigated further. A common surgical treatment in case of severe incontinence is the *artificial urinary sphincter* placement and, since the initial concept was introduced in 1949 with a lot of clinical complications, the artificial urinary sphincter has undergone multiple improvements and modifications, resulting as the gold standard treatment [Brandes et al., 2014]. Artificial sphincters are devices allowing the continence by means of urethral duct occlusion obtained by the application of a constant pressure within an occluding cuff. In healthy conditions, the physiological occlusion is provided by the external sphincter muscle and the internal sphincter. Consequent mechanical effects on the urethral tissues may induce some modifications and possible degenerative phenomena. Moreover, the prosthetic device can have a limited life. The occluding cuff has undergone some improvements, as the addition of a fluoro-silicone gel in the inner surface of the cuff to prevent excessive internal friction induced by local bending. Moreover, a narrow-backed cuff was adopted, leading to a modified shape of the cuff shell that interacts with soft tissue in the border region with reduced shear effect, thus decreasing the risk of erosion and tissue atrophy. Despite positive post-surgery outcomes, a relevant proportion of patients requires revision surgery, due to complications including infection, urethral atrophy, erosion, and mechanical failure [Brandes et al., 2014]. In particular, urethral atrophy and tissue erosion are

different effects of the same problem, due to persistent cuff-induced urethral compression. Urethral atrophy consists in the circumferentially reduction of bulk tissue properties in time. As a consequence of atrophy, a cuff that was initially sized appropriately may become inadequate for ensuring continence. Over time, tissue degradation may become erosion, inducing degenerative effects that are related to the stress and strain distributions within urethral tissues during occlusion.

The design of an artificial urinary sphincter is mostly performed on a clinical and surgical basis, but it should be supported by investigation of its mechanical interaction with the surrounding tissues. In this way, it is possible to identify the sphincter pressure conditions that ensure continence, as well as the conformation of the device to minimize the invasiveness of the prosthesis.

Computational methods can be adopted for the analysis of biological tissues and structural response, mostly with regard to the evaluation of the lumen occlusion process. The development of reliable computational models requires the exhaustive experimental characterization of the constituent tissues through histological analysis and mechanical testing. The histological analysis aims to identify the configuration of tissues, including the content of collagen or muscle fibers in the different layers. This information allows a preliminary hypothesis to be formed regarding the mechanical behavior and suggesting the experimental tests to develop [Natali et al., 2016a]. Experimental investigation on humans is complex and must take into account an extended group of subjects of similar age, body conformation and health conditions. At present, experimental testing on human urethra is performed *in vivo*. In order to carry out *ex vivo* tests, a suitable animal model should be selected, presenting similarity to the human penile urethra in terms of histology and overall conformation aiming at developing a method that can be extended on the basis of an experimental investigation on human samples already in progress. The experimental results allow the definition of an appropriate constitutive formulation and identification of the related constitutive parameters [Natali et al., 2016b; Natali et al., 2017].

To address these issues, the goal of the current work is to provide both a computational approach to the design of an innovative endoscopic bariatric technique and an experimental setup design for the mechanical test of the urethral structure during the duct occlusion given by an artificial urinary sphincter cuff. The *chapter 1* considers both clinical problems of obesity and urinary incontinence, starting from the anatomical analysis of both the *gastrointestinal* and *lower urinary* tracts involved to such diseases to an overall description of current state of arts in the relative surgical treatments. *Chapters 2* and *3* describe experimental and computational approach to give a complete mechanical characterization of both tissues and structures of the stomach and the urethra. In detail, pig stomach and horse urethra are mechanically investigated by means of tensile test of tissue samples sectioned from their wall and by means of inflation test of their entire structure. Numerical solid models of the structures were developed to simulate their mechanical behaviour and validated by experimental results. Such models are the basis which allow to design both the novel surgical and experimental procedure required. According to these latter issues *chapter 4* focus on the design of clips involved to the specific endoscopic gastric bending procedure proposed and their mechanical analysis by means of computational tools. On the other hand, *chapter 5* describes all the devices designed and realized in order to set up experimental inflation tests of the urethra under artificial sphincter occlusion and their corresponding data acquisition.

CHAPTER 1

CLINICAL PROBLEMS: SURGICAL SOLUTION FOR THE TREATMENT OF OBESITY AND URINARY INCONTINENCE

In this chapter are discussed the main treatments of the two clinical problems of obesity and urinary incontinence. For both problems a first description of the same problems as such is given, followed by an overall anatomical description of the involved body parts. Finally are discussed the main surgical solutions currently adopted for the resolution of these clinical conditions.

1.1 OBESITY

Obesity is a condition of abnormal accumulation of fat in adipose tissues as a result of an imbalance between food intake and energy expenditure, and it may adversely affect the health of individuals. It varies not only in the amount of excess fat, but also in the distribution of that fat within the body. Many are the variables that underlie the mechanism of weight gain within the organism and health consequences vary considerably between obese individuals.

Body Mass Index (BMI) is the most widely used measure of obesity. It is defined as the weight in kilograms divided by the square of height in meters (kg / m^2). Table 1.1 is given by the World Health Organization (WHO) and shows a classification of overweight and obesity, according to BMI. An overweight condition is classified obesity when $\text{BMI} > 30.0$. Although BMI can be used to estimate the prevalence of obesity within a population and the risks associated with it, it does not consider the distribution of body fat. For this reason, it cannot be considered as a discriminating index to individuals or populations having different amounts of fat

and health risks associated with it. However, the NHANES (National Health and Nutrition Examination Survey, USA), by means of X-ray absorptiometries investigations, showed a high correlation between BMI and percentage of body fat [Flegal et al., 2012].

Classification	BMI	Risk of comorbidities
Underweight	<18.50	Low (but risk of other clinical problems increased)
Normal range	18.50–24.99	Average
Overweight:	≥25.00	
Preobese	25.00–29.99	Increased
Obese class I	30.00–34.99	Moderate
Obese class II	35.00–39.99	Severe
Obese class III	≥40.00	Very severe

Table 1.1. Classification of adults according to BMI from World’s Health Organization.

Obesity is often associated with multiple co-morbidities. Health consequences of obesity are many and varied, ranging from an increased risk of premature death to several debilitating complaints that have an adverse effect on quality of life. Obesity is a major risk factor for non-insulin dependent diabetes mellitus (type 2 diabetes), cardiovascular diseases and cancer. It has also important metabolic complications: enlarged adipose tissue results in the infiltration of macrophages and unbalance of pro-inflammatory and anti-inflammatory factors secreted by adipose tissue, which lead to the promotion of inflammation, impairment of insulin sensitivity and dysregulation of lipid metabolism. The adipose tissue can affect many other tissues, including the liver, skeletal muscle and heart, via the production of free fatty acids and therefore has a critical role in the pathogenesis of insulin resistance, dyslipidemia and non-alcoholic fat liver disease [Jung et al., 2014]. Furthermore, overweight and obese patients usually present other debilitating health conditions, called functional diseases. Functional diseases have a mechanical origin due to the large amounts of excess weight that must be carried and have adverse health consequences. The main related complications are osteoarthritis and gout, pulmonary diseases such as hypoxemia and sleep apnea

that can have fatal consequences associated with cardiac arrhythmias [WHO, 2000].

In many industrialized countries obesity is associated with various psychological and psychosocial problems in terms of undesirable bodily appearance and discrimination. These problems often lead to a worsening of the situation resulting in depression and binge-eating disorders. Analyses of large social surveys have shown that, compared with their non-obese peers, obese are likely to complete fewer years at school, and less likely to be accepted by prestigious schools or to enter desirable professions. Furthermore, overweight young women in the United Kingdom and the USA earn significantly less than healthy women who are not overweight or than women with other chronic health problems [WHO, 2000; Huston et al., 2009; Booth et al., 2015].

When the failure to control for cigarette smoking and unintentional weight loss are removed from the analysis of mortality data, there is an almost linear relationship between BMI and death. The longer the duration of obesity, the higher the risk. Severe obesity is associated with a 12-fold increase in mortality in 25-35-year-olds compared with lean individuals [WHO, 2000].

1.1.1 ANATOMY OF THE GASTROINTESTINAL TRACT

The gastrointestinal tract is comprised of the gastrointestinal tube and forms the digestive system together with accessory organs such as teeth, tongue, salivary glands associated with the oral cavity, the pancreas and liver whose secretions are delivered into the duodenum of the small intestine (figure 1.1). The principal functions of the digestive system are mechanical and chemical digestion of food, absorption of nutrients, fluid, electrolytes and elimination of indigestible material in feces. In addition, since the lumen of the digestive tube is an extension of the outside world, its epithelial surface must serve as a barrier that allows maintenance of physiological conditions in body tissues distinct from conditions in the lumen. Moreover, the tube must prevent entry of potential pathogens, and hence it also has significant immunological functions [Amerongen, 2010].

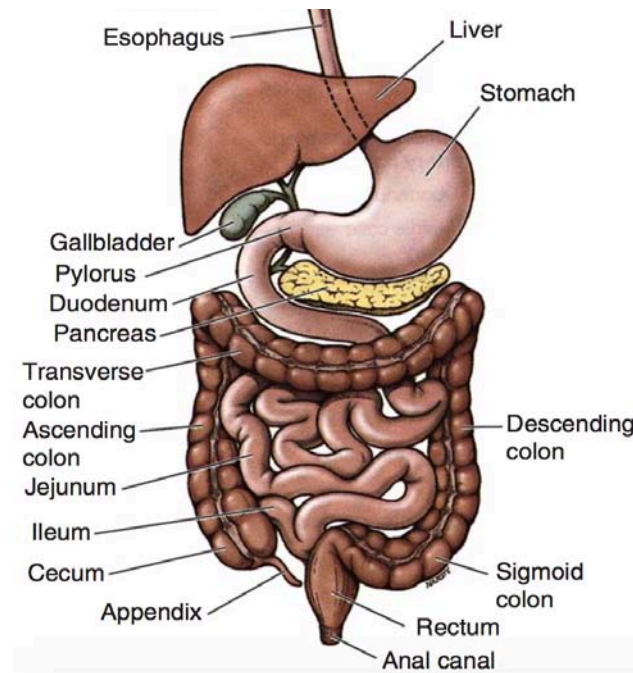


Figure 1.1. Illustration of the digestive system [Amerongen, 2010].

The gastrointestinal tract is covered by a thin layer of serosa called peritoneum, specifically visceral peritoneum (as opposed to parietal peritoneum, which covers the wall of the abdominal cavity). The stomach, small intestine, and portions of the large intestine are suspended in the abdominal cavity by mesenteries, which are sheets of tissue connecting these organs to the body wall. Mesenteries are continuous with the serosa of parietal and visceral peritoneum, and they carry blood vessels, nerves, and lymphatics to serve the digestive tube. Mesenteries are also a common location for fat to deposit.

The small intestine is the first part of the intestine it completes the chemical breakdown of food and is the absorption of almost all nutrients.

THE STOMACH

The stomach is a J-shaped organ that stores, blends, grinds and digest the food before the delivery into the duodenum (figure 1.2). The shape of the stomach varies among individuals and depends on its filling. When food is ingested, the body is stretched by a tubular shape to a bag-like shape. Its mean capacity

increases from around 30 ml at birth, to 1000 ml during puberty and until 1500 in adults.

The different parts of the stomach have physiological differences well defined. It has a front and rear surface, a major and minor curving and two orifices, the cardiac orifice and the pylorus. Along the lesser curvature of the stomach there is a distinct notch, the incisura angularis, which is characterized by the arrangement of the involuntary muscle fibres of the stomach wall.

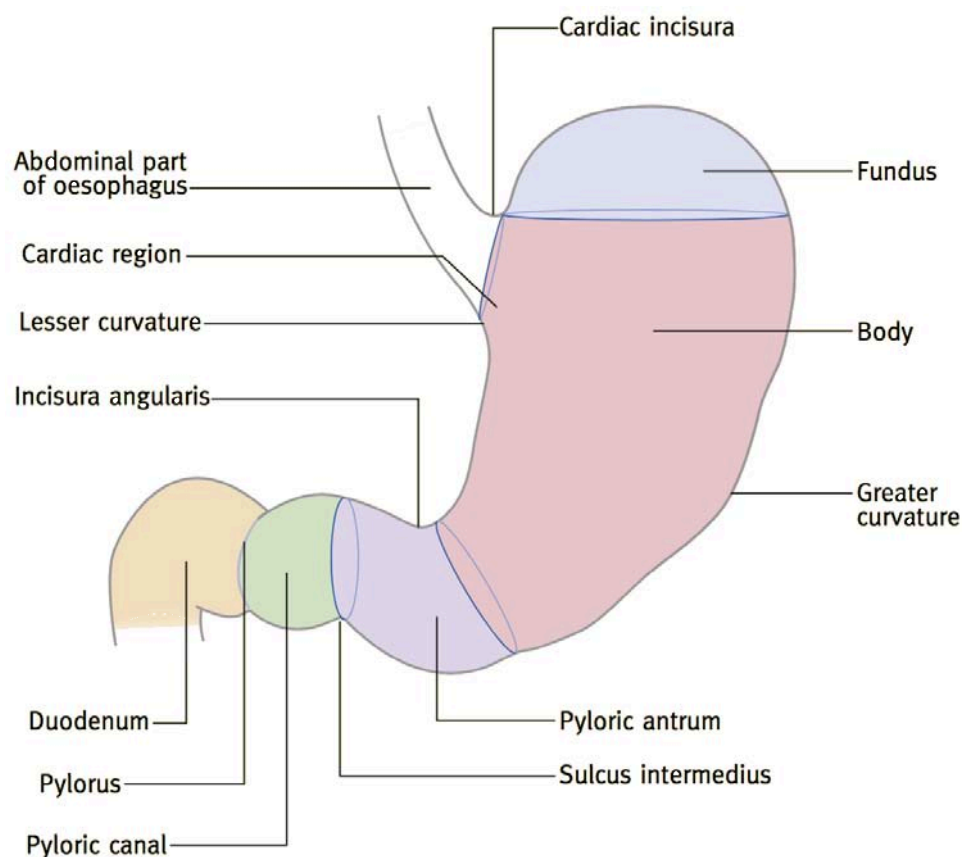


Figure 1. 2: The parts of the stomach from Hellis, 2011.

However, the three main functional regions of the stomach are the fundus, the body and the pyloric antrum (figure 1.2). The fundus is on the left of the cardiac orifice and often filled with air. The body of the stomach passes from the cardiac orifice to the incisura angularis, stores food and is the part of the organ that contains the parietal cells which secrete HCl. The pyloric antrum is a muscular

antrum that mixes food with digestive fluid and generates fluid motions, contributing to the breakdown of the particles until they are small enough to pass through the pyloric sphincter. In the pyloric antrum is produced the hormone gastrin, responsible for the hormonal phase of gastric acid secretion. The pylorus is easily identified by palpation of the very distinct ring of sphincter muscle and is also marked by a constant vein (of Mayo) that crosses at this level. [Bellmann et al., 2016; Hellis, 2011].

BLOOD SUPPLY AND INNERVATIONS OF THE STOMACH

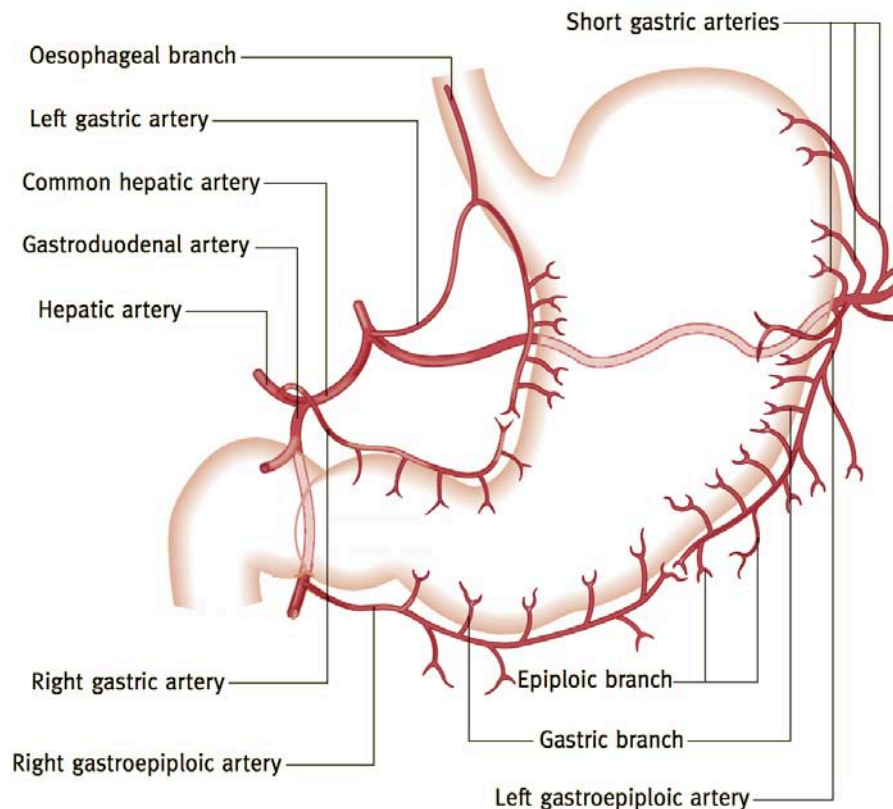


Figure 1.3. Stomach vessels supply from Hellis, 2011.

The stomach is the only organ characterized by a blood supply in both its sides, along the greater and smaller curvature. Gastric arteries arise from all three branches of the celiac trunk: the left gastric artery (the largest vessel) and the right gastric artery that come from the first hepatic artery branch, the right

gastroepiploic artery comes from the gastro-duodenal branch of the hepatic artery, the left gastroepiploic artery and short gastric arteries that come from the splenic artery.

The corresponding veins drain into the portal system, mostly either in the mesenteric splenic vein or in the superior, although some flow directly into the portal vein.

The left gastric artery also presents an esophageal branch, passing through the esophageal hiatus of the diaphragm to provide the lower esophagus. It is accompanied by the corresponding esophageal vein that flows into the left gastric vein. Lymphatic drainage follows the usual rule of accompanying the blood supply of the organ. It passes primarily to lymph nodes along the gastric curvatures [Hellis, 2011].

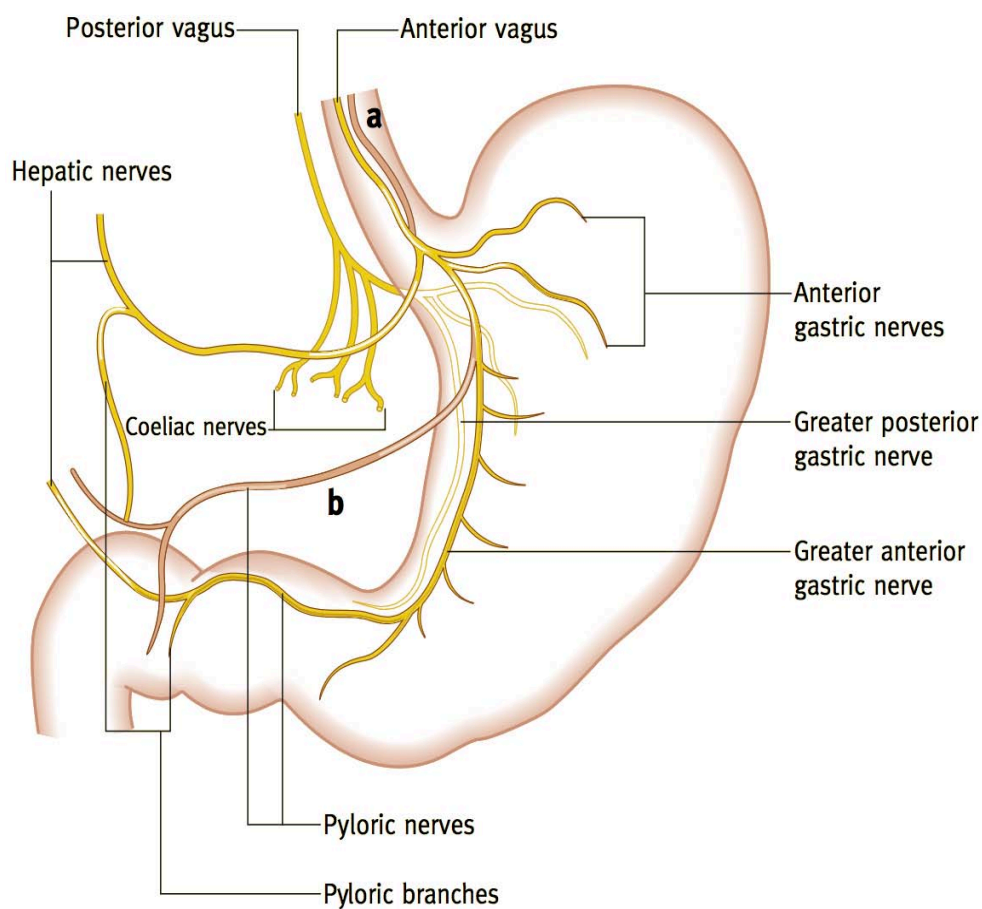


Figure 1.4. Stomach innervation from Hellis, 2011.

HISTOLOGY OF THE STOMACH

The walls of stomach have four major layers (figure 1.5). From the external surface and going toward the lumen, they are respectively serosa (peritoneum), muscularis propria, submucosa and mucosa [Amerongen, 2010].

The serosa is comprised of simple squamous epithelium overlying a thin layer of connective tissue. By means of its smooth mesothelium, a serosa allows the stomach to slide past adjacent serosa-covered structures.

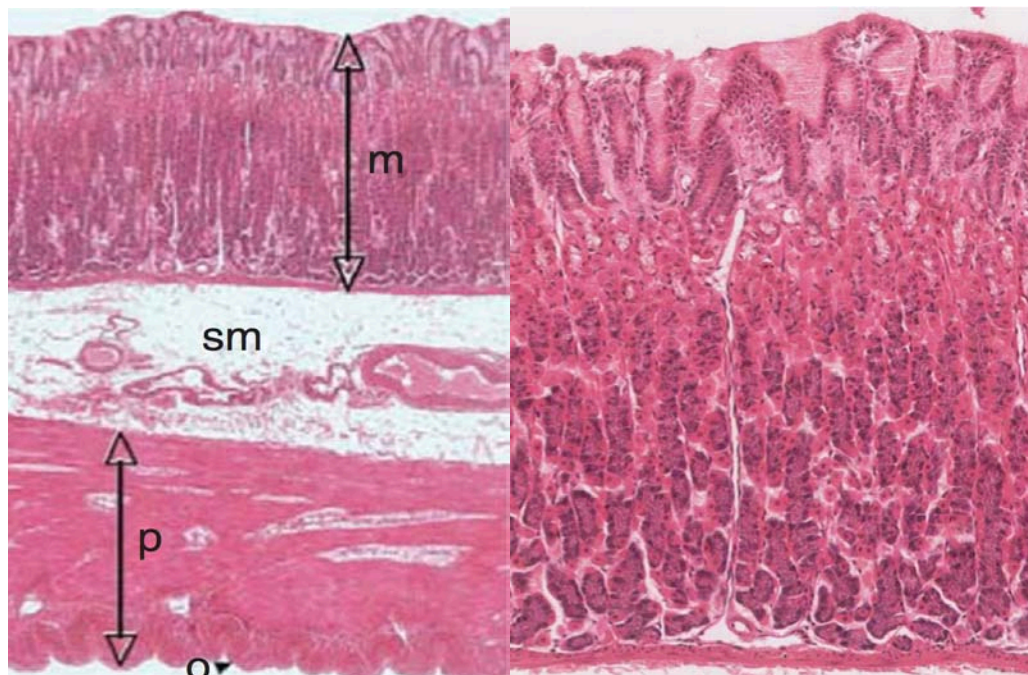


Figure 1.5: On the left the major layers of the stomach (outer layer(O), muscularis propria(P), submucosa(SM), mucosa(M)); on the right the mucosa of the stomach: At the top, the lumen of the stomach is covered by pale surface mucous cells, which also line the gastric pits that invaginate the mucosa for about one-quarter of its thickness. Gastric pits lead into tubular gastric glands lined in their upper half with pink-staining parietal cells and in their lower half with purple-staining chief cells [Amerongen, 2010].

The muscularis propria of the stomach consists of outer longitudinal, middle circular, and inner oblique layers of smooth muscle. At the pyloric–duodenal junction, the circular layer is enlarged to form the pyloric sphincter.

The submucosa is a layer of loose connective tissue that carrying arteries, veins, and larger lymphatics to supply the muscularis propria and the mucosa.

The mucosa (figure 1.5) is itself made up of three layers: muscularis mucosae, lamina propria and epithelium [Amerongen, 2010].

The muscularis mucosae is a thin layer of muscle, which, like the muscularis propria, is organized into inner circular and outer longitudinal fibers. The lamina propria is a layer of loose connective tissue containing capillaries and nerves that supply the epithelium. The epithelium is the innermost layer of the mucosa that is extensively invaginated into the lamina propria to form the stomach glands. The superficial segment of each tubular invagination is called a gastric pit. Each gastric pit branches at its base to form the deeper cardiac, gastric, and pyloric glands. Thus, the gastric pits can in a sense be regarded as ducts of the deeper glands. Undifferentiated stem cells are located at the bases of gastric pits. These cells undergo mitosis and provide replacements for surface mucous cells that are lost as well as for other cells in the deeper glands. Mucous cells at the stomach surface are replaced by stem cells approximately every 3 to 6 days. Parietal cells and chief cells have a much slower turnover rate. The cardiac glands of the stomach are situated near the junction with the esophagus. They are coiled tubular glands made up of mucous cells. The pyloric glands, like the cardiac glands, are coiled tubular glands. They are mainly made up of mucous cells but enteroendocrine cells are also present, and indeed are most numerous in this part of the stomach. Gastric pits are most prominent in the pyloric region, being conspicuously longer in this region than in the cardiac region and body of the stomach.

The lining of the contracted stomach is characterized by folds called rugae. They have a core of submucosa and flatten out when the stomach is full, allowing a degree of distensibility.

STOMACH FUNCTION

The ingestion of food stimulates gastric acid secretion and changes the motility of the stomach. The high acidity of the gastric juice helps to kill potentially harmful bacterial contamination of the ingested food. The acidity of the gastric juice also

activates pepsin that helps to digest ingested peptides. At the same time the smooth muscles of the fundus of the stomach initially relax via a vagal reflex to allow to store the ingested nutrients in the proximal stomach while the distal stomach 'grinds' the gastric content and slowly delivers the chime into the duodenum where it is sensed and duodenogastric reflexes are stimulated altering the gastric function. The tone of the proximal stomach gradually increases and the ingested food is moved towards the distal stomach. The distal part is able to crush the soft food particles and controls the delivery of food into the duodenum. Besides the exposure to the acidic gastric juice the stomach ensures that the ingested nutrients are delivered into the duodenum at a rate that does not exceed the digestive capacity of the intestine. Thus, the coordinated gastric motor function is considered critical for the gastric phase of the digestion of food.

This complex process is regulated by different and most likely redundant feedback mechanisms: the nutrient stimuli (volume and chemical properties of intraluminal nutrients) are sensed by mechanosensory and chemosensory receptors. These receptors trigger either enteric (intrinsic) or vagal and sympathetic (extrinsic) pathways to regulate and control motor and secretory function sensed by specific receptors in the gut wall and initiate reflexes via either the intrinsic (enteric) nervous system or extrinsic (vagal and sympathetic) pathways, to control and coordinate gastric contractile activity [Holtmann et al., 2014].

THE BRAIN-STOMACH AXIS

The digestive tract and not only the stomach senses the gastrointestinal content including nutrients ingested with meals in various ways. Volume or wall tension, osmolality, acidity, and macronutrient composition represent the dominant sensory modalities [Holtman et al., 2014]. This sensory information is partly mediated via the enteric nervous system to facilitate secretion, absorption, and motility and does not reach a level of consciousness. Awareness of digestive sensations, such as fullness and satiation, is required to regulate eating behavior. On the other hand, visualization of food and the anticipation of eating initiates profound changes of digestive function characterized by a significant increase of

gastric acid secretion and the release of a variety of gastrointestinal hormones. [Holtmann et al., 2014].

THE SMALL INTESTINE

The small intestine continues the gastrointestinal tract from the stomach. It is the place in which the chyme becomes kilo and the longest of all the digestive tract organ. The small intestine is long more than 7 m and the diameter of 2.5 cm, folded on itself.

The small intestine starts from the pylorus and ends with the ileocecal valve in the terminal ileum. It is in relation with the abdominal wall and is connected to the spinal column via a mesentery. The distension of the viscera, due to the food bolus, unleashes a nervous reflex that causes the contraction of the circular smooth muscle. The peristaltic reflex is due to an involuntary contraction linked to the activity of the autonomic nervous system that sends impulses to the peripheral nerve distributed network in the intestines such as the myenteric plexus of Auerbach. This contraction causes the so-called *peristaltic wave*, characterized by short duration both in space and time: in fact, it invests bowel segments limited and runs out after a few seconds, then resume soon after. The movement allows substances to proceed in a certain direction and promotes the mixing of the chyme with gastro-enteric juices. Furthermore, it pushes the chyme in contact with the intestinal wall favoring the absorption of liquids, completes the chemical breakdown of food and is involved in the absorption of almost all nutrients. It plays a major role in glucose homeostasis and in the pathogenesis of diet-induced diabetes. Within the mucosa of the small intestine, enteroendocrine cells sense luminal nutrients and release gut peptides that are thought to mediate satiety and enhance insulin secretion.

Thus, for all these reasons, bypass of the proximal small intestine may contribute to weight loss and diabetes improvement.

The small intestine is divided into three portions: the *duodenum*, *jejunum* and *ileum*.

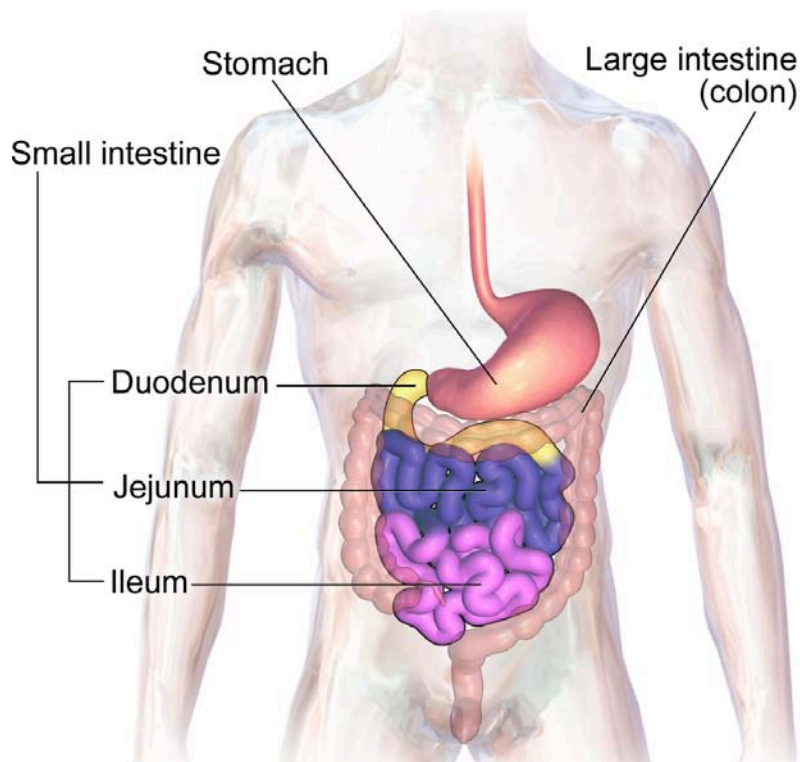


Figure 1.6. A small intestine illustration from Wikipedia: duodenum (yellow), jejunum (purple), ileum (pink)

THE DUODENUM

The duodenum is the first, as well as the shortest small intestine. It is placed above the navel, is about 25 cm long and has a diameter of about 4 cm. It has a “C-like” shape with the lower tract elongated, whose convexity is directed to the right and the curve is anteroposterior. The pancreatic and epatic ducts flow in it and is the fixed and thicker portion of the small intestine.

THE JEJUNUM

This is the second part of the small intestine, has a mean length of about 2.5 m and has a thick and very vascularized wall. Its membrane has circular folds, each of which has many tiny finger-like projections on its surface known as villi. In turn, the epithelial cells that line these villi possess even larger numbers of microvilli. The folds of the intestinal part increase the useful surface to maximize the absorption.

THE ILEUM

The ileum is the third and final part of the small intestine. It follows the jejunum and ends at the ileocecal junction, where the terminal ileum communicates with the cecum of the large intestine through the ileocecal valve.

The function of the ileum is mainly to absorb vitamin B12 and bile salts and whatever products of digestion were not absorbed by the jejunum. The wall itself is even made up of folds, each of which has many villi, thinner than jejunum ones. Therefore, the ileum, as well as the jejunum, has an extremely large surface area both for the adsorption (attachment) of enzyme molecules and for the absorption of products of digestion. Jejunum and ileum form the small intestine mesenteric portion, which comes with a very large structure, highly convoluted, folded on itself and characterized by greater mobility than duodenum.

1.1.2 BARIATRIC SURGERY

The psychological associations related with food showed that a substantial number of obese people eat for reasons other than hunger. These may include addiction, comfort or recreation, and these psychosocial aspects may make lifestyle modification almost impossible [Owers et al., 2014].

For patients who have failed with lifestyle measures or weight loss medications, bariatric surgery is often considered to be the next logical step towards achieving substantial weight loss and becoming more commonplace for patients with morbid or severe obesity. Consensus guidelines from a National Institutes of Health conference include BMI > 40 kg/m² or BMI > 35 kg/m² with obesity-related comorbidity as approved clinical indications for bariatric surgery [Chang et al., 2014; Owers et al., 2014].

Several surgical procedures to promote weight loss have been developed over the past few decades. These procedures vary in terms of the amount of gastric surface area restriction, intended nutrient malabsorption, effects on gastrointestinal hormones, weight loss outcomes, and risk of complications (table 1.2). Initial efforts in bariatric surgery started in the 1970s with the jejunoileal bypass, which

was a purely malabsorptive procedure, bypassing most of the small intestine. The jejunoileal bypass has since been abandoned due to the high rate of complications, which included deficiency of fat-soluble vitamins, bacterial overgrowth, calcium oxalate nephrolithiasis, and kidney and liver failure.

Contemporary bariatric surgery techniques involve a total weight loss with an average ranging from 20% to 35% of total body weight. The most common bariatric procedures performed worldwide are *laparoscopic Roux-en-Y gastric bypass* and *laparoscopic vertical sleeve gastrectomy*. Other two less common procedure are the *laparoscopic adjustable gastric banding* and the *biliopancreatic diversion with duodenal switch*.

	RYGB	LSG	LAGB
Weight loss	Highest	Moderate	Lowest
Gastric emptying	↑ or ↓	↑	No change
Plasma GLP-1 levels	↑	↑	No change
Plasma PYY levels	↑	↑	No change
Plasma ghrelin levels	Variable	↑	↓
Plasma leptin levels	↓	↓	↓
Plasma bile acid levels	↑	↑	No change
Fat malabsorption/fat-soluble vitamin deficiency	↑	No change	No change
Nephrolithiasis risk	↑	No change	No change
Diabetes remission	Highest	Moderate	Lowest
Short-term complications	Higher	Lower	Lower
Need for reoperation	Lower	Lower	Higher

Table 1.2. Comparison of the most common surgical procedures for weight loss from Chang et al., 2017

LAPAROSCOPIC ROUX-EN-Y GASTRIC BYPASS

The Roux-en-Y gastric bypass works as both a malabsorptive and restrictive operation. First, as shown in the figure 1.7, the stomach is divided into an upper stomach pouch (15÷30 ml) and a lower gastric remnant. The stomach pouch is then anastomosed to the mid-jejunum, and a jejuno-jejunal anastomosis is created to reconnect the biliopancreatic limb and the gastric remnant, thereby

allowing gastric, pancreatic, and biliary secretions to mix with food, which has passed through the pouch and proximal jejunum through the jejuno-jejunal anastomosis. Prior to this point, food is not absorbed, and the amount of food is restricted by the limited size of gastric pouch [Chang et al., 2017; Owers et al., 2014].

Newer versions of the gastric bypass, such as the ‘mini’ gastric bypass, are gaining in popularity as they involve only one anastomosis, although long-term results are not yet available, and there are sometimes problems with excessive bile reflux.

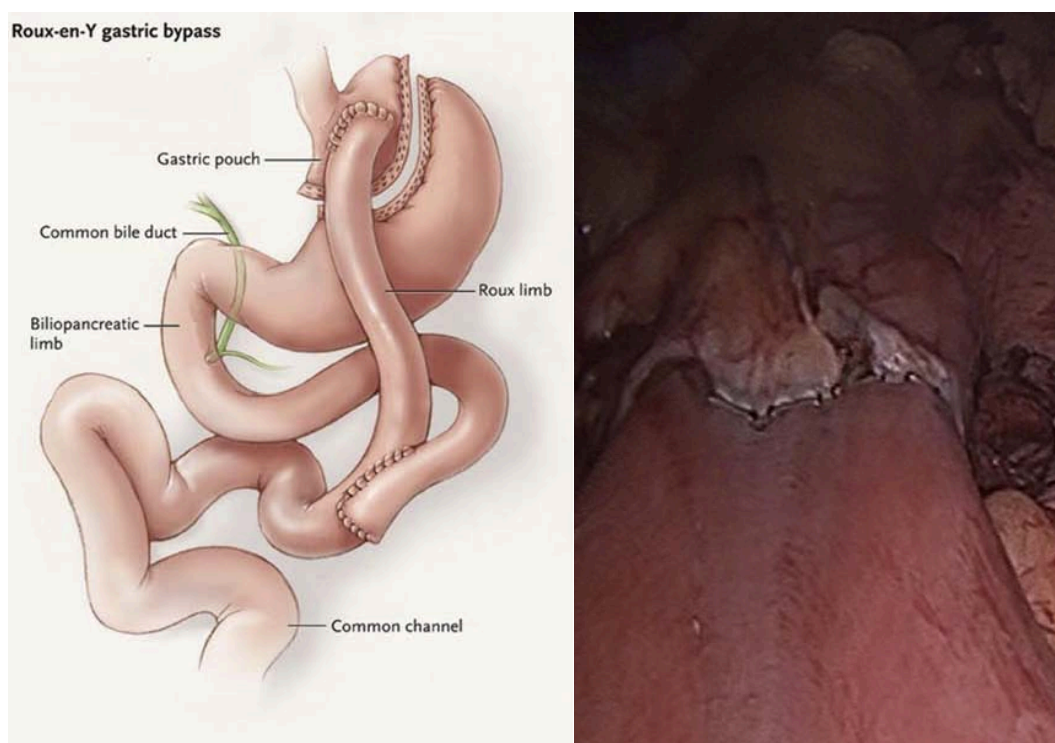


Figure 1.7. Illustration scheme of the Roux-en-Y gastric bypass from Chang et al (left) and intraoperative view of the gastro-jejunal anastomosis from Owers et al(right).

The gastric bypass is often considered the ‘gold standard’ and is the most commonly performed procedure in the USA and UK. Weight loss is about 60-70% and diabetes remission is as high as 80% at 3 years. With a mortality of 0.25% and a low long-term complication rate, the gastric bypass is often an ideal operation for patients with a larger BMI as it has a dual action of restriction and

malabsorption. Complications include anastomotic leak, bleed or stricture, but nutritional abnormalities are less common than in other malabsorptive operations such as the biliopancreatic diversion and duodenal switch [Owers et al., 2014].

LAPAROSCOPIC VERTICAL SLEEVE GASTRECTOMY

As figure 1.8 shows, this is a restrictive surgery that involves the removal of 70% to 80% of the lateral stomach. Due to its success in achieving weight loss and perhaps better safety profile compared to Roux-en-Y bypass, laparoscopic sleeve gastrectomy has become more common in the past few years and has eclipsed bypass techniques in the United States [Chang et al, 2017].

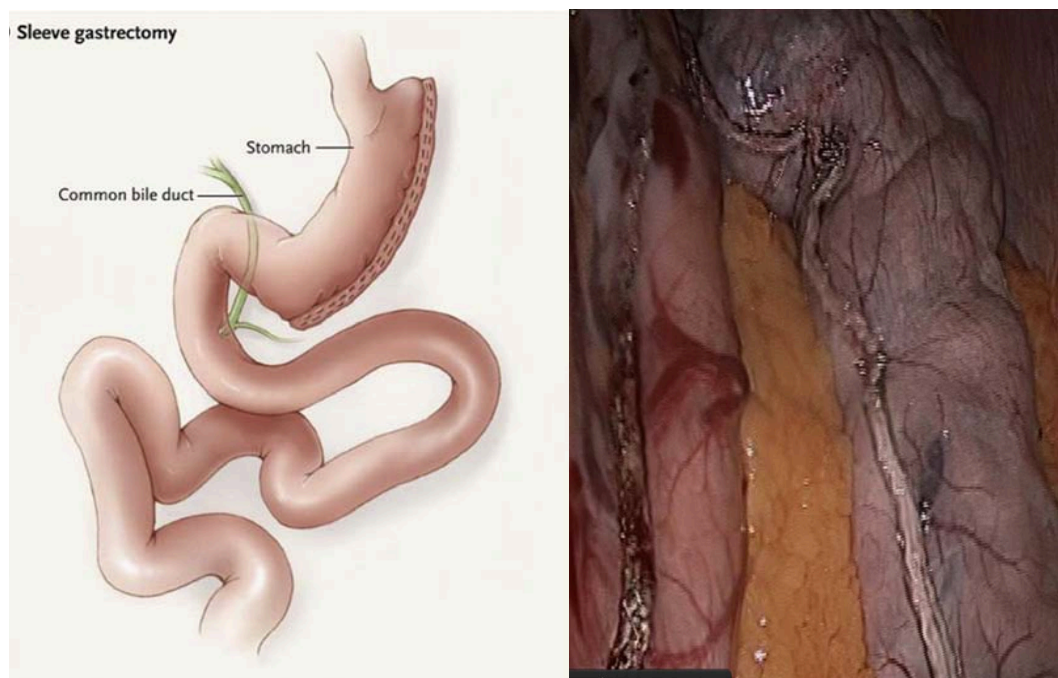


Figure 1.8. Illustration scheme of the sleeve gastrectomy bypass from Chang et al (left) and an its intraoperative view from Owners et al(right).

Patients still require a high level of compliance as liquid or soft foods and alcohol can pass easily and quickly through the sleeve, preventing maximum weight loss, or contributing to weight regain.

Although the sleeve does not cause a large degree of malabsorption, due to the decreased secretion of intrinsic factor from the remaining stomach, vitamin B12 deficiencies are more likely than following the gastric band [Owers et al.,2014].

Some patients who undergo sleeve gastrectomy may require subsequent conversion to a bypass or duodenal switch surgery, in which biliopancreatic secretions are diverted from the food until the last portion of the small bowel to increase malabsorption. Reported reasons for conversion of sleeve gastrectomy to gastric bypass or duodenal switch surgery include weight regain and intractable acid reflux [Chang et al., 2017].

LAPAROSCOPIC ADJUSTABLE GASTRIC BANDING

Laparoscopic adjustable gastric banding is another purely restrictive procedure that involves the insertion of an adjustable band immediately below the gastroesophageal junction on the proximal stomach (figure 1.9) [Chang et al., 2017]. The restriction of the band is adjusted with fluid via a port, connected to the tubing and placed subcutaneously on the anterior abdominal wall. This causes early satiety once the pouch is full, and the amount of food is restricted until ingested foodstuff has passed through the band. The band can be adjusted in the outpatient setting, either clinically based on patient comfort with swallowing, or with radiological assistance. Over-inflation of the band can lead to oesophageal dysmotility or dilatation, therefore optimum tightness must allow for food to pass through in reasonable time. A high level of patient compliance with dietary changes is required. Gastric banding has a significant number of long term complications, such as band slippage, erosion, port infections, and tubing issues. Average weight loss with the gastric band is around 50-60%. Resolution of type 2 diabetes is less than other operations [Owers et al., 2014].

Due to lower success in achieving weight loss and high risk of reoperation, gastric banding has fallen out of favor during the past few years and is now much less commonly performed than bypass or sleeve gastrectomy procedures, but remains in the repertoire of most bariatric surgeons. All 3 procedures are now almost exclusively done laparoscopically; the proportion of laparoscopic bariatric surgery procedures in a worldwide survey increased from 63% in 2003 to 96% in 2013 [Chang et al., 2017]. Unlike gastric banding, than bypass or sleeve gastrectomy

procedures have favorable effects on various hormones linked to hunger, satiety, and food preferences (table 1.2).

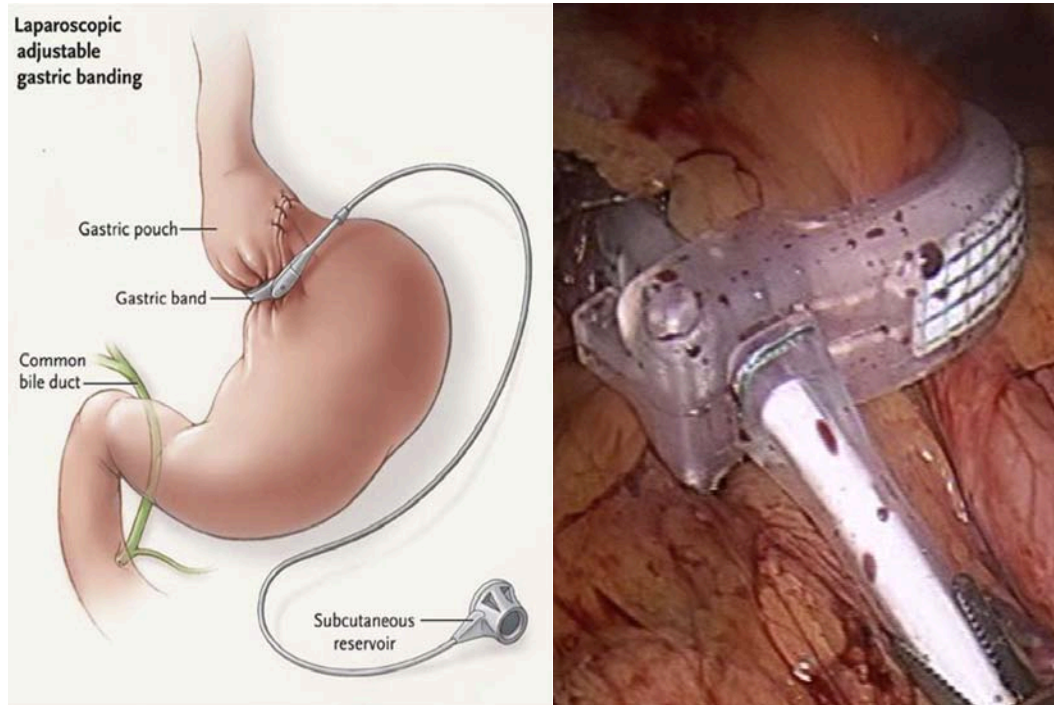


Figure 1.9. Illustration scheme of the gastric banding from Chang et al (left) and an intraoperative view from Owners et al (right).

BILIOPANCREATIC DIVERSION WITH DUODENAL SWITCH

This solution is a variation of the Roux-en-Y bypass technique and involves increasing the length of the Roux limb to upwards of 200 cm, resulting in increased malabsorption (figure 1.10) [Chang et al., 2017]. Although increasing malabsorption results in greater weight loss, these operations are less commonly performed due to the high risk of nutritional abnormalities following surgery. Although more successful in the super-obese patient, care must be taken to ensure they receive an adequate supply of vitamins and minerals, as the greater length of bypassed small bowel contributes to a high degree of malabsorption. In many cases, these operations are reserved for patients who have failed to lose weight following the gastric bypass [Owers et al., 2014].

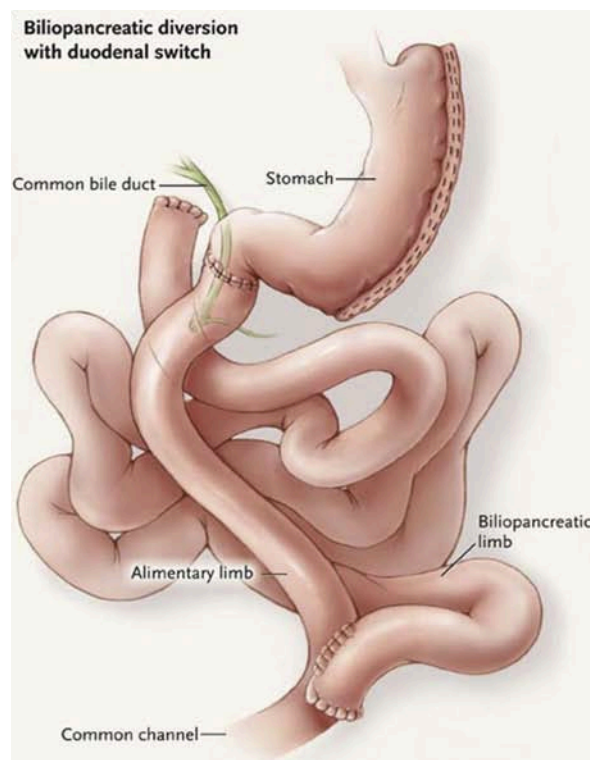


Figure 1.10. Illustration scheme of the biliopancreatic diversion from Chang et al.

COMPLICATIONS AND LONG TERM RISK OF DEATH

Bariatric surgery presents perioperative and postoperative risks, including infection, respiratory failure, acute kidney injury (AKI), and death. In an analysis of 27,736 bariatric surgery patients from 2006 to 2008 in the American College of Surgeons National Surgical Quality Improvement Program, it is found that 30-day mortality was relatively low (0.7%) and noted a shift from gastric banding to sleeve gastrectomy in more recent years, similar to overall trends in bariatric surgery.

Over the long-term, observational studies suggest that bariatric surgery is associated with a 30% to 45% lower risk of death compared to similar patients with severe obesity who did not undergo bariatric surgery. Most of the observed reduction in mortality risk is due to lower risks of deaths from cardiovascular disease, diabetes, and cancer. However, patients who undergo bariatric surgery are likely healthier than severely obese others so caution should be advised in interpreting these results. Patients undergoing surgery go through a rigorous, multistep process that includes evaluations and multiple appointments with a

multi- disciplinary team, and require successful weight loss prior to bariatric surgery, thereby displaying their commitment and motivation. It is important to note that 1 study found a 58% higher rate of non-disease related deaths (e.g., accidents, suicide) among patients who underwent bariatric surgery compared to matched controls. [Chang et al., 2017].

ENDOSCOPIC BARIATRIC TREATMENTS

Although mortality rates associated with bariatric surgery have decreased significantly and are now comparable to those of cholecystectomy or appendectomy in bariatric centers with high surgical volumes, early and late rates of adverse events associated with bariatric surgery remain problematically high.

There is consequently a need for less-invasive weight loss interventions to bridge the current gap in our management approach to obesity and also to improve access. Emerging endoscopic technologies can reproduce some of the anatomic alterations created during bariatric surgery and are proving to be effective treatments for obesity in selected patients. They additionally offer the potential advantages of reduced invasiveness, reversibility, repeatability, and cost-effectiveness. These advantages may allow endoscopic procedures to be applied to a larger segment of the population with moderate obesity.

In addition to inducing early satiety, it is thought that reducing the gastric reservoir capacity increases the stimulation of gastric mechanical and chemical receptors, alters gastric emptying, and modulates the level of gastric orexigenic hormones, which further contribute to weight loss. Several endoscopic bariatric techniques attempt to mimic these mechanisms by decreasing effective gastric capacity. These technologies include space-occupying devices and those that alter gastric anatomy. Space-occupying devices most commonly take the form of temporarily placed prostheses such as balloons. Endoscopic techniques that alter gastric anatomy use endoscopic suturing or plication devices.

INTRAGASTRIC BALLOON

The intragastric balloon (figure 1.11) is a relatively cheap and simple adjunct to weight loss. Performed endoscopically, a balloon is inflated within the fundus and left for up to 6 months. This helps the patient feel satiated more quickly and reduce appetite. Weight loss is usually modest compared to other operations, and weight regain commonly occurs once the balloon is removed.

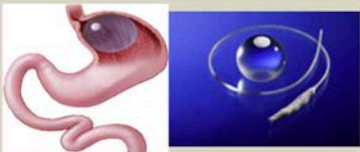
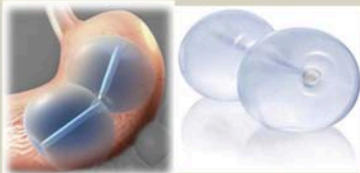

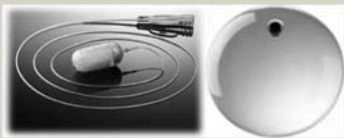
Intragastric Balloons (IGB)		
Orbera Apollo Endosurgery		Elastic spherical balloon made from silicone and filled with about 500-700 ml of saline. It is inserted and retrieved endoscopically.
ReShape Duo ReShape Medical		Saline solution-filled, dual intragastric balloon system with 2 balloons attached to each other by a flexible tube. Each balloon has independent channels so that unintentional leaks or deflation in 1 balloon do not impact the other balloon.
Spatz Adjustable Balloon System Spatz Medical		Saline filled intragastric balloon with an extractable inflation tube for volume adjustment, while the IGB remains in the stomach.
Obalon Gastric Balloon Obalon Therapeutics		Gas-filled balloon with a maximal volume of 250ml. It is compressed, folded, and fitted in a large gelatin capsule. Once the capsule is ingested, the catheter extends from the stomach to outside the body through the esophagus and the mouth. After balloon inflation, the catheter is detached and removed. One or more balloon can be swallowed during the same session.

Figure 1.11: Main intragastric balloons from ASGE.

Average weight loss of 10 to 15 kg can be seen, and this procedure is often used in morbidly or super obese patients prior to definitive surgery, in order to help them lose weight and reduce their operative risk.

Complications are mainly related to the endoscopic procedure required to place or remove the balloon, such as pharyngeal trauma or perforation, although vomiting, gastric reflux and balloon rupture are not uncommon. In rare cases, gastric or intestinal obstruction has been seen as a result of the gastric balloon [Owers et al., 2014].

ENDOSCOPIC SLEEVE GASTROPLASTIC

Endoscopic sleeve gastroplasty (figure 1.12) is a transoral endoscopic gastric volume reduction technique that reduces gastric capacity by creating an endoscopic sleeve in a fashion similar, but not identical, to sleeve gastrectomy. This is accomplished by a series of full-thickness sutures through the gastric wall, extending from the pyloric antrum to the gastroesophageal junction.

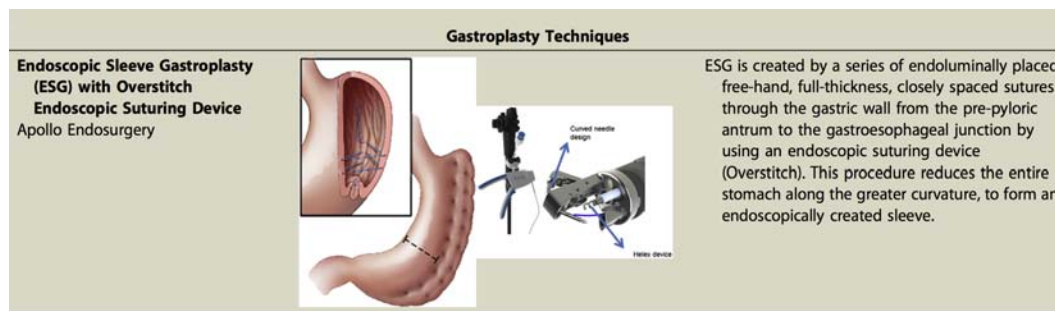


Figure 1.12: Endoscopic sleeve gastroplasty from ASGE .

This technique reduces the entire stomach along the greater curvature, creating a sleeve. Endoscopic sleeve gastrectomy is created by using a U.S. Food and Drug Administration (FDA)–approved and commercially available endoscopic suturing device (Overstitch; Apollo Endosurgery, Austin, Tex) that requires a double-channel therapeutic gastroscope to operate. Full-thickness suture placement is aided by the use of a tissue helix device that captures the targeted suture placement site on the gastric wall and retracts it into the suturing arm of the device [ASGE, 2015].

GASTROINTESTINAL BYPASS SLEEVE (ENDOBARRIER)

The endobarrier (figure 1.13) is a further endoscopic procedure, although a general anesthetic is usually required. The barrier sits in the first part of the duodenum, extending through the proximal jejunum and preventing absorption of food for approximately the first meter.

The endobarrier is licensed for use for up to 1 year, after which it is removed in the same manner. A mean weight loss of 19% has been demonstrated, although

long-term results are required to see if it is successful after removal. The endobarrier is marketed primarily as a cure for type 2-diabetes rather than a method for pure weight loss. Therefore, it is most useful in obese patients with type 2-diabetes who need to lose weight in order to improve their glycemic control.



Figure 1.13: Main endobarrier techniques from ASGE.

1.2 URINARY INCONTINENCE

Urinary incontinence is a condition that involves the loss of urine and can have a profound negative impact on quality of life. It is estimated that urinary incontinence potentially affects over 200 million people worldwide. In addition, it is likely that less than half of all incontinent individuals never seek medical treatment [Sievert et al., 2012]. Urinary incontinence is essentially considered a symptom of a primary cause, such as muscle damage or nervous system, loss of storage capacity, as well as the main diseases of the pelvic floor. The treatment options for urinary incontinence ranging from conservative treatment types, such as medications and behavioral changes, to surgical solutions.

A first classification of incontinence can be made considering the severity of the condition, distinguishing between transient and chronic incontinence. Transient

incontinence is caused by temporary factors that are usually solved and it's a common and reversible clinical problem. It is estimated that 30-50% of incontinence which afflicts the elderly population is transient [Griebing et al., 2014]. This dissertation work focus on chronic incontinence, a condition that persists over time and is not related to factors such as illness and use of medications.

1.2.1 CHRONIC URINANRY INCONTINENCE

When chronic incontinence develops in older adults, it is often associated with long-term persistent abnormalities in the structure or in the lower urinary tract function. Urinary incontinence in elderly patients with functional alterations usually can be attributed to hyper or hypo-activity bladder, urethral obstruction, or urethral incompetence.

Chronic urinary incontinence can be further classified in stress, urge, mixed, overflow, functional, and continuous urinary incontinence.

STRESS URINARY INCONTINENCE

Stress incontinence is the involuntary loss of urine associated with physical efforts. Events that are commonly associated with stress incontinence are coughing, laughing, sneezing or standing up from a sitting position, all characterized by an increase in intra-abdominal pressure. This type of phenomenon, in fact, takes place when the intra-abdominal pressure exceeds the urethral occlusion pressure, often due to a urethral hypermobility or ineffective action sphincter. In elderly male, stress incontinence may result consequently to the prostate surgery such as radical prostatectomy, transurethral resection or ablation procedure for the treatment of benign prostatic hyperplasia. However, this type of incontinence mostly affects women, due to a deficiency of the urethral sphincter mainly due to surgery events, childbirth, muscle weakness or urethral hypermobility.

URGE URINARY INCONTINENCE

Urge urinary incontinence is characterized by an involuntary loss of urine associated to a strong and sudden desire to empty the bladder due to over-activity of the detrusor muscle or an increase of fullness due to an overactive bladder. Urge incontinence occurs when the detrusor muscle contracts involuntarily during filling of the bladder, forcing the urine exiting through the urethra. It is the type of incontinence more encountered in patients located in long term care facilities [Griebing et al., 2014]. Common causes of urge incontinence are neurological lesions (i.e. multiple sclerosis, spinal cord injury, stroke, Parkinson's disease), which further complicate the treatment of incontinence.

MIXED URINARY INCONTINENCE

Mixed urinary incontinence is a condition of patient whom presents more than a type of incontinence in the same time and this generally complicate the treatment of patients. The main case of mixed incontinence is the stress-urge [Griebing et al., 2014]. In many cases treat stress incontinence can adversely affect urge incontinence, while in many other cases it has no effect.

OVERFLOW URINARY INCONTINENCE

This Condition occurs when there is an incomplete emptying of the bladder during the voiding. Common causes overflow urinary incontinence are represented by the obstruction of the urethra or the poor bladder contractility. In women obstructions are rare and usually the overflow incontinence is related to a poor detrusor activity. In men, instead, obstruction is a common cause for this condition. Treatment of obstruction usually leads to resolution of urinary retention that caused incontinence and the solution may be pharmacological or surgical. Patients with poor detrusor contractility often require a urinary catheterization either intermittent or constant, to adequately drain the bladder.

FUNCTIONAL URINARY INCONTINENCE

This condition is an inability or unwillingness of an individual to use the toilet facilities. This is commonly associated with cognitive or mobility limitations. Cognitive disorders include both delirium and dementia are often associated with the loss of awareness of bladder filling sensation. Patients may also lose the ability to recognize the toilet or lose the understanding of the process to adjust the clothes in order to void. Some patients develop a personal unwillingness to go to the toilet. In most cases, the individual who suffers from functional incontinence has an intact urinary system. However, this is not always true in elderly patients. Elderly patients who need assistance to evacuate have a high risk of functional incontinence [Griebing et al., 2014].

CONTINUOUS URINARY INCONTINENCE

Some older adults complain continuous wetness. This is a case which may involve an underlying urologic disease and therefore requires a lot of attention by health operators. In case overflow incontinence exclusion, this raises the suspicion of other anatomical abnormalities. Women with vaginal fistula or ureterovaginal fistula are more subjected of constant urinary leakages. In some cases, in which there is presence of a small fistula, can be very difficult to confirm the diagnosis of continuous incontinence for vaginal cause. A further study of the problem by means of imaging and cystoscopy techniques may be appropriate in order to confirm the diagnosis. Special attention by the operators is required to a possible history of pelvic surgery, radiation therapy, or other vaginal procedures.

ANATOMY OF THE LOWER URINARY TRACT

The urinary tract is formed by a set of internal organs that enables the expulsion of urine from the organism. It may be anatomically subdivided into “high urinary tract” (kidneys and ureters), the same in both sexes, and “lower urinary tract” (urinary bladder and urethra), which is different between man and woman.

Differences consists mainly in the urethral tract, longer in man due to the anatomical difference of the genitalia (figures 14 and 15) and in the posterior, superior and inferior topographic relations of the bladder.

The immediate posterior relations of the female bladder are the anterior wall of the vagina, the anterior surface of the supravaginal cervix and body of uterus. The posterior surface of the bladder is firmly attached by connective tissue to these structures (figure 1.14). In the male, applied to the posterior surface of the bladder on each side of the midline, are the corresponding seminal vesicles and the terminal portions of the vas deferens and ureter (figure 1.15). Inferiorly, the bladder neck continues directly into the urethra. In the female, the latter is seen to be embedded in the anterior wall of the vagina, and together these structures traverse the levator hiatus. The male bladder neck, instead, lies immediately above the upper surface of the prostate. An overall description of the lower urinary tract, particularly focused on the histological and morphometric analysis of the urethra is necessary for a better understanding of the micturition principle and of the different anatomical mechanisms involved in the urinary incontinence.

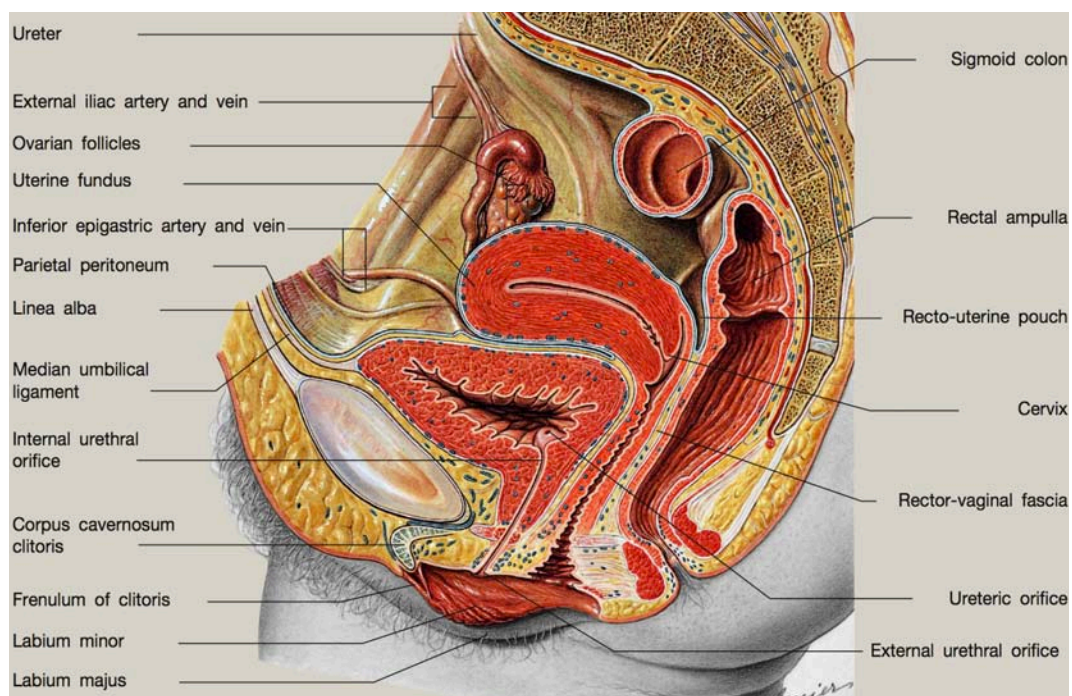


Figure 1.14. Sagittal view of the female pelvic structure [Mahadevan, 2016].

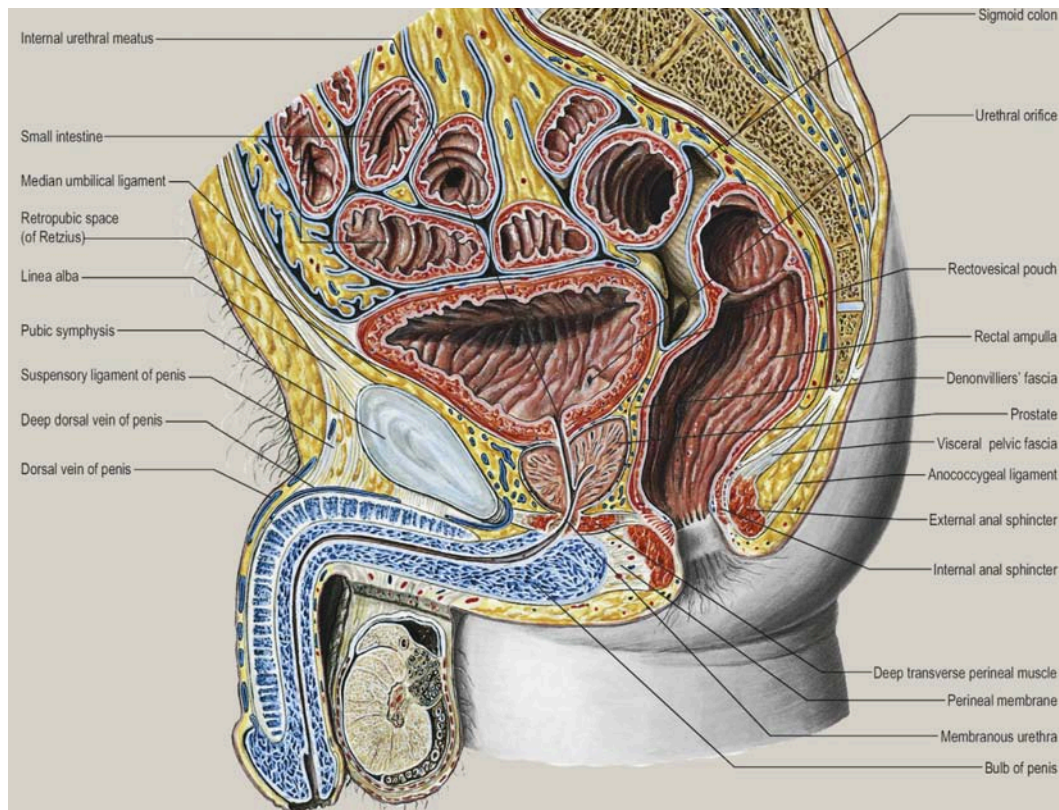


Figure 1.15. Sagittal view of the male pelvic structure [Mahadevan, 2016].

THE URINARY BLADDER

The urinary bladder is a distensible and hollow viscus which functions as a temporary reservoir for the urine that is conveyed to it continuously by the two ureters. With the inflow of urine and progressive distension of the bladder, the vague demarcations between the surfaces of the bladder gradually disappear and the bladder assumes a globoid or ovoid shape. The size, shape and position of the bladder and the relationship of the bladder to nearby structures are determined by the degree to which the bladder is distended by the contained urine and by the state of the adjacent viscera. In the adult, the empty urinary bladder lies entirely within the true pelvic cavity, occupying the anterior part of the pelvic cavity, behind the pubic symphysis and pubic bones. As the bladder distends it ascends above the level of the pelvic brim and thus into the abdomen.

The bladder body, between the apex and the base, is covered by the peritoneum in the upper surface. Besides the upper surface, which is concave upwards, it's

made of other two inferior-lateral convex surfaces and of a lower portion, the more stable, called the bladder neck. The region on the bottom of the bladder, of triangular shape, is called trigone and represents the source of the stimuli that depend on the state of fullness of the bladder. The outline of the trigone is that of an inverted triangle, with the internal urethral orifice at the apex of the triangle and the right and left ureteric orifices marking the other two angles (figure 1.16). The outer wall of the bladder corresponding to trigonal region is firmly fixed to the upper surface of the prostate (in the male) and to the anterior vaginal wall (in the female). This makes the trigone the least mobile part of the bladder. The mucous membrane of the empty bladder is rugose but this rugosity disappears when the bladder is distended with fluid, as is readily observed during cystoscopy. Over the trigone which is the least distensible part of the bladder, the mucous membrane is always smooth.

The bladder is attached to the surrounding tissue due to the peritoneum, the bladder fascia (thin thickening of connective sub-peritoneal tissue), the urethra and ligaments.

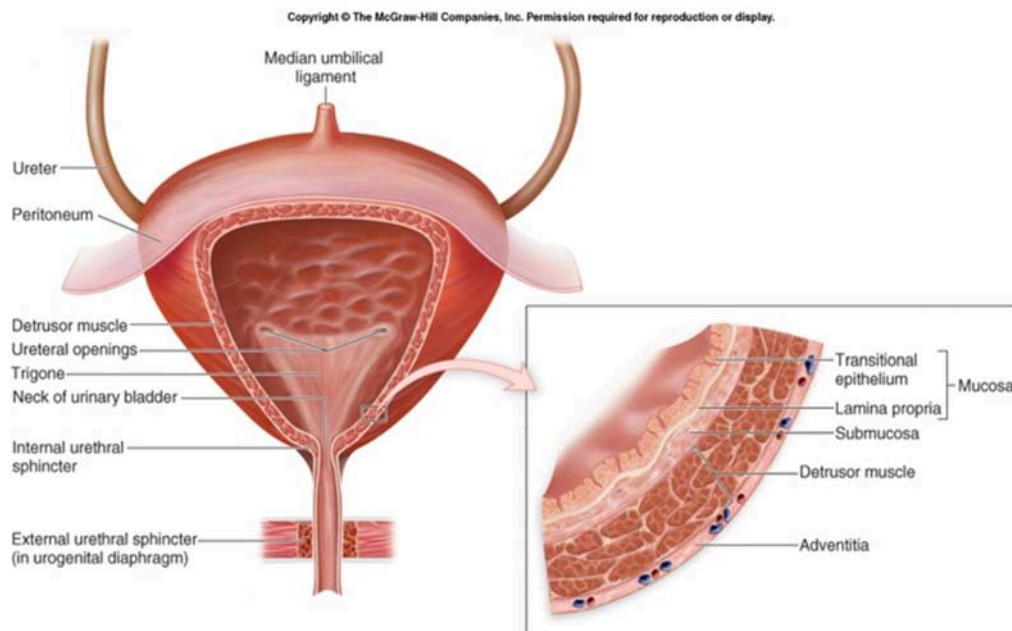


Figure 1.16: Illustration of the urinary bladder and its wall.

These latter are the medial umbilical ligament (from umbilical scar to the bladder apex), the lateral umbilical ligaments (descended from the umbilical scar and, diverging, go to fixate the bladder lateral faces), front vesicular ligaments (from the posterior of the pubic symphysis to the base of the bladder), bladder rear ligaments (only present in the male and establishing the fibro-muscular connection of the base of the bladder and prostate with the lateral surfaces of the rectum).

The retention of urine in the bladder is ensured by the *internal sphincter* (smooth), consists of an anterior and a posterior half-ring, which has the function of keeping closed the orifice of the bladder (*urethral lumen*) and from the voluntary contraction of the *external sphincter* (striatum).

The muscular wall of the bladder confers an impressive degree of contractility to the bladder.

HISTOLOGY OF THE BLADDER WALL

Histologically the bladder wall may be said to consist of four layers (figure 1.16). From within to outwards these are: an inner lining of *urothelium*, the *lamina propria*; a muscular layer made up of the *detrusor muscle* and the *serosa*. The *urothelium* is a layer of stratified epithelial cells. Within the *urothelium* the cells are arranged in three zones or layers: a basal zone, an intermediate zone and a superficial zone e the latter being adjacent to the bladder lumen. The superficial zone forms an impermeable and protective layer for the underlying layers.

The *lamina propria* is a supporting layer of connective tissue that contains capillaries, lymphatic vessels and neuroreceptors. It is demarcated from the *urothelium* by a distinct basement membrane. The muscular layer made up of the *detrusor muscle*. The *detrusor muscle* is an interlacing network of multi-directional smooth muscle fibres that produce a trabeculated appearance on gross inspection. The detrusor is richly supplied by parasympathetic, cholinergic fibres and is responsible for the contractility of the bladder.

In the trigonal region, however, the musculature consists of two histologically and biochemically distinct muscle layers: an outer layer of parasympathetically-

innervated detrusor muscle fibres and an inner layer of smooth muscle that is sympathetically-innervated by noradrenergic fibres. The inner layer of muscle is termed the superficial trigonal muscle.

The *serosa* forms a partial covering for the bladder being related only to the dome of the bladder. The *serosa* is lined externally by mesothelium. Other surfaces of the bladder are covered by a thin layer of non-serosal fibro-fatty connective tissue.

THE MALE URETHRA

The male urethra may be divided into proximal (posterior) and distal (anterior) segments. The proximal segment is comprised of prostatic and membranous portions, while the distal segment is made up of bulbous and penile segments (figure 1.17). Besides anatomical differences these segments also have certain important functional differences. The prostatic urethra is 3–4 cm in length, is formed at the bladder neck, turns anteriorly 35° at its midpoint (the urethral angle), and continues with the membranous urethra. The urethral angle divides the prostatic urethra into proximal (so-called pre-prostatic) and distal (so-called prostatic) segments. The prostate wraps around the proximal urethra. The main prostatic ducts from this zone drain into posterolateral recesses of the urethra at a point just proximal to the urethral angle [Brandes et al., 2014]. The *pre-prostatic urethra* is approximately 1 cm in length and extends vertically from the internal urethral meatus at the bladder neck to the superior aspect (base) of the prostate and possesses a stellate lumen. The non-striated smooth muscle fibre bundles surrounding the bladder neck and pre-prostatic urethra are arranged as a collar [Mahadevan et al., 2016].

The *membranous urethra*, with a mean length of 2–2.5 cm, is the shortest segment of the male urethra and is surrounded by skeletal muscle fibers of the external urethral sphincter [Brandes et al., 2014].

Internal urethral smooth muscle and the external urethral sphincter form the *urinary sphincter complex*. This latter (widely described below), is the contractile element of the lower urinary tract mainly involved to the contraction of the urethral duct permitting the urinary continence [Reeves et al., 2016].

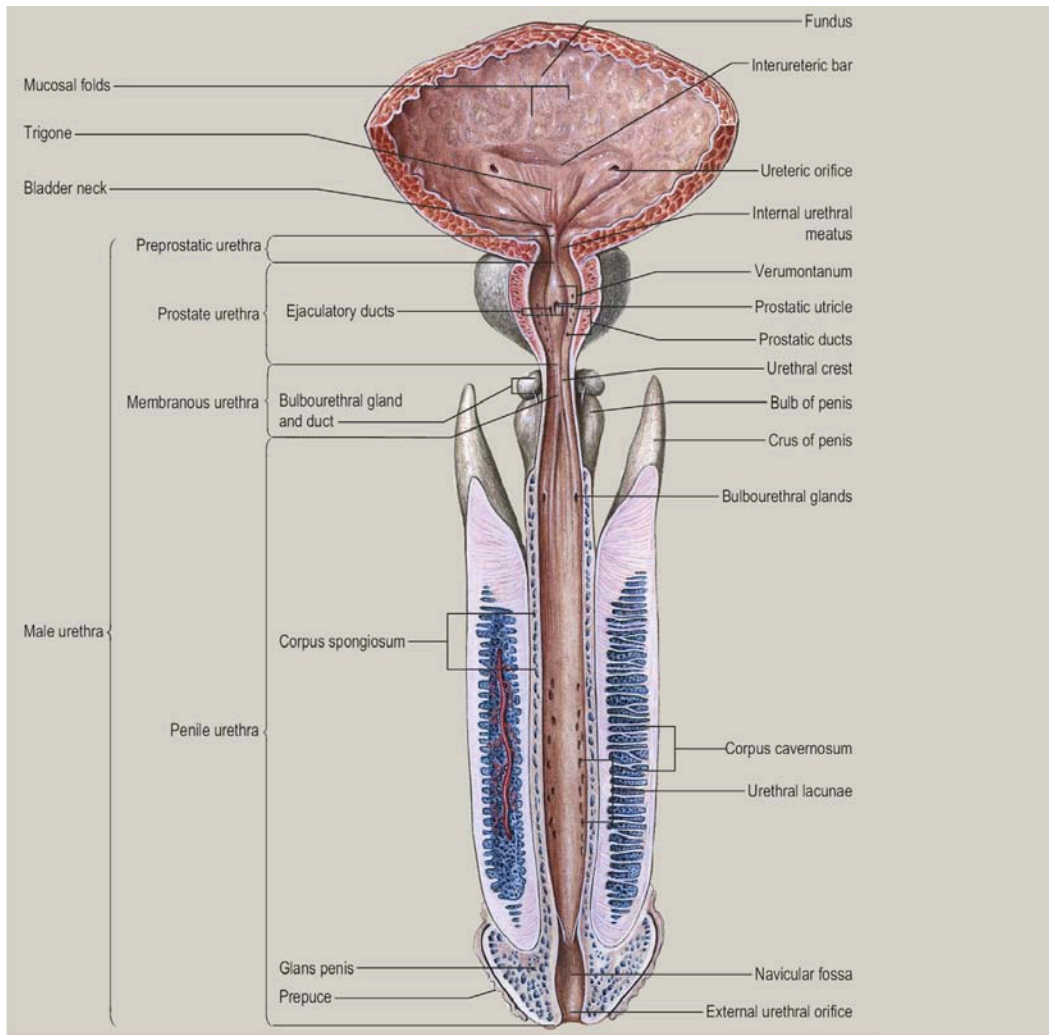


Figure 1.17: frontal view of the male urinary tract [Mahadevan, 2016]

The *spongiose urethra* is approximately 15 cm in length and is enclosed, along its entire length, by the corpus spongiosum (figure from 1.17 and 1.18). The latter which consists of erectile tissue, lies in the ventral groove between the two corpora cavernosa (figure 1.19). The corpus spongiosum is enlarged proximally to form the bulb of the penis.

At its distal end the corpus spongiosum is expanded to form a broad cap called the glans. The *spongiose urethra* is the direct continuation of the membranous urethra, and is subdivided into bulbous, penile and glanular parts.

The *bulbous urethra* extends from the membranous one, below the external sphincter, to the *penile urethra* and has an average length of about 6 cm. It

presents a very wide and thick initial tract called bulb, whose lumen has inner diameter of approximately 10 mm and is surrounded by spongy tissue, which walls have a variable thickness between 4 and 12 mm. As shown in figure 1.18, going toward the penile urethra, the lumen reduces progressively and the *corpus spongiosum* becomes thinner.

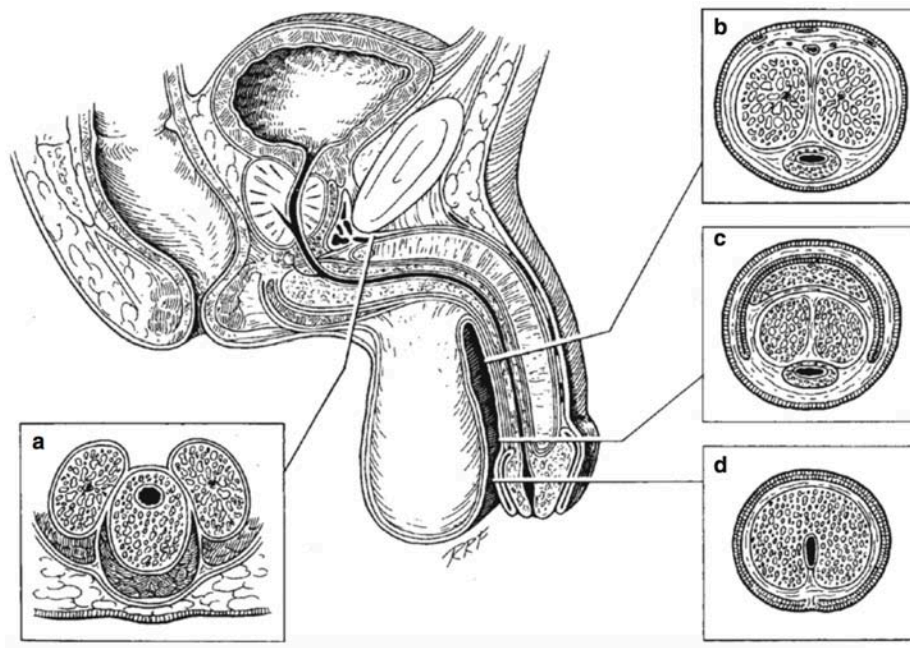


Figure 1.18: Sagittal view of the male urinary tract from Brandes et al. with four different cross section of distal urethra: bulbous urethra (a), penile urethra (b), penile margin(c) and glans (d) from Brandes et al., 2014.

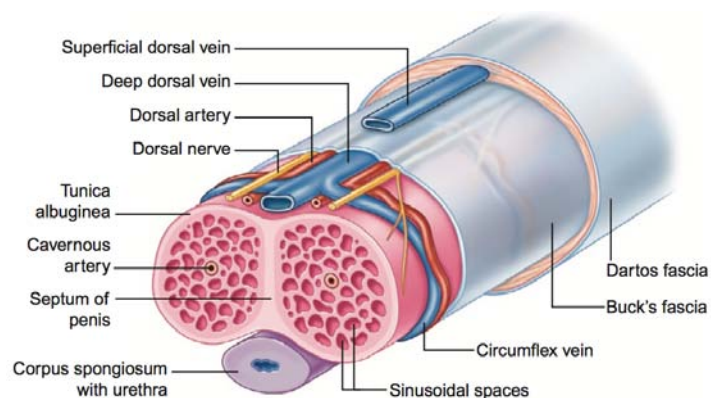


Figure 1.19. Anatomical structure of the penis (cross section corresponding to spongiose urethral tract).

At the bulb level, particular glands, called Cowper's glands, flow into the ducts of the *bulbous urethra*. They are placed in the urogenital diaphragm and involved in a proteic liquid secretion to lubricate the urethral duct just before the ejaculation. The distal half of the *spongiose urethra* presents minute ducts of multiple mucus-secreting periurethral glands called *glands of Littrè*, which drain mucus directly to the epithelium or in little recesses called *Morgani's lacuna*. Just proximal to the external urethral orifice, the *glanular urethra* features a short and dilated portion, called the navicular fossa (figure 1.17) [Mahadevan et al., 2016].

URINARY SFINCTER COMPLEX

The urinary sphincter complex is comprised of an internal smooth muscle sphincter and a striated external sphincter, which extend from the bladder neck to the perineal membrane (figure 1.20). These two sphincters are responsible for passive continence and continence under conditions of stress, respectively.

The smooth and striated components of the urethral sphincter muscles are indistinctly separated, and are supported by the paraurethral musculature and connective tissue of the pelvic floor.

EXTERNAL URETHRAL SPHINCTER

The *external urethral sphincter* or *rhabdosphincter* is an omega-shaped or horseshoe-shaped muscle that is most prominent at the anterior and lateral aspects of the membranous urethra. Its striated fibers are continuous distally to the perineal membrane, and extend proximally over the anterior prostate to the base of the bladder where they thin out as they intermingle with the smooth muscle fibers of the bladder (figure 1.20).

The *rhabdosphincter* is an independent morphological unit, which is separated from the surrounding pelvic floor muscles by connective tissue. Due to the small size of the individual muscle fibers of the rhabdosphincter (25–30% smaller than fibers of the associated muscles) and the fact that these are embedded in connective tissue, visualization of the *rhabdosphincter* at radical prostatectomy is obscured. Its fascia is inseparable from the prostatic capsule.

The *rhabdosphincter* is comprised of slow and fast twitch muscle fibers, with a greater proportion of fast twitch fibers seen in the main caudal part. The *rhabdosphincter* is activated proportionally with increased intra-abdominal pressure to maintain continence in stress conditions [Reeves et al., 2016].

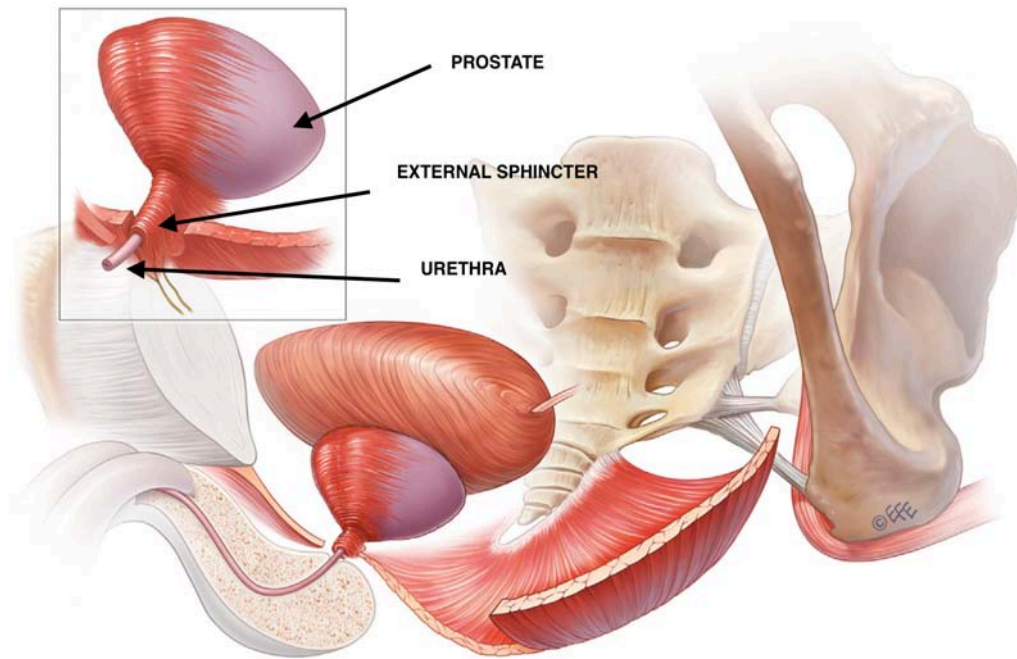


Figure 1.20. View of external urethral sphincter from Reeves et al.

INTERNAL URETHRAL SPHINCTER

The *internal urethral sphincter* or *lissosphincter* is a smooth muscle sphincter that completely encircles the urethra. It consists of an inner longitudinal layer and an outer circular layer. In contrast to the rhabdosphincter, the *lissosphincter* is most prominent proximally at the bladder neck and thins out distally. The smooth muscle surrounding the pre-prostatic urethra is involved in causing muscle contraction at the time of ejaculation. Contraction of the pre-prostatic sphincter serves to prevent retrograde flow of ejaculate through the proximal urethra into the bladder. It is a feature unique to the male [Mahadevan et al., 2016].

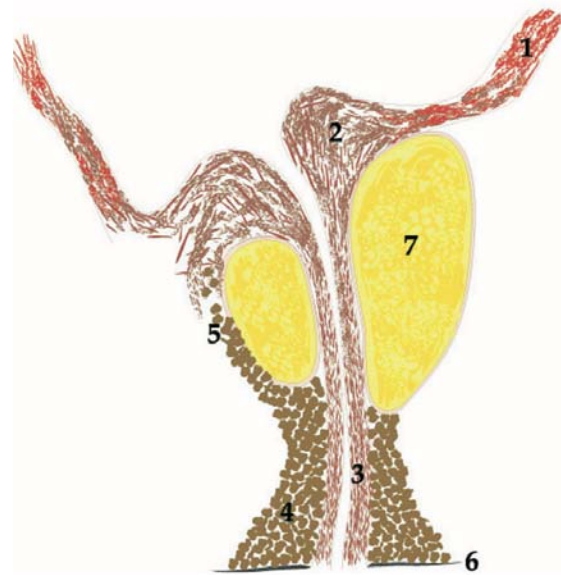


Figure 1.21. Illustration of a sagittal section of urinary sphincter complex from Koraitim, 2008, representing the bladder wall (1), the pre-prostate lissosfincter (2), the distal lissosfincter (3), the rhabdosfincter (4), the prostatic rhabdosfincter (5), the perineal membrane (6) and the prostate body (7).

HISTOLOGICAL ANALYSIS OF THE MALE URETHRA

The tissues of the male urethra are composed of a mucosa with different composition which are related to the different urethral tracts [Ovalle et al., 2013]. Urethral mucosa is made of two main layer, the epithelium that lining the internal cavity and the lamina propria, a layer of a fibro-connective and highly vascularized tissue (figure 1.22).

In the prostatic urethra, the epithelium is mainly constituted by urothelium (transitional epithelium), with interposed sections of stratified columnar epithelium.

The corresponding lamina propria is rich in cells with isolated smooth muscular cells [Ovalle et al., 2013]. The pre-prostatic urethra also has a muscular coat consists of three layers of smooth muscle tissue, with muscle fibers arranged in three different orientations similarly to the muscle structure of the urinary bladder [Andretto, 2013].

In the distal part of the prostatic tract, the muscularis the muscle layer assumes a double stratification, a longitudinal internal and an external circular one (figure 1.23) [Delancey et al., 2002].

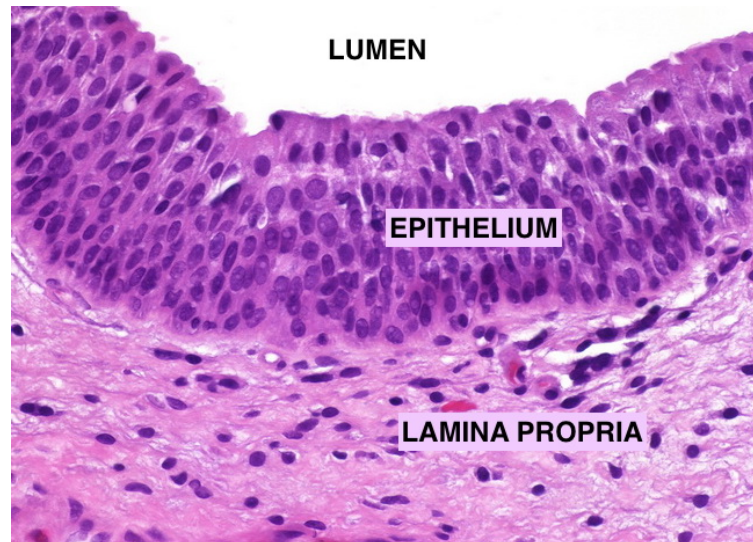


Figure 1.22: Optic microscopy of the urethral mucosa from Ovalle et al., 2013.

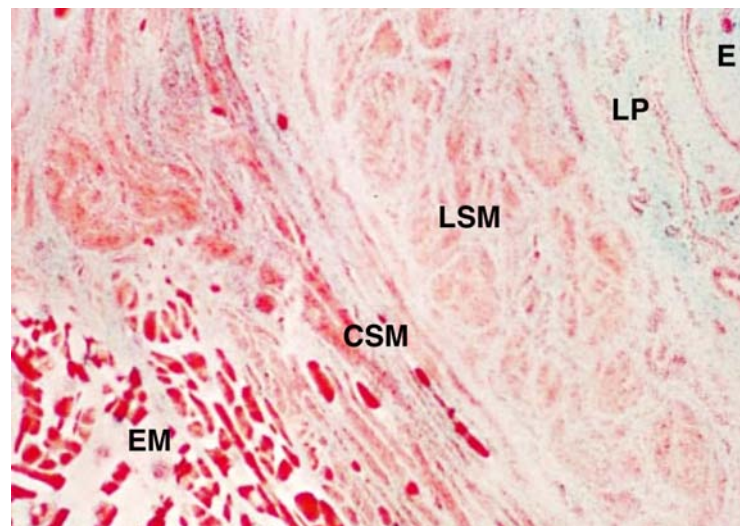


Figure 1.23. Optic microscopy of a cross section of the urethra from DeLancey et al., 2002, showing external striated muscular fibers (EM), circular smooth muscolar fibers (CSM), internal longitudinal smooth muscolar fibers (LSM), the lamina propria and the epithelium.

Most of the penile urethral lining is a stratified/pseudostratified columnar epithelium, whereas the distal penile urethra, including the fossa navicularis, is lined by stratified non-keratinizing squamous epithelium (figure 1.24). The lamina propria of the penile urethra is a fibro-connective tissue with elastic fibers and scattered, longitudinally oriented smooth muscle [Brandes et al., 2014; Ovalle et al., 2013].

The mucosa of the spongiose urethra is wrapped by the corpus spongiosum of the penis which is a cancellous, labyrinth-disposed masses of fibro-elastic connective tissue and smooth muscle. These trabeculae of connective tissue are ramified in a wide cavernous net of vascular sinuses, which are full of blood during the penile erection (figure 1.25) [Brandes et al., 2014; Ovalle et al., 2013].

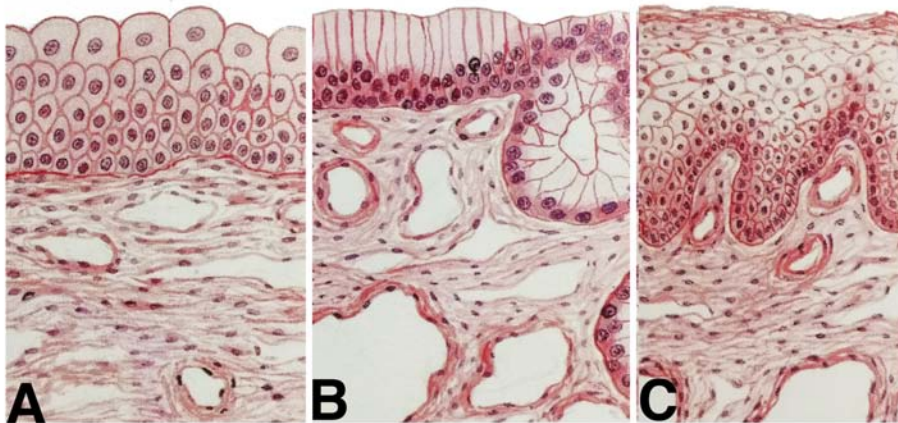


Figure 1.24: Illustration of the urethral epithelium from Ovalle et al., 2013, showing transitional epithelium of prostatic urethra (A), pseudostratified columnar epithelium of the penile urethra (B) and stratified non-keratinizing squamous epithelium of the Fossa Navicularis (C).

The mucosa of the spongiose urethra is wrapped by the corpus spongiosum of the penis which is a cancellous, labyrinth-disposed masses of fibro-elastic connective tissue and smooth muscle. These trabeculae of connective tissue are ramified in a wide cavernous net of vascular sinuses, which are full of blood during the penile erection (figure 1.25) [Brandes et al., 2014; Ovalle et al., 2013].

The corpus spongiosum, as shown in figure 1.25, is then covered by the Tunica Albuginea, a thick layer of dense connective tissue, composed about 80% by collagen fibers immersed in a network of elastic fibers [Andretto, 2013]. The external coat is a thin cutis, the so-called Bulk's fascia.

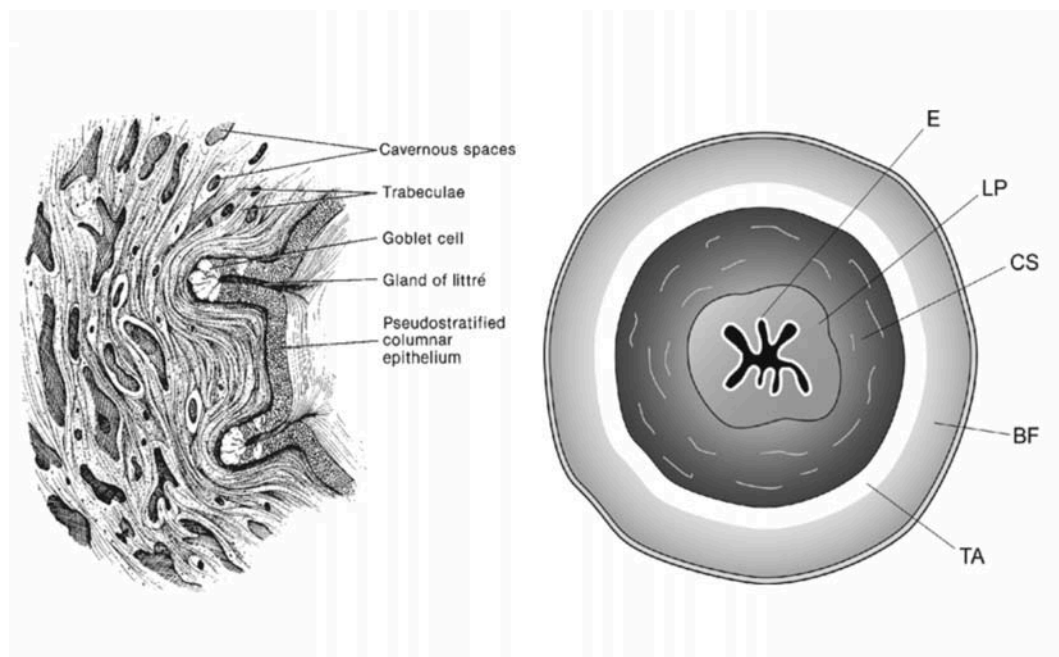


Figure 1.25. Urethral wall structure (left) and transversal cross section of spongiöse urethra (right) from Brandes et al., 2014: Epithelium (E), Lamina Propria (LP), Corpus Spongiosum (CS), Tunica Albuginea (TA) and Bulk's Fascia (BF).

THE FEMALE URETHRA

The female urethra in the adult is approximately 4 cm in length and 8 mm in diameter [Ovalle et al., 2013]. Commencing at the internal urethral orifice within the bladder neck, it passes antero-inferiorly below and behind the pubic symphysis to end at the external urethral orifice. The latter is located in the vestibule immediately anterior to the vaginal orifice and 2.5 cm postero-inferior to the clitoris. For its entire length the urethra lies immediately in front of the anterior wall of the vagina, and except for its very proximal part, which lies embedded in the anterior vaginal wall. Thus the long axis of the urethra is parallel to that of the anterior vaginal wall.

Together the urethra and vagina pass successively through the pelvic floor, the external urethral sphincter and the perineal membrane. The *external urethral sphincter* in the female, as in the male, is made up of slow-twitch fibres and is innervated by the perineal branch of the pudendal nerve. Multiple, small mucus-secreting glands situated in the subepithelial tissue of the proximal urethra, open directly into the urethra. In addition, there is an aggregation of small glands (termed Skene's glands) on either side of the distal part of the urethra. Each of these collections of glands opens into a para-urethral duct which in turn opens through a minute aperture alongside the external urethral orifice.

In proximity to the bladder, its semilunar lumen is lined with urothelial mucosa, gradually substituted with stratified columnar epithelium in an intermediate level and with squamous stratified epithelium at vestibular aperture. The female urethral mucosa, as well as in membranous male urethra, is surrounded by an internal longitudinal and external circular smooth muscle stratum.

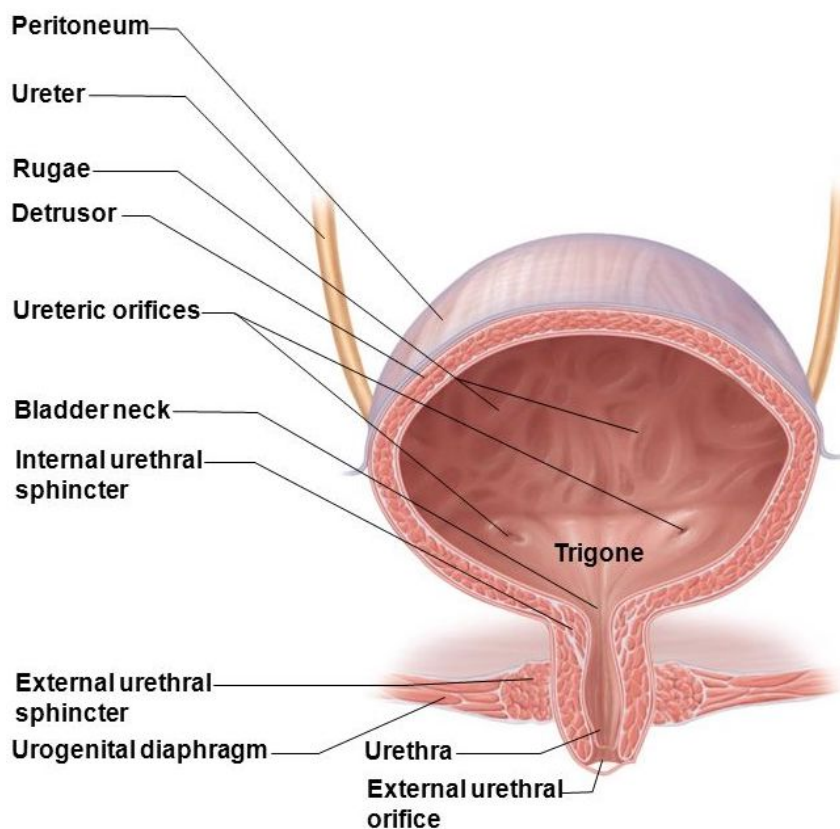


Figure 1.26. Female urinary bladder and urethra.

SURGERY SOLUTIONS FOR THE TREATMENT OF URINARY INCONTINENCE

Depending on the severity of the condition, conservative management should be considered prior to surgery such as pelvic floor exercises by a trained pelvic floor physiotherapist or other conservative measures in terms of lifestyle modifications such as fluid management, weight loss and smoking cessation. Treatments such as duloxetine, urethral plugs may be considered. Surgery for stress urinary incontinence should only be undertaken following a comprehensive assessment and when conservative treatments have failed [Hussain et al., 2013].

Surgical treatments are mainly adopted for the treatment of stress urinary incontinence. Common procedures for stress incontinence are urethral bulking agents, colposuspension, tape procedures, sling procedures and artificial urethral sphincters [Hussain et al., 2013]. Surgery is less used in case of urge urinary incontinence and overflow incontinence. For the first condition, lately solutions adopted consists of neuromodulation, such as sacral neuromodulation or posterior tibial nerve stimulation. Other approaches consist of auto-augmentation and augmentation enterocystoplasty [Griebing, 2014]. For the second ones, the only methods involved to avoid an overflow of urine consist of catheters (clean intermittent or indwelling).

Follows an overall description of surgical treatments of stress urinary incontinence, especially focused on the artificial male urethral sphincter placement, in due to the aim of this work.

URETHRAL SLINGS

These surgical procedures are mainly involved for female stress incontinence treatment, but recently urethral slings are becoming an accepted treatment for men with persistent post-prostatectomy incontinence who do not desire, or are not candidates for artificial urinary sphincters [Brandes et al., 2014].

Female treatments involve tapes being inserted inside the vagina and behind the urethra to support the urethra. There are three main slings procedure for women:

the *transobturator sling* procedure, the *retropubic sling* procedure (*tension-free vaginal tape* procedure) and the mini-sling procedure [Hussain et al., 2013; IUGA, 2011].

A transobturator sling approach to the operation requires a small incision to be made in the vagina at the same place as for the retro-pubic operation. The ends of the sling are through two small incisions made, this time, in the groin. Each ends of the slings passes through the obturator foramen (figure 1.27), which is a gap between the bones of the pelvis. The ends are cut off once the sling is confirmed to be in the in the correct position and the skin closed over them [IUGA, 2011].

During the retro-pubic operation the sling is placed through a small cut made in the vagina over the midpoint of the urethra. Through this the two ends of the sling are passed from the vagina, passing either side of the urethra to exit through two small cuts made just above the pubic bone in the hairline, about 4-6 cm apart (figure 1.27).

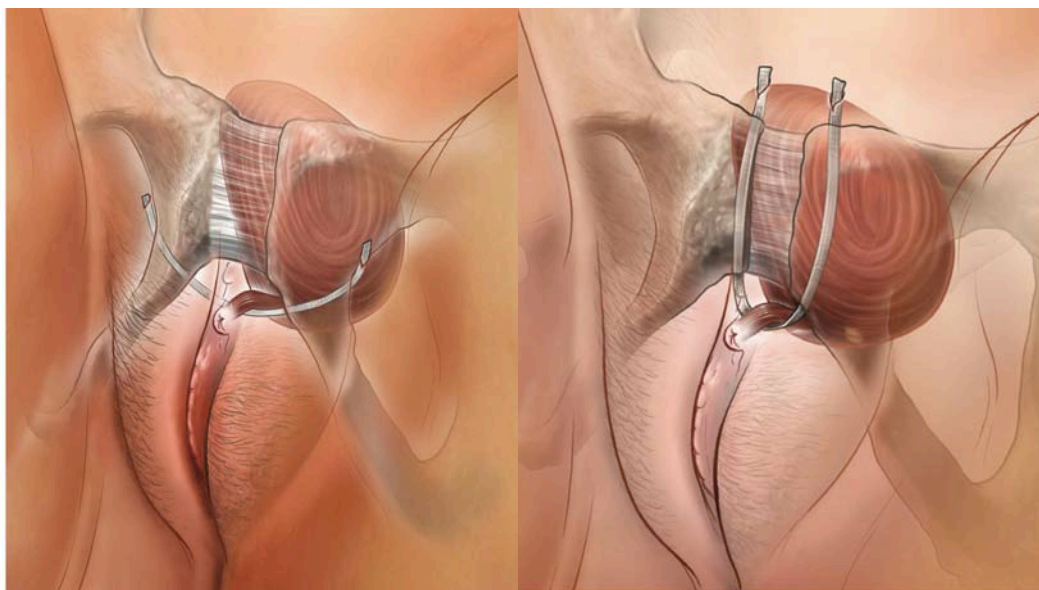


Figure 1.27. Sling procedures: transobturator sling (left), retropubic sling (right) from IUGA.

The surgeon will then use a cystoscope to check that the sling is correctly positioned and not sitting within the bladder. The sling is then adjusted so that it

sits loosely underneath the urethra and the vaginal cut stitched to cover the sling over [IUGA, 2011].

The mini-sling procedure is similar to the initial part of retropubic approach, except that the ends of the sling do not come out onto the skin and are anchored in position by one of a number of different fixation techniques [IUGA, 2011].

Bulbourethral slings were designed to be an alternative to artificial sphincters in the treatment of male stress urinary incontinence. Patients with persistent or recurrent post-prostatectomy incontinence following sling placement may be candidates for salvage treatments, depending on patient reference.

Figures 28 shows a primary procedure for a male sling placement.

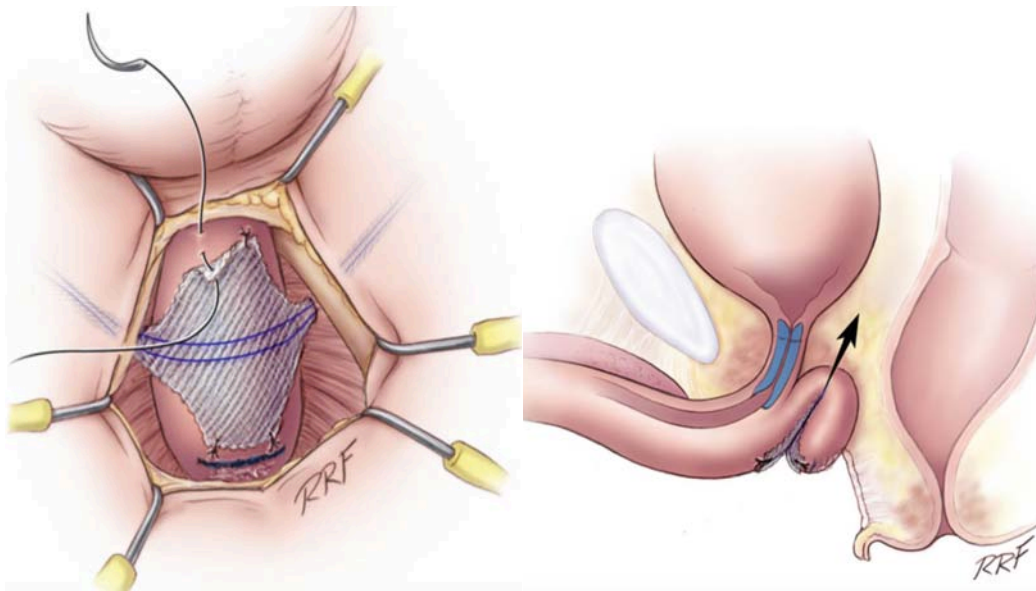


Figure 1.28. Male urethral sling placement procedure: after a perineal incision between (between anus and scrotus), the broad portion of the mesh is fixed to the corpus spongiosum with 4 sutures, two proximal and two distal (left); With tensioning of the sling, the corpus spongiosum is pulled proximally causing coaptation of the urethra (right) [Brandes et al., 2014].

Patients competent and willing to operate an artificial urinary sphincter may undergo an artificial sphincter placement following failed sling. This is easily accomplished without removing the sling mesh, by placing the cuff around the spongiosum distal to the urethral sling. Early success rates following repeat sling

placement has approached 70%, and success following salvage artificial urethral sphincter is expected to be similar to a primary artificial sphincter placement [Brandes et al., 2014].

COLPOSUSPENSION

In open colposuspension, the retropubic space is entered through a low transverse abdominal incision and blunt dissection. Two non-absorbable sutures are placed on each side in the endopelvic fascia on either side of the urethra and bladder neck and these sutures are attached to the ipsilateral iliopectineal ligament. The sutures are tied without causing hyper elevation of the urethra (figure 1.29).

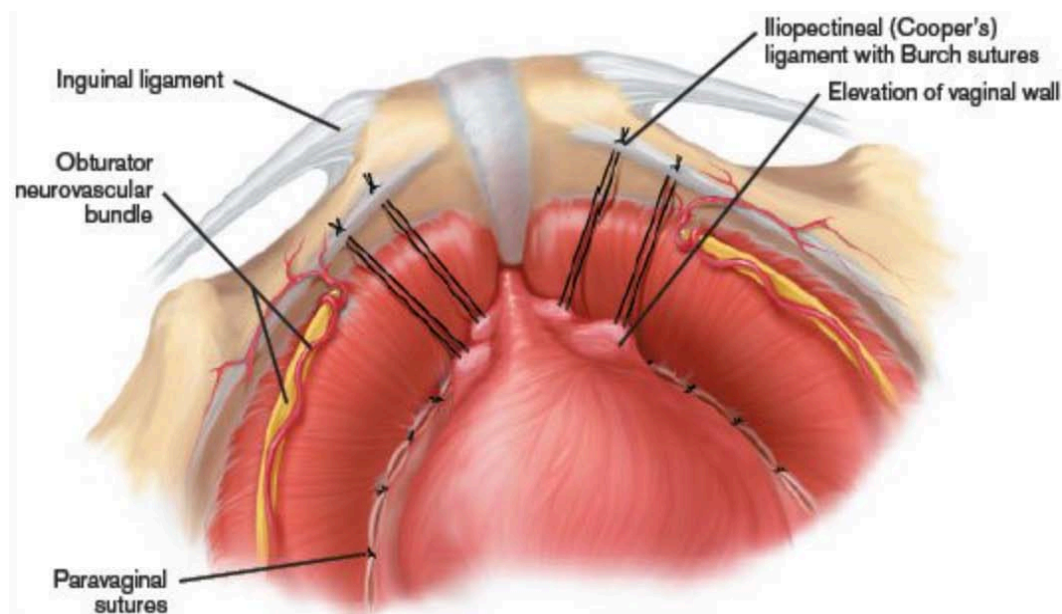


Figure 1.29: the colposuspension approach.

In the laparoscopic approach, three or four ports are used (umbilical, suprapubic and two lateral). Either a transperitoneal or extraperitoneal approach can be used to enter the space of Retzius. Two non-absorbable sutures are placed in either side as in open procedure [Hussain et al., 2013].

Complications of colposuspension include hemorrhage and bladder trauma. Cystoscopy is recommended at the end of the procedure to rule out bladder trauma. The other potential complications include voiding difficulties, de novo

urgency, chronic pain, dyspareunia, osteitis pubis and prolapse especially of the posterior compartment [Hussain et al., 2013].

The decision to perform an open or laparoscopic procedure depends upon the skills of the surgeon. The laparoscopic procedure requires the surgeon to have advanced laparoscopic suturing skills. Laparoscopic colposuspension should be undertaken only by an experienced laparoscopic surgeon working in a multidisciplinary team with expertise in the assessment and treatment of urinary incontinence.

The overall long-term success rates are reported as 68.9-88.0%. Urinary retention rate of up to 21% has been reported and the risk of de novo urinary urgency has been reported as 5-30% [Hussain et al., 2013].

URETHRAL BULKING AGENTS

Injectable therapy use bulking agents composed of synthetic materials, bovine collagen, or an autologous substance augments the urethral wall by creating artificial cushioning in the urethral submucosa, improving urethral coaptation, increasing urethral resistance to urinary flow and hence preventing urinary leakage. Injection of bulking agents to treat a dysfunctional urethra is a minimally invasive method of correcting intrinsic sphincteric deficiency and can be performed as an outpatient procedure [Hussain et al, 2013]. They can be injected transurethrally or paraurethrally with or without cystoscopic guidance. The ideal agent for injection should be long lasting, hypoallergenic, and non-migratory and should cause the least inflammatory response. There are various agents available at present such as GAX-collagen (Contigen), ethylene vinyl alcohol copolymer, carbon-coated zirconium beads, calcium hydroxylapatite, and vulcanized silicone [Hussain et al., 2013].

A review of periurethral injection therapy for urinary incontinence in women in 2007 concluded that there is still an unsatisfactory basis for the use of urethral bulking agents as a first line treatment for stress urinary incontinence.

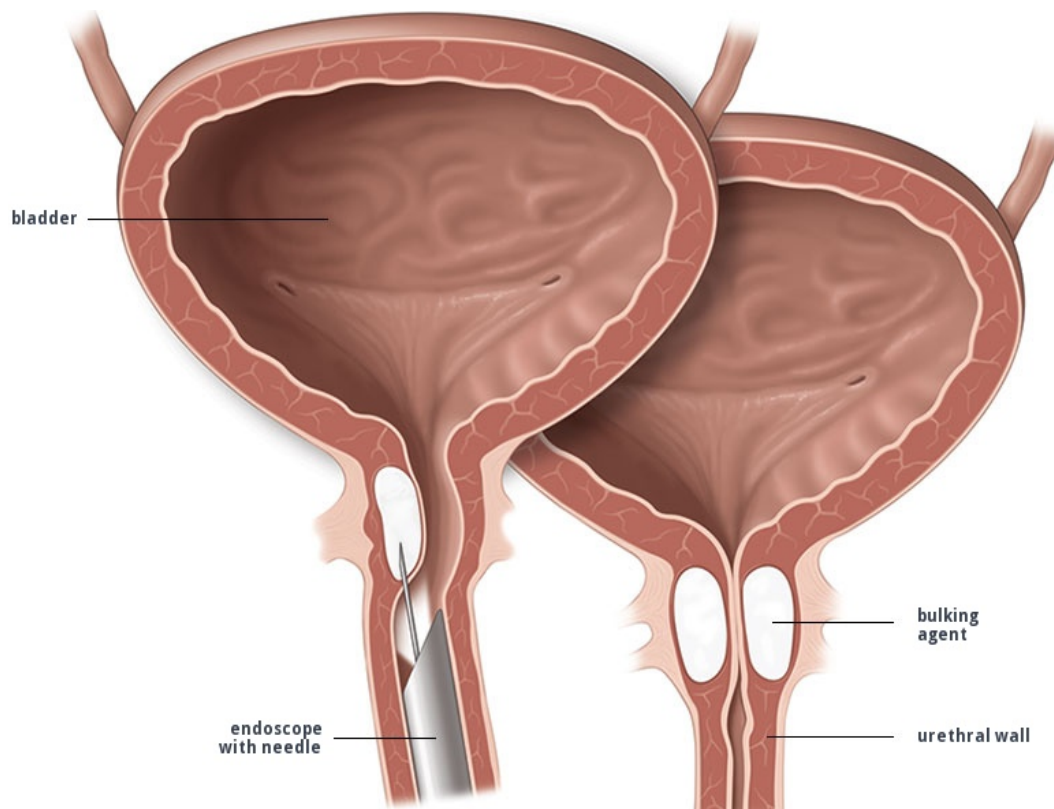


Figure 1.30. Transurethral injection of a bulking agent using an endoscope.

It also suggested that transurethral route resulted in fewer complications than para-urethral administration, the success rate was lower than colposuspension and both synthetic and autologous fascial slings and that it was inferior to open surgery at 12 months but with a better safety profile and a lower morbidity rate. The review recommended other surgical procedures as first line treatment for women who are fit for surgery and injectable therapy reserved for those who have extensive co-morbidity and are not fit for surgery. Women need to be counselled regarding the possibility of requiring more than one injection to achieve improvement and the risk of reduced efficacy with time. There had been reports of granulomatous reactions and abscesses following injectable therapy [Hussain et al., 2013].

ARTIFICIAL URINARY SFINCTERS

An artificial sphincter is an artificial pump device which does the work of the urinary sphincter muscle that closes to stop urine flow. Patients being considered

for artificial sphincter placement should undergo a full preoperative history and physical examination with further studies, as clinically indicated. In fact, despite excellent first-time success rates, a big percentage of men managed with artificial sphincter had experienced complications including urinary retention, urethral atrophy, erosion, and device malfunction, among others. Available surgical options for patients with either recurrent incontinence following initial artificial urinary sphincter placement or those with prior complications include placement of a tandem cuff, trans-corporal cuff, cuff down- sizing, reservoir upsizing, or tissue interposition with artificial sphincter [Brandes et al., 2104].

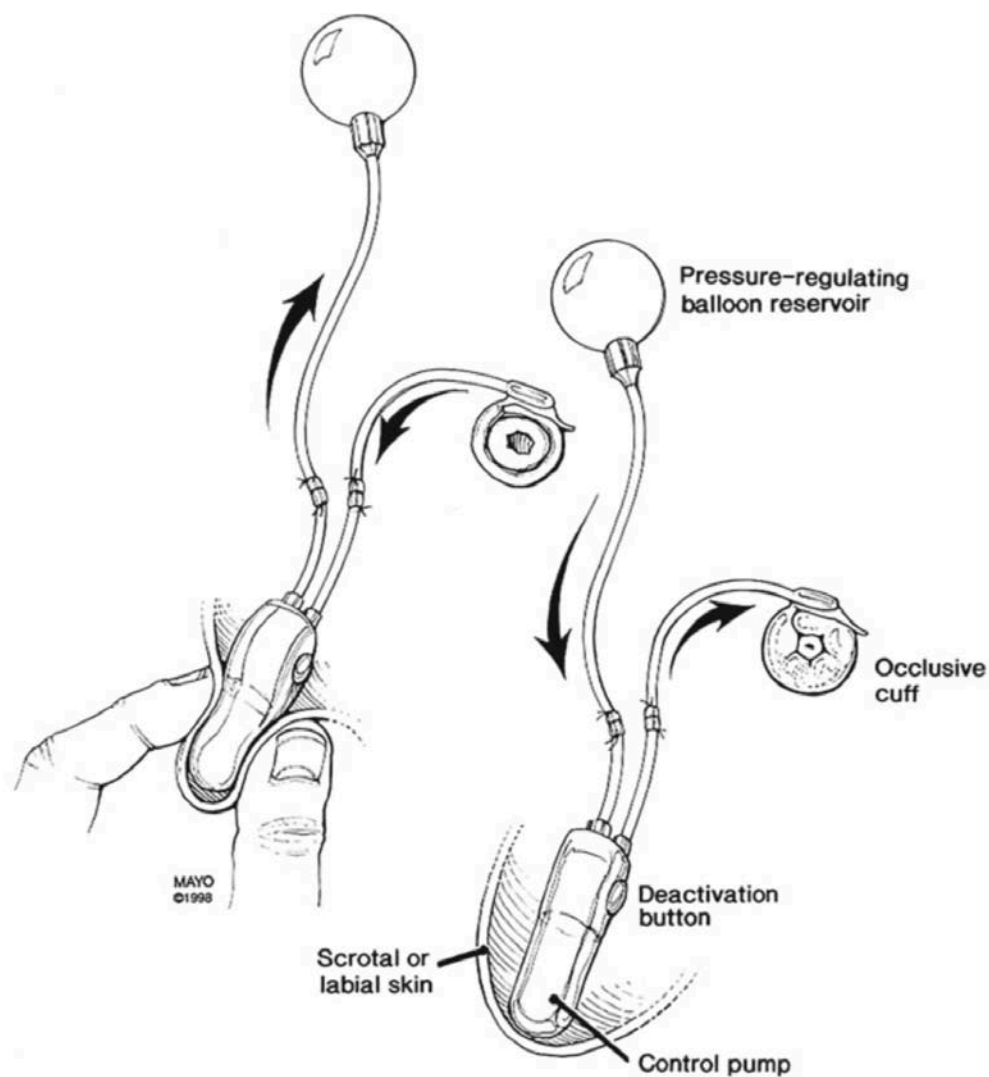


Figure 1.31. Functioning principle of AMS 800.

Currently, the most commonly surgically implanted artificial sphincter is the AMS 800 (American Medical Systems, Minnetonka, MN). The device consists of a three-piece system with an inflatable urinary cuff, reservoir, and pump (figure 1.31). Cuff sizes vary according to application and range from 3.5 to 14.0 cm, with available reservoir pressures ranging from 41–50 to 81–90 cmH₂O. The pump serves several functions including cuff cycling, permit cuff deactivation, and restrict retrograde transmission of reservoir fluid to the urinary cuff.

Although the artificial sphincter has reported success rates of 59–91 %, surgeons who routinely treat stress urinary incontinence frequently are required to the maintenance of devices and consider any surgical complications, as well as recurrent incontinence resulting from various etiologies [Brandes et al., 2014].

PREOPERATIVE EVALUATION

Patients initially presenting with stress urinary incontinence should undergo a thorough history and physical examination with further testing tailored to each clinical scenario. Important aspects of the preoperative history include a review of the underlying etiology for the incontinence (e.g., prostatectomy, transurethral resection of the prostate [TURP]), degree of incontinence (number of pads, objective pad weights), prior therapies performed, history of urethral or bladder pathology (stricture disease, urothelial carcinoma), radiation therapy, associated lower urinary symptoms, urinary tract infections, bladder calculi, as well as a review of the patient's capacity to maintain his activities of daily living without need for assistance from caregivers. Patients should be at least 6–12 months out from the inciting cause (e.g., TURP, prostatectomy) to assure stabilization of the incontinence. Additionally, pathology requiring repeated transurethral interventions such as recurrent urothelial carcinoma of the bladder should be factored into the decision as to the patient's candidacy for artificial sphincter placement.

In addition to obtaining a thorough history, patients should be examined to assess their mental and physical capacity to self-manage the artificial sphincter. Patients

should be able to cycle the pump without assistance and should be free of mental pathology (e.g., dementia) which might otherwise compromise overall health. Examination should include direct confirmation of the stress urinary incontinence, either from a standing or reclined position, and may be performed concomitantly with other procedures, such as cystoscopy.

ARTIFICIAL URETHRAL SFINCTER IMPLANTATION (from Brandes et al., 2014)

Following appropriate anesthetic induction, the perineum is shaved and cleansed with antiseptic solution. A lower midline incision is made in the perineal region, posterior to the scrotum and overlying the proximal bulbar urethra (figure 1.32). The underlying subcutaneous tissues are dissected to isolate the bulbar urethra as proximally as possible to provide additional tissue support for artificial sphincter placement (figure 1.32). The bulbar urethra is further dissected with a plane created between the corpus cavernosum and spongiosum sufficient to permit placement of the sphincter cuff. Care is taken during dissection to avoid inadvertent injury to the urethra during perforation of the intercorporal septum as the overlying corpus spongiosum is thin in this region. A syringe is next placed alongside the catheter with the urethral meatus occluded and the catheter placed on tension. Figure 1.32 demonstrates appropriate dissection of the proximal bulbar urethra.

The bulbar urethra is next measured and an appropriately sized cuff size selected. Manipulation of the prosthetic components is minimized during surgery with strict attention paid to sterile technique throughout the procedure. Rubber-shodded clamps are utilized when necessary for occlusion of the device tubing to prevent inadvertent crush injury and damage to the device. If a right-sided pump placement is desired, a right angle instrument is passed deep to the bulbospongiosus from the right to the left with the cuff grasped. The cuff is then passed posterior to the bulbospongiosus and secured by passing the cuff tubing through the open tab. Figure 1.33 demonstrates final connection of the cuff

surrounding the urethra. Following placement of the urethral cuff, a reservoir size is selected, with the most common pressure utilized of 61–70 cmH₂O.

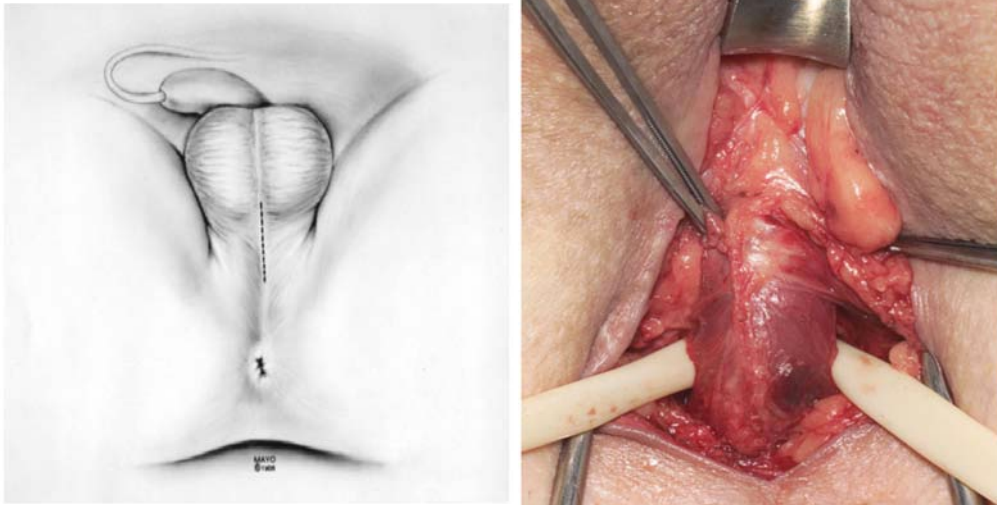


Figure 1.32. Location of perineal incision for AUS placement (left) and proximal bulbar urethral dissection (right) [Brandes et al., 2014].

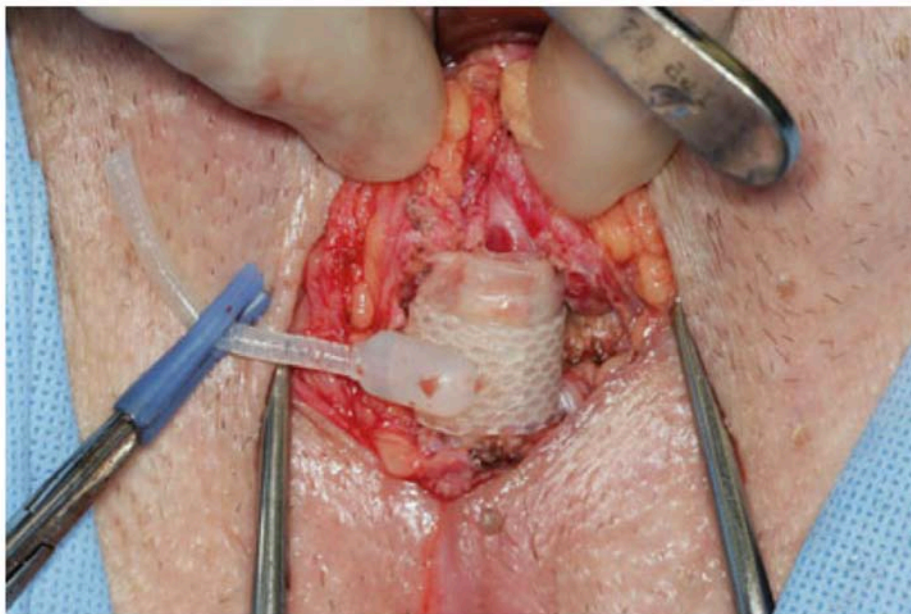


Figure 1.33. Artificial urethral sphincter cuff in situ.

Decreased reservoir pressure may be selected when concern exists for possible erosion including prior sphincter placements and radiation therapy. An approximately 5 cm, transverse incision is made several centimeters lateral to the pubic symphysis on the ipsilateral side to the anticipated pump location. The

anterior rectus fascia is incised and pocket created deep to the rectus muscle. This results in placement of the reservoir deep to the rectus muscle.

Following reservoir placement, the fascia is closed, and a dilator is passed from the abdominal incision through the subcutaneous tissue towards the right testicle. Care is taken to direct the dilator to the anterolateral position towards the desired final position for the scrotal pump. The dilator is withdrawn and the pump placed in the newly created space. A clamp is placed around the pump tubing on the external surface of the scrotum with downward traction applied to prevent proximal migration of the pump during device connection. The pump is then secured to the reservoir. A long clamp is then passed from the abdominal incision towards the perineal incision, with the cuff tubing grasped. This is then retracted to the abdominal incision with the second connection secured. The wounds are then closed, and a sterile dressing is applied.

MANAGEMENT OF COMPLICATIONS

The most common complication encountered intraoperatively is injury sustained to the dorsal bulbar urethra at the time of initial dissection. Care should be taken during dissection of the 12 o'clock position of the bulbar urethra and during perforation of the inter-corporal septum to avoid the urethra.

In the case of a small, intraoperatively recognized urethral injury, this may be closed primarily with the artificial sphincter placed at a separate location. With larger urethral injuries, artificial urinary sphincter placement should be abandoned with the urethrotomy closed primarily and a catheter placed. Final placement of the artificial sphincter may be rescheduled following complete resolution of the urethral injury.

Cautery injury occurring on the urethra may be managed with an indwelling catheter alone versus primary debridement with primary anastomosis. In contrast to sharp urethral injury, cautery injuries typically result in a larger region of damage sustained, thus more frequently necessitating cancellation of artificial sphincter placement.

Post complications occurring with artificial urethral sphincter placement are typically categorized as occurring early (<90 days) or late (>90 days) in the postoperative period. The most commonly encountered complications in the early postoperative period include urinary retention, infection, and erosion, while late complications are predominantly urethral atrophy due to tissue remodeling, sphincter erosion, infection, or device malfunction.

Patients with new onset of urethral erosion or device infection typically present with acute onset of voiding irritation including frequency, urgency, and dysuria and may progress to experience localized or systemic signs of infection of scrotal/perineal pain, warmth, erythema, cellulitis, fevers, or chills.

In contrast to erosions, urethral atrophy typically presents as a progressive return of incontinence over a period of several months to years despite appropriate device function and utilization [Brandes et al., 2014].

Early complications are likely to be treated with the device explantation with a catheter placement. In case of erosion, solutions should carefully use special catheter instrumentation in attempt to limit the chances for erosion augmentation.

Late complications treatments include explantation of the device as well as early managements. Other late solutions may be tandem cuff placements, that is a further cuff installation proximal to the first; the cuff downsizing or reservoir upsizing and a biologic tissue interposition, such as the placement of a porcine small intestinal submucosal between the cuff and the urethra.

CHAPTER 2

EXPERIMENTAL AND COMPUTATIONAL METHODS FOR THE INVESTIGATION OF STOMACH MECHANICS

In this chapter is reported a coupled activity by Zhao et al 2008 and Carniel et al 2017, considered one of first biomechanical approach to the investigation of the stomach pre- and post-surgical conformation in order to improve actual bariatric procedures. In fact, the specific bariatric procedure and the post-surgical conformation of the operated gastrointestinal organs are usually defined on clinical basis only, considering calories intake requirement and surgical parameters. Further physiological investigations can be performed to identify quantitative relationships between mechanical stimulation of the gastrointestinal wall, adsorption capacity and feeling of satiety.

The here reported activities aimed at developing computational tools for the mechanical analysis of the stomach structure and of the bariatric procedures, with specific regard to gastric banding. A coupled experimental and numerical approach was adopted, considering data and measurements from experimental activities on piglet stomachs. In order to develop the computational model of the stomach, tissue mechanics data are needed to assign material properties to the virtual model which must simulate the real stomach behavior. At this purpose, is also reported the activity by Zhao et al, which gave an overall biomechanical description of the stomach wall by means of tensile stretch mechanical tests of pig stomach specimens of different regions. As showed in appendix A.1, pig stomachs are selected to be representative of the human ones according to histological

analogies even if difference in the digestive process are relevant [Swindle et al, 2012; Roger Burnet in www.minipigs.dk].

Post-processing of experimental data made it possible to develop and to validate computational models. Such computational tools were exploited to evaluate the influence of surgical parameters, as gastric band position and tension, on stomach functionality in the post-surgical conformation.

2.1 EXPERIMENTAL TESTS

2.1.1 EXPERIMENTAL INVESTIGATION OF THE STOMACH WALL TISSUES MECHANICS

In order to further study the anisotropic biomechanical properties of the stomach, Zhao et al designed an in-depth biomechanical test for the layered gastric wall in different regions. They hypothesized that the mechanical properties of the pig stomach are layer- dependent and the properties of individual layers (such as mucosa–submucosa) can explain the wall stiffness. The hypothesis is tested by using uni-axial tensile testing on the intact layer, mucosa–submucosa layer and muscle layer strips from the fundus, corpus and antrum parts of the pig stomach. Five stomachs including part of the oesophagus and the duodenum from pigs weighing about 100 kg were obtained from the local slaughterhouse. The stomach was removed and put in cold calcium-free Krebs solution with EGTA (3.0mM) aerated with a gas mixture of 95% O₂ and 5% CO₂ at pH 7.4. The stomachs were transported to the laboratory within one hour. The composition of the Krebs solution (g/L) was NaCl, 6.89; KCl, 0.35; NaHCO₃, 2.1; NaH₂PO₄, 0.16; MgCl, 0.24 and glucose, 2.1. Approval of the protocol was obtained from the Danish Committee for Animal Experimentation.

The stomach was immersed in the Krebs solution with a gas mixture of 95% O₂ and 5% CO₂ at pH 7.4. Muscle activity were not observed visually or recorded in the test machine after immersion in this solution. The stomach was opened paramedian to the greater curvature and gently washed by using saline. Two strips

(about 40 mm long and 8 mm wide) of the stomach wall were cut both in longitudinal direction (parallel with the greater curvature) and circumferential direction (perpendicular to the greater curvature) from the gastric fundus, corpus and antrum (figure 2.1). Tissue strips cut this way follow the orientation of most fibers in the stomach wall. One of the two strips was used for the non-separated (intact) wall strip test and the other strip was separated into the mucosa–submucosa layer and muscle layers that were tested separately. The length of the strips was measured before the uni-axial stretch experiment.

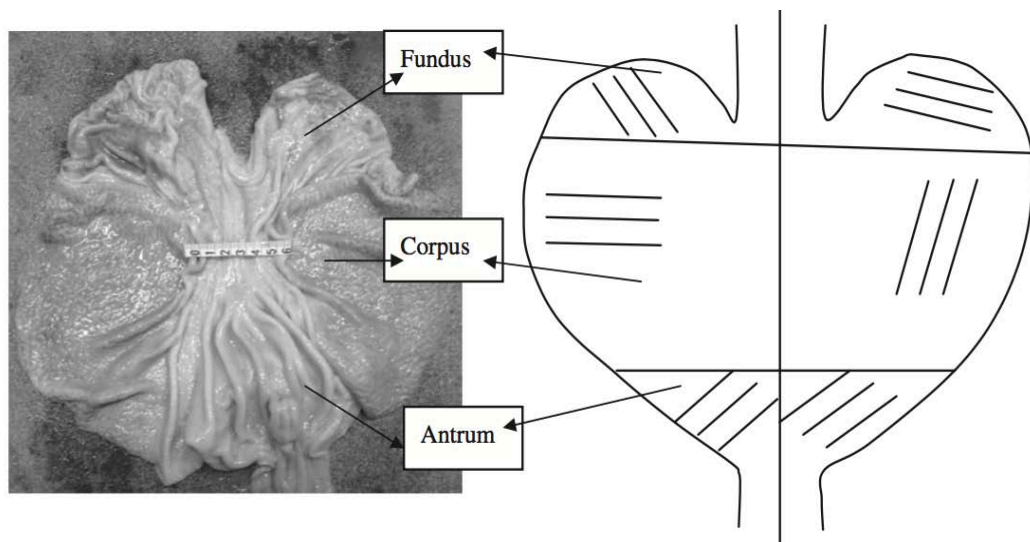


Figure 2.1. Photo and sketch of pig stomach opened paramedian to the greater curvature. Two strips of the stomach wall both in longitudinal (parallel with the greater curvature) and circumferential (perpendicular to the greater curvature) directions were cut from the fundus, corpus and antrum. One strip was used for non-separated (intact) strip test and the other one was separated into the mucosa–submucosa and muscle layers.

The test was conducted in a self-developed tensile test machine consisting of an organ bath, motion table, force transducer and electronics. The gastric strip was bathed in the Krebs solution. The two ends of each strip were tied with silk threads to cannulas and the length between the threads was measured in the organ bath. The cannulas were connected to rods that could be moved at controlled velocities by a motor. One of the rods was attached to a force transducer. The distance

between the rods was adjusted manually to the in vitro length of the strips. The force (F) was recorded in real time by the force transducer. Three cycles of loading and unloading were done (figure 2.2).

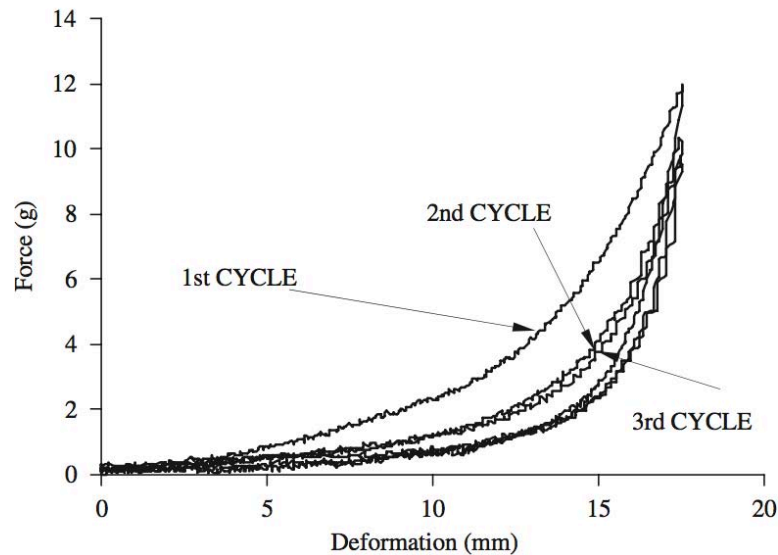


Figure 2.2. Recording of force–deformation relationship during the preconditioning process. The hysteresis loop decreases with succeeding cycles until the third cycle. The preconditioning behaviour is believed to be due to strain softening in the tissue in response to the loading.

The first two cycles were for preconditioning the strip mechanically. The preconditioning behavior was believed to be due to strain softening (a non-viscoelastic behavior observed during preconditioning) in the tissue in response to the loading. The third cycle was used for the stress–strain analysis. The strain rate was 0.5 mm/s. The whole segment was photographed using a video camera (SONY CCD Camera, DXC-151A, Tokyo, Japan) for later analysis of length and width. Morphometric data as the length, thickness and width were obtained from digitized images and from the strips in the no-load state and stretched states. Measurements were done using image analysis software (Sigmascan 4.0, Sigma Corporation, San Rafael, CA, USA). Parameters h and w refer to the thickness and width at the no-load state. The wall thickness and the width were averaged from 10 measurement points along the whole length of the strip.

Three-way analysis of variance was used to detect differences among the locations, directions and layered structures. Linear regression and multiple linear regression analyses were used to analyze the association between the stiffness of the intact wall with the stiffness and thickness of mucosa–submucosa and muscle layers. The results were regarded as significant when $P < 0.05$.

2.1.2 STRUCTURAL TESTS IN PRE- AND POST-SURGICAL CONFIGURATION OF THE STOMACH

The structural behavior of the stomach in pre- and post-bariatric surgery conformations was analyzed by inflation tests. Stomachs of eight piglets (weight: 30 ± 2 kg) were provided by a local abattoir. All the animals were clinically healthy. Animals sacrifice occurred in early morning and mechanical testing of one stomach lasted about five hours. Consequently, only one sample was processed in one day. Within 15 min from pig sacrifice, the stomach was harvested, packed in physiological saline (0.9% NaCl) at 4°C and brought to the laboratory. Each sample was composed of the stomach and short portions of esophagus and duodenum. The sample was gently washed with cold physiological saline to remove any residual chime, and maintained in saline at low temperature (4°C) up to the development of mechanical tests. All the experimental activities were concluded within at most seven hours from the animal sacrifice, at room temperature. Details about the inflation protocol are reported below. Preliminarily, the sample was placed on a laminated graph paper and spread out to its physiological bean-shape conformation (figure 2.3). Pictures of the stomach were taken for subsequent measurements.

A peristaltic pump (VerderFlex Vantage 5000, Verder Ltd, UK) and a pressure transducer (142 pc 01d, Honeywell, USA) were connected to the sample by rubber tubes. Pump and transducer tubes were fixed to esophageal and duodenal stubs, respectively, by means of elastic seams (figure 2.3 b). The transducer was interfaced to a laptop PC by a microcontroller (Arduino MEGA 2560, Arduino LLC). Data

storage was fixed at 4 Hz sample rate. The instrumented stomach was completely immersed in saline to prevent gravity effects (figure 2.4). Sample experimenting was performed by a multi-step inflation test. Each step was composed of 100 ml inflation of saline (0.9% NaCl, room temperature) at 50 ml/s inflation rate, and subsequent 300 s of rest to allow the almost complete development of relaxation phenomena.

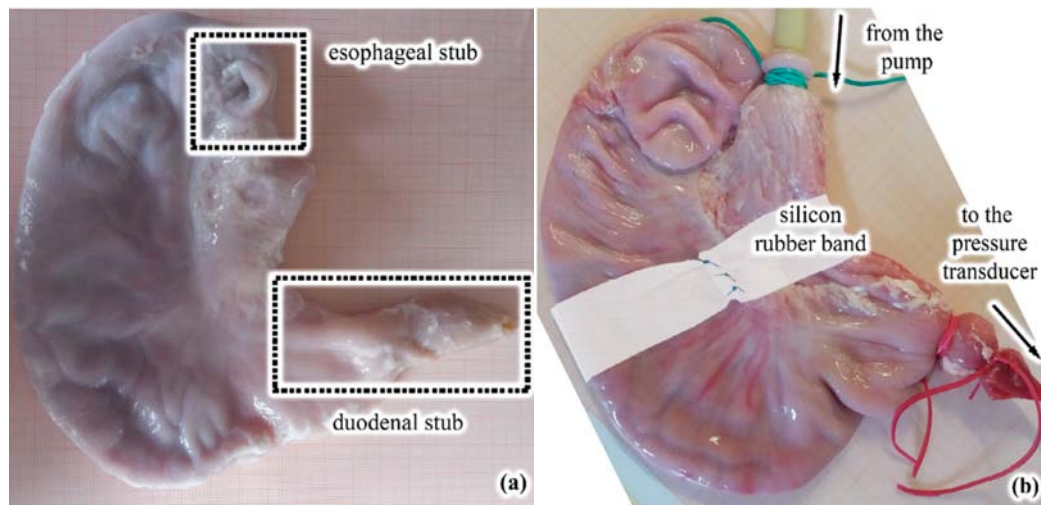


Figure 2.3. the stomach was placed on a laminated graph and spread out to physiological bean-shape (a). The stomach was connected to a peristaltic pump and a pressure transducer by rubber tubes. After preliminary experimentations in the pre-surgical conformation, a silicon rubber band was applied to simulate stomach configuration after gastric banding (b).

The rest period was assumed in consideration of typical values of relaxation times of soft biological tissues, which range between 0.01 and 100 s. The step was repeated up to 1000 ml inflation. Subsequently, the stomach was completely deflated at 50 ml/s deflation rate (figure 2.5a). The overall inflation test was repeated five times on each stomach. The different inflation tests were interspersed among each other by 600 s of rest to allow the development of viscous recovery phenomena (Carniel et al., 2015; Natali et al., 2017).

After mechanical testing, the stomach sample was further dissected and wall thickness was measured in different positions by a digital caliper.

Considering the typical time- and loading history- dependent behavior of biological tissues and structures, preliminary experimentations were performed

on the first two stomachs. In detail, the activities aimed at evaluating the possible mutual influence of subsequent inflation tests.

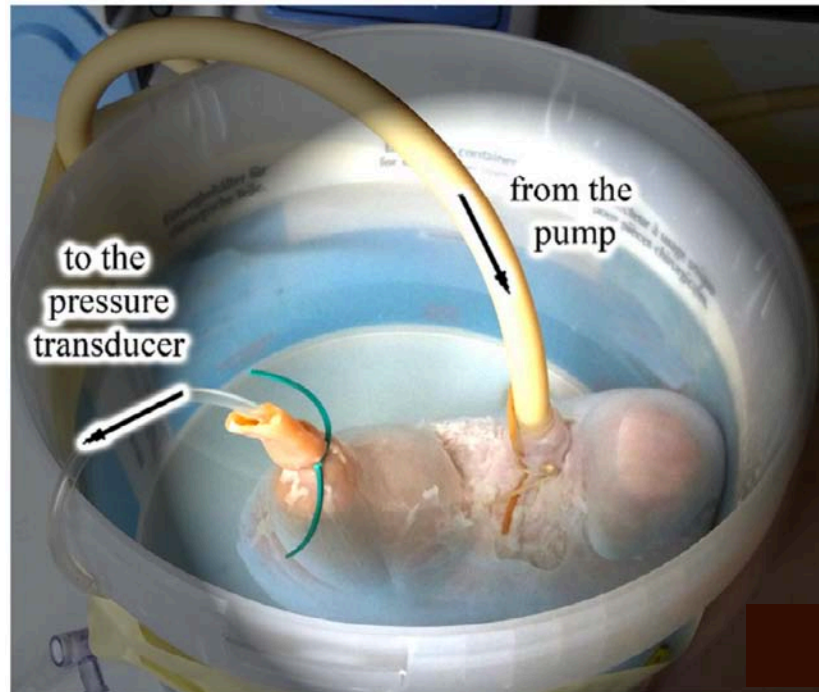


Figure 2.4 Inflation tests on piglet stomachs: during mechanical testing, the stomach was immersed in saline to prevent gravity effects.

With regard to both the stomachs, a significant difference was observed between the first and the second inflation test, while the stomach exhibited similar response during the last four inflation tests. The first inflation test was consequently assumed as a preconditioning action, while the subsequent four inflation tests actually provided data about the structural behavior of the stomach. Experimentations on the other six stomachs were performed considering both pre- and post-bariatric surgery configurations. Gastric banding was simulated by applying a homemade silicon rubber (Siltec RTV 930, Thechim Group Srl, Milano, Italy) band all around the body of the stomach, from the lesser curvature region to the greater curvature region. The silicon band was 25 mm wide and 0.5 mm thick. The length of the band was defined to avoid band tension in the stomach un-inflated configuration. The band was fixed to the stomach wall by three or four transmural stitches to prevent band migration during testing (figure 2.3b). Three

inflation tests were performed on the not operated stomach, providing data about the mechanical behavior of the sample in the pre-surgical configuration. Subsequently, surgical intervention was developed, and two further inflation tests were performed on the same stomach, providing information about the structural response in the post-surgical configuration.

Experimental activities led to pressure–time data (figure 2.5b) depending on the assumed volume-time inflation history (figure 2.5a).

Results were post-processed aiming at characterizing the stomach structural behavior in both pre- and post- surgical configurations. With regard to each inflation test, the collection of pressure and volume data at the end of the rest stages (red empty circles in figure 2.5b) led to pressure–volume almost equilibrium curves (figure 2.6a). The equilibrium pressure–volume response specifies the stomach behavior when all the time- dependent micro-structural rearrangement phenomena are allowed to completely develop during testing, as at the end of pressure relaxation stages, or during continuous inflation test developed at a sufficiently low inflation rate.

The analysis of pressure–time results during the constant volume stages (gray rectangles in figure 2.5b) led to relaxation curves (figure 2.6b). With regard to each stomach, curves from the analysis of the first inflation test were discarded, because of pre- conditioning phenomena. Curves from the subsequent inflation tests were collected from experimentations performed on all the stomachs, and statistically processed. Curves from tests performed before and after gastric band application were separately analyzed.

Although the stomachs have been harvested from similar piglets, the stomach dimensions were necessarily lightly different. Consequently, the comparison of pressure–volume curves from tests developed on different stomachs required to properly weight the volume data.

A volumetric ratio was defined, as the ratio between the volume of the inflated stomach V and the volume of the stomach at rest V^0 (Carniel et al., 2014; Natali et al., 2016 and 2017). Considering the flaccidity of stomach wall in the completely

empty configuration, volume V^0 of each stomach was defined as the volume of the saline that had to be inflated to reach a 0.3 kPa pressure at the end of relaxation phenomena. Volume V^0 of the specific stomach was evaluated considering equilibrium pressure–volume data from the second inflation history performed on the specific stomach itself.

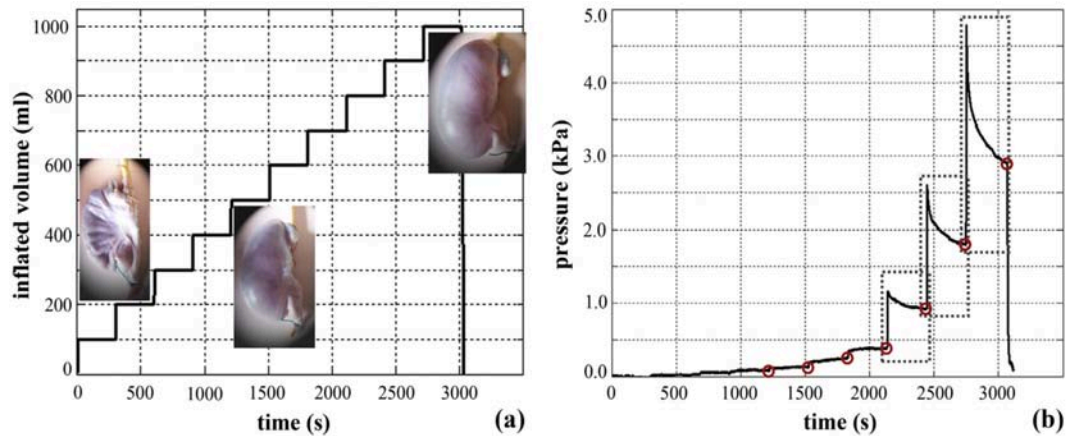


Figure 2.5. Experimental procedure and results: inflated volume–time history assumed during all the inflation tests (a) and example of pressure–time data recorded during an inflation test (b) with pressure values at the end of the volume rest stages, as the almost equilibrium pressure conditions, while gray rectangles highlight pressure relaxation phenomena.

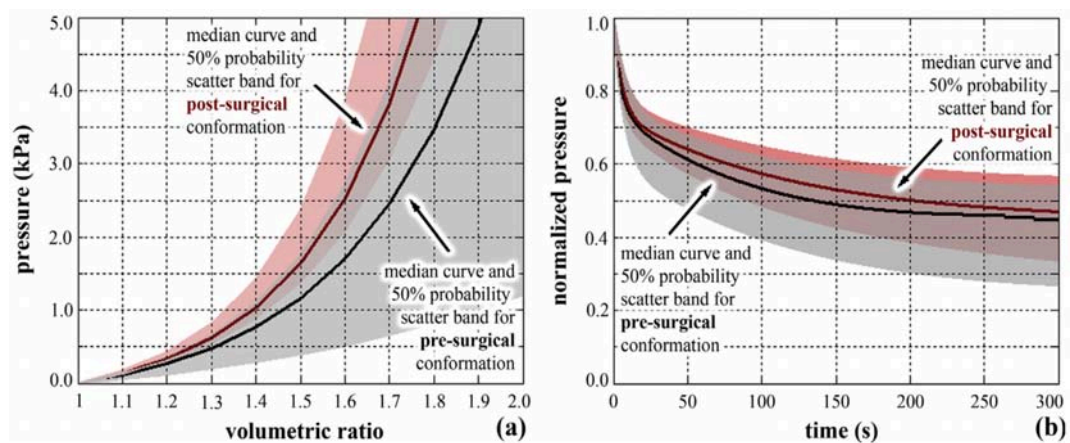


Figure 2.6. Experimental results from inflation tests: statistical distributions (median curves and 50% probability scatter bands) of equilibrium pressure–volume (a) and relaxation curves (b). Results are reported for experimental activities performed on stomachs in both pre- (black curves and gray bands) and post- (red curves and pink bands) surgical conformations.

2.2 STOMACH TISSUE MECHANICS

The stress and stretch ratio in a gastric wall strips were computed by Zhao et al as:

$$\text{Stress: } T = \frac{F}{A_0}$$

where F is the force recorded, and A_0 is the cross-sectional area (computed from wall thickness h and width w as $A_0 = wh$)

$$\text{Strech ratio: } \lambda = \frac{L_s}{L_0}$$

where L_s is the stretched state and L_0 is the initial state. The stress and stretch ratio curve obtained from previous equations can be curve fitted by using the function

$$T = b (e^{a(\lambda-1)} - 1)$$

where T and λ are the stress and stretch ratio, a and b are the material constants, where a relates to the stiffness.

When a strip is tested in a tensile testing machine by imposing a cyclically varying strain, the stress response will show a hysteresis loop for each cycle. Figure 2.2 shows a recording of the force–deformation relationship from a fundus intact layer strip. The area of the hysteresis loop decreases with succeeding cycles and the curves shifted to the right, rapidly at first, then tending to a steady state at the third cycle. This mechanical phenomenon observed in soft tissues is called. For the stomach three preconditioning cycles were necessary to obtain repeatable results. The stress– strain data provided below are from the last (preconditioned) loading curve.

The longitudinal and circumferential stress–strain curves differed between the strips obtained from different layers. Figure 2.7 shows the circumferential stress–strain curves of the layers. For the fundus, corpus and antrum, the circumferential stress–strain curves of the mucosal–submucosal strips were located to the left, indicating that those strips were the stiffest. The curve for the muscle strips was

located to the right for the fundus and corpus, indicating it was softest. However, the curves obtained from muscle and intact layer strips did not differ in antrum. The same pattern was observed for the longitudinal stress–strain curves.

Both the longitudinal and circumferential stress–strain curves differed between the strips in different locations. Figure 2.8 shows the longitudinal stress–strain curves at different locations. The same pattern was found for the circumferential stress–strain curves.

For the intact, muscle and mucosa–submucosa layers, the stress–strain curves for the corpus strips were located to the left, indicating that those strips were the stiffest. The curves obtained in intact and muscle strips from the fundus was located to the right, indicating they were softest. The curves of mucosa–submucosa layer strips did not differ between fundus and antrum.

The stress–strain curves differed between the strips obtained in different directions for all three locations. Figure 2.9 shows circumferential and longitudinal stress–strain curves obtained in the intact layer at different locations. A similar pattern was found for the muscle and mucosa–submucosa layers. Both for the intact and muscle layers, the stress–strain curve for the longitudinal strips was located to the left, indicating that those strips were the stiffest whereas the curve for the circumferential strips was located to the right, indicating it was softest. For the mucosa–submucosa layers, the longitudinal strips were stiffer than the circumferential strips in the fundus and corpus, but not in the antrum.

	Fundus		Corpus		Antrum	
	Circ	Long	Circ	Long	Circ	Long
Intact layer	9.67 ± 0.85	11.05 ± 1.09	19.46 ± 2.81	22.37 ± 1.58	12.51 ± 1.89	14.71 ± 1.14
Muscle layer	6.84 ± 0.87	7.16 ± 0.84	16.02 ± 2.02	18.31 ± 0.92	15.09 ± 1.07	17.08 ± 2.49
Mucosa–submucosa layer	11.31 ± 1.07	12.34 ± 1.39	24.51 ± 1.94	27.35 ± 1.61	11.21 ± 1.55	13.11 ± 2.44

Table 2.1. Mechanical constant a obtained by Zhao et AL.

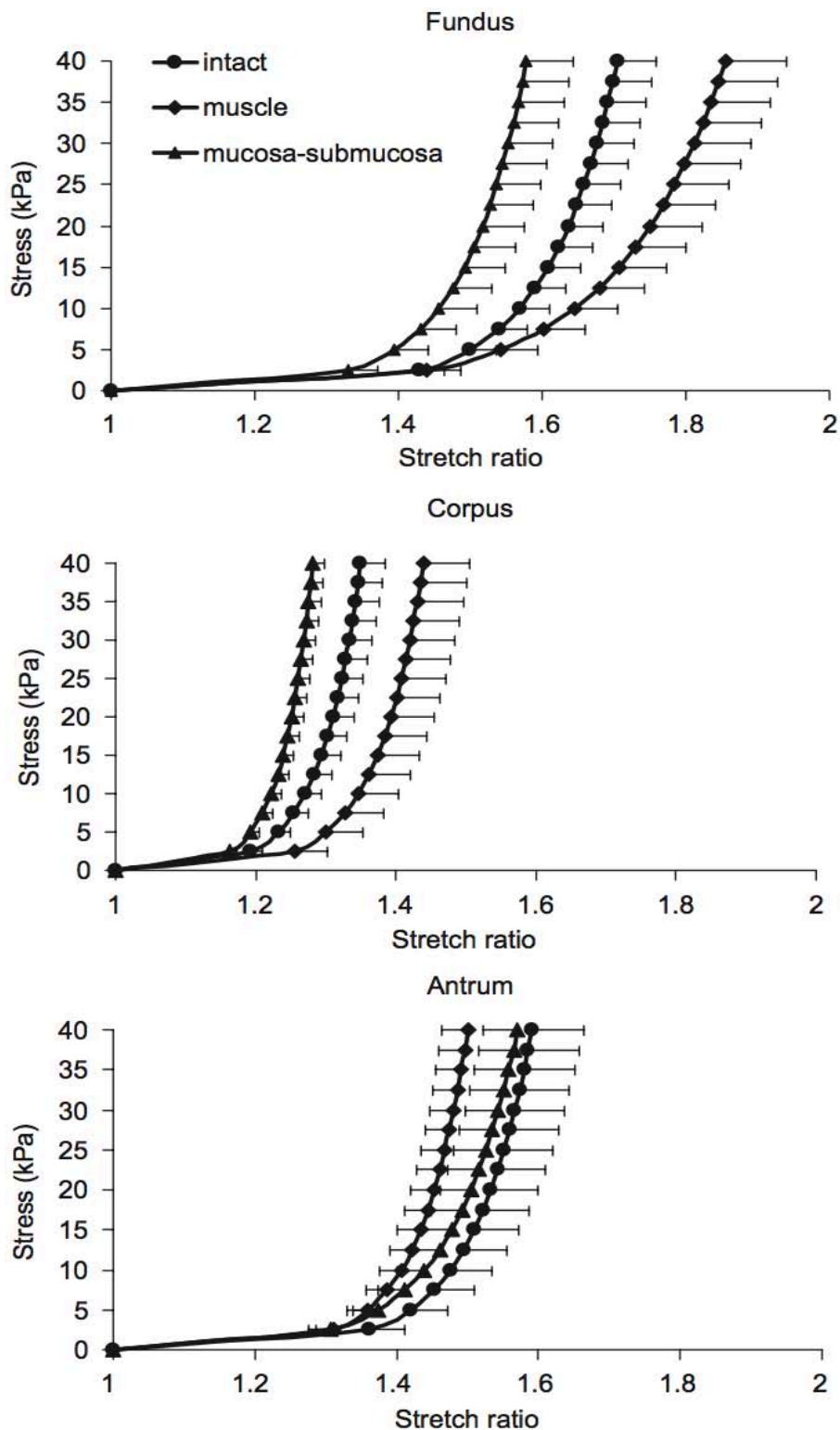


Figure 2.7. Circumferential uni-axial stress–strain relationships of gastric strips. The stress–strain curves differed between the strips obtained in different layers. At all locations, the stress–strain curve for the mucosa–submucosa strips was located to the left whereas the curve of the muscle strips was located to the right. It indicated that the mucosa strips were the stiffest and the muscle strips were the softest.

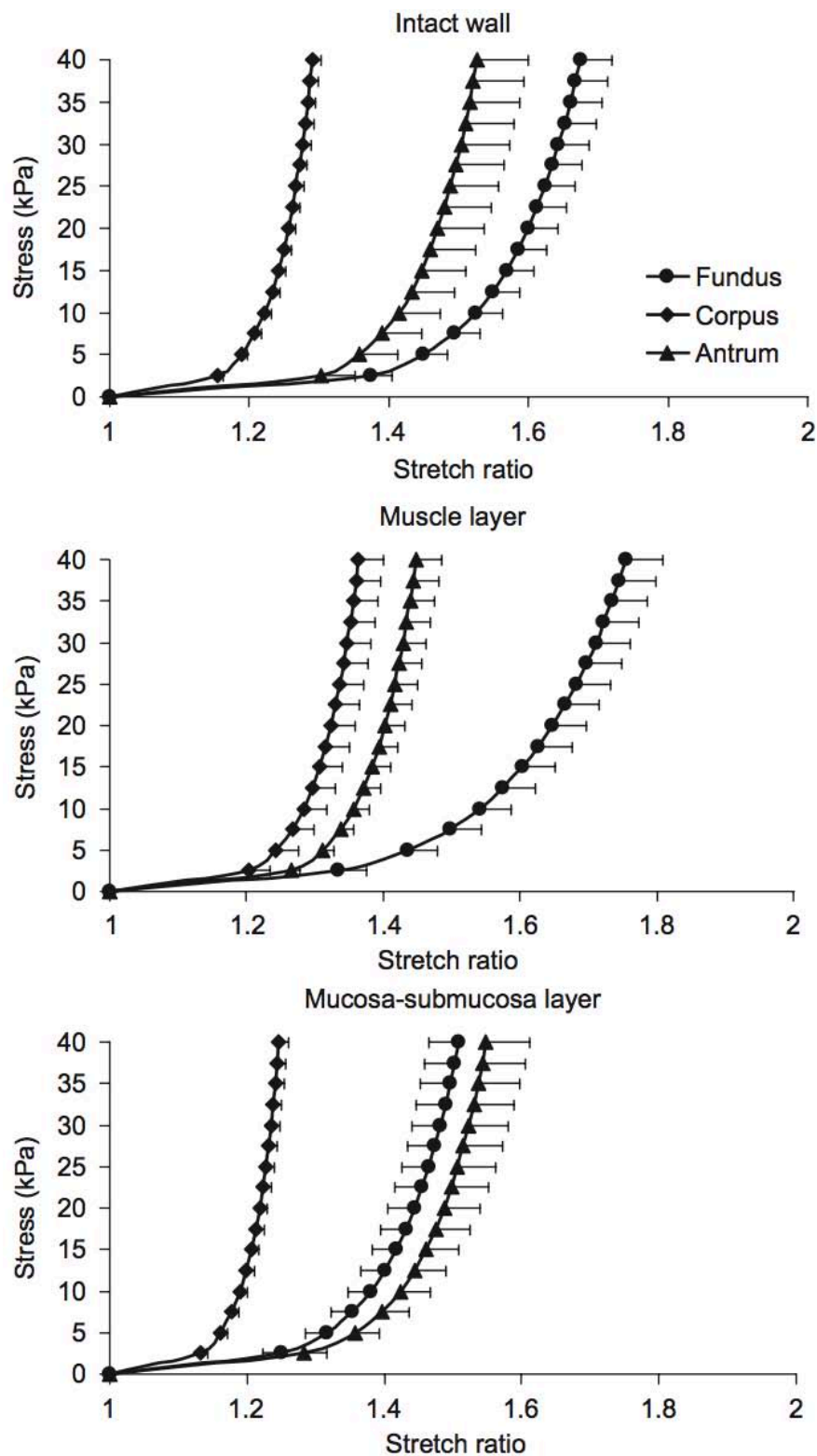


Figure 2.8. Longitudinal uni-axial stress–strain relationships of the gastric strips. The curves of the corpus strips were located to the left and the curves of the fundus strips were located to the right. It indicated that the corpus strips were the stiffest and the fundus strips were the softest.

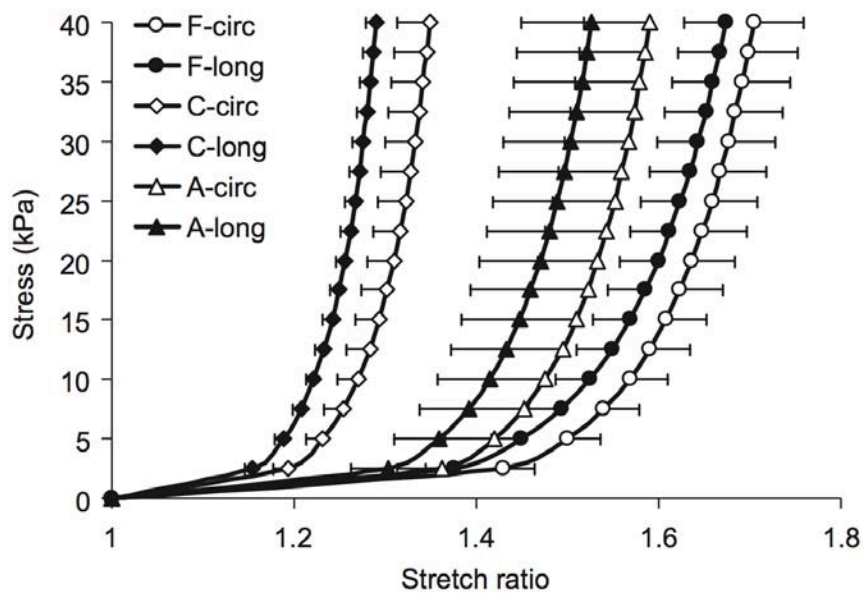


Figure 2.9. Uni-axial stress–strain relationships of the intact gastric strips. The longitudinal stress–strain curves were located to the left, indicating that those strips were the stiffest, whereas the curves for the circumferential strips were located to the right, indicating they were softest. Notes: F, fundus; C, corpus; A, antrum; circ, circumferential direction; long, longitudinal direction.

2.3 COMPUTATIONAL MODEL

The average virtual solid model is obtained by processing the pictures of the eight stomachs in unstrained configuration. Border lines of the pictures were manually identified (figure 2.10). Esophageal and duodenal stubs were distinguished, aiming at defining a region composed of stomach body, fundus, antrum and pylorus. Points from the border lines were identified and interpolated by splines (Matlab, The MathWorks Inc., Natick, MA, US). Stomach width and length, as the minimum distance between lesser and greater curvature and the maximum distance between fundus and pylorus, respectively, were measured.

Averaging of splines data from the different stomachs led to a mean border line, which was smoothed and lightly morphed considering the mean values of stomach width and length. The mean border line was imported to a 3D CAD software (UGS NX, Siemens PLM Software, Plano, TX, US).

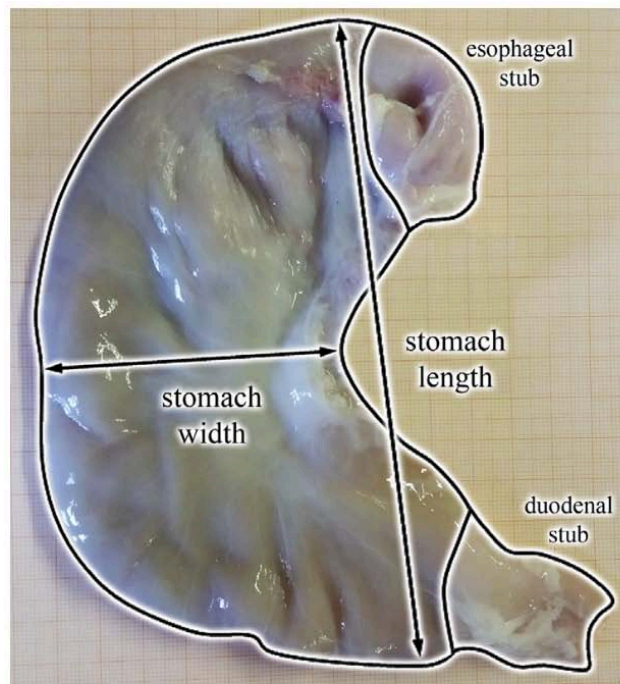


Figure 2.10. Identification of stomach border lines and dimensions (a).

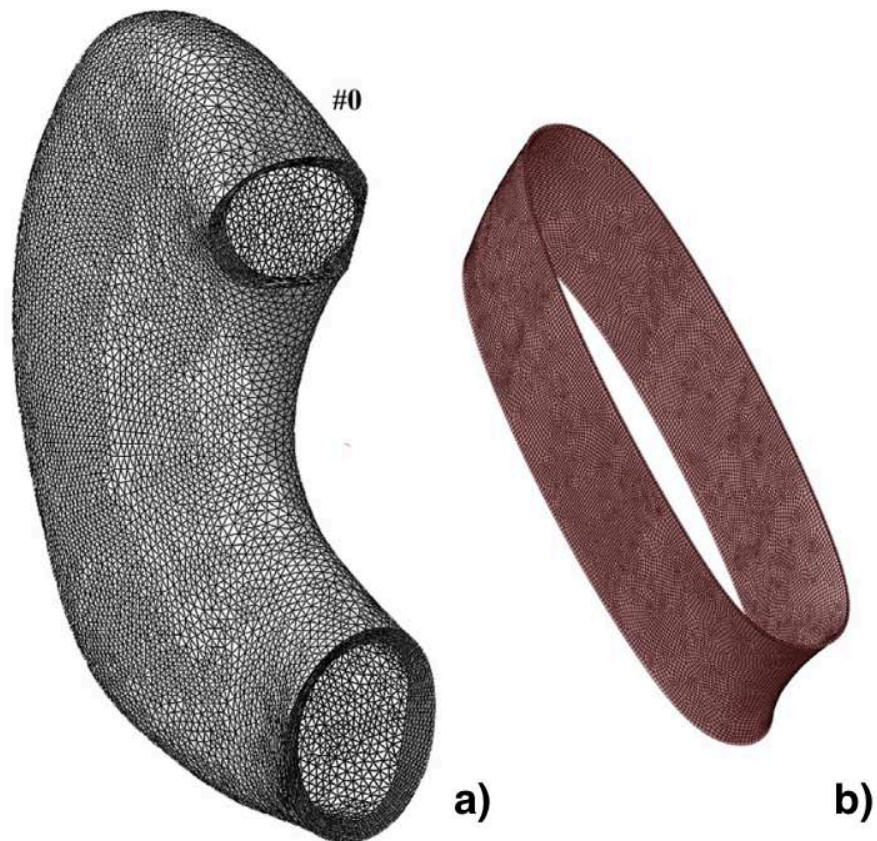


Figure 2.11. Finite element models of the stomach in the pre-surgical conformation #0 (a) and the gastric band (b).

An almost flattened and closed surface was constructed on the mean border line. Holes were provided to define esophageal and duodenal junctions. Finally, surface extrusion led to the virtual solid model of the stomach. A homogeneous 4.1 mm extrusion thickness was assumed, considering measurements that were performed on the experimental samples after mechanical testing. The virtual solid model was imported into the finite element pre-processing software Abaqus/CAE 6.14 (Dassault Systèmes Simulia Corp., Providence, RI). Three-nodes tetrahedral hybrid elements were adopted to mesh the stomach wall, leading to a computational model composed of about 400.000 elements and 90.000 nodes (figure 2.11a). Hybrid pressure–displacement formulation was assumed because of the typical almost incompressible behavior of soft biological tissues.

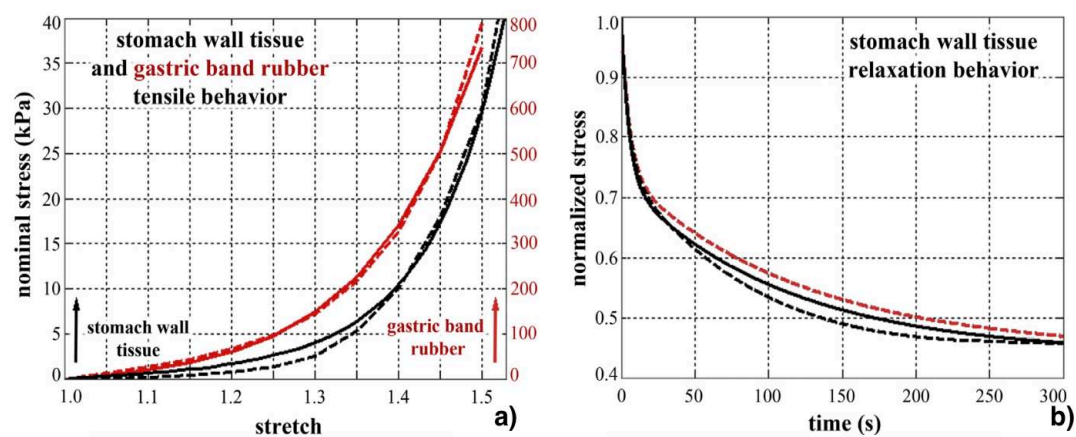


Figure 2.12. Constitutive identification of stomach wall tissue and gastric band rubber: comparison of experimental data from uni-axial tensile tests (discontinuous lines) and model results (continuous lines) (a). Relaxation behavior of stomach wall tissues: median experimental results from structural tests on stomachs in pre- (discontinuous black line) and post- (discontinuous red line) surgical conformation and model results (continuous black line) (b).

2.3.1 CONSTITUTIVE MODEL OF THE STOMACH TISSUES

Aiming at a preliminary investigation of stomach mechanical functionality, isotropic and homogeneous mechanical properties were assumed. The visco-hyperelastic constitutive formulation was developed considering the following stress–strain history relationship (Carniel et al., 2013b, 2014b):

$$\mathbf{P}(\mathbf{C}, t) = \mathbf{P}^0(\mathbf{C}) - \sum_i \mathbf{q}^i(\mathbf{C}, t)$$

$$\mathbf{P}^0(\mathbf{C}) = -p\mathbf{F}^{-T} + C_1^0 e^{\alpha_1(I_1-3)} \left(2\mathbf{F} - \frac{2}{3}I_1\mathbf{F}^{-T} \right)$$

where \mathbf{P} is the first Piola–Kirchhoff stress tensor, \mathbf{F} is the deformation gradient, p is a Lagrange multiplier that specifies the hydro- static pressure, I_1 is the first invariant of the right Cauchy-Green strain tensor $\mathbf{C} = \mathbf{F}^T \mathbf{F}$. \mathbf{P}^0 defines the instantaneous mechanical behavior of the tissue, as the tissue mechanical response when deformations are sufficiently fast imposed. Constitutive parameter C_1^0 specifies the tissue instantaneous shear stiffness, while parameter α_1 regulates the non-linearity of the mechanical response because of stiffening phenomena with stretch. The reported formulation of \mathbf{P}^0 was assumed because of its capability to interpret the typical features of soft tissue mechanics, as almost incompressibility and non-linear elastic behavior (Carniel et al., 2014b). Viscous variables \mathbf{q}^i evaluate the relaxed stresses because of viscous phenomena. Their evolution is specified by differential equations:

$$\dot{\mathbf{q}}^i + \frac{1}{\tau^i} \mathbf{q}^i = \frac{\gamma^i}{\tau^i} \mathbf{P}^0$$

relaxation time τ^i makes it possible to evaluate the time which the i th viscous process requires to develop. Relative stiffness parameter γ^i specifies the contribution of the i th viscous process to the stress drop the material undergoes because of relaxation phenomena. The following parameter is introduced:

$$C_1^\infty = \left(1 - \sum_i \gamma^i \right) C_1^0$$

C_1^∞ characterizes the tissue shear stiffness at equilibrium (Carniel et al., 2013a). The constitutive formulation was implemented in Abaqus which adopts an updated lagrangian formulation for the solution of mechanical problems when geometrical non-linearity occurs.

Tissue parameters C_1^∞ and α_1 were identified by the inverse analysis of mechanical tests that have been developed on pig stomach samples by Zhao et al. (2008). Mechanical tests have been performed considering uniaxial loading conditions on specimens that have been harvested from the different regions of the stomach and along different directions. Considering the homogeneous and isotropic configuration of the assumed constitutive model, experimental results from the different specimens have been averaged, leading to a mean stress–strain curve (figure 2.12a). The experimental protocol and the adopted strain rate suggested assuming equilibrium response of the tissue. Considering the specific configuration of mechanical tests, the following equilibrium formulation was derived from previous equations and it was applied to fit experimental data (figure 2.4d):

$$P_u = C_1^\infty e^{\alpha_1(\lambda_u^2 + 2\lambda_u^{-1} - 3)}(\lambda_u - \lambda_u^{-2})$$

where λ_u and P_u are stretch and nominal stress, respectively, along the uniaxial loading direction. Viscous parameters τ^i and γ^i were identified by analyzing results from the developed inflation tests on pig stomachs (figure 2.6b). Results from structural tests can be adopted to identify tissue viscous parameters, because viscous phenomena usually exhibit similar trend at both tissue and structure level (Natali et al., 2016). Normalized pressure-time curves were fitted by the following relaxation function (figure 2.12b):

$$p^{norm}(t) = (1 - \gamma_u - \gamma_2) + \gamma_1 e^{-\frac{t}{\tau_1}} + \gamma_2 e^{-\frac{t}{\tau_2}}$$

The function considered two viscous branches. The number of viscous branches was defined to contemporarily minimize the number of parameters and correctly interpret the trend of experimental data (Carniel et al., 2014). The identified constitutive parameters are summarized in (table 2.2).

	Data source/notes	C_1^∞ (kPa)	α_1		
Stomach wall tissue equilibrium hyperelastic behavior	Zhao et al. (2008)	0.86	4.83		
	Data source/notes	γ_1	γ_2	τ_1 (s)	τ_2 (s)
Stomach wall tissue viscoelastic behavior	Fig. 3b pre-surgical (median)	0.23	0.32	4.61	98.36
	Fig. 3b post-surgical (median)	0.30	0.26	5.50	119.81
	Assumed values	0.27	0.29	5.06	109.09
	Data source/notes	μ (kPa)	α		
Gastric band silicon rubber hyperelastic behavior	Technical data	48.76	12.15		

Table 2.2 Identified constitutive parameters of stomach wall tissue and gastric band silicon rubber.

2.3.2 COMPUTATIONAL ANALYSIS OF THE GASTRIC BANDING

The numerical model of the gastric band was developed by eight-nodes hexagonal elements (figure 2.11b). The mechanical behavior was specified by an Ogden hyper-elastic formulation and parameters were identified by the analysis of technical data from tensile tests performed on the specific silicon rubber (figure 2.12a, table 2.2). The numerical model of the gastric band was located around the stomach model. Computational models contemplated different band positions, which were defined based on the developed experimental activities (figure 2.13, conformation #1) and on standard surgical procedures (figure 2.8, conformations #2, #3, #4). Friction contact condition (0.01 friction coefficient) allowed characterizing interaction between the stomach and the band.

The influence of gastric band pre-tensioning was analyzed. Band pre-stretching and pre-tensioning were imposed by assuming a fictitious thermal contraction of the band. Fictitious thermal expansion coefficient was set at 1.0. With particular regard to post-surgical conformation #4, different models for different values of band pre-tension were developed. The relationships between fictitious temperature and band mean stretch (figure 2.14a) and between bands mean stretch and mean tension (figure 2.14b) were identified by performing numerical analyses. In detail, computational models of post-surgical conformation #4 were developed assuming four different pre-tension conditions (figure 2.15). Finally, computational models of all the post-surgical conformations, #1, #2, #3 and #4, were developed assuming an almost 30% mean band pre-stretch (figure 2.16).

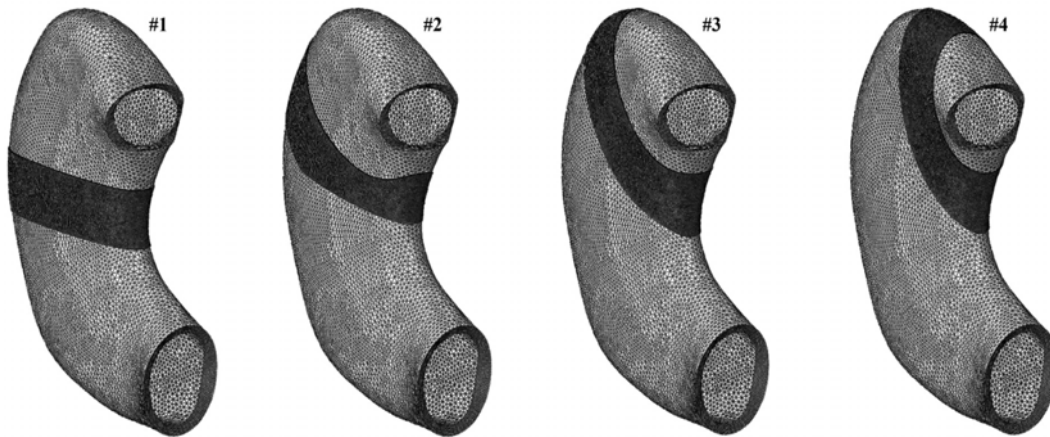


Figure 2.13. Finite element models of the stomach in different post-surgical conformations.

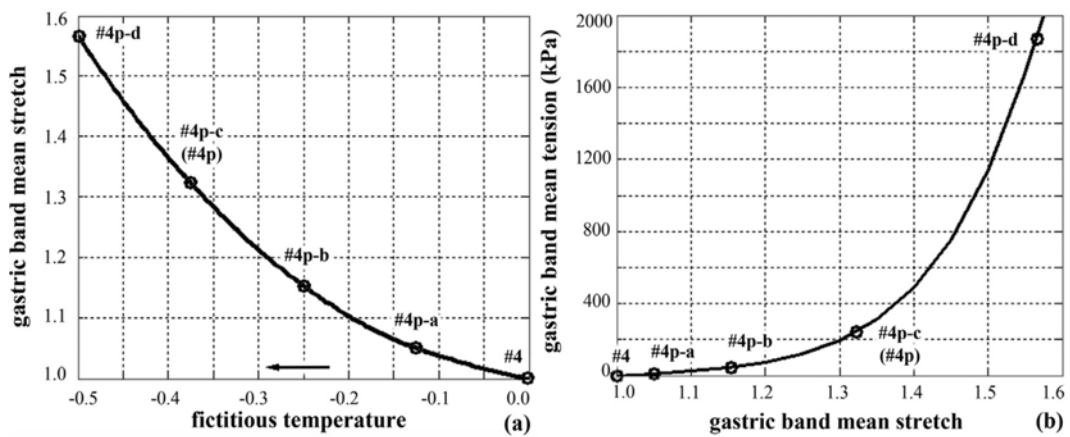


Figure 2.14. relationship between mean stretch and fictitious temperature (a), relationship between mean tension and mean stretch (b).

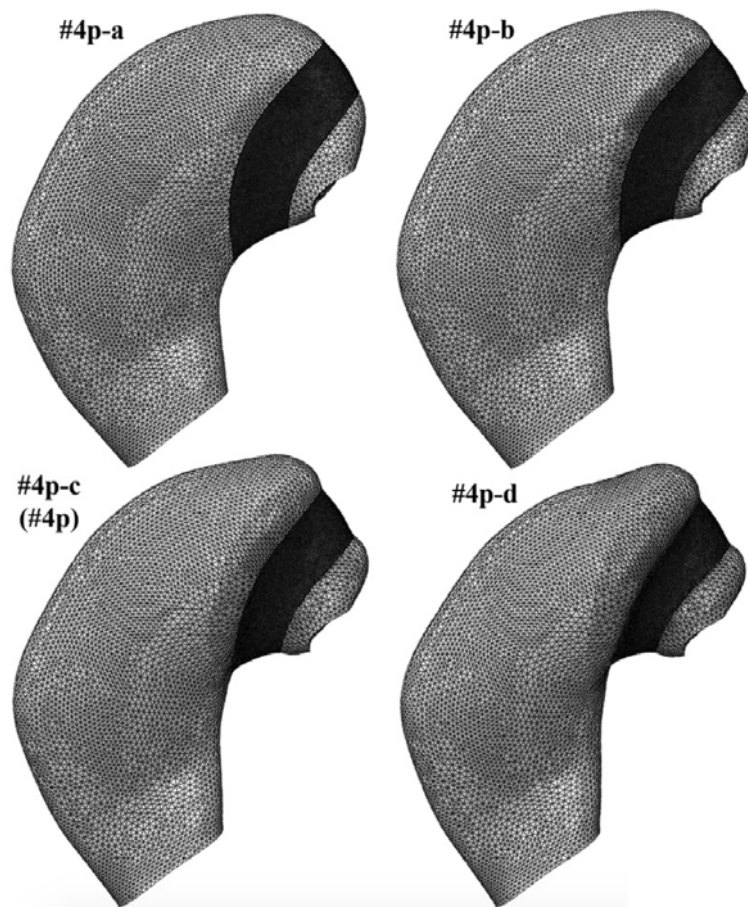


Figure 2.15. computational model conformation for different band pre-tension conditions.

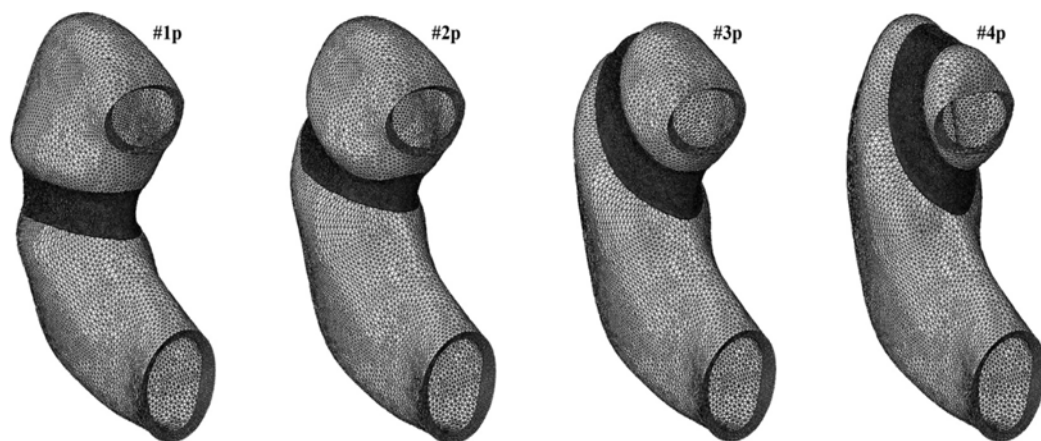


Figure 2.16. Finite element models of the stomach in different post-surgical conformations with band pre-tension (almost 30% band pre-stretch).

2.3.3 NUMERICAL ANALYSIS

Numerical analyses were performed by the general purpose finite element software Abaqus Standard 6.14 (Dassault Systèmes Simulia Corp., Providence, RI). A fluid filled-cavity was defined to characterize the internal region of the stomach and to simulate the inflation process. Considering the boundary conditions imposed during experimental inflation tests, the upper and the lower extremity of the cavity, at the gastroesophageal and the gastroduodenal junctions, were fixed. The volume of the cavity was progressively raised up to a 1000 ml volume increment. Aiming at validating the computational model, by comparing computational results with pressure–volume equilibrium curves from experimental activity, a 0.1 ml/s inflation rate was set. Preliminary computational analyses showed that the selected inflation rate led to almost equilibrium response. Numerical analyses were developed considering the stomach in the pre-surgical configuration and in the different post-surgical conformations. Analyses aimed at evaluating stomach functionality depending on inflation rate, band position and band pre-tension.

Inflated volume data from numerical analyses were post-processed to compute volumetric ratio information. Similar to experimental activities, the volume of the stomach at rest was evaluated considering the volume of the fluid that had to be inflated to reach a 0.3 kPa pressure during a 0.1 ml/s inflation process in the pre-surgical conformation #0.

2.4 RESULTS

Experimental testing provided data about the stomachs mechanical functionality in both pre- and post- bariatric surgery conformations, as pressure–time data (figure 2.5b) depending on volume–time inflation history (figure 2.5a). Post-processing of experimental results made it possible to characterize the stomach structural behavior.

The collection of pressure–volume data at the end of the rest stages led to statistical distributions of equilibrium curves (figure 2.5a), while the analysis of

pressure–time results during the constant volume stages led to statistical distributions of relaxation curves (figure 2.5b). Statistical distributions were provided in terms of median curves and associated 50% probability scatter bands. Starting from experimental data, a computational model of the stomach was developed (figure 2.11a), also considering different post- surgical configurations (figure from 2.13 to 2.16). Stomach morphometry was defined considering a mean border line and average dimensions of the experimental samples (figure 2.10), which were measured before (stomach width: 73.4 ± 6.2 mm; stomach length 168.6 ± 9.5 mm) and after (wall thickness: 4.1 ± 1.8 mm) mechanical testing. Constitutive parameters (table 2.2) were identified by the inverse analysis of data from experimental activities (figure 2.12a and 2.12b). The reliability of the stomach models was assessed by simulating the experimental inflation processes and comparing experimental and numerical results (figure 2.17a).

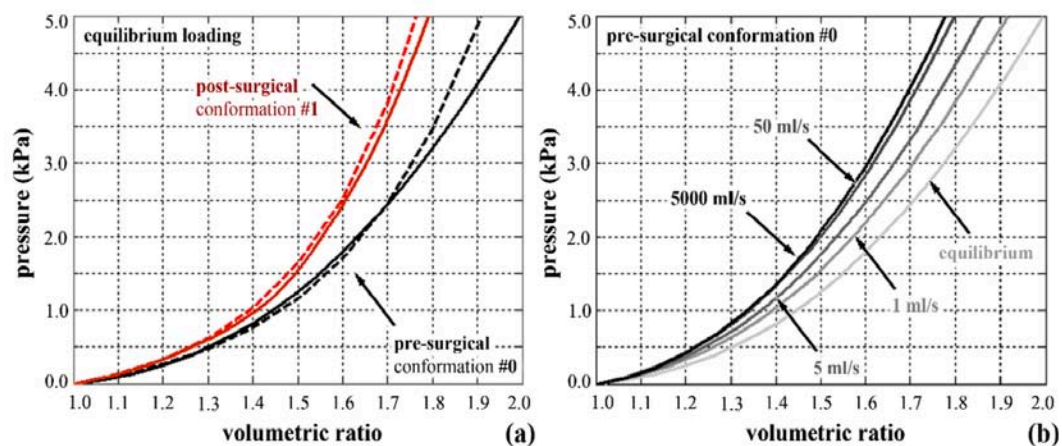


Figure 2.17. Comparison of pressure–volume behavior in pre- and post-surgical configurations: experimental (discontinuous lines) and model (continuous lines) results (a). Influence of inflation rate on pressure–volume behavior: results from computational analyses for the stomach pre-surgical conformation #0 (b).

Such analyses were performed considering both the stomach pre-surgical conformation #0 and the experimentally investigated post-surgical conformation #1.

Aiming at evaluating the influence of filling rate on stomach functionality, the model of the stomach in the pre-surgical conformation #0 was exploited to

perform computational analyses at different inflation rates, (i.e.: equilibrium inflating, 1 ml/s, 5 ml/s, 50 ml/s and 5000 ml/s). Computational results were post-processed leading to pressure–volume curves (figure 2.17b) and contours of tensile stress, as the maximum principal component of the Cauchy true stress tensor (figure 2.18). Computational methods allowed investigating the relationship between stomach post-surgical conformation and stomach mechanical functionality. Model of different post-surgical conformations were developed assuming different gastric band positions and different band pre-tension values.

Numerical results are summarized from figure 2.19 to 2.21. The influence of band position and pre-tension on stomach pressure–volume behavior is depicted in figure 2.19a and 2.19b, respectively, while the contours of tensile stress are reported in figure 2.20 and 2.21.

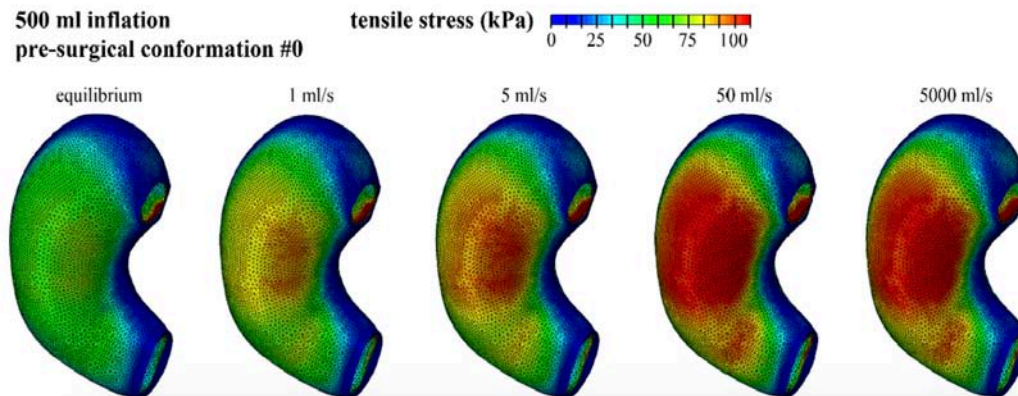


Figure 2.18. Contours of tensile stress at 500 ml inflation: equilibrium, 1 ml/s, 5 ml/s, 50 ml/s and 5000 ml/s inflating in pre-surgical conformation #0 (c).

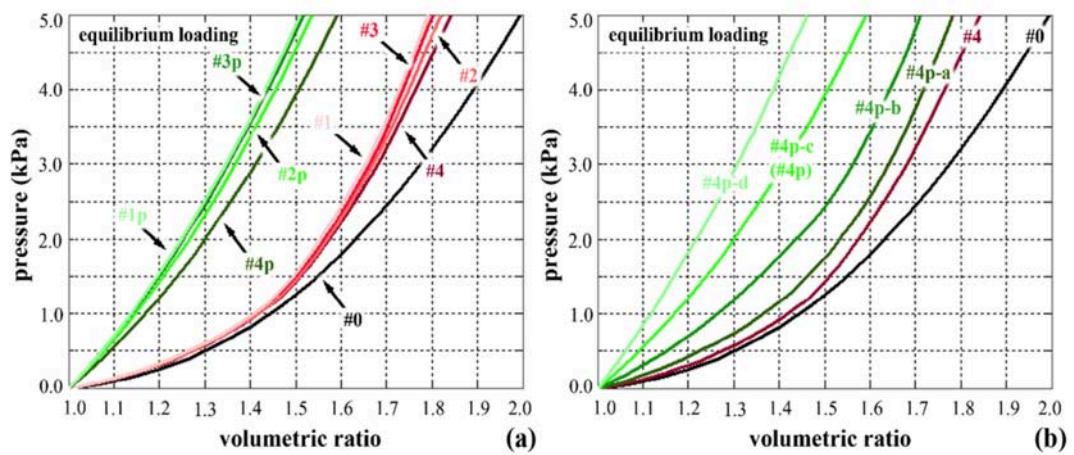


Figure 2.19. Contours of tensile stress at 500 ml inflation: equilibrium, 1 ml/s, 5 ml/s, 50 ml/s and 5000 ml/s inflating in pre-surgical conformation #0 (c).

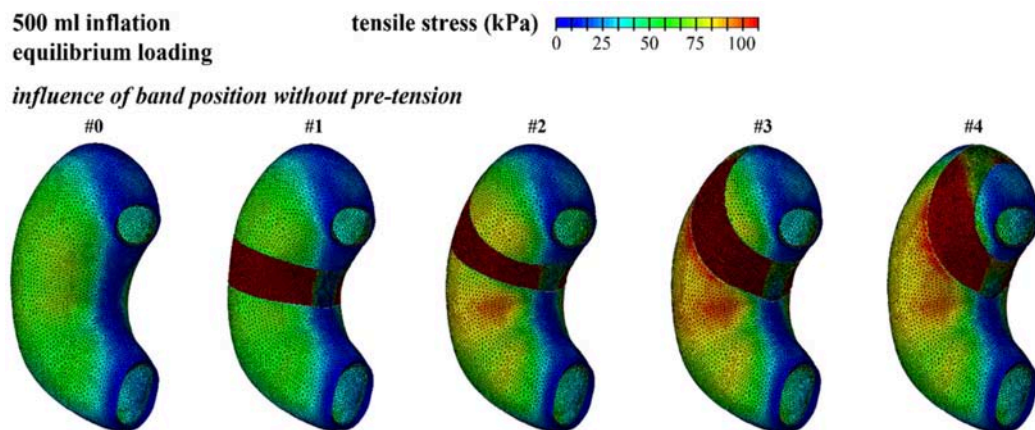
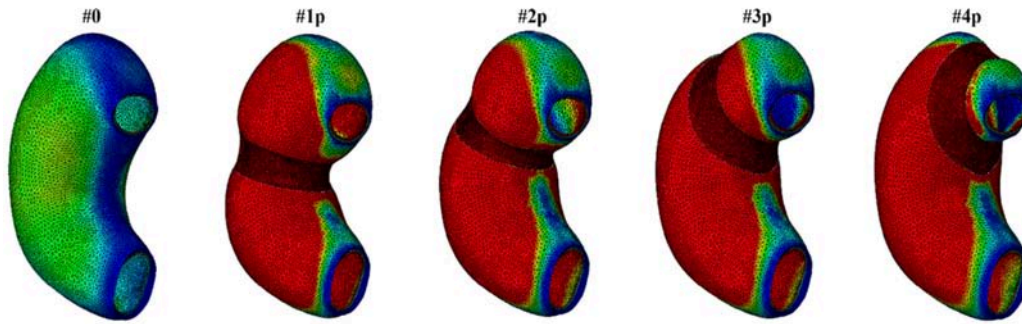


Figure 2.20. Influence of band position with band pre-tension (almost 30% band pre-stretch).

influence of band position with pre-tension (almost 30% pre-stretch)



influence of band pre-tension value (post-surgical conformation #4)

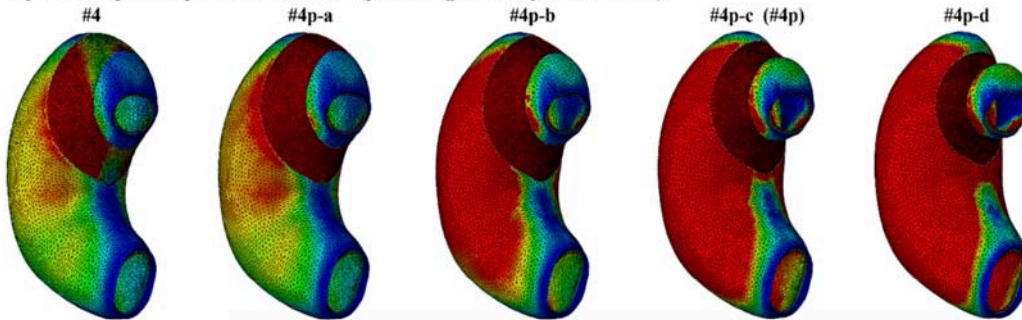


Figure 2.21. influence of band position with band pre-tension (almost 30% band pre-stretch) (up); influence of band pre-tension value for band position #4 (down).

2.4 DISCUSSION

To fully understand the physiology of stomach function we need to know the basic mechanical characteristics of the tissue, starting with the geometry of the zero-stress state and the passive stress–strain properties. From Zhao et al. study the anisotropic biomechanical properties of the pig stomach wall is confirmed, i.e., the uni-axial stress–strain was location- and direction-dependent. Furthermore, we demonstrated that the stress–strain properties are layer-dependent and that the properties of the mucosa–submucosa layer determine the wall stiffness.

The pig stomach wall was thinnest in fundus and thicker in the corpus and antrum. Measurement of the layered wall showed that the muscle layer was thickest in the antrum and the mucosa–submucosa layer was thickest in the corpus. Hence, the pig stomach has a composite structure and each layer has different mechanical behavior at different locations. Zhao et al relaxed the smooth muscle in order to

obtain the true passive biomechanical properties which trend in an exponential way. It was clearly shown that the longitudinal and circumferential uni-axial passive biomechanical properties both in intact wall and layered wall differ between fundus, corpus and antrum. Furthermore, the mechanical properties differ between the stomach layers. Therefore, the anisotropic mechanical behavior of the stomach is not surprising due to the complex geometry and the composite structure. They demonstrated that association exists between the stiffness of the intact wall and the thickness and stiffness of the mucosa–submucosa. Furthermore, the mucosa–submucosa layer is stiffer than intact wall and muscle layer. Therefore, the properties of a mucosa–submucosa layer determine the stiffness of the intact wall.

The current study showed that the material properties of the fundus as well as the corpus and antrum were highly anisotropic. The material properties of the pig stomach are not only location- and direction- dependent, but also layer-dependent. Therefore, investigations of gastric tone must take into account the complex geometry and the anisotropic biomechanical properties of the gastric wall.

However, the different material properties in different part of the stomach relate to the various function of the stomach. Therefore, the material properties of the proximal stomach wall should be taken into account for the accommodation of the stomach. The thinner and softer fundus wall can increase compliance and is thus suitable for accommodation. Similarly, the thicker and stiffer wall of the corpus and antrum is suitable for stomach emptying promoted by the intense peristaltic contractions. The peristaltic ontractions create pressure, >100 mmHg, which is counteracted by the thick and stiff mucosa–submucosa. Furthermore, it is well known that the mechanoreceptors in the gastric wall are located both in the submucosa and in the muscle layers. This suggests that the populations of receptors from different locations in the wall may have different zero-stress and -strain settings and respond differently to the stimuli. Both distension and contraction may activate the mechanoreceptors. In order to optimize the

activation of such mechanoreceptors in post-surgical configuration of the stomach Carniel et al. 2017 designed a specific experimental procedure leading to a specific mechanical description of the stomach structure. Post- processing of experimental results showed the typical pressure–volume and pressure-time structural behavior of the stomach. Non-linear stiffening phenomena were observed, as a typical feature of soft biological tissues and structures mechanics.

Experimental activities were performed considering both pre- and post- bariatric surgery conformations, pointing out the influence of the specific bariatric intervention on structural stiffness, as the pressure–volume trend (figure 2.6a). Differently, the influence on time-dependent response, as the relaxation behavior (figure 2.6b), looked to be minor. Bariatric surgery modifies the stomach geometrical conformation and, as a consequence, the structural behavior. At the same time, micro-structural re-arrangement phenomena at tissue level determine the typical time dependent behavior, and bariatric surgery has not direct effects on such phenomena.

Results from experimental activities were exploited to develop, identify and validate a computational model of the stomach. Computational activities analyzed stomach natural configuration and different post-surgical conformations, which were defined considering different gastric band positions and band pre-tension values. With regard to stomach mechanical functionality, computational analyses pointed out the significant influence of filling rate, as reported by both pressure–volume behaviors and stress contours (figure 2.17-2.18).

Computational results highlighted the great influence of bariatric surgery parameters on stomach mechanics (figure 2.19-2.21). In detail, the surgical procedure strongly affects the stomach structural stiffness and the stress field conformation and intensity. Attention was here focused on gastric banding, because of its wide application and effectiveness. Nevertheless, the same approach can be adopted to analyze other surgical techniques and to design innovative and more reliable procedures.

The results show the potentiality of experimental and computational biomechanics for the investigation of stomach functionality and the planning of bariatric surgery procedures and techniques. Experimental activities allow evaluating stomach pressure–volume behavior depending on surgical methods and parameters. The increased stomach stiffness after surgery confirms the clinical evidence that bariatric intervention reduces the stomach capacity. On the other side, computational methods make it possible to broaden experimental results to an extremely wider scenario, considering many different surgical procedures. Furthermore, computational models provide information that experimental methods cannot supply. In detail, the computational approach makes it possible to identify the stress and the strain fields in stomach tissues, whose distribution is strongly affected by the bariatric procedure. As an example, position and pre-tension value of the gastric band have a relevant impact on both the stomach capacity and the areas of gastric wall that are mainly stressed (figure 2.16). As mentioned also in the first section of chapter 1, mechanical stimuli, as stress and strain, act on receptors that contribute to regulate the feeling of satiety. Considering the mechano-transduction capabilities and the locations of gastric receptors, it follows the relevance of methods that allow to evaluate the intensity and the conformation of stress and strain fields. The relevance of this topic is enforced by the recent trends in bariatric surgery, which aim not to restrict stomach capacity, but to induce satiety with small meals. More in details, new insights have been developed about the mechanisms that can explain the loss of body weight because of bariatric surgery. For example, there is nowadays a large body of evidence indicating that mechanistic mechanisms, such as stomach restriction and/or malabsorption, do not entirely and exclusively explain the results in obese patients after bariatric surgery. Post-surgical weight loss correlates to a large extent with reduced spontaneous eating. Available data indicate that operated individuals develop a new set point of their body weight, and changes in concentration of some hormones play a significant role. Such changes may be related to mechano-transduction phenomena.

Further efforts are mandatory for a more exhaustive and accurate analysis of stomach mechanical functionality before and after bariatric surgery. For example, the here reported experimental activities have been developed considering only a specific post- surgical conformation of the stomach. Moreover, stomachs were dissected from piglets. Samples were effectively smaller than the stomach from obese persons. Activities are under development on samples from adult pigs and aim at experimentally evaluating the influence of gastric band position and pre-tension. With regard to computational modeling, a more refined morphometric and constitutive characterization of stomach wall is being defined aiming at considering the wall non-homogeneous thickness and configuration, the tissues stratification and the anisotropic distribution of fibrous elements. Furthermore, a more reliable investigation of stomach mechanics should consider motility, as the active contribution of muscular components, and fluid–structure interaction phenomena between bolus and stomach wall. Such approach should entail a more reliable investigation of physio-mechanical processes that develop during stomach activities

CHAPTER 3

EXPERIMENTAL AND COMPUTATIONAL METHODS FOR THE INVESTIGATION OF URETHRAL MECHANICS

The design of an artificial urinary sphincter is mostly performed on a clinical and surgical basis, but it should be supported by investigation of its mechanical interaction with the surrounding tissues. In this way, it is possible to identify the sphincter pressure conditions that ensure continence, as well as the conformation of the device to minimize the invasiveness of the prosthesis. Consequent mechanical effects on the urethral tissues may induce some modifications and possible degenerative phenomena such as infection, urethral atrophy, erosion, and mechanical failure. Moreover, the prosthetic device can have a limited life.

Experimental investigation on humans is complex and must take into account an extended group of subjects of similar age, body conformation and health conditions. At present, experimental testing on human urethra is performed *in vivo*.

In order to carry out *ex vivo* tests, a suitable animal model should be selected, presenting similarity to the human penile urethra in terms of histology and overall conformation. The equine urethra can be considered similar to the human urethra in terms of the lumen, histomorphometric conformation and functional process of micturition (appendix A.2). These reasons motivate the selection of horse urethra for investigation of the biomechanical response of the urethra under sphincteric contraction. In general, it should be remarked that a limit of any animal model is an uncertain correlation with humans about changes in mechanical properties owing to age and health conditions.

For this purpose, in this chapter is treated a multiple activity by Natali et al., 2016a, 2016b and 2017 by which coupled experimental and computational methods are applied to investigate the mechanical behavior of urethral tissues and structure, mostly with regard to the evaluation of the lumen occlusion process. In the first experimental tests (Natali et al., 2016a) different-shaped samples are harvested from the urethral wall, depending on the specific test loading condition. Tissue mechanical tests, together with information about the microstructural configuration of the tissue, allow the preliminary identification of the constitutive model and the related. Additional tests are developed at the structural level, such as inflation tests on tubular segments, in order to evaluate the overall structural behavior. Moreover, a numerical model of the male urethra is developed to evaluate the biomechanical response of urethral tissues and structure to an imposed pressure. A first two-dimensional model of a urethra section was developed by Natali et al., 2016b, based on the first experimental data on urethral tissue mechanical properties here proposed. The virtual solid model was defined through histological image processing and a specific hyperelastic formulation was developed to characterize the non-linear mechanical behavior. Constitutive parameters were preliminary identified by the inverse analysis of tensile tests on urethra tissue and then refined by numerical analysis of inflation tests on urethral duct. The present work refers also to an upgrade of that first two-dimensional model to a three-dimensional urethral duct model, evaluating the subsequent phases of micturition that determines the lumen opening and the occlusion by artificial urinary sphincters. The consideration of animal samples determines an approximation in the comparison with human case. Nonetheless, this chapter aims at developing a method that can be extended on the basis of an experimental investigation on human samples already in progress.

3.1 EXPERIMENTAL TESTS

Fresh penises from 15 male saddle horses were obtained from a local slaughterhouse. The horses were 4–11 years old and 300–400 kg in weight. All the

animals were intact and clinically healthy. Within 15 min from slaughter of the horse, the penis was harvested (figure 3.1a), packed in physiological saline solution at 4°C and transported to the laboratory. The penises were carefully cleaned with cold physiological saline solution to eliminate skin debris. Next, glands and the skin were surgically removed. A soft urinary catheter was temporarily inserted in the lumen of the urethra to serve as a palpable guide for facilitating the correct identification of the shape. A surgical incision was performed on the lateral aspect of the penis, between the tunica albuginea and the bulbospongiosus muscle (figure 3.1b). By blunt dissection, the corpus cavernosum was separated from the bulbospongiosus muscle surrounding the urethra, starting from the proximal part of the penis. The dissection continued from the proximal end of the penis to the distal end, isolating the penile urethra (figure 3.1c). During dissection, the sample was continuously dampened with cold physiological saline solution to preserve the tissues. The dissected urethra was cleaned from bulbospongiosus muscle and residual surrounding tissues.

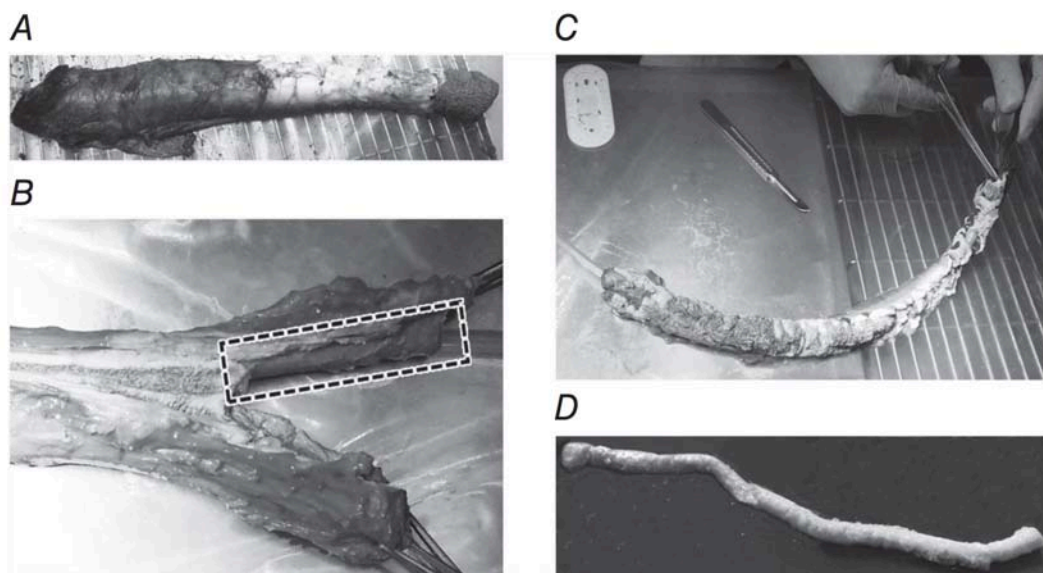


Figure 3.1. Procedure for dissection of the horse urethra A, intact horse penis. B, cutting of the corpora cavernosa up to the albuginea; the dashed box indicates the urethra. C and D, dissected urethra before (C) and after (D) final cleaning from residuals of surrounding tissues.

Finally, the urethral sample was composed of the lumen surrounded by the corpus spongiosum (figure 3. 1d). The length of the urethra was about 400–450 mm.

Two urethrae were assigned to histological investigation, stored in formaldehyde for fixation. The other 13 urethrae were divided to provide the specimens for the mechanical tests of urethral tissues and structures. The most proximal and the most distal regions of each urethra were assigned to tensile and stress-relaxation tests. The residual parts of the urethrae were almost equally divided into two segments to provide proximal and distal specimens for inflation tests. All the mechanical tests were concluded within 6 h from the slaughter of the animal, at room temperature. Previous experiences confirm that similar temperature conditions do not alter the mechanical response of soft tissues.

3.1.1 MECHANICAL TESTS OF URETHRAL TISSUES

Mechanical tests of urethral tissues were performed on specimens from both distal and proximal regions after an histological analyses (Appendix A.2). Each segment was cut longitudinally (figure 3.2a) and straightened on a metal plate (figure 3.2b). Rectangular specimens (with a grip-to-grip length of ~20 mm and width ~5 mm) were dissected along longitudinal and circumferential directions (figure 3.2c). Depending on the specific segment size, two to four specimens for each cutting direction were prepared. Digital image processing was used to measure sample thickness and width at different positions. Cross-sectional area of each specimen was calculated assuming mean values of thickness and width. The samples were continuously dampened with physiological saline solution at room temperature during the preparation and testing.

A Bose ElectroForce machine (Bose Corp., ElectroForce Systems Group, Eden Prairie, MN, USA) was used to perform tensile tests. Each specimen was stretched up to 60% strain, and the strain was then kept constant for 300 s to investigate stress-relaxation phenomena. Based on a preliminary evaluation of the tissue stiffness, a load cell with capacity of 20N with accuracy of $\pm 0.1\%$ was adopted.

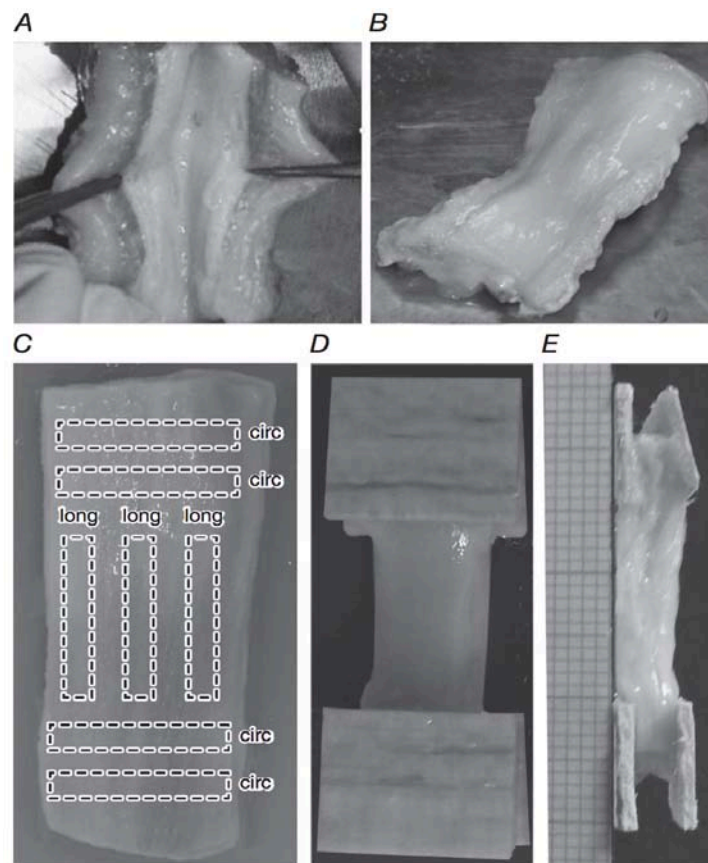


Figure 3.2. Preparation of samples for mechanical tests of urethral tissues. A and B, the tubular segment is cut longitudinally (A) and straightened (B). C, tissue specimens are dissected according to a rectangular shape; two to four specimens are prepared along longitudinal and circumferential directions. D and E, patches of balsa wood are glued to the sample ends to enable the specimen to be gripped; frontal (D) and lateral views (E).

Preliminary tests were also performed to evaluate the influence of strain rate on viscous effects. The results showed that a $60\% s^{-1}$ strain rate minimizes the influence of viscous phenomena and prevents the dynamic effects that may develop when higher strain rates are adopted.

In order to hold the specimen at its ends, two patches of balsa wood were glued to each end of the sample (figure 3.2d and 3.2e) and interposed between the grips. The pressure of the grips was adjusted to avoid slippage and damage of the specimens. The strain was computed as the ratio between the elongation and the initial grip-to-grip length. The stress was calculated as the ratio between force

measured by the load cell and the initial cross-sectional area of the specimen. Data from stress-relaxation tests were processed to identify the reduction of normalized stress with time. The normalized stress is defined as the ratio of the stress at the present time and the peak stress at the beginning of the relaxation phase.

The median curves and the related 50% probability scatter bands are reported in terms of stress–strain and normalized stress–time. These curves were calculated separately for distal or proximal and longitudinal or circumferential specimens.

3.1.2 MECHANICAL TESTS OF URETHRAL STRUCTURE

Mechanical tests of urethral structure were performed on tubular specimens taken from distal and proximal regions. Each sample was placed over a metal plate and straightened along the longitudinal direction. Two small slices of the sample (~3 mm in length) were removed at the extremities. The length of the remaining tubular portion was measured with digital calipers. The extremity slices were used to measure the urethral wall thickness and external diameter.

The proximal extremity of the sample was fixed by means of a surgical elastic seam to a Teflon cannula with internal and external diameters of 4 and 6 mm, respectively. The other extremity was sealed to prevent any liquid leak (figure 3.3a). The sample was placed over a Teflon plate and straightened along the longitudinal direction. The cannula was also connected to a mechano-electrical transducer (142 pc 01d pressure transducer; Honeywell, USA) that was interfaced to a data storage device (1326 Econo Recorder; BioRad, Italy).

The inflation test was performed according to a two-step procedure. The first step was an almost instantaneous liquid inflow, up to a prescribed volume of inflation (figure 3.3b). Therefore, in this phase an elastic response of the structure may be assumed. In the second step, the volume of the sample was held constant for ~300 s to allow the development of viscoelastic processes, up to steady-state conditions. Five to seven inflation tests were performed on each sample according to different inflation volumes, ranging between 5 and 50 ml. The inflation time

was always <0.1 s. During the test, physiological saline solution was poured onto the external surface of the samples to prevent drying.

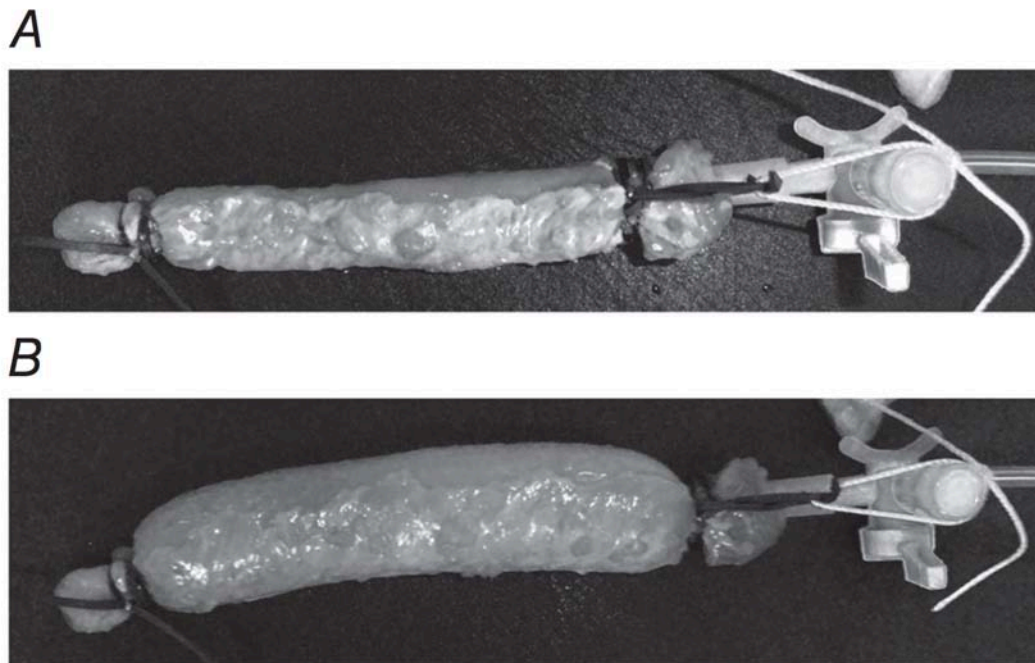


Figure 3.3. Preparation of samples and mechanical testing at the structure level. The proximal end of the tubular sample is fixed by means of a surgical elastic seam to a Teflon cannula, attached to a syringe, whereas the other end is hermetically sealed. A and B, not inflated (A) and inflated conformations (B) of a typical experimental sample.

To compare samples with morphological differences, the volume data were homogenized by considering the ratio between sample volume during testing and sample volume at rest $v = \Delta V/V_0$, where v is the volumetric ratio, ΔV the inflated volume and V_0 the initial volume of the sample. The initial volume, V_0 , was obtained from the shape of the sample during experimental testing. Median curves of pressure-volumetric ratio and normalized pressure-time, with the associated 50% probability scatter bands, were computed for inflation and relaxation tests on proximal and distal samples. The normalized pressure was obtained as the ratio of the pressure at present time and the peak pressure at the beginning of the relaxation phase.

3.2 PRELIMINARY MODEL FORMULATIONS

3.2.1 ANALYSIS OF TENSILE TESTS ON TISSUE SPECIMENS

Exponential functions were adopted to interpret stress–strain and stress–time behavior and to obtain preliminary information about elastic and viscous behavior of the tissue, as follows:

$$\sigma(\varepsilon) = \frac{k}{\alpha} (e^{\alpha\varepsilon} - 1)$$
$$\sigma^{norm}(t) = (1 - \gamma_u - \gamma_2) + \gamma_1 e^{-\frac{t}{\tau_1}} + \gamma_2 e^{-\frac{t}{\tau_2}}$$

The first equation aims at interpreting the non-linear stress (σ) *versus* strain (ε) response of the tissue during loading. The parameter k specifies the tissue initial stiffness, while α is related to the non-linearity of the response due to stiffening. The second equation interprets the exponential decay of the normalized stress σ^{norm} with time t because of stress-relaxation phenomena. The second equation accounts for two viscous branches. The number of viscous branches was defined contemporaneously to minimize the number of parameters and correctly interpret the trend of experimental data. According to the standard theory of viscoelasticity, the parameter $\gamma_\infty = 1 - \gamma_1 - \gamma_2$ identifies the ratio between the equilibrium stress (when relaxation phenomena are completed) and the peak stress (at the beginning of the relaxation phase). The parameters τ_1 and τ_2 are the time constants of relaxation. Data from tensile and stress-relaxation tests developed on each specimen were fitted by both the mentioned equations. The minimization of the discrepancy between experimental data and model results represents a non-linear least-squares problem, solved by using the '*lsqnonlin*' function in Matlab and adopting the trust region reflective algorithm to minimize the residual sum of squares (RSS). The RSS is defined as follows:

$$RSS = \sum_{i=1}^n (f_{exp,i} - f_{num,i})^2$$

where n is the total number of experimental data, $f_{\text{exp},i}$ is the i th experimental datum and $f_{\text{num},i}$ the corresponding i th model result. Statistical data of the elastic parameters k and α and of the viscous parameters γ_1 , γ_2 , τ_1 and τ_2 were computed, allowing a preliminary evaluation of the influence of specimen location and direction on tissue mechanical properties.

The effects of the imposed strain on the results from tensile tests were evaluated by means of a multivariate ANOVA, considering three levels of strain (10, 20 and 40%) and comparing the mean stress values among different groups of samples (proximal longitudinal, proximal circumferential, distal longitudinal and distal circumferential samples). The same kind of analysis was performed for the statistical interpretation of results from stress relaxation by evaluating the stress-relaxation process at four time instants (1, 10, 100 and 300 s) and by making a comparison of the mean stress value of each of the above-mentioned groups with the others.

3.2.2 ANALYSIS OF INFLATION TESTS ON URETHRAD SAMPLES

Exponential functions were adopted to interpret the behaviour of pressure *versus* volumetric ratio and normalized pressure *versus* time to identify preliminary information about the structural elastic and viscous response of the tubular structure (Carniel et al. 2014), as follows:

$$P(v) = \frac{K}{A} (e^{Av} - 1)$$

$$P^{\text{norm}}(t) = (1 - \Gamma_u - \Gamma_2) + \Gamma_1 e^{-\frac{t}{T_1}} + \Gamma_2 e^{-\frac{t}{T_2}}$$

The first of this latter mentioned equations describes the pressure (P) *versus* volumetric ratio (v) response of the tissue during the inflation step. The parameter K specifies the initial stiffness of the tubular segment, while A is related to the non-linearity of the mechanical response because of stiffening phenomena. The last equation describes the exponential decay of normalized pressure P^{norm} over time

t because of viscoelastic phenomena. The parameter $\Gamma_{\infty} = 1 - \Gamma_1 - \Gamma_2$ identifies the ratio between the pressure when viscoelastic phenomena are completed and the peak pressure at the beginning, while T_1 and T_2 are parameters related to structural relaxation times. Data from tests developed on each specimen were fitted both the equations above mentioned. The fitting of the models to experimental data is obtained with the same procedure adopted for tissue samples. Also, in this case, statistical data of the elastic parameters K, A and of the viscous parameters Γ_1, Γ_2, T_1 and T_2 were computed.

The multivariate ANOVA was applied to data from inflation and relaxation tests with the same method described above, distinguishing samples into two groups (proximal and distal).

3.3 URETHRAL MECHANICS

3.3.1 TISSUE MECHANICS OF URETHRA

Generally, the results of mechanical testing showed that urethral tissue has a non-linear stiffening and time-dependent behavior, which is also anisotropic only in the proximal region. The statistical distributions of the experimental results are shown in the graphs of figure 3.4 where median curves are reported together with the 50% probability scatter bands. Processing of the experimental curves from mechanical tests performed on the different samples led to a preliminary evaluation of elastic and viscous parameters, whose statistical distributions are reported in table 3.1. The analysis of median curves made it possible to identify further sets of parameters (table 3.2). Such parameters should interpret the general trend of the experimental data.

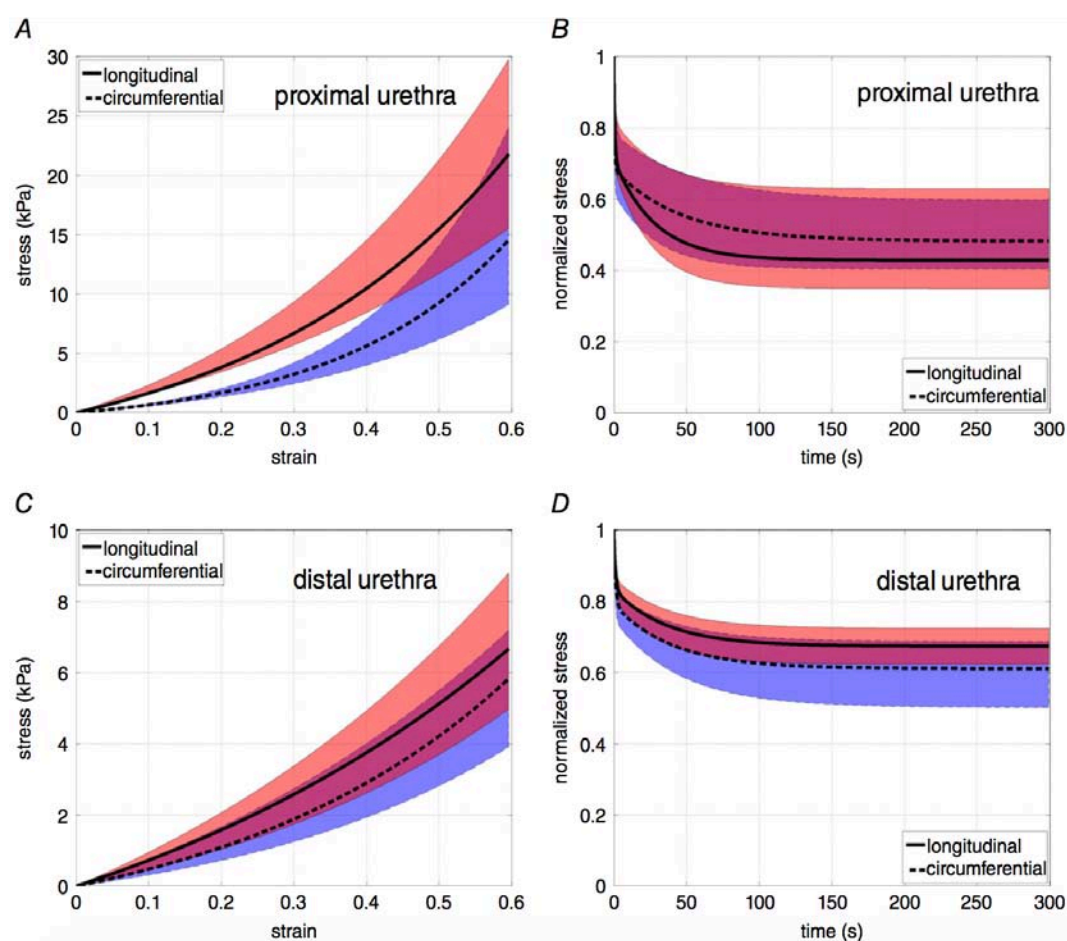


Figure 3.4. Results from mechanical tests of the urethral tissues. Tests were performed on specimens from proximal (A and B) and distal regions (C and D) of the urethra and accounting for constant strain rate (A and C) and stress-relaxation conditions (B and D). Median curves are reported together with 50% probability scatter bands. Data pertain to tests performed along both longitudinal (continuous lines and pink bands) and circumferential directions (dashed lines and blue bands). Violet regions indicate the superposition of longitudinal and circumferential scatter bands.

Region and direction	k (kPa)	α	γ_1	γ_2	τ_1 (s)	τ_2 (s)
Proximal region,	4.88	3.48	0.33	0.17	0.87	51.66
circumferential direction	(4.55, 8.95)	(2.98, 4.97)	(0.24, 0.43)	(0.15, 0.18)	(0.73, 1.78)	(48.14, 62.67)
Proximal region,	15.66	2.11	0.33	0.24	1.40	38.92
longitudinal direction	(13.59, 18.89)	(1.62, 2.75)	(0.21, 0.37)	(0.15, 0.28)	(1.03, 1.77)	(35.97, 42.11)
Distal region,	3.84	2.30	0.24	0.16	1.98	59.09
circumferential direction	(2.61, 8.93)	(1.83, 2.67)	(0.19, 0.29)	(0.13, 0.22)	(1.45, 2.68)	(51.00, 64.41)
Distal region,	6.35	1.63	0.18	0.15	1.84	47.47
longitudinal direction	(3.86, 8.33)	(1.44, 1.83)	(0.16, 0.20)	(0.10, 0.15)	(1.51, 1.95)	(40.39, 48.37)

Median values (25th, 75th percentiles) are reported. k is the initial stiffness, α is a constant related to the non-linearity due to stiffening, γ_1 and γ_2 are relative stiffness parameters, τ_1 and τ_2 are the time constants of relaxation.

Table 3.1. Identification of tissue parameters by analysis of mechanical tests of the urethral tissues: statistical distribution of elastic and viscous parameters.

Region and direction	k (kPa)	α	γ_1	γ_2	τ_1 (s)	τ_2 (s)
Proximal region, circumferential direction	5.41	4.22	0.33	0.18	0.74	52.72
Proximal region, longitudinal direction	14.41	2.75	0.32	0.26	1.07	37.02
Distal region, circumferential direction	4.46	2.32	0.23	0.17	1.46	51.13
Distal region, longitudinal direction	6.55	1.69	0.18	0.15	1.53	41.33

k is the initial stiffness, α is a constant related to the non linearity due to stiffening, γ_1 and γ_2 are relative stiffness parameters, τ_1 and τ_2 are the time constants of relaxation.

Table 3.2. Identification of tissue parameters by analysis of mechanical tests of the urethral tissues: elastic and viscous parameters from median curves

3.3.2 STRUCTURAL MECHANICS OF THE URETHRA

Experimental results on the urethral structure are reported in figure. 3.5 by means of median curves and 50% probability scatter bands. Also in this case, a non-linear stiffening is evident during inflation and time-dependent phenomena in the following step. Distributions of structural parameters were achieved by processing experimental data from the different samples and median curves (table 3.3 and 3.4).

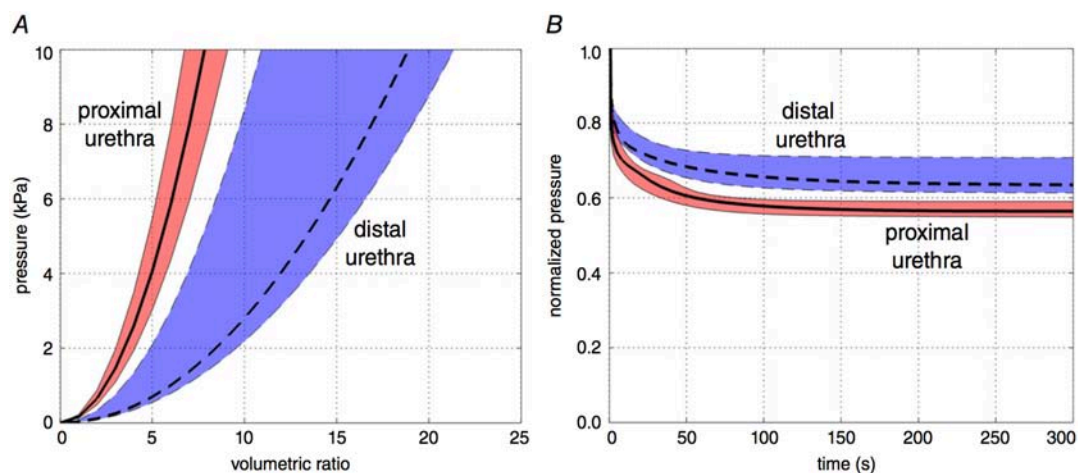


Figure 3.5. Results from mechanical tests performed at the structure level. Tests were performed on tubular specimens accounting for inflation (A) and stress-reduction conditions (B). Median curves are reported together with 50% probability scatter bands. Data pertain to tests performed on samples from proximal (continuous lines and pink bands) and distal regions (dashed lines and blue bands) of the urethra.

Region	K (kPa)	A	Γ_1	Γ_2	T_1 (s)	T_2 (s)
Proximal region	1.93 (1.38, 2.48)	0.19 (0.17, 0.20)	0.24 (0.20, 0.25)	0.20 (0.18, 0.24)	0.43 (0.39, 0.93)	23.85 (22.13, 28.16)
Distal region	0.32 (0.25, 0.95)	0.18 (0.16, 0.21)	0.18 (0.17, 0.19)	0.17 (0.15, 0.18)	0.74 (0.42, 0.78)	28.93 (26.88, 32.03)

Median values (25th, 75th percentiles) are reported. K is the initial stiffness, A is a constant related to the non-linearity due to stiffening, γ_1 and γ_2 are relative stiffness parameters, T_1 and T_2 are the time constants of relaxation.

Table 3.3 Identification of structural parameters by analysis of mechanical tests at structure level: statistical distribution of structural elastic and viscous parameters

Region	K (kPa)	A	Γ_1	Γ_2	T_1 (s)	T_2 (s)
Proximal region	1.92	0.18	0.25	0.18	0.42	24.05
Distal region	0.33	0.18	0.20	0.16	0.72	29.94

K is the initial stiffness, A is a constant related to the non-linearity due to stiffening, γ_1 and γ_2 are relative stiffness parameters, T_1 and T_2 are the time constants of relaxation.

Table 3.4. Identification of structural parameters by analysis of mechanical tests at structure level: structural elastic and viscous parameters from median curves.

3.4 COMPUTATIONAL MODELS OF THE URETHRA

3.4.1 2D FEM MODEL DEFINITION

Numerical model refers to results on histologic conformation and experimental mechanical behavior of urethral tissues and structures, reported in the previous investigation (Natali et al., 2016) by which transversal sections of urethras were collected for histological analysis and stained with Masson trichrome solution to enable the identification of different layers. Serial sectioning was carried out for an overall evaluation of tissue conformation and a specific histological section is selected for the development of the model (appendix A.2), assumed in the mean position of the urethra region loaded by constant sphincteric pressure. A virtual geometrical model of urethra section is obtained from the histological image, enlarged in scale to correct shrinkage phenomena that occurred during tissue processing (Dobrin, 1996). Specific image analysis routines are implemented in Matlab (The MathWorks Inc., Natick, MA, USA) aiming to geometrically characterize the conformation of urethra transversal section and to identify the different tissue layers. Median, 25th and 75th percentiles thickness values of the layers are: 0.06 [0.03 ÷ 0.08] mm, 0.14 [0.12 ÷ 0.19] mm and 5.13 [4.21 ÷ 5.47] mm for epithelium, dense connective tissue and loose tissue, respectively.

The geometrical model of the urethral section (figure 3.6a) is imported into the finite element pre-processing software Abaqus/CAE 6.14 (Dassault Systèmes Simulia Corp., Providence, RI). Six node triangular quadratic elements (CPS6 plane strain elements) and three node triangular linear elements (CPS3 plane strain elements) are adopted to mesh the dense connective tissue layer and the loose tissue stratum (figures 3.6b and 3.6c). Tie contact condition ensures the proper mechanical interaction at the interface between the two differently meshed regions for compatibility requirements. The mechanical contribution of the epithelial layer, due to its limited stiffness characteristics, is almost negligible. Anyway, it must be taken into account in the interaction phenomena induced by compression loads, interpreted by means of a self-contact condition.

The typical non-linear mechanical behavior of soft biological tissues suggests the assumption of an exponential pressure-overclosure relationship (Abaqus 6.14-1 Analysis User Manual, Dassault Systèmes Simulia Corp., Providence, RI). In detail, facing portions of lumen begin to interact once the clearance between them, measured in the contact normal direction, reduces to almost the double of the epithelium thickness. The contact pressure between lumen surfaces then increases exponentially as the clearance continues to diminish. When clearance approaches zero, pressure is getting to 10 kPa, in agreement with results from experimental activities on epithelial tissues (Raub et al., 2010; Chen et al., 2015). Contact frictional properties ensure the transmission of shear loads between lumen surfaces, usually fully hydrated, with a 0.02 friction coefficient (Prinz et al., 2007). Model and mesh configurations are defined through the procedures of computational mechanics. Models are developed assuming incremental mesh refinement. Numerical analyses simulating inflation tests are performed comparing the different models results, aiming to evaluate the influence of mesh conformation. Results show to be mostly affected by the size of element within the dense connective tissue layer. With regard to this region, reducing element size below 0.03 mm does not provide significant variation of results. With regard to the final configuration of the model, mean element size within the dense

connective tissue layer is 0.03 mm, while it ranges between 0.03 and 0.3 mm in the loose tissue stratum. The model is composed by 31553 nodes (18142 and 13411 nodes, respectively in dense connective layer and loose stratum) and 33695 elements (8034 and 25661 elements, respectively in dense connective layer and loose).

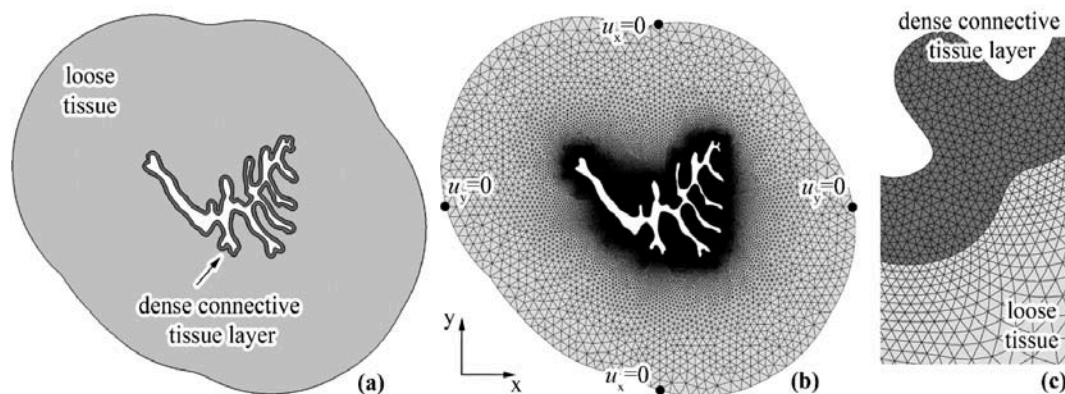


Figure 3.6. Urethra geometrical model (a); finite element model with boundary conditions for numerical analysis of structural inflation and lumen occlusion (b); detail of the finite element model showing the different discretization of loose and dense tissue layers (c).

The computational model interprets urethral tissues mechanical response when external occluding loads are applied. With the aim to mimic the action of artificial sphincters, a homogeneous pressure field is applied all around the external boundary of the urethral model. The model refers to the mean section within the area where the occlusion is induced, leading to a better approximation of results in consideration of the assumption of a two dimensional model. According to the configuration of commercial devices, the occluding pressure can reach the limit of 10 kPa, in consideration of the intraluminal pressure that ranges between 0 and 10 kPa (Griffiths, 1971; Aagaard et al., 2012). Numerical analyses are performed by a two steps procedure. During the first step, the urethra is progressive inflated up to the target intraluminal pressure. During the second step, the occluding pressure is increased up to 10 kPa.

3.4.2 3D FEM MODEL DEFINITION

The definition of the 3D solid and numerical model is based on histological and morphometric investigation and experimental mechanical behavior of urethral tissues and structure, reported by Natali et al. (2016b) as well as the 2D previous model. The solid modeling was exploited by an extrusion of the basic section given from the previous 2D models. Within the small tract involved in the analysis in the specific bulbar region, the variation from section to section, also considering the approximation in data acquisition, allows for the assumption of a constant conformation of different regions and corresponding lumen shape.

The geometrical model (figure 3.7a) is imported into the finite element pre-processing software Abaqus/CAE 6.14 (Dassault Systèmes Simulia Corp., Providence, RI) as basis to provide a three dimensional model of the urethral duct (figure 3.7b). Boundary displacement conditions along transversal directions are imposed on the outer surface of the three dimensional model (figure 3.7b), in order to provide constraints to interpret the “in vivo” mechanical environment of the urethral duct after artificial urinary sphincter placement. The artificial urinary cuff acts on the urethra by a pressure field (figure 3.7c), which is distributed along a 20 mm portion of the urethral duct. Null displacement condition along longitudinal direction is expected on the transversal section at the midpoint of the pressure field (figure 3.7b). Eight node hexahedral elements with reduced integration are adopted to mesh the dense connective tissue layer and the loose tissue stratum (figures 3.7d, 3.7e and 3.7f).

The mechanical contribution of the epithelial layer, in consideration of stiffness characteristics, is taken into account when compressive loads are present. The local interaction response on the facing portions of lumen surfaces must be associated with a self-contact condition strategy. The tissues mechanical behavior entails the assumption of an exponential pressure-overclosure relationship. The contact pressure increases exponentially up to 10 kPa. Contact frictional properties ensure the transmission of shear actions between lumen surfaces and

it is assumed as 0.02. Incremental mesh refinement technique is adopted. Obviously, result sensitivity is associated with the size of elements. Results show to be mostly affected by the transversal size within the dense connective tissue layer, whose reduction below 0.03mm does not provide significant variations. With regard to the final configuration of the model, transversal element size within the dense connective tissue layer is close to 0.03 mm, while it ranges between 0.03 and 0.5 mm in the loose tissue stratum. Element size along longitudinal direction is set to 0.3mm. The model is comprehensively composed by nine hundreds thousands of nodes and nine hundreds thousands of elements. Aiming at evaluating the functionality of different cuff conformations, both constant and parabolic pressure distributions are considered. The occluding pressure of artificial urinary sphincter can reach the limit of 10 kPa, in consideration of the intraluminal pressure that ranges between 0 and 10 kPa.

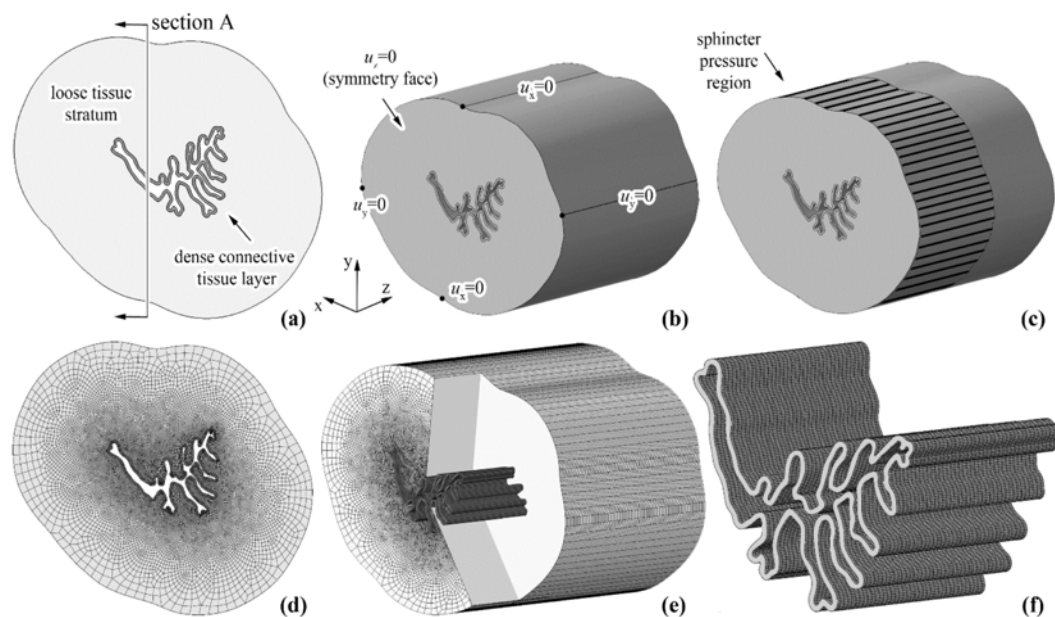


Figure 3.7. Model of the urethral duct. Geometrical model of the urethra transversal section and identification of constituent tissues (a). Three dimensional solid model of the urethral duct showing the assumed boundary (b) and loading (c) conditions. Finite element discretization: transversal section (d); three dimensional representation of urethral duct with spongy region and dense connective tissue layer (e); detail of the dense connective tissue layer (f).

Numerical analyses are performed by a two steps procedure. During the first step, the urethra is progressive inflated up to the target intraluminal pressure. During the second step, the occluding pressure is increased up to 10 kPa (figure 3.14 and 3.15).

The sphincter pressure field determines lumen occlusion. During the process, large deformation phenomena develop and complex contact interactions occur between different portions of the lumen surface. Despite lumen occlusion can be approximated as a quasi-static process, an efficient numerical interpretation of the problem can be achieved by adopting explicit solution algorithms (Abaqus Explicit 6.14-1, Dassault Systèmes Simulia Corp., Providence, RI). The explicit solution method is a true dynamic procedure that is based upon the implementation of an explicit integration algorithm. The equations of motion for the body are integrated using the explicit central-difference integration scheme that is conditionally stable, in direct proportion to element dimension and material density and inversely to material stiffness. The specific configuration of the developed computational model leads to extremely small stable time increments, as low as 10^{-8} s, causing the high computational effort in solving the corresponding quasi-static occlusion process, which requires a time period ranging between 0.1 and 1 s. Elements of the dense connective tissue layers determine the small value of the time increment, because of their small size and relatively high stiffness. Aiming at reducing the computational effort, mass scaling technique can be adopted. Considering the small thickness of the dense connective tissue layer, mass scaling of such layer does not significantly modify the mass of the system and, consequently, does not introduce relevant fictitious inertial contributions. Semi- automatic mass scaling procedure was adopted, setting the stable increment time at 10^{-6} s. The numerical analysis must afford a relevant computational effort but the specific formulation adopted leads to valid performances, monitored by means of nodal accelerations and model total kinetic energy.

3.4.3 CONSTITUTIVE FORMULATION

The mechanical behavior of dense connective and loose tissue is defined by a specific hyperelastic formulation that proved its capability to interpret the typical features of soft tissue mechanics in previous investigations.

The adopted strain energy function is reported below, aiming at the description of parameters assumed:

$$W(\mathbf{C}) = -p(J - 1) + C [e^{\alpha_1(I_1-3)} - 1]$$

Its results in the the following stress-strain relationship:

$$\mathbf{P}(\mathbf{C}) = -p\mathbf{F}^{-T} + C_1 e^{\alpha_1(I_1-3)} \left(2\mathbf{F} - \frac{2}{3}I_1\mathbf{F}^{-T} \right)$$

where \mathbf{P} is the first Piola-Kirchhoff stress tensor, as a measure of nominal stress, \mathbf{F} is the deformation gradient, p is a Lagrange multiplier that specifies hydrostatic pressure and ensures the incompressibility of the material, I_1 is the first invariant of the right Cauchy-Green strain tensor $\mathbf{C} = \mathbf{F}^T\mathbf{F}$. J is the deformation Jacobian, as $J = \sqrt{\det \mathbf{C}}$. The constitutive parameters C_1 is related to tissue shear stiffness in the unstrained configuration, while the non-linearity parameter α_1 specifies tissue stiffening with stretch. Constitutive parameters are identified by the inverse analysis of tensile tests performed on horse urethra. According to the specific boundary conditions, in case of uni-axial tensile loading, the following relationships between stress and stretch components is computed from the general model:

$$P_{cc} = 2C_1 e^{\alpha_1(\lambda_c^2 + 2\lambda_c^{-1} - 3)} (\lambda_c - \lambda_c^{-2})$$

where λ_c and P_{cc} are stretch and nominal stress, respectively, along circumferential direction. Different sets of parameters are identified analyzing the statistical distribution of experimental results, as median, 25th and 75th percentiles. With regard to processing of experimental results, stretch is computed as the ratio between the gauge-length of the tissue specimen in deformed and undeformed configurations, nominal stress is evaluated as the ratio between tensile force and specimen mean cross-section area in the undeformed configuration.

The minimization of discrepancy between experimental data and model results lead to the following parameters: $C_1 = 1.09 [0.95, 1.37]$ kPa, $\alpha_1 = 1.26 [1.07, 1.40]$. Such parameters describe the mechanical behavior of a homogenized urethral structure. Nevertheless, tissue layers with different mechanical properties compose the urethral wall. The multi-layered configuration leads to a non-homogeneous stress and strain distribution.

A tensile test on a circumferential urethra sample is replicated by computational modeling in figure 3.8, with reference to a specific section figure 3.6a. Finite element analysis investigates all the different steps of the experimental procedure, including urethra ring opening for the preparation of the sample (figure. 3.8b), straightening as during sample gripping (figure 3.8c) and tissues stretching through tensile testing (figure 3.8d).

The mechanical behavior of the tissues is defined by the specific hyperelastic formulation mentioned, which is implemented in the finite element software by a user subroutine.

Different sets of parameters must be identified for the different tissues. Experimental test faces the problem of providing specimens where different tissues are combined and their separation should induce relevant damage. To overcome this problem, the interpretation of stiffness characteristics is performed by the support of numerical model simulation. In the present case, this consideration can be referred to the coupling of dense and loose tissue with regard to the evaluation of the parameters C_1 and α_1 . A numerical analysis of tensile tests is developed considering different values of a multiplier k , ranging between 1 and 1000 (figure 3.9), that represent the ratio of C_1 values attributed to the different components. The large range of k values makes it possible to evaluate a complete set of conformations of urethra tissues: $k = 1$ specifies a homogenous structure, while $k = 1000$ describe a thin and highly stiff layer surrounded by a thick and tenuous stratum.

Additional investigations are developed with regard to experimental results from inflation tests that were performed on urethra tubular specimens (11 distal samples from different male horses).

A homogeneous hydrostatic pressure field is applied to the intraluminal border of the urethra model. Pressure value is progressively increased to simulate the experimental progressive inflation. Null displacement conditions are imposed on four diametrically opposite nodes along single directions, on the outer boundary of the model (as shown in figure 3.6b), in order to provide minimal constraints and to satisfactorily interpret the actual constraint of the sample during experimental testing.

Different analyses are performed considering the different values of the multiplier k (figure 3.10). Numerical results from both tensile and inflation tests are compared with median experimental data. The multiplier value $k = 208$ entails the minimal overall discrepancy between computational and experimental median results. Parameters $C_1 = 34.89$ kPa, $\alpha_1 = 1.26$, and $C_1 = 0.17$ kPa, $\alpha_1 = 1.26$ are finally assumed to specify the median behavior of dense connective tissue layer and loose tissue stratum, respectively.

3.5 RESULTS OF NUMERICAL ANALYSES

3.5.1 2D NUMERICAL ANALYSES RESULTS

A tensile test on a circumferential urethra sample is replicated by computational modeling in figure 3.8, with reference to a specific section (figure 3.8a). Finite element analysis investigates all the different steps of the experimental procedure, including urethra ring opening for the preparation of the sample (figure 3.8b), straightening as during sample gripping (figure 3.8c) and tissues stretching through tensile testing (figure 3.8d). The agreement between the experimental and computational investigations at both tissue and structure levels is reported in figure 3.9. The numerical analysis of inflation tests allows evaluating the tissues mechanical functionality when intraluminal pressure is applied. The

contours of radial displacement and stress fields are reported in figures 3.10 and 3.11, respectively, for different values of intraluminal pressure.

Finally, urethral structure and tissues response is investigated when external occluding actions are applied. Numerical analyses that take into account different conditions, as different intraluminal pressure and occluding loads, are summarized in figure 3.12. The different curves specify the structural behavior of the urethra, as the trend of occluding pressure with lumen volume variation. Each curve pertains to a specific value of the intraluminal pressure under different compression up to occlusion and subsequent compression induced.

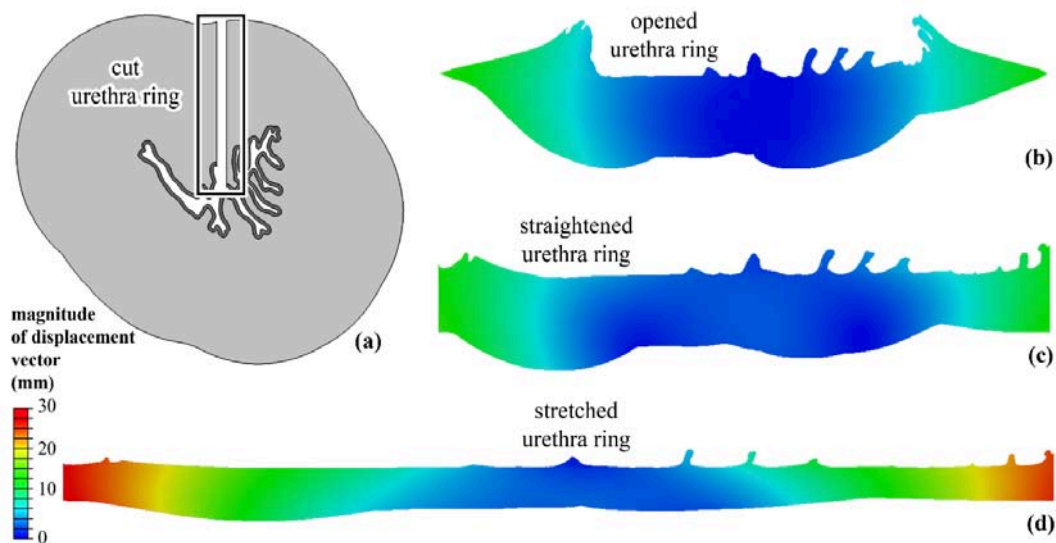


Figure 3.8. Tensile tests on urethra samples. Mimicking the experimental procedure, the finite element model of the cut urethra samples (a) undergoes the opening (b) and straightening (c) up to large tensile stretching (d).

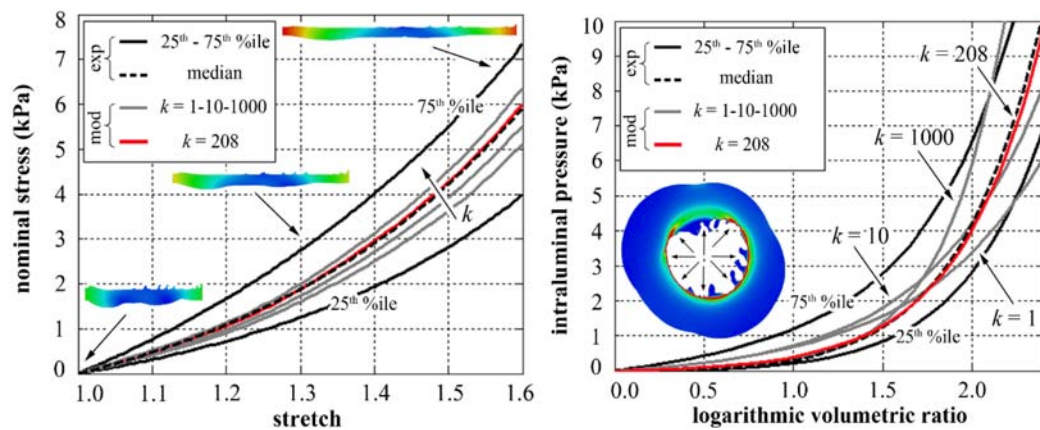


Figure 3.9. Comparison of experimental and computational results from tensile tests on urethra circumferential samples (a) and comparison of experimental and computational results from inflation tests on urethra tubular samples (b). Median, 25 and 75th percentiles experimental curves are reported. Computational results are defined depending on different sets of constitutive parameters according to the values of multiplier k . The logarithmic volumetric ratio is defined as the logarithm of the ratio between the volume of the urethra lumen, when mechanical action is applied and the final volume of the lumen.

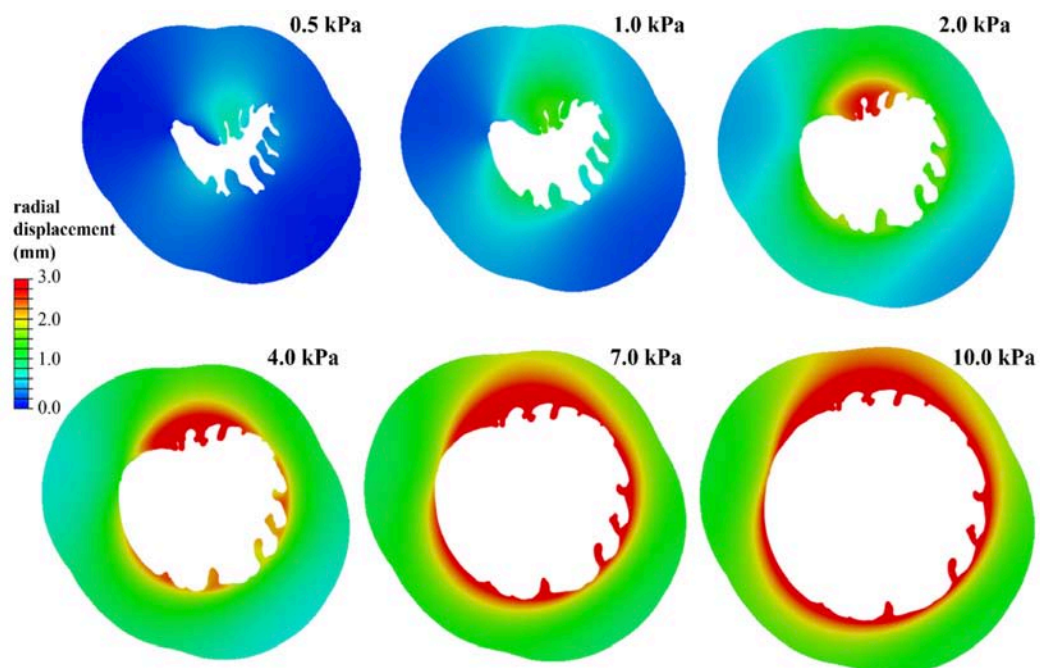


Figure 3.10. Numerical analysis of structural inflation tests. Contours of radial displacement field at different intraluminal pressure conditions.

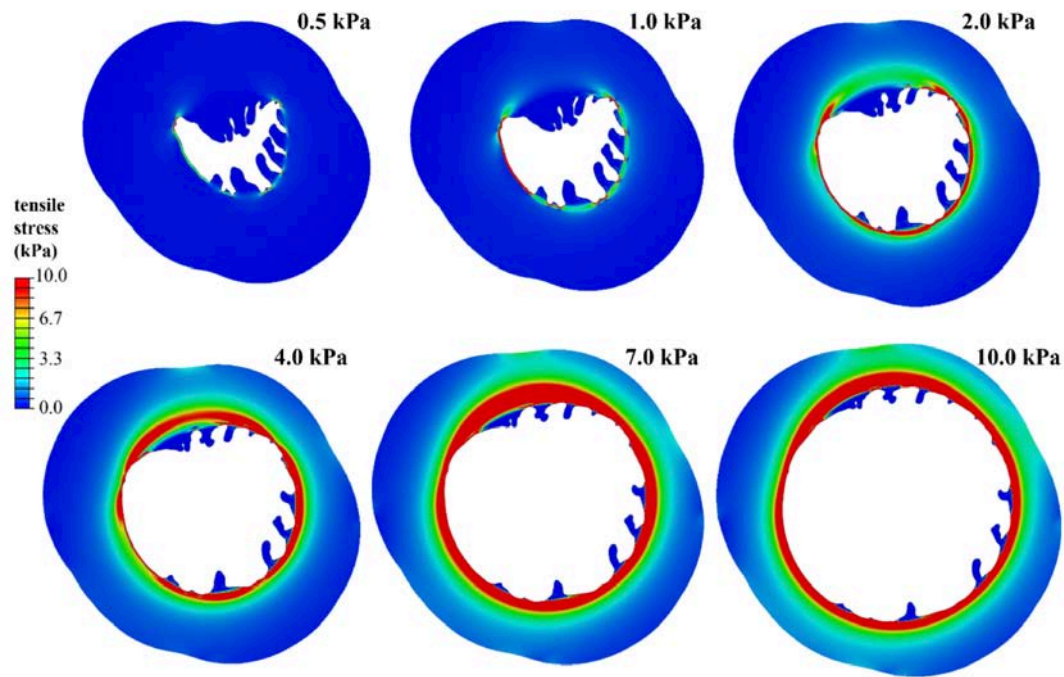


Figure 3.11. Numerical analysis of structural inflation tests. Contours of tensile stress field, as the maximum principal value of the Cauchy stress tensor, at different intraluminal pressure conditions.

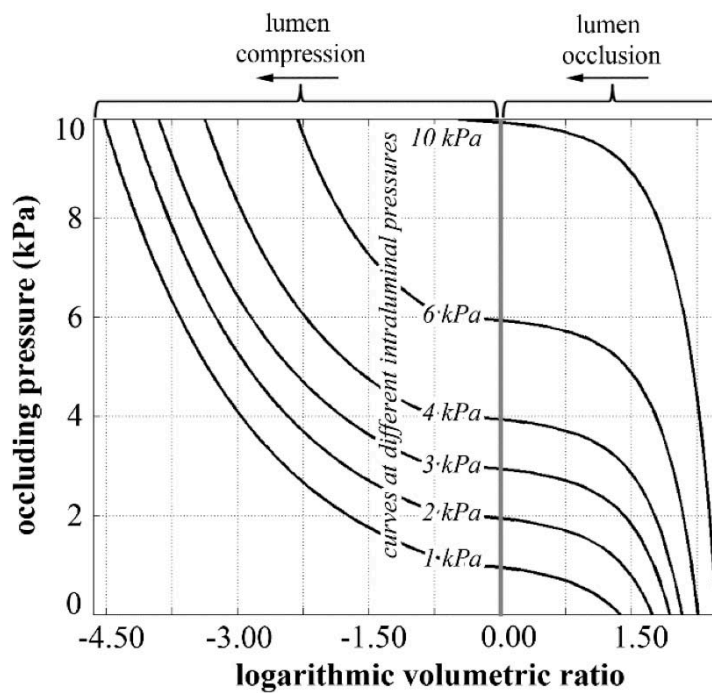


Figure 3.12. Results from numerical analysis of lumen occlusion. Each curve describes the structural behavior of the urethra at a specific value of intraluminal pressure and for increasing occluding pressure conditions.

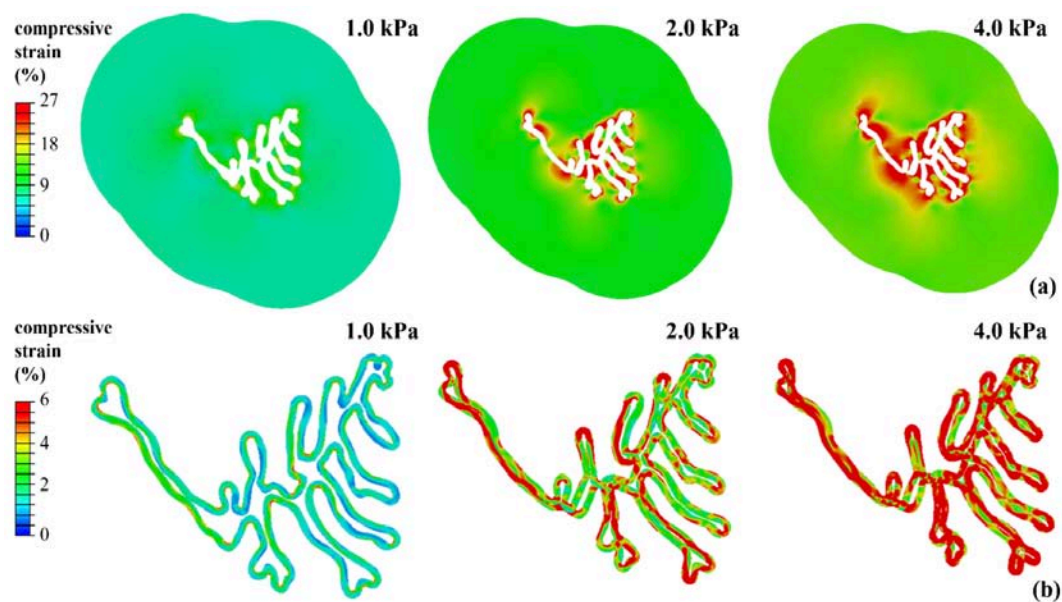


Figure 3.13. Numerical analysis of lumen occlusion. Contours of compressive strain field, as the minimum principal value of the logarithmic strain tensor, into loose tissue (a) and dense connective layer (b), assuming an intraluminal pressure of 1KPa.

The data are reported with regard to the volume variation depending on the load induced. Information about tissues behavior during occlusion are reported in figure 3.13. The compressive strain field is reported for both loose tissue and dense connective tissue layer for different values of the occluding pressure conditions, while intraluminal pressure is 1 KPa.

3.5.2 3D NUMERICAL ANALYSES RESULTS

The configuration of the model, as reported in figure 3.7, allows for an interpretation of the overall conformation of the urethral duct, also with a detail of the lumen. Results are reported with regard to the different artificial urinary sphincters loading schemes, as constant and parabolic, in figures 3.14 and 3.15 respectively. This analysis is correlated with different conformations of the most used AUS devices and represents a very important aspect with regard to the evaluation of the interaction phenomena with urethral tissues. The three dimensional model of the urethral duct is represented and, with larger scaling, a

detail of the longitudinal section, just to offer a more accurate representation of the effects induced in tissues up to lumen occlusion. Specific transversal sections are reported in figure 3.14, in case of constant load, with uniform results for sections #1, #2 and #3, and in Fig. 3, in case of parabolic loading, with a different response at different sections. In a similar way, compressive strain field (as the minimum eigenvalue of the logarithmic strain tensor) is reported for the different loading schemes in figure 3.16 and figure 3.17. In figure 3.18 a comparison of compressive strain distributions is reported in dependence on longitudinal position with reference to constant and parabolic pressure schemes.

The compressive stress field (as the minimum eigenvalue of the Cauchy stress tensor) induced by the cuff action is reported in figure 3.19, again with differentiation by loading schemes. The comparison of compressive stress distribution in dependence on longitudinal position with reference to constant and parabolic pressure schemes is reported in figure 3.20.

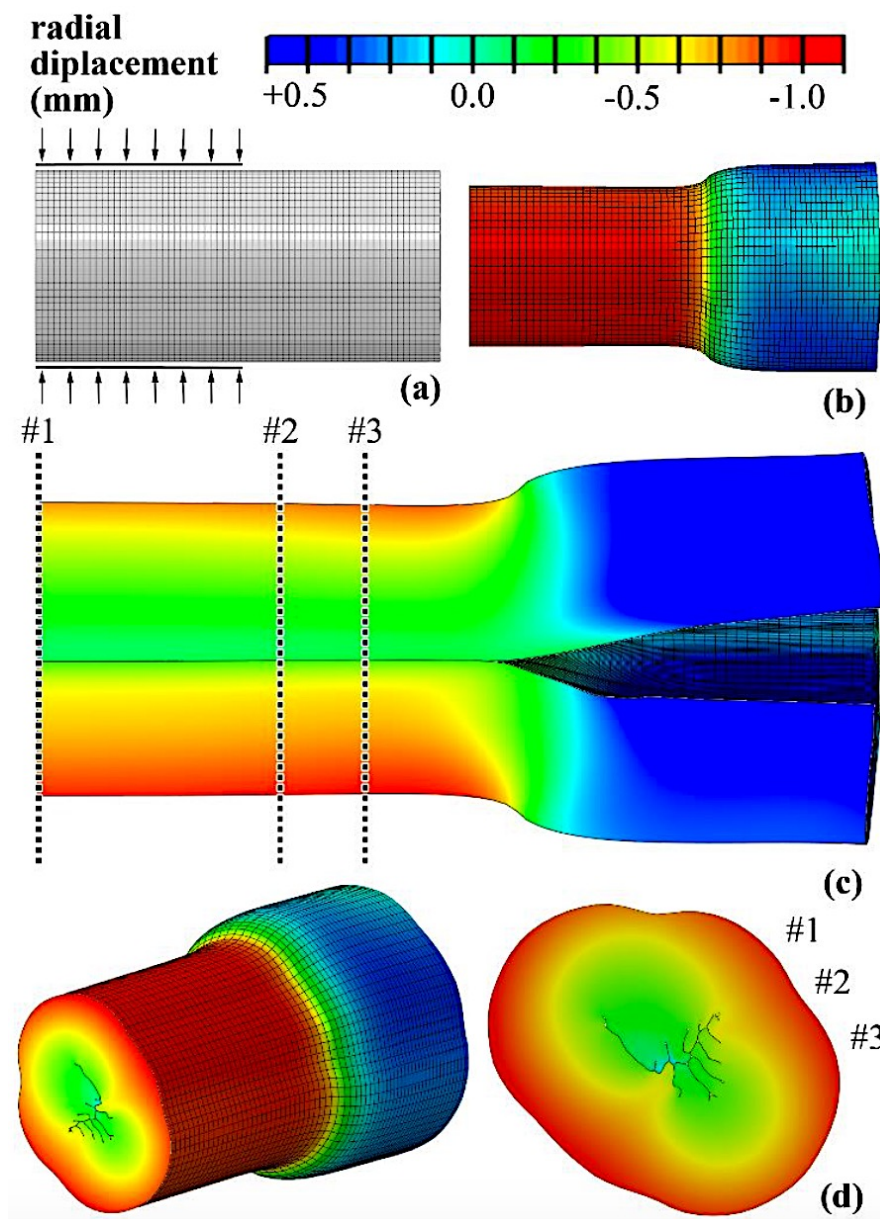


Figure 3.14. Numerical analysis of urethra occlusion by constant pressure cuff: radial displacement field. Contours are reported on the undeformed (a) and deformed (b) three-dimensional model, on longitudinal section A shown in Fig. 1a (c) and subsequent transversal sections #1, #2 and #3 (d).

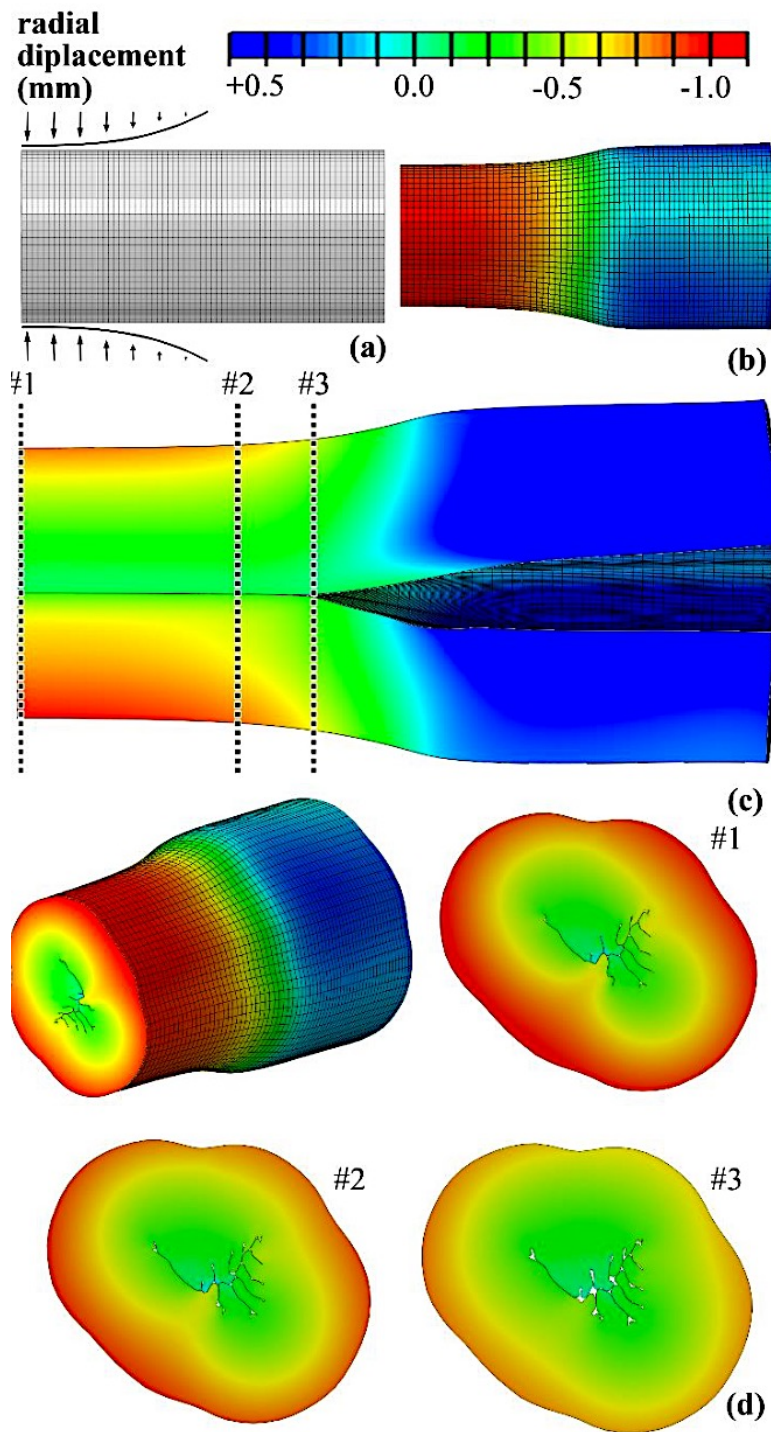


Figure 3.15. Numerical analysis of urethra occlusion by parabolic pressure cuff: radial displacement field. Contours are reported on the undeformed (a) and deformed (b) three-dimensional model, on longitudinal section A shown in Fig. 1a (c) and subsequent transversal sections #1, #2 and #3 (d) showing the different configurations.

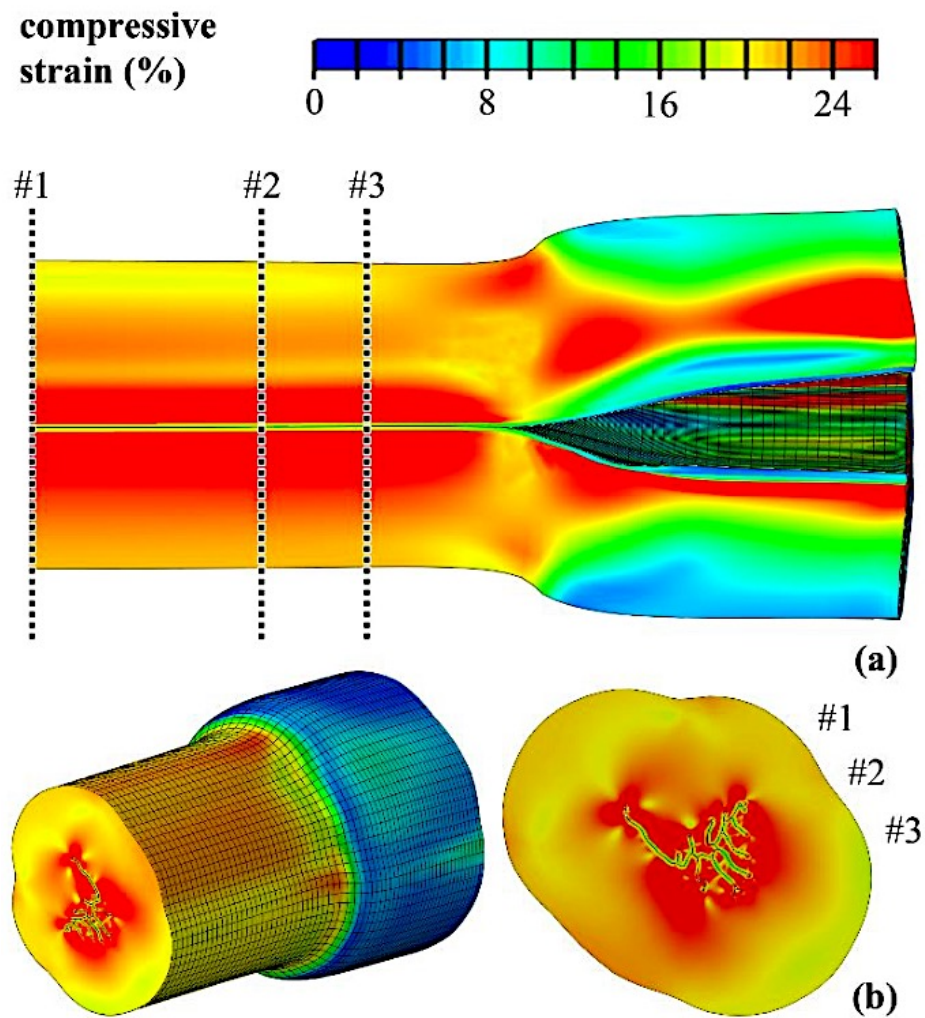


Figure 3.16. Numerical analysis of urethra occlusion by constant pressure cuff: compressive strain field. Contours are reported on longitudinal section A shown in Fig. 1a (a) and subsequent transversal sections #1, #2 and #3 (b).

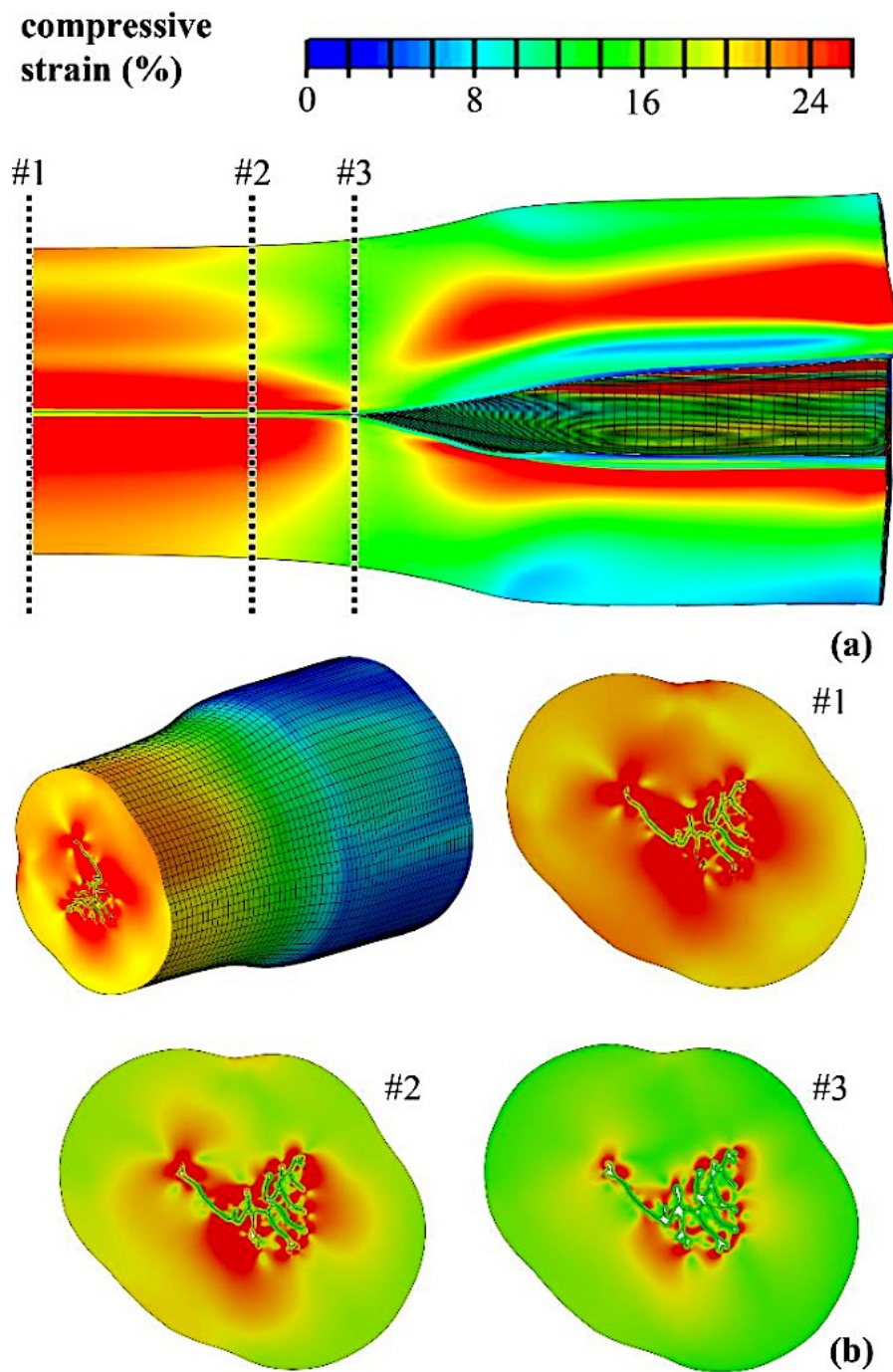


Figure 3.17. Numerical analysis of urethra occlusion by parabolic pressure cuff: compressive strain field. Contours are reported on longitudinal section A shown figure 3.7a (a) and subsequent transversal sections #1, #2 and #3 (b), showing the different configurations.

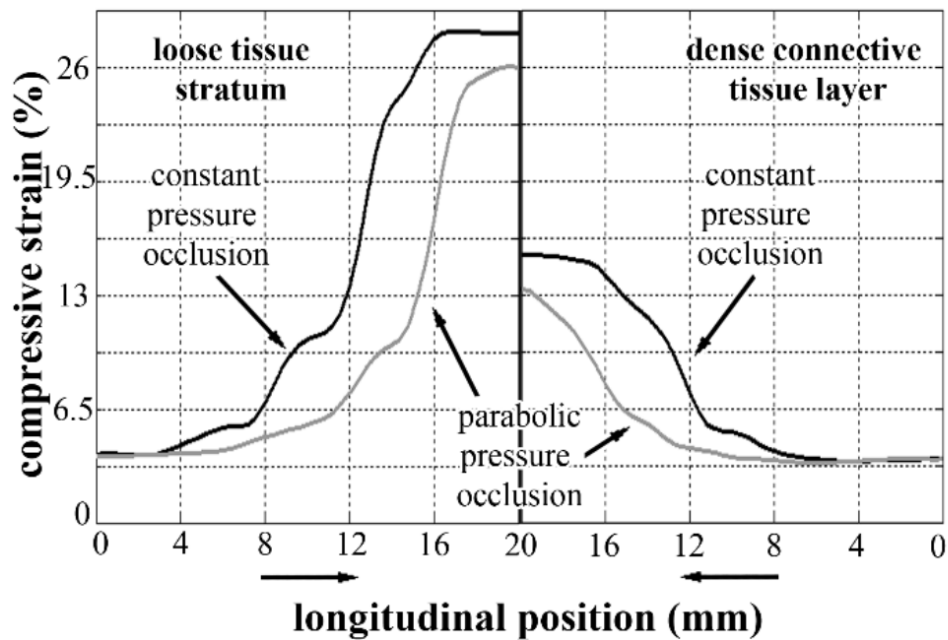


Figure 3.18. Compressive strain distribution along the urethral duct. Results are reported for both the loose tissue stratum (left side of the graph) and the dense connective tissue layer (right side of the graph) and for both constant (black lines) and parabolic (gray lines) occluding scheme. Data are reported with regard to the half symmetric portion 20 mm long.

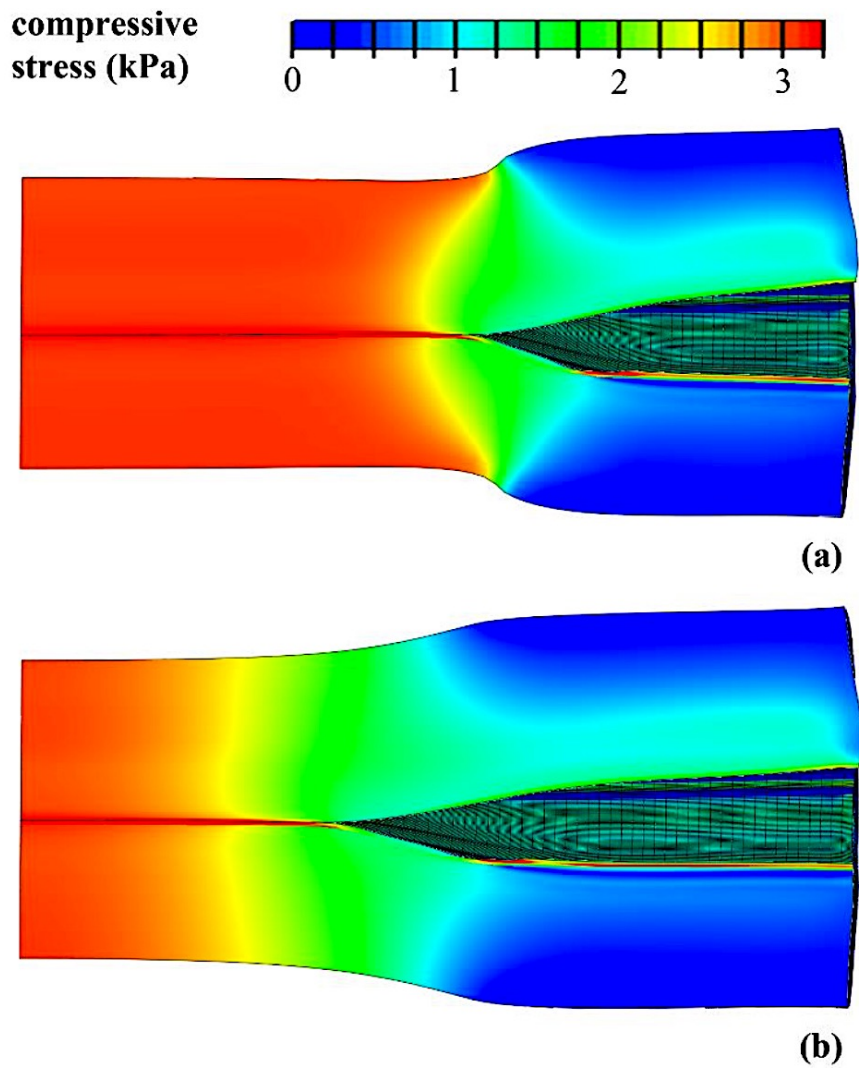


Figure 3.19. Numerical analysis of urethra occlusion: compressive stress field corresponding constant (a) and parabolic (b) pressure scheme on longitudinal sections A shown in figure 3.7a.

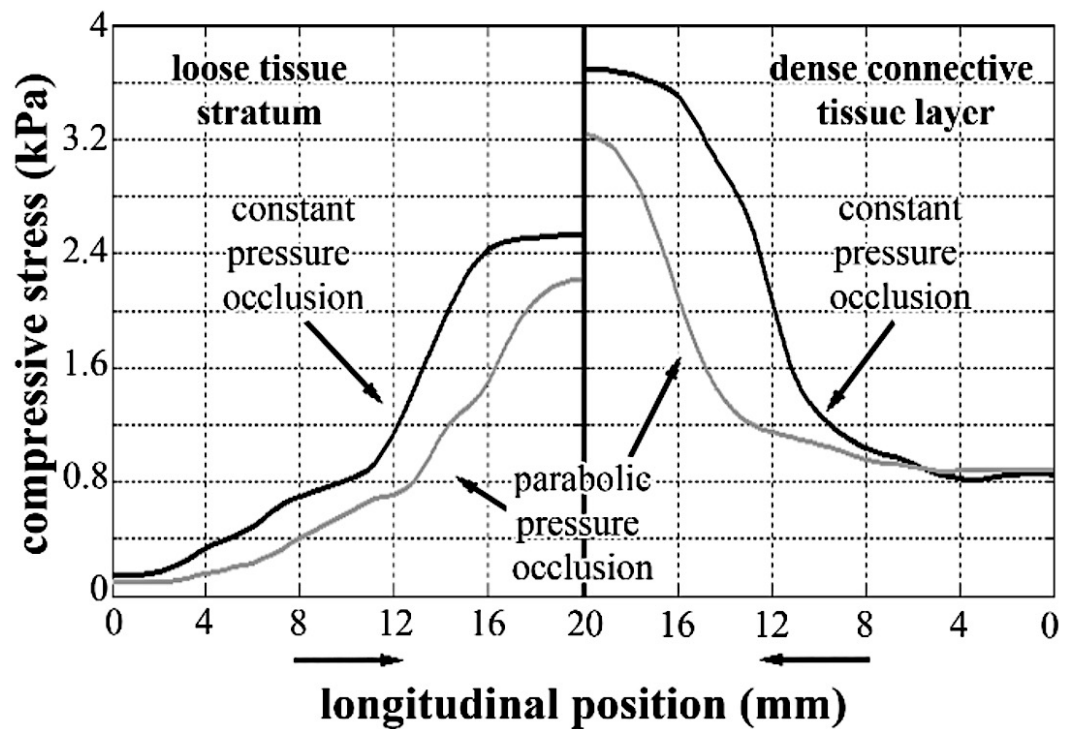


Figure 3.20. Compressive stress distribution along the urethral duct. Results are reported for both the loose tissue stratum (left side of the graph) and the dense connective tissue layer (right side of the graph) and for both constant (black lines) and parabolic (gray lines) occluding scheme. Data are reported with regard to the half symmetric portion 20 mm long.

3.6 DISCUSSION

The preliminary investigation of the urethral tissue mechanics was carried out with the aim of defining an experimental protocol to investigate its mechanical behaviour owing the lack of knowledge about it. The proposed experimental activities were developed on horse urethra, because of the similar configuration of equine and human tissues (AppendixA.2) and the ready availability of *ex vivo* samples.

Tensile tests on specimens from the proximal region showed greater stiffness along the longitudinal direction than along the circumferential direction (figure 3.4a). The spatial orientation of muscle fibres along the longitudinal direction can explain the anisotropic behaviour in the proximal region.

On the contrary, no significant differences were found between longitudinal and circumferential specimens from the distal region (figure 3.4c). Furthermore, no significant differences were found between all distal specimens and circumferential specimens from the proximal region.

Regarding the stress-relaxation tests, the viscoelastic behaviour showed little dissimilarity among the considered groups of samples (longitudinal proximal, circumferential proximal, longitudinal distal and circumferential distal; figure 3.4b and 3.4d).

Data from mechanical tests of the urethral structure showed a larger structural stiffness (figure 3.5a) and a higher percentage of pressure relaxation for the proximal urethra when compared with the distal urethra (figure 3.5b).

The results of the mechanical tests can be related to the microstructure of the urethral tissue evidenced by histological analysis. With particular regard to the proximal region of the urethra, the histology showed a preferential orientation of muscle fibres along the longitudinal direction that may be regarded as the reason for tissue anisotropy. Moreover, the amount of muscle fibres was found to decrease from the proximal to the distal urethra. Owing to this conformation, tissue stiffness is higher in the proximal region and along the longitudinal

direction. This method leads to a qualitative correlation, which could be supported by quantitative measurements on the mechanical properties of collagen fibres, based on additional histological and mechanical characterization.

Structural rearrangement processes produce stress-reduction phenomena influencing the amplitude and duration of viscoelastic phenomena, which are quantitatively defined by the parameters γ_i , Γ_i , τ_i and T_i , respectively. The parameters γ_i and τ_i are computed by processing results from tests of the urethral tissues (tables 3.1 and 3.2), whereas the parameters Γ_i and T_i account for data from tests of the urethral structure (tables 3.1 and 3.2). Although the same microstructural rearrangement processes should be expected at tissue and structure levels, differences have been found between parameters. The differences can be explained in part because the sample preparation for tissue tests requires dissection of the tubular urethra into rectangular specimens. The procedure may disrupt tissue continuity, with particular regard to collagen and muscle fibres, also modifying their rearrangement over time and viscoelastic phenomena.

The choice of the optimal number of viscous branches is based on the evaluation of the RSS for different numbers of viscous branches assumed. For experimental data on the relaxation of tissue samples, the fitting with two viscous branches gives an RSS value of the order of 10^{-2} . Concerning the inflation results, the fitting with two viscous branches makes it possible to find a lower RSS value, of the order of 10^{-3} . Therefore, the choice of two viscous branches for the models is suitable for describing the viscoelastic response of tissue and structures. The choice of an additional branch would enable a further reduction of the RSS value, resulting in a more complex model without effective improvement in the numerical simulation of the viscoelastic response.

Aiming at the mechanical characterization of human urethra, the next step of the investigation will account for experimental activities on human samples.

A complete biomechanical characterization of urethral tissues and structures *in vivo* cannot be achieved by using experimental techniques only. Computational models are suitable for providing additional information, on the basis of constitutive formulation and structural model variations. For this purpose, numerical models of equine urethra are developed. The developed computational framework allowed the investigation of urethral structure and tissues mechanical response considering different configurations depending on intraluminal and occlusion pressure. Two-dimensional analyses are performed by assuming different sets of constitutive parameters. The sets differ from one another by the multiplier k , which specifies the stiffness ratio between dense connective tissue layer and loose tissue. While the specific value of k modestly influences the tensile behavior of the urethra samples (figure 3.9a) the effect on the inflation tests shows different trends and larger intensity variation (figure 3.9b). In any case, the numerical results are well placed within the statistical band of experimental results for a broad range of k values. Low k values entail an almost homogenous distribution of stiffness along the urethra thickness. On the contrary, high values of k better describe the configuration of the urethra, as an inner thin and stiff layer surrounded by a thick and compliant stratum. The trend of intraluminal pressure with lumen volume significantly varies with the multiplier k , in accordance with the stiffness contribution of the dense connective tissue layer that progressively increases with the distension of the lumen. The optimal multiplier k is identified by minimizing the discrepancy between model curves and median experimental data. This assumption can be justified by considering that median data describe the average behavior of all the tested experimental samples.

As concern the tissue response in the central region within the area where the sphincteric device provides the pressure action, the accuracy of the present results can be satisfactory, in spite of the limitation that pertains to the two dimensional model conformation. This preliminary approach is justified also by the relevant computational effort determined by a highly non-linear problem, related to

material, geometry and contact conditions. The three dimensional analysis in progress led to a more accurate and general interpretation of the overall response. In general, the computational models allow the evaluation of tissues mechanical response with detail and accuracy. In figure 3.11 the stress distribution for different values of intraluminal pressure depending on urine is reported.

An interesting aspect of the analysis pertains to the tissues response when artificial sphincters, induces lumen occlusion. Figure 3.12 summarizes results from numerical analyses that took into account the combination of different values of intraluminal and external occluding pressures. Occlusion occurs when external and intraluminal pressures almost equalize and subsequently urethral epithelial tissues undergo compression phenomena. Occluding actions determine substantial compressive strains within dense connective tissue and loose tissue. Artificial sphincters steadily induce such non-physiological strains within urethral tissues and potentially lead to degenerative phenomena.

CHAPTER 4

COMPUTATIONAL INVESTIGATION OF THE DEVICES FOR AN INNOVATIVE APPROACH TO BARIATRIC SURGERY

The need of endoscopic bariatric techniques is discussed in the first section of chapter 1, due to the many post-surgical complications arising from laparoscopic treatments. Although actual endoscopic treatments of obesity seem to be safe there is a high incidence of removal. A lot of patients endoscopically treated experienced serious adverse events including nausea and vomit, gastric ulcers and erosion, esophageal perforation secondary to trauma, cholangitis, and liver abscess [American Society for Gastrointestinal Endoscopy, 2015]. For these reasons, there is a need of a novel reliable bariatric surgery techniques aiming at optimizing the post-surgical conformation of the stomach and to reduce surgical traumatism, post-surgical complications and anesthetics requirement.

In this chapter is presented a computational approach for the design of a device involved in an innovative endoscopic gastric banding of obesity, focusing on the mechanical analysis of clips involved to restraining the gastric band on the stomach wall. Gastric banding is chosen due to its successful and conservative functioning principle of restricting the stomach instead of other more invasive techniques which will require too much sedation. This work will be part of a research proposed project called BIO-OBESE (**BIO**mechanical **O**ptimization of **B**ariatric **surgE**ry procedures and **deS**ign of devices for **E**ndoscopic approach), which involve a multidisciplinary approach of different research units from Padova, Ancona and Palermo universities. In this project coupled biomechanical,

biomechatronical, physiological and surgical studies are integrated to investigate the relationships between food intake, mechanical stimulation of stomach wall and filling of satiety, to establish criteria for the definition of the optimal post-surgical configuration of the stomach depending on the specific patient parameters and finally to develop prototypes of the different devices involved.

4.1 ENDOSCOPIC GASTRIC BANDING TECHNIQUE

From chapter 2, as food interacts with the lining of the stomach, stress and strain fields develop and their magnitudes exponentially increase with the volume of food intake [Carniel et al., 2017]. Chapter 1 describe the mechanism by which the wall stretch is sensed by related receptors and neural signals to the brain, where those signals are converted to the sensation of satiety. The magnitude of the sensation is related to the intensity of the mechanical stimulation of the stomach wall.

The purpose of this technique is to insert an annular device into the stomach cavity, which will be able to make a mechanical stimulation of the stomach wall with an internal restrictive action during the food incoming. An overall description of the procedure is given as follows by Carniel et al., within the BIO-OBESE project proposal. After intubation, a gastroscopy will be performed to evaluate the actual conformation of the stomach. A rolled gastric band will be positioned in the desired place and will be fixed to the gastric wall by clips. A specific endoscopic device will apply the clips to fix the band to the stomach wall according to an almost circumferential pattern (figure 4.1). The specific location and conformation of the clips pattern will depend on the desired magnitude of the stomach stricture. The first step to this technique design is given through another thesis work, made at the same time by Gioela Pluchino, in which a computational model of the stomach is made to evaluate the mechanical response of the stomach wall because of clips application, gastric band stretching and stomach filling. The analyses will make it possible to identify the clips and the band conformation and properties that are required to avoid both removal of the gastric band and

biomechanical damage of the stomach tissues. A second step, that is a final target of this work activity, will focus on the clips design. They must be reliable, biocompatible and easy to apply to the stomach wall by an opportune endoscopic device.

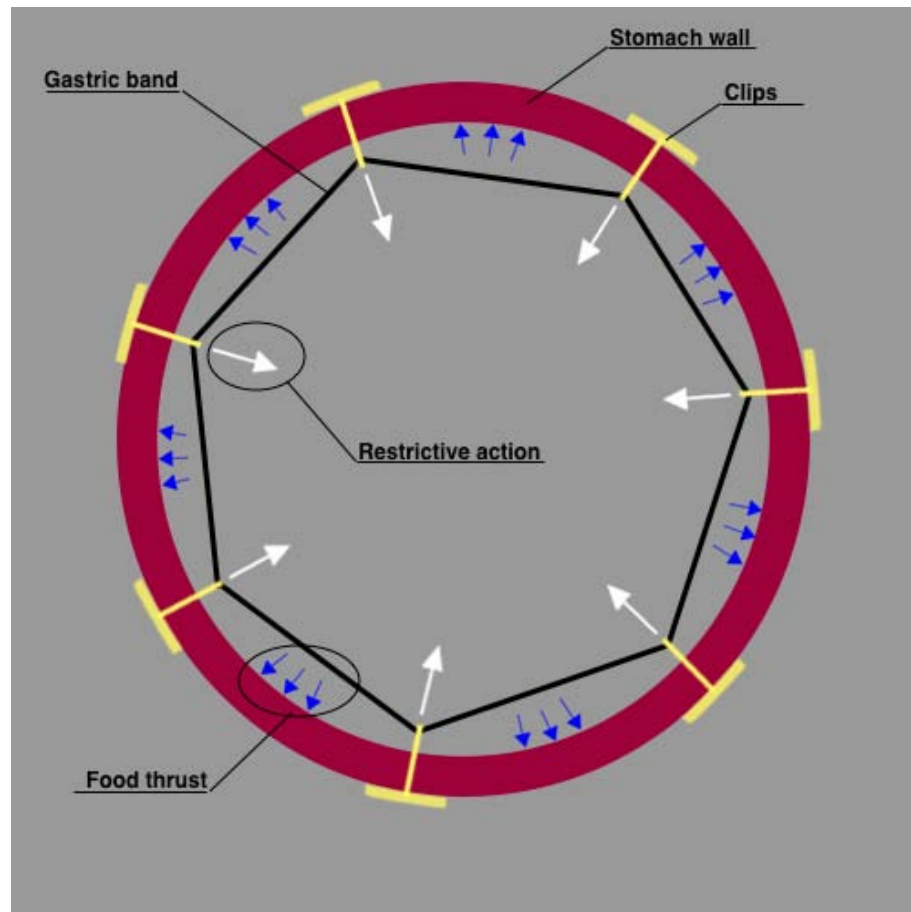


Figure 4.1. Overall scheme of the internal gastric band functioning principle. Clips (yellow colored) force the stomach wall (red colored) to be restrained to the gastric band (black colored) due to the expanding action of the food incoming and to the inextensible properties of the band.

The third step of the project is to design an endoscope that should easily reach the stomach, have a cartridge containing the clips and mechanisms for clip and band application. The last step is to develop prototypes of the surgical devices, evaluate them reliability through “in silico” test at the beginning, experimental surgery on animal models and clinical surgery on human cadavers at the end.

4.2 DESIGN OF THE CLIPS

Initially, the purpose of this activity was to analyze the mechanical behavior of a well-defined clip geometrical model (figure 4.2) as a function of different geometrical configurations.

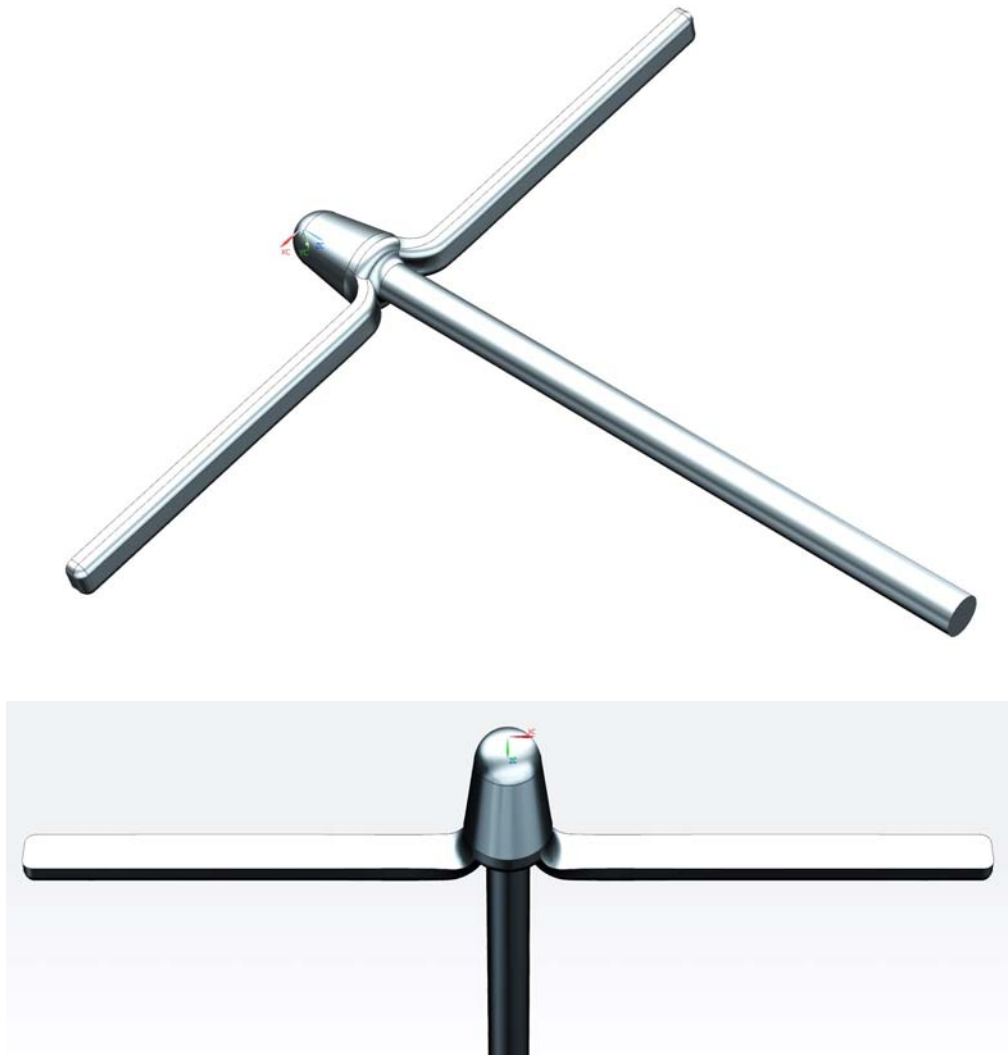


Figure 4.2. 3D model of the first clip to analyze.

This model shows a stem with a larger and sharpened head in the upper end. From this head originate two thin and symmetrical wings disposed orthogonally to the stem and attached to the head with a curvature describing an arch of a quarter of circumference. The head is designed to be suitably sharpened according to the stomach wall perforation by the clip, that must pass through it and anchoring to

the external surface of the stomach. The head must be not too much sharpened due to its adjacency to external organs and tissues, which could be pained and scarred.

On the other end of the stem a little hole will be made in order to passing the gastric band through it. The two wings implement the gripping action of the clip to the external wall due to the internal force given from the restricting action of the gastric bend. According to minimize the wound dimension due to the clip passage the two wings must be bended along the stem by the endoscope (figure 4.3). Once the clip pass through the stomach wall, the wings are able to return in their initial position due to the elastic behavior of the material.

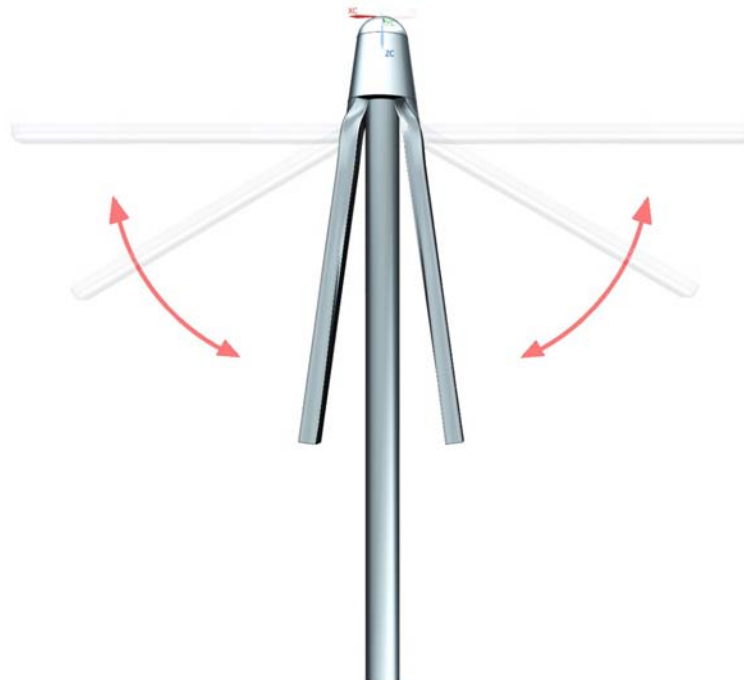


Figure 4.3. Bending of the wings before the perforation of the stomach wall.

4.2.1 AN OPTIMIZED GEOMETRICAL MODEL OF THE CLIPS

In order to minimize the clips dimensions and to simplify the mechanism involved to the clips fixation, a novel geometrical model is conceived (figure 4.4). As figure 4.5 shows, this model is made by two different solid parts, a stem and a flat rocker, connected with a cylindrical hinge.



Figure 4.4. Advanced geometrical model of the clip.

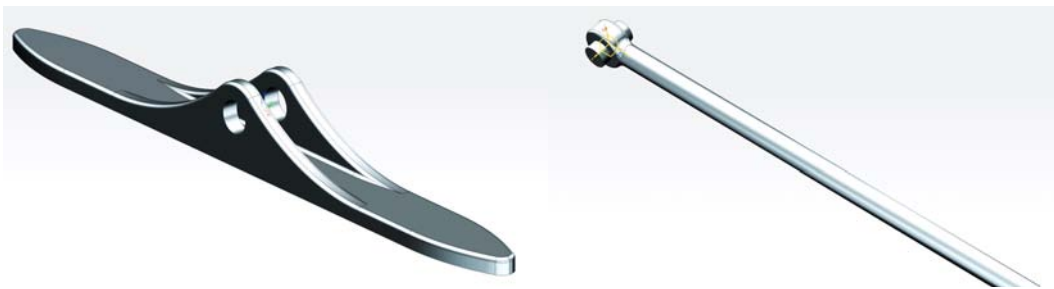


Figure 4.5. Parts of the novel geometrical model: the rocker (left) and the stem (right).

Because of the cylindrical constraint, the stem and the rocker may rotate relatively one on the other, to obtaining a straight conformation showed in figure 4.6. This conformation has a lot of advantages, such as the reduction of the transversal section of the clip passing through the stomach wall and the endoscopic channel, the possibility to use both ends of the rocker to perforate the stomach wall, the absence of a sharpened head that may pare external adjacent tissues and the possibility to simplify the endoscope. Furthermore, the two arches of the rocker supporting the hinge and the hinge itself act as a cap that allows wound to remain closed.

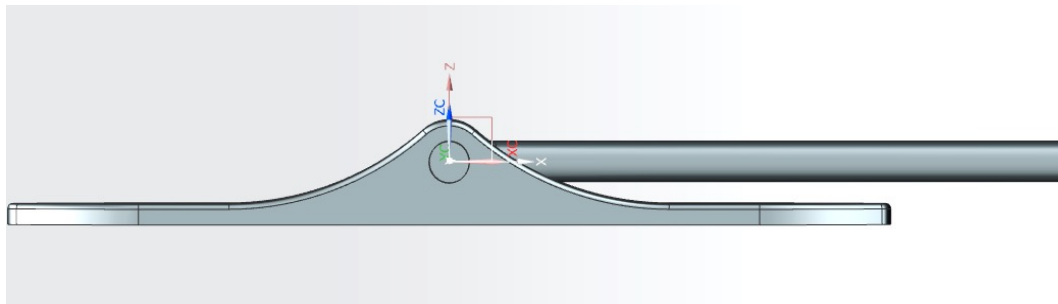


Figure 4.6. Straight configuration of the clip during its application to the stomach wall and during the passage through the endoscopic channel.

After the evaluation of functional advantages, the goal is verifying that mechanical behavior conforms the function needed. Thus, the next step of the clips design is the realization of multiple 3D CAD models characterized by different values of the main geometric parameters. This allows the investigation of the mechanical response of the structure as a function of the geometric main variables, aiming to assess the right compromise between size and functionality and then proceeding with the prototyping of the optimal devices.

4.2.2 3D CAD MODELLING OF THE CLIPS

To simplifying the discussion, the first model of the clip is called *M1* while the second is called *M2*. Clips *M1* are designed with a basic geometry configuration (table 4.1) according to the dimensions of the endoscope channel, which is supposed to be a cylindrical channel with a diameter of $1.5 \div 2.0$ mm. Because of these geometrical restrictions, wings thickness (*T*) and width (*W*) are the parameters chosen to vary and thus incremented of 0.1 mm one by one. *M2* clips are designed according with *M1* dimensions, in order to adequately compare the two different shapes by a functional and mechanical point of view. Thus, while the stem is maintained with the same dimensions, the rocker is designed to have the same width of an entire *M1* clips when it has the wings close to the stem, to simulate the same wound that they will create to the stomach wall. Parameters chosen to be the geometrical variables of the *M2* models are, therefore, the rocker

thickness (T) and width (W). These latter vary within $0.8 \div 1.2$ mm and $0.2 \div 0.5$ mm respectively, with an incrementing step of 0.1 mm.

Another geometric variable supposed to be interesting to evaluate is the distance of the hinge axis to the rocker plate. For this reason, two different types of M2 clips are designed: type A and type B in which a rocker - hinge axis distance is of 0.2 mm and 0.1 mm respectively. The hinge has a diameter of 0.4 mm; thus, the rocker of type B clips is characterized of a central pit that receive the distal part of the hinge (figure 4.8).

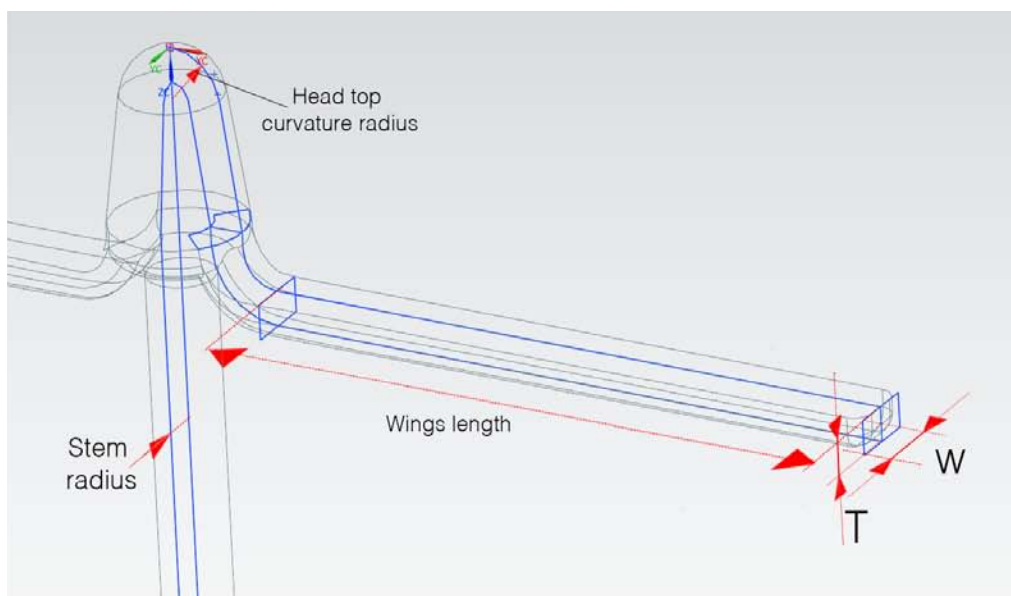


Figure 4.7. Principal dimensions involved to the 3D CAD of the clips.

Parameters	Dimension [mm]
Head high	1.0
Head largest diameter	0.4
Curvature radius of the top	0.3/0.4
Stem radius	0.2
Stem length	8.0
Wings length	4.0
Wings Thickness (T)	0.2
Wings Width (W)	0.4

Table 4.1. values of the main geometrical parameters of the basic M1 clip.

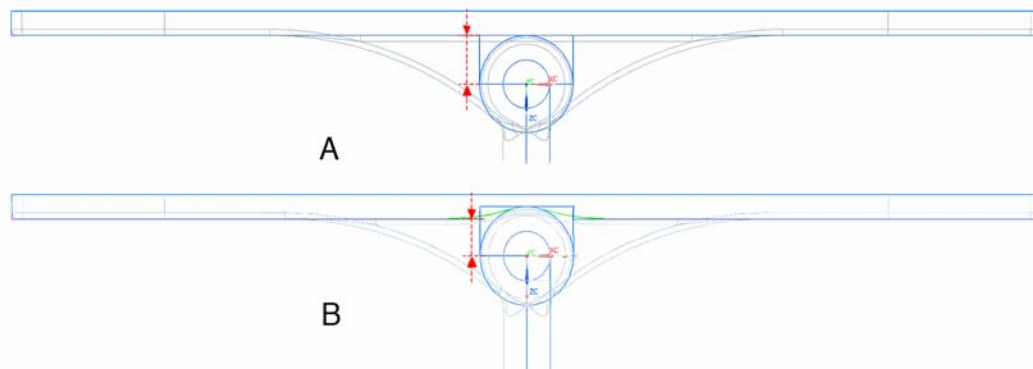


Figure 4.8. M2 CAD sketch of both type A and type B clips, marking differences between them.

Solid models of the clips were designed using a 3D CAD software (UGS NX 9.0, Siemens PLM Software, Plano, TX, US). which involve a first 2D layers design of the elements followed by a 3D solid rendering by means of extrusion, rotation or sliding surfaces.

In order to conduct a numerical analysis of the clip structure by means of FEM analyses, geometrical models were exported into a *parasolid* geometrical format. To simplify the numerical analysis, *M2* models were exported as a unique solid composed by the union on the two elements.

4.2.3 THE MATERIAL

The ideal material suitable for this application should be a biocompatible material but it should have a high mechanical strength according to the stresses involved to the structure itself. These considerations lead to consider Titanium alloy as a suitable material involved to this application due to its high biocompatibility well approved over time and to its reliability on supporting high stresses considering its wide use in the orthopedic field.

Thus, a Grade 5 Titanium Ti-6Al-4V alloy is chosen, and material parameters have been taken from a data storage of materials (www.matweb.com) (table 4.2).

Parameter	Value	Unit
Elastic Modulus E	109.863	GPa
Poisson's ratio ν	0.342	-
Yield strength σ_y	880	MPa
Ultimate strength σ_u	950	MPa
Fatigue limit σ_f (Unnotched and smooth bar)	510	MPa
Number of cycle to failure N	10^7	-

Table 4.2. Material parameters of Ti-6Al-4V alloy used.

4.3 COMPUTATIONAL MODELS OF THE CLIPS

4.3.1 MODELS DISCRETIZATION

The realization of numerical models of the clips structures is performed within Abaqus Standard 6.14 (Dassault Systèmes Simulia Corp., Providence, RI) FEM software, in which *parasolid* 3D CAD models of the clips are imported. For each model is suddenly created a material section assigning material parameters, showed in table 4.2, to the geometrical model. An independent instance is then created discretized by means of an opportune tetrahedral and linear elements mesh (figures from 4.9 to 4.12). The meshes of each numerical model have a number of element ranging between 63632 and 77971, while they have a number of node ranging between 157413 and 193723.

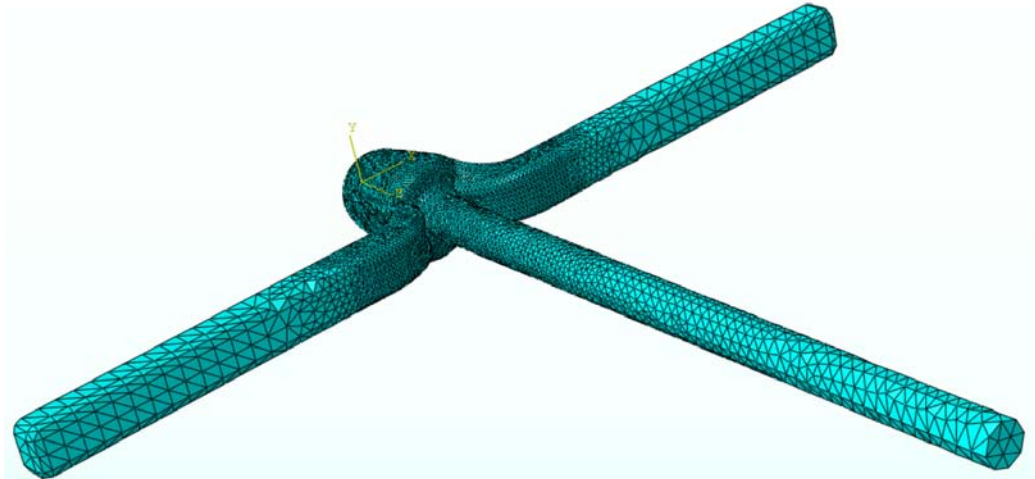


Table 4.9. Mesh of the basic M1 clip related to a CAD model with $T=0.2$ and $W=0.4$.

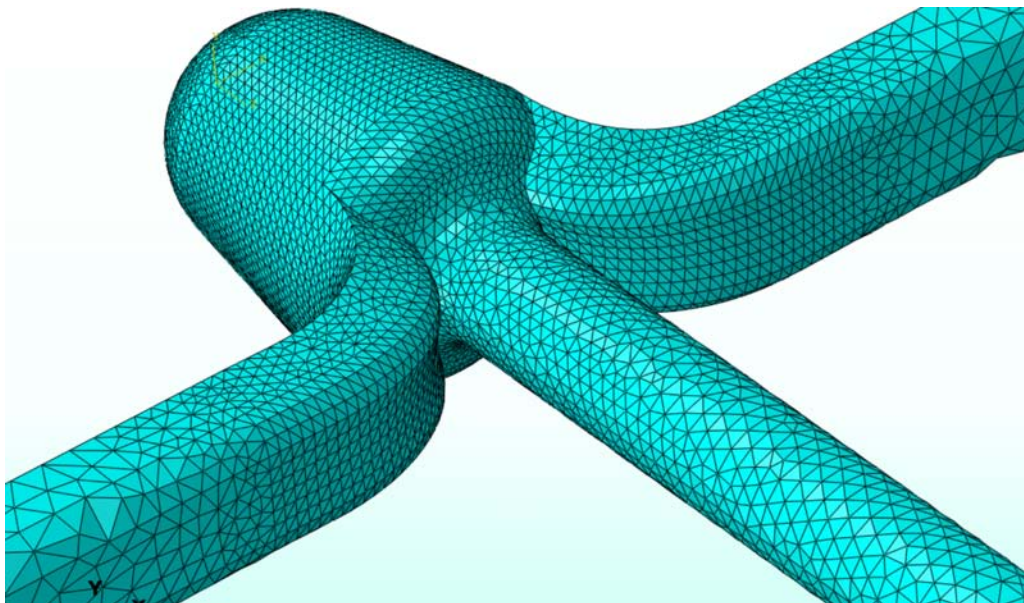


Figure 4.10. Zoom of the mesh in figure 4.8.

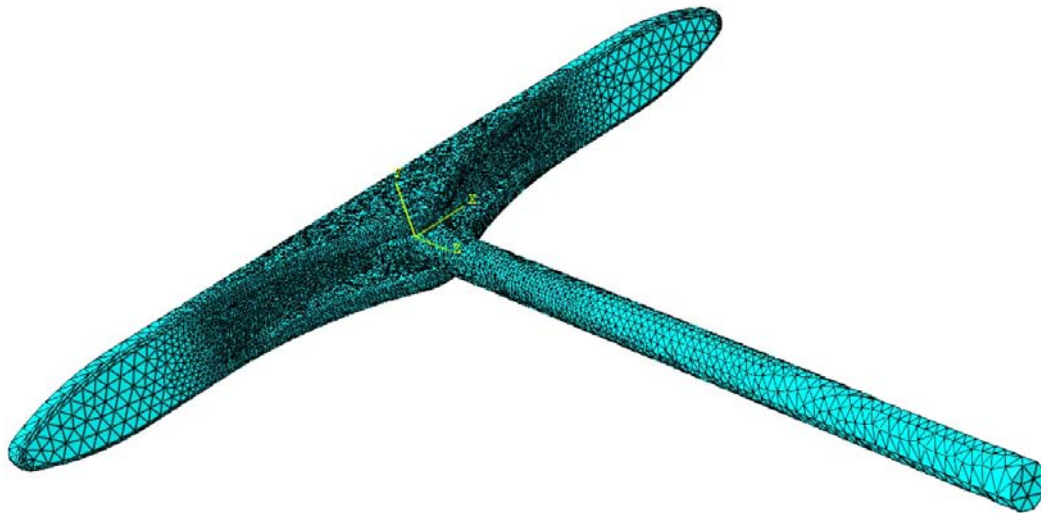


Figure 4.11. Mesh of the basic M2 clip related the CAD model with $T=0.2$ and $W=0.8$.

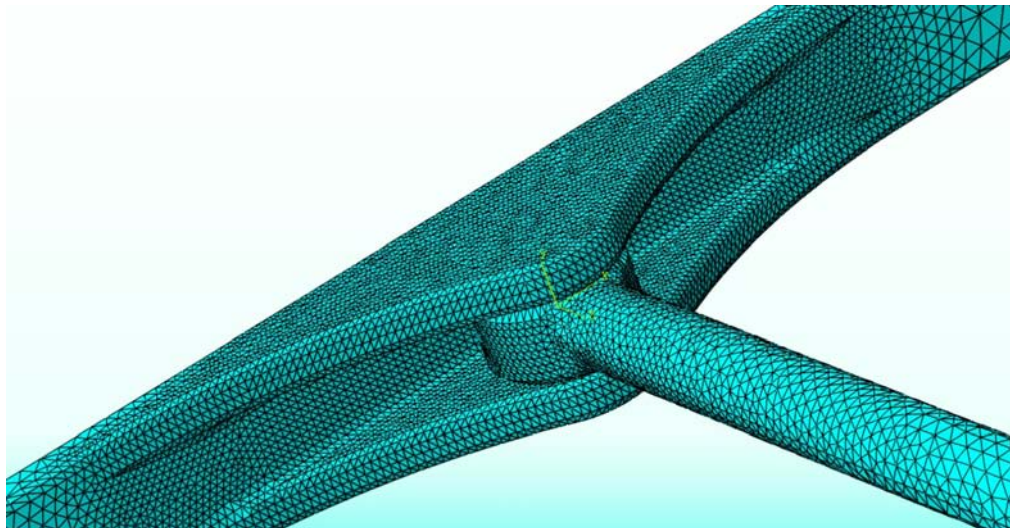


Figure 4.12. Zoomed mesh of figure 4.10.

4.3.2 LOAD BOUNDARY CONDITIONS SETUP

A linear incrementing pressure until 10 MPa is applied on each numerical model, orthogonally to the surface which will be in direct contact to the external wall of the stomach, simulating the pressure of the latter on the device while stomach expands due to the food intake (figures 4.13 and 4.14).

According to the internal restrictive action given by the internal gastric band, the entire surface on the proximal end of the stem is constrained, blocking each translational movement possible ($u_x=0$, $u_y=0$, $u_z=0$) (figures 4.15 and 4.16).

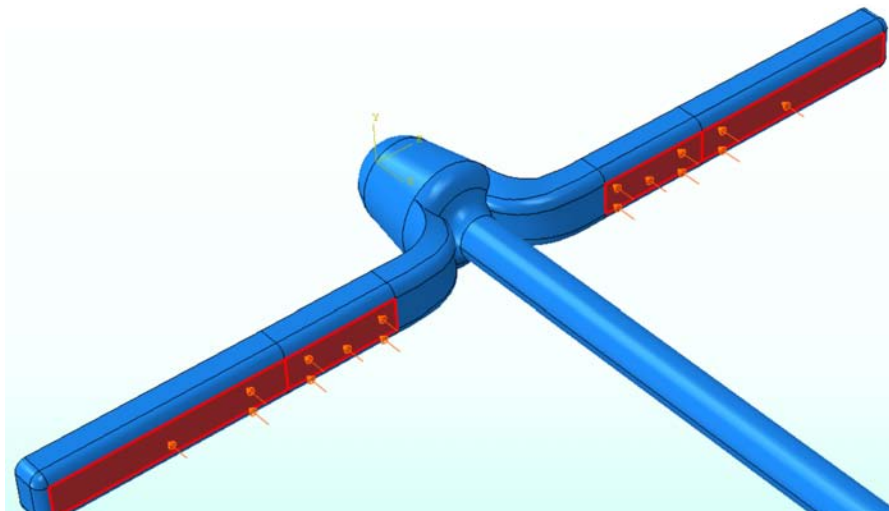


Figure 4.13. Load acting on the basic M1 clip numerical model.

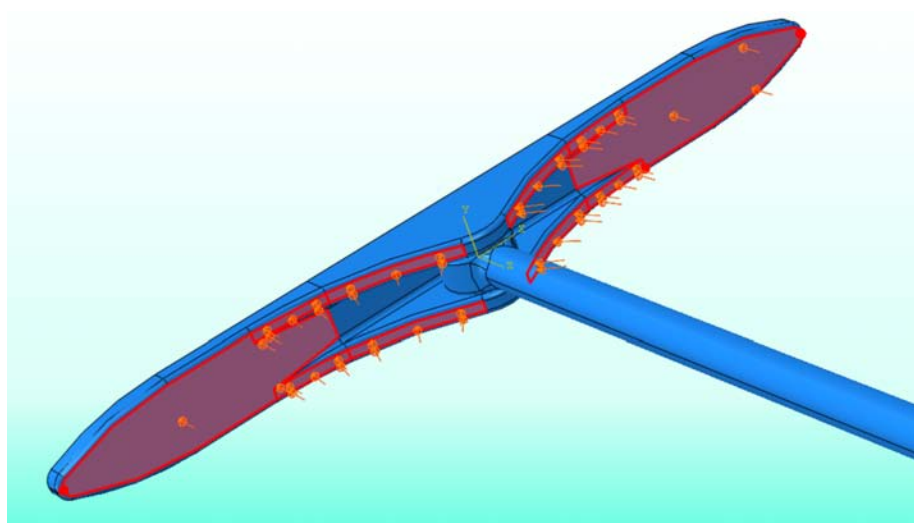


Figure 4.14. Load acting on the basic M2 clip numerical model.

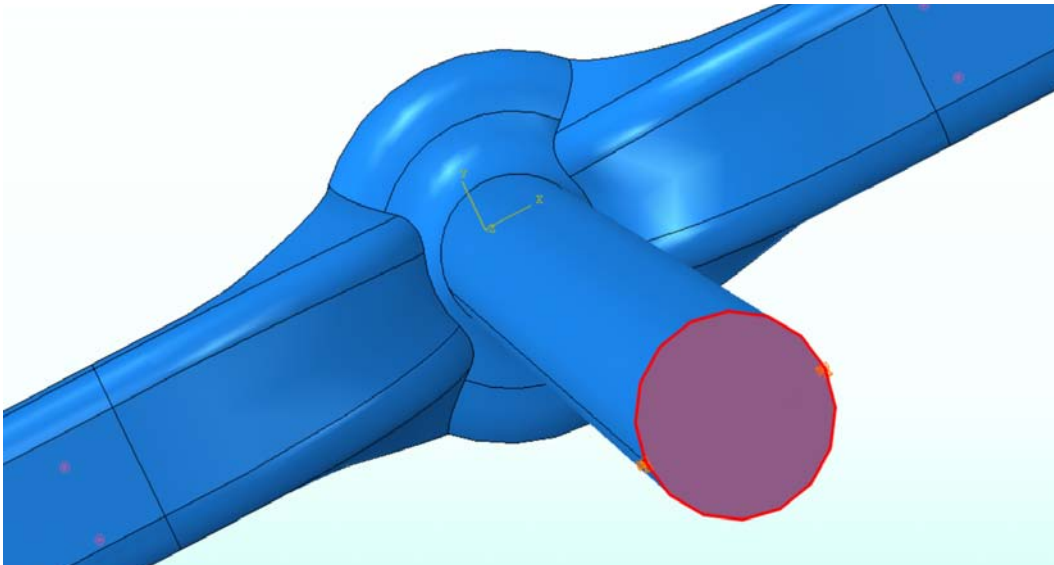


Figure 4.15. M1 structure constraints on the proximal stem end surface.

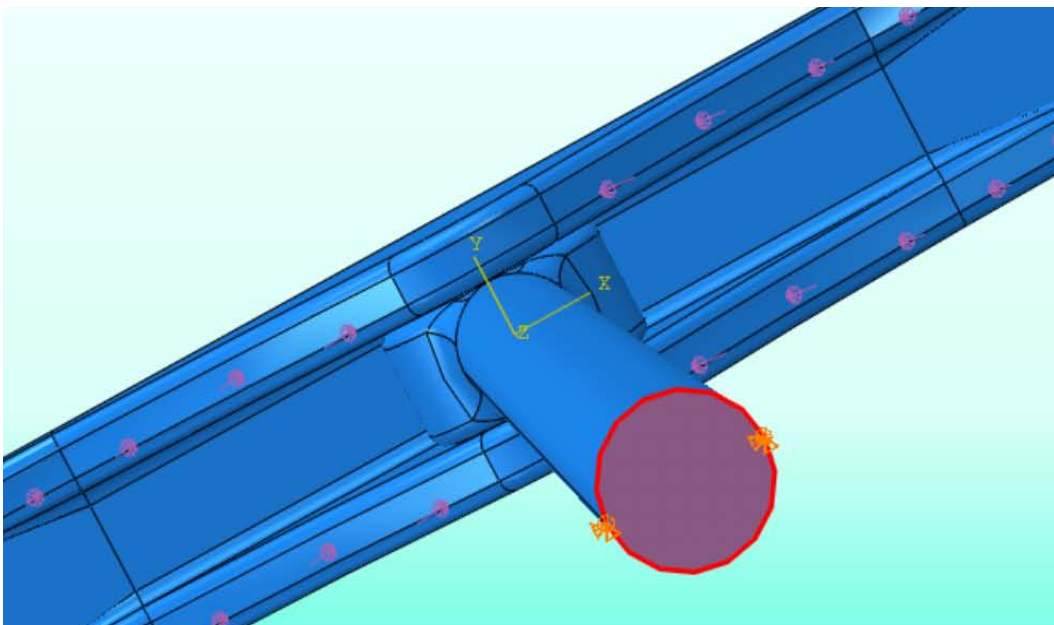


Figure 4.16. M2 structure constraints on the proximal stem end surface.

4.4 RESULTS

4.4.1 FIRST RESULTS OF BASIC M1 AND M2 MODELS

The first part of the analysis process is dedicated to comparing the mechanical response between M1 and M2 clips. Therefore, the first results reported are related to the basic numerical models: $T=0.2\text{mm}$ and $W=0.4\text{mm}$ for M1 and $T=0.2\text{mm}$ and $W=0.8\text{mm}$ for M2. In order to compare the different basic models results, the latter are reported in correspondence of the same reaction force value of 2N. According to the first results further numerical analyzes are performed focusing on the clips model which present the better mechanical response in the first results.

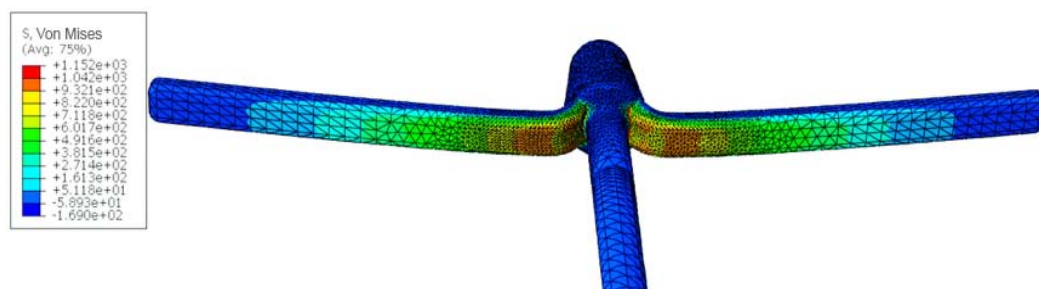


Figure 4.17: colored contour of the basic M1 clip model results while a reaction force of 2N is detected on stem base surface

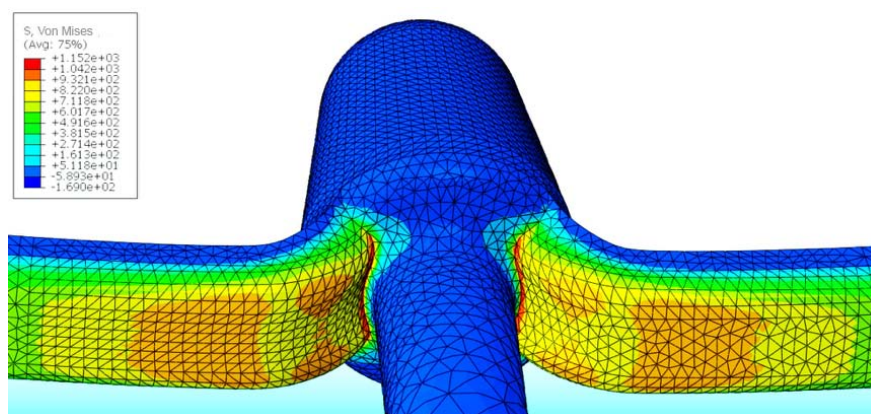


Figure 4.18. Zoom of the previous figure in proximity of stresses intensification area.

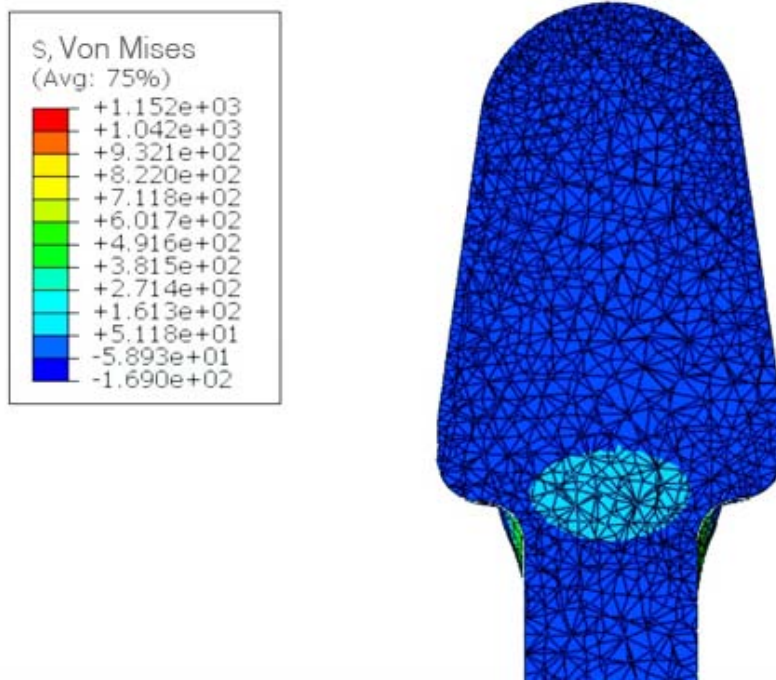


Figure 4.19. Colored contour of M1 a model sagittal section.

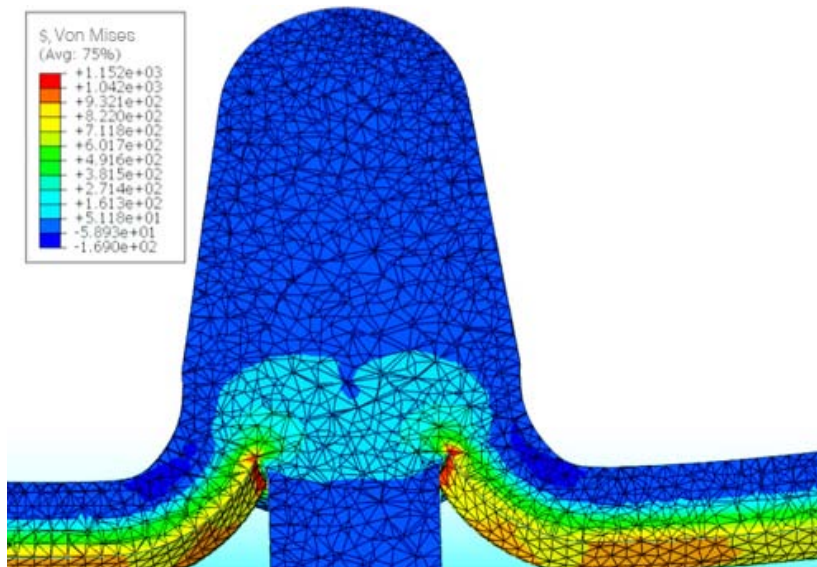


Figure 4.20. Colored contour of M1 a model frontal section.

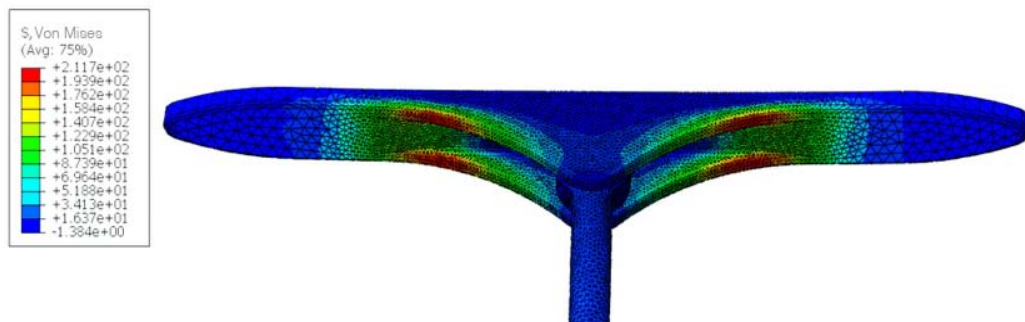


Figure 4.21. Colored contour of the basic M2 type A clip model results while a reaction force of 2N is detected on stem base surface.

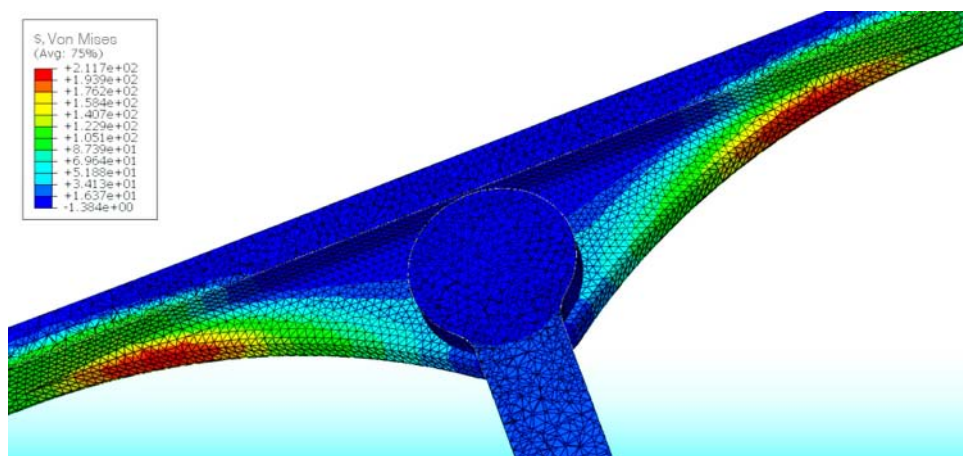


Figure 4.22. Colored contour of M2 type A model section.

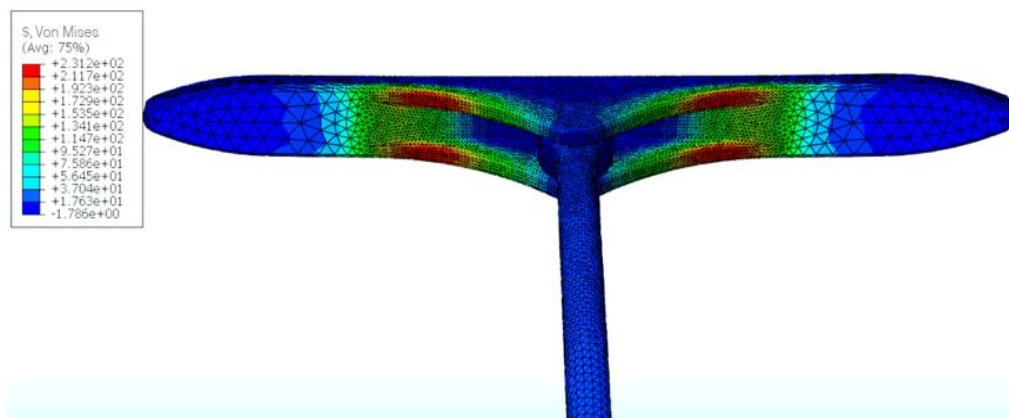


Figure 4.23. Colored contour of the basic M2 type B clip model results while a reaction force of 2N is detected on stem base surface.

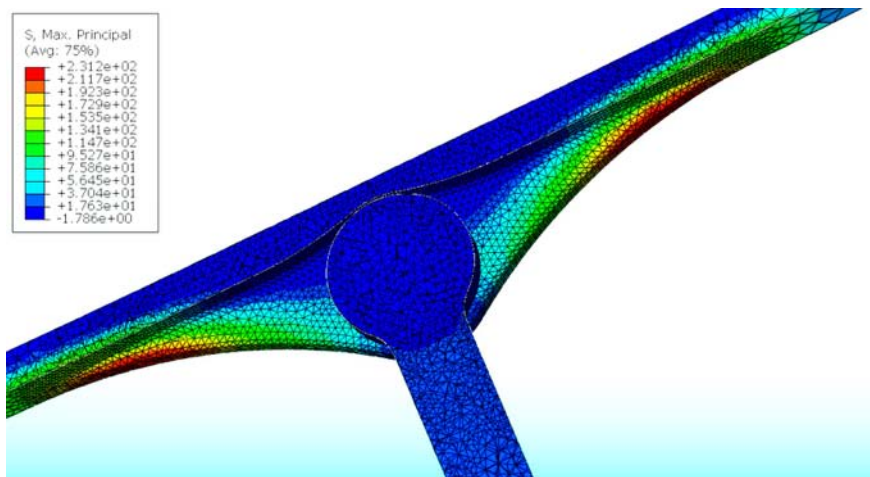


Figure 4.24. colored contour of M2 type B model section.

4.4.2 FIRST M1 AND M2 RESULTS COMPARISON AND DISCUSSION

Previous results showed a better mechanical response in terms of a lower value of *Von Mises stresses* involved in models during the same reaction force resulting at the constrained surface.

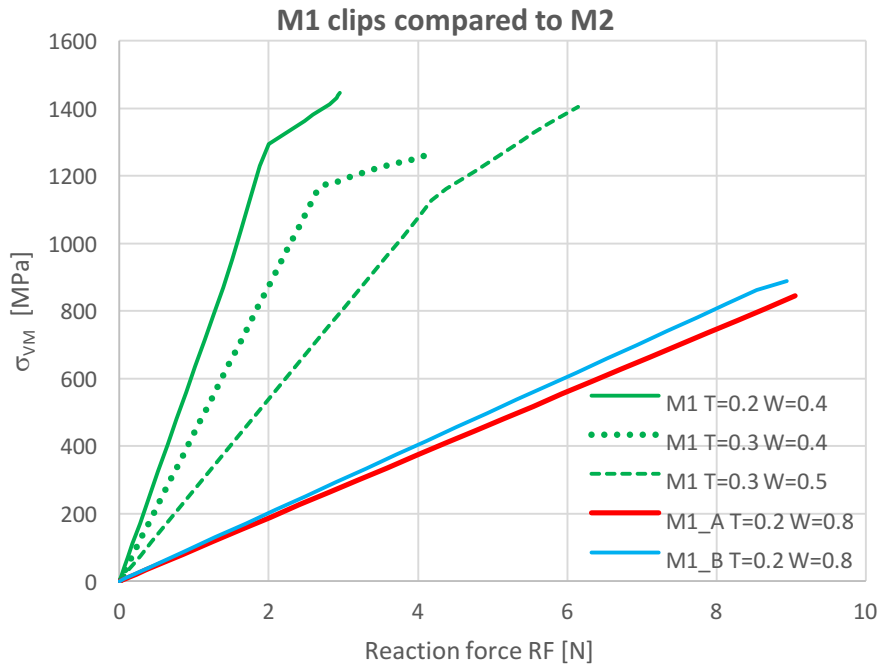


Figure 4.25. comparison between M1 (green) and M2 (red and blue) basic models results.

Figure 4.25 shows graphs of the entire load history of each basic models and the corresponding Von Mises stresses observed. These graphs showed that M2 clips curves are relatively far below from M1 curves, in both A and B cases. This means that M2 clips present mechanical and structural advantages which lead to focus numerical analyzes on these optimized geometrical models.

As a consequence of previous results, 40 different numerical models of M2 clips are realized (20 for each type), corresponding to the combinations of the 4 different thickness values ($T \in [0.2, 0.5]$) and of the 5 different width values ($W \in [0.8, 1.2]$) of the clip rocker. Due to the better response in terms of lower stresses perceived in all the cases, the next section shows a comparison between analysis results of the 20 M2 type A clips numerical models.

4.4.3 M2 TYPE A FURTHER RESULTS

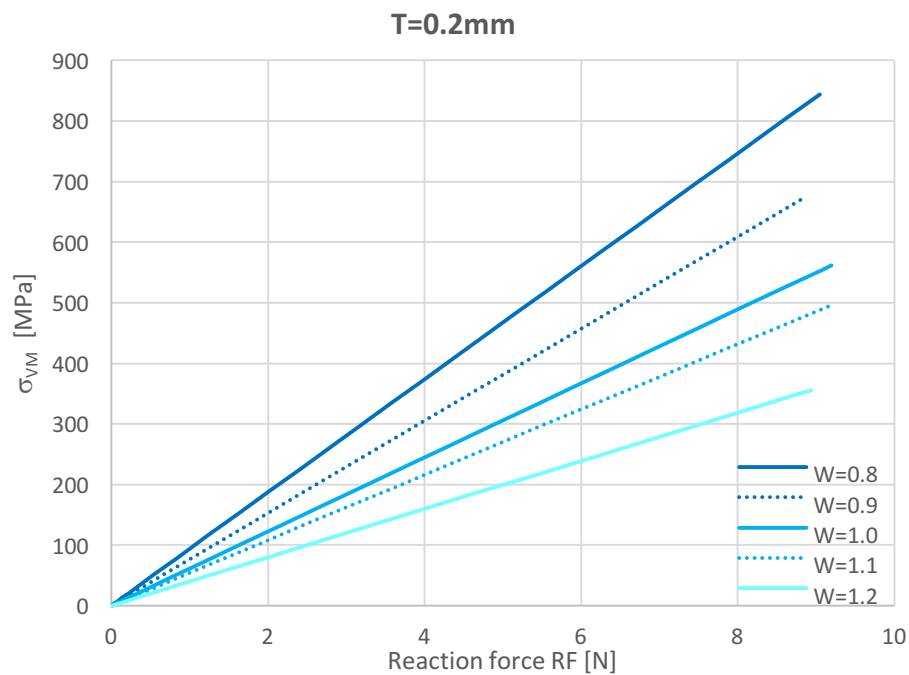


Figure 4.26. M2 Type A models Von Mises fixing thickness to $T = 0.2$ mm and varying W .

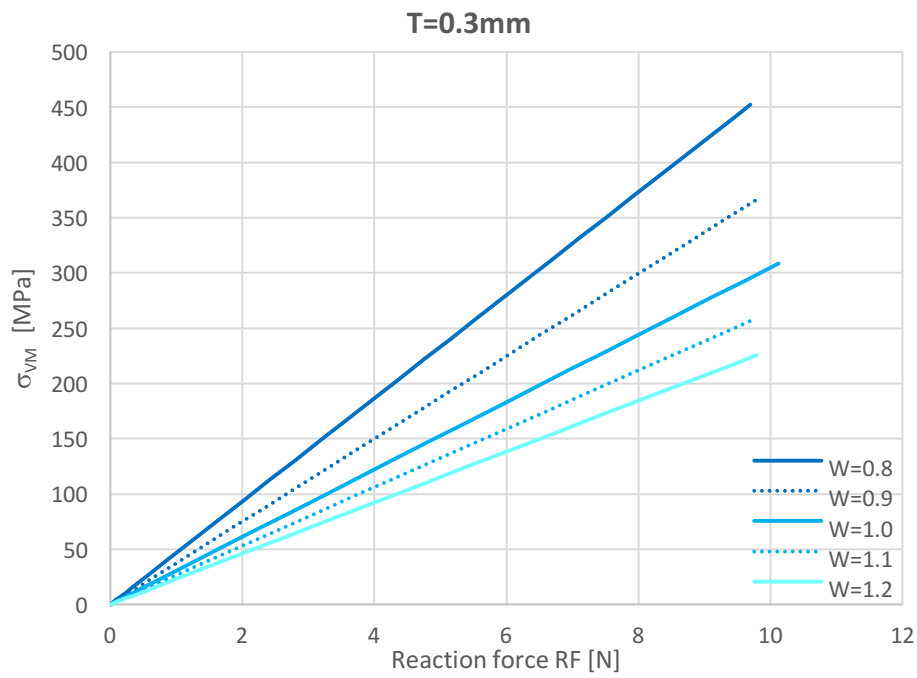


Figure 4.27. M2 Type A models Von Mises fixing thickness to $T= 0.3$ mm and varying W .

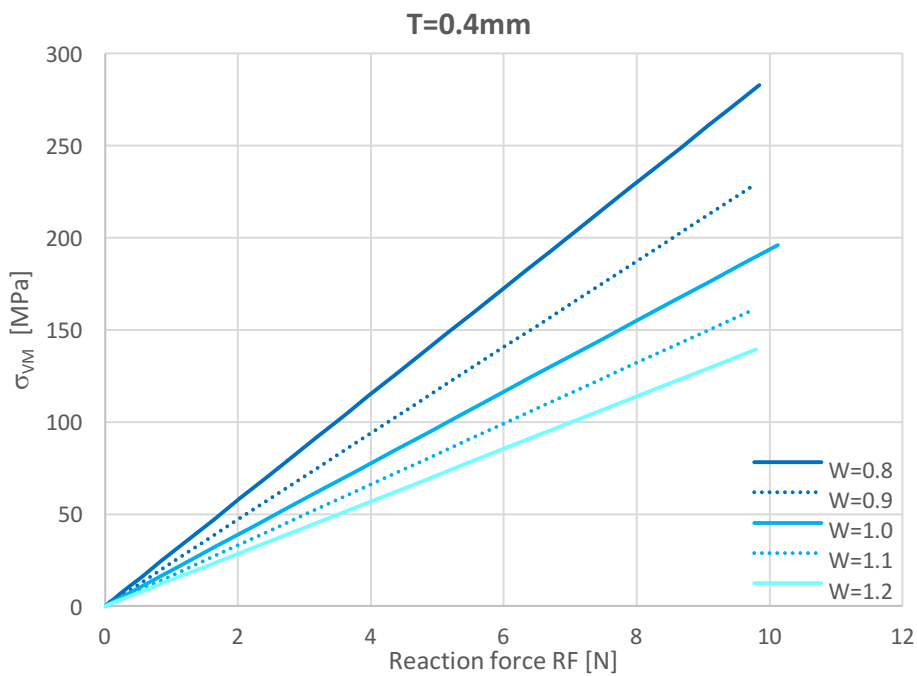


Figure 4.28. M2 Type A models Von Mises fixing thickness to $T= 0.4$ mm and varying W .

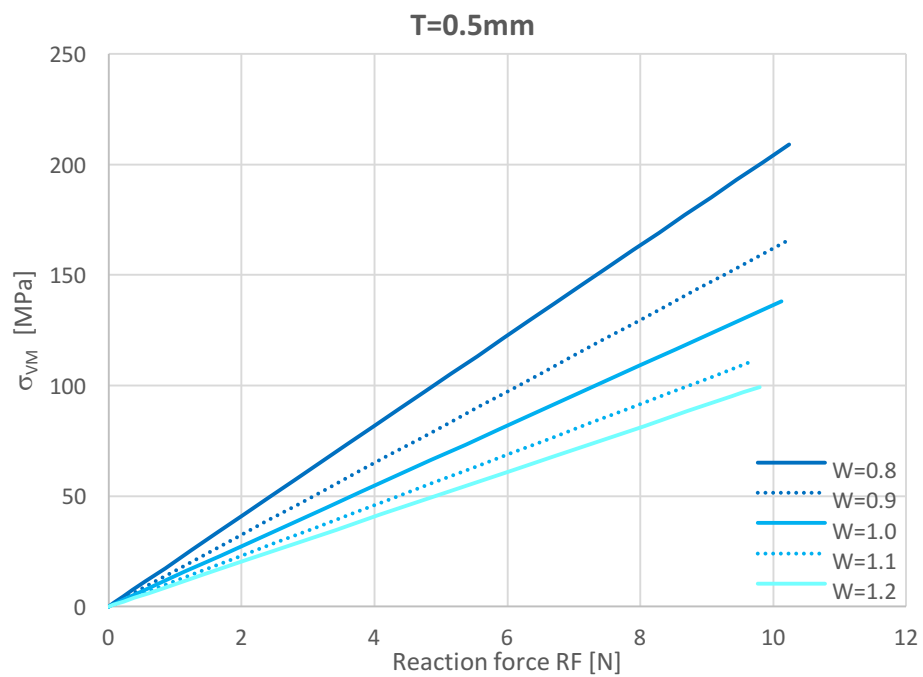


Figure 4.29. M2 Type A models Von Mises fixing thickness to $T=0.5$ mm and varying W .

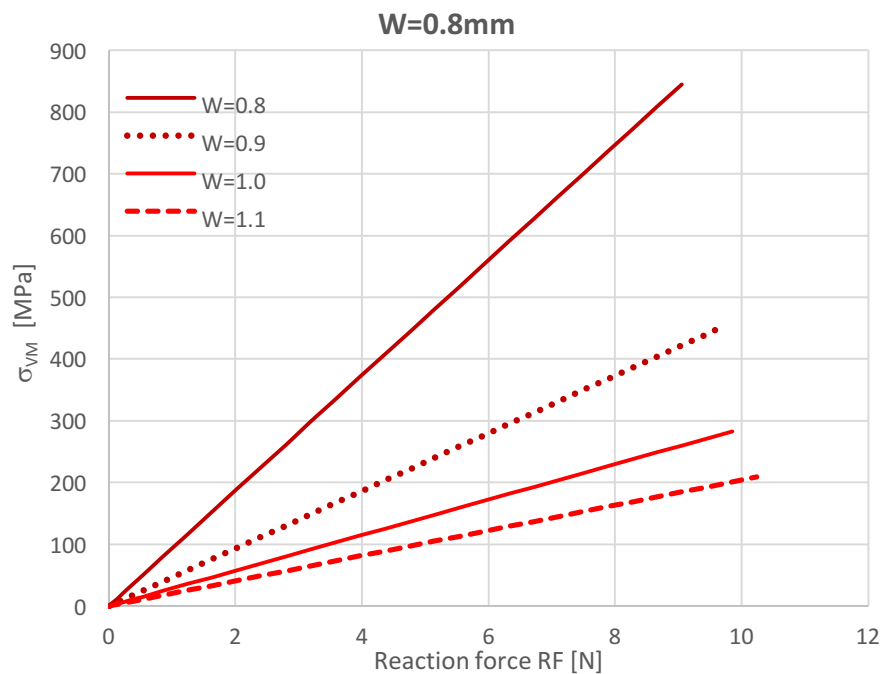


Figure 4.30. M2 Type A models Von Mises fixing width to $W=0.8$ mm and varying T .

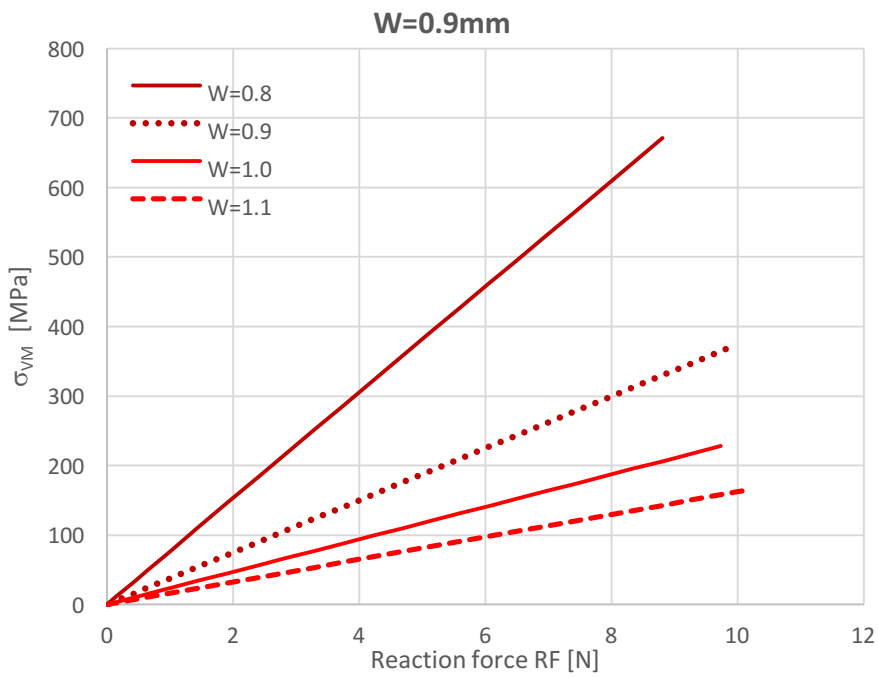


Figure 4.31. M2 Type A models Von Mises fixing width to $W= 0.9$ mm and varying T .

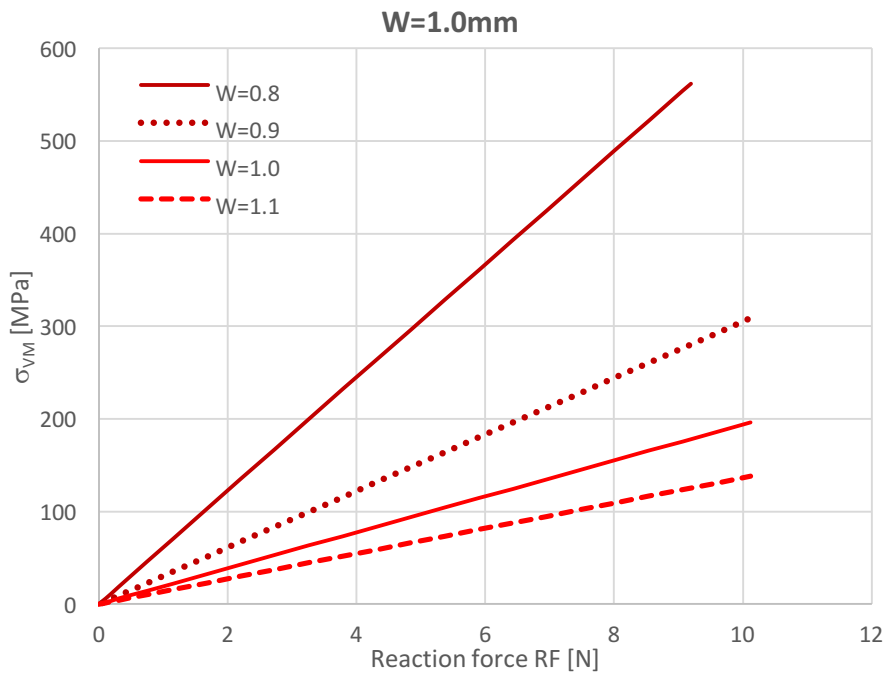


Figure 4.32. M2 Type A models Von Mises fixing width to $W= 1.0$ mm and varying T .

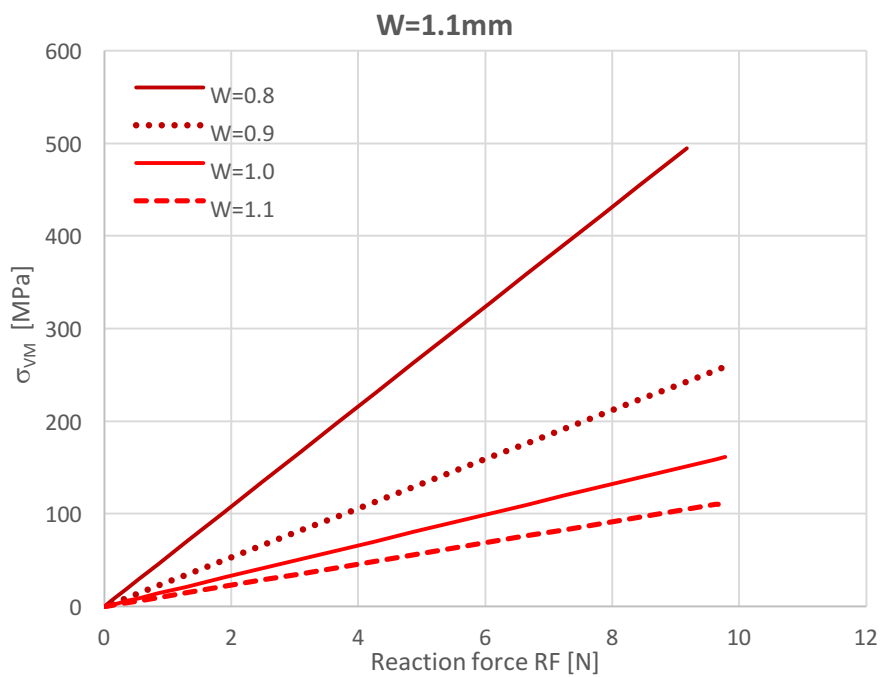


Figure 4.33. M2 Type A models Von Mises fixing width to $W= 1.1$ mm and varying T .

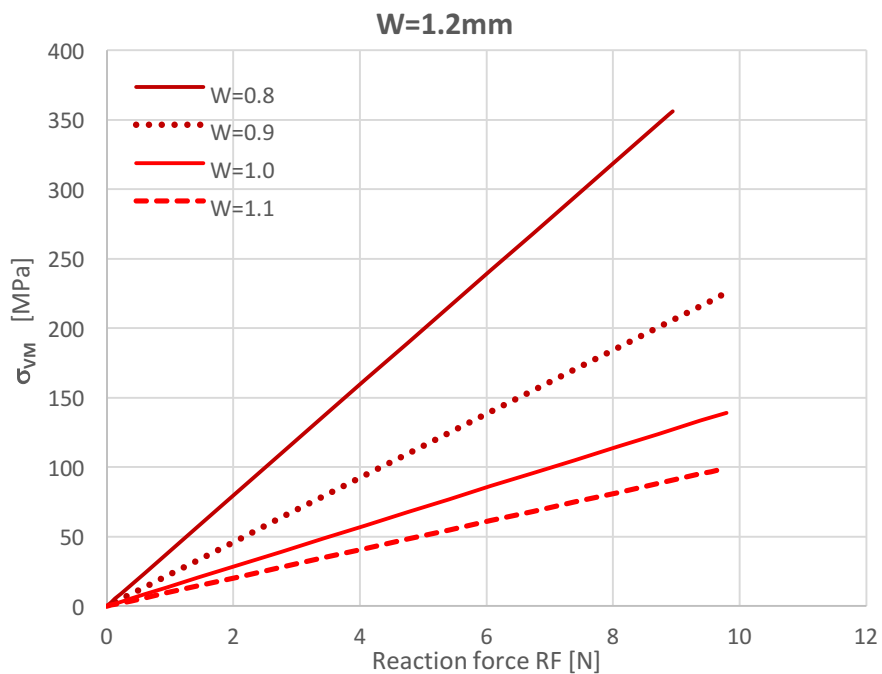


Figure 4.34. M2 Type A models Von Mises fixing width to $W= 1.2$ mm and varying T .

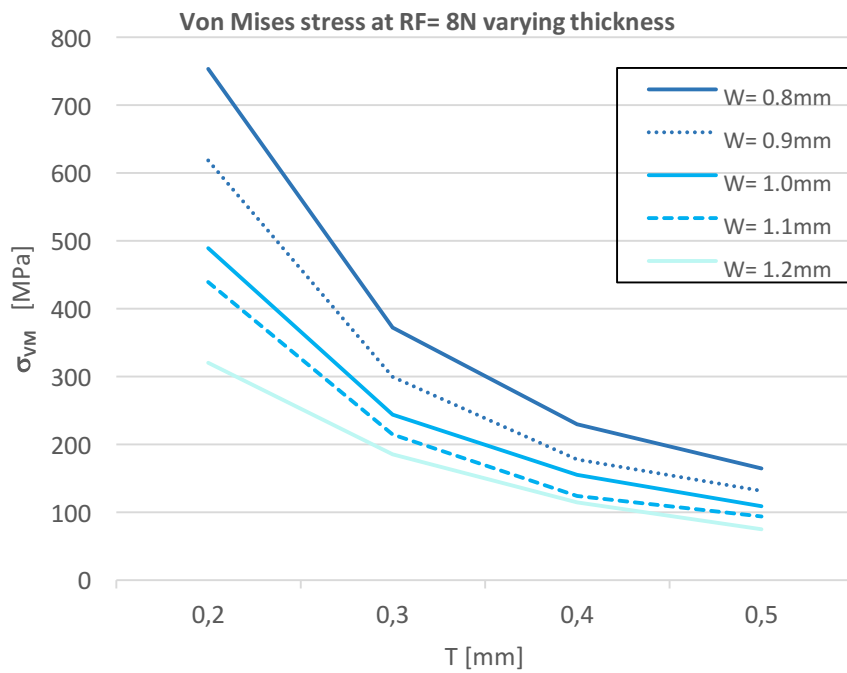


Figure 4.35. trend of Von Mises during a reaction force RF of 8N varying the thickness (T) of the type A rocker.

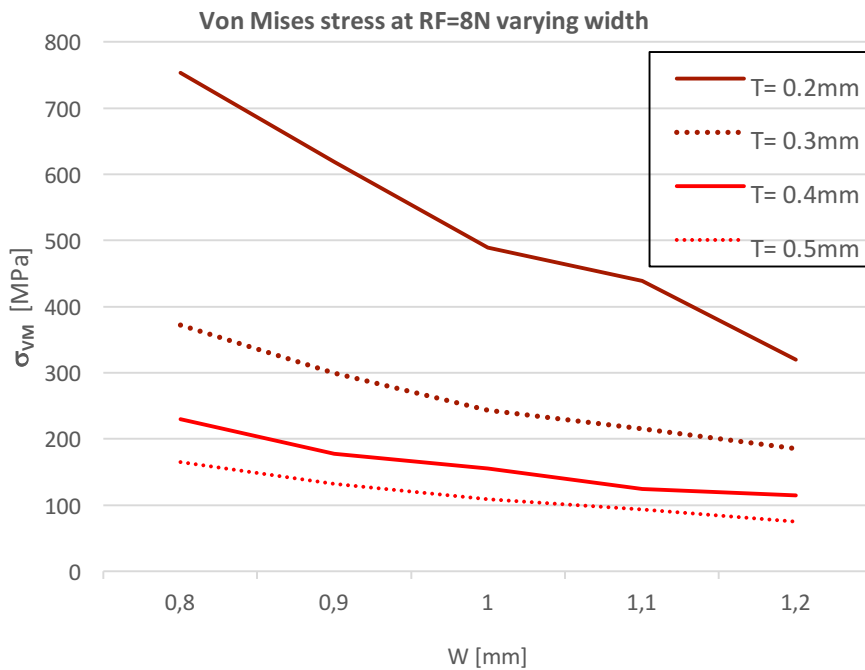


Figure 4.36. trend of Von Mises stresses during a reaction force RF of 8N varying the width (W) of the type A rocker and maintaining 4 different constant values of thickness (T).

4.5 SAFETY OF THE CLIPS

4.5.1 PROOF OF YIELD STRENGTH

To prove the static strength of the clips the Von Mises yield criterion is chosen.

The following relation must be verified:

$$\sigma_{VM} = \frac{1}{\sqrt{2}} \sqrt{(\sigma_1 - \sigma_2)^2 + (\sigma_2 - \sigma_3)^2 + (\sigma_3 - \sigma_1)^2} \leq \sigma_y$$

where σ_y for the Ti-6Al-4V alloy is 880 MPa, as reported in table 4.2.

The higher Von Mises stress obtained in clips structure loaded with a reaction force of 8N is about 753 MPa. Thus, the relation above is verified:

$$\sigma_{VM} = 753 \text{ MPa} \leq 880 \text{ MPa} = \sigma_y$$

and the strength criterion is satisfied.

The factor of safety is:

$$FS = \frac{\sigma_y}{\sigma_{VM}} = 1.17 > 1$$

This suggests that the basic M2 model is safe if loaded with a static 8N force. To improve the safety of the structure an augmentation of geometrical dimension is needed, leading to a subsequent compromise between safety and encumbrance of the clip. Following figures show the factor of safety trend of the structure within a reaction force of 8N and varying thickness and width respectively (figures 4.37 and 4.38).

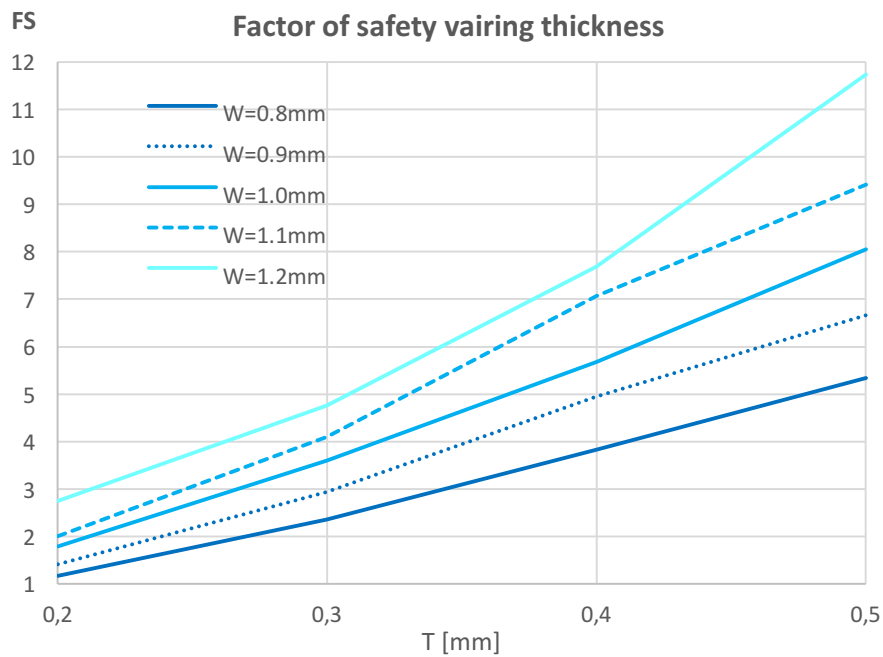


Figure 4.37. trend of factor of safety during 8N of reaction force R_F , varying thickness (T) of the type A rocker.

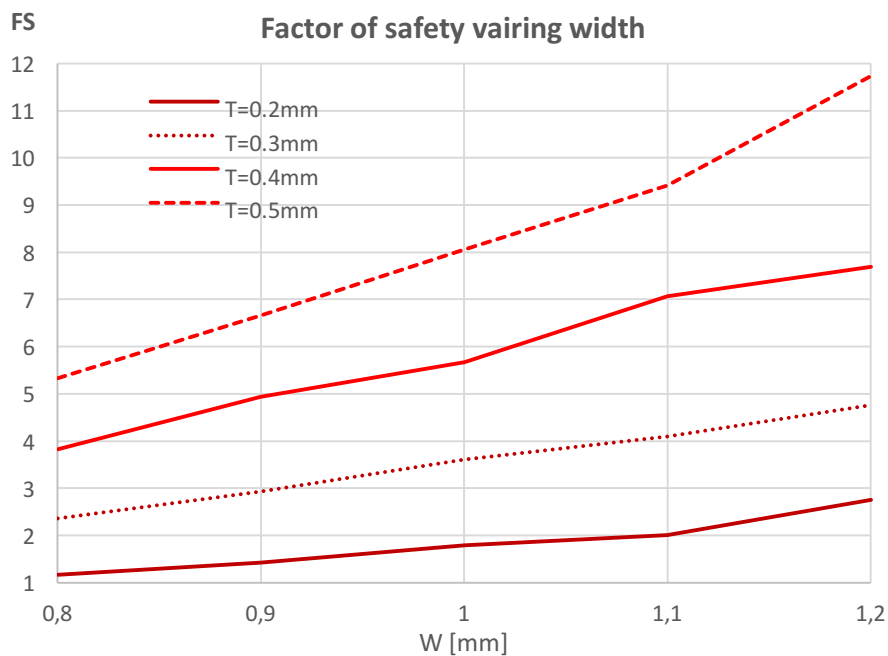


Figure 4.38. trend of factor of safety during 8N of reaction force R_F , varying width (W) of the type A rocker.

4.5.2 FATIGUE STRENGTH

The fatigue life of a clip is evaluated considering the dynamic range of loads acting on stomach wall. This condition is evaluated by means of the Haigh criterion, which lead to representing the fatigue strength into a diagram (Haigh diagram). The diagram is made evaluating the stress amplitude σ_a as function of mean stress σ_m involved to the structure on which a sinusoidal load is considered to act.

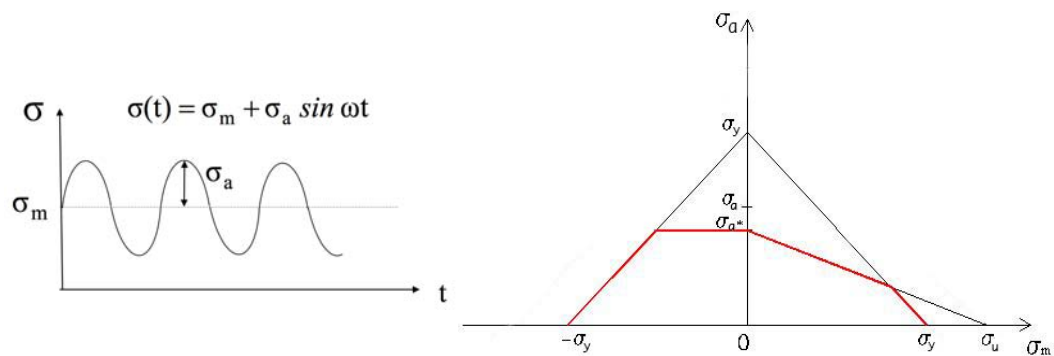


Figure 4.39. sinusoidal load considered and High's diagram.

The mentioned stresses are evaluated as follows:

$$\sigma_a = \frac{\sigma_{max} - \sigma_{min}}{2}$$

$$\sigma_m = \frac{\sigma_{max} + \sigma_{min}}{2}$$

A fundamental quantity is given by the fatigue ratio, defined as

$$R = \frac{\sigma_{min}}{\sigma_{max}}$$

Other parameters involved to the diagram realization are the fatigue limit σ_f , the yield and the ultimate tensile strength σ_y and σ_u of the material involved. The diagram is obtained plotting the equilateral triangle with σ_y on vertices $[(0, -\sigma_y) (0, \sigma_y) (\sigma_y, 0)]$ and the line expressed by the following equation called the Goodman equation:

$$\frac{\sigma_a}{\sigma_{f^*}} + \frac{\sigma_m}{\sigma_u} = 1$$

where σ_{f^*} is the reduced value of the fatigue limit of the material according to the stresses concentration factor due to the material irregularity. This latter consideration is explained by the following relations:

$$\sigma_{f^*} = \sigma_f c_m c_s c_{fin} c_d$$

where $c_m=0.35\div 0.6$ is the material constant; $c_s=1/K_s$, with $K_s=1\div 1.6$, is the constant related to the standard deviations of material data; $c_{fin}<1$ and $c_d<1$ are the surface finishing and dimensional coefficients of the material.

According to the purpose of this work these coefficients are chosen as $c_m=0.5$, $k_s=1.6$, $c_{fin}=1.4$ and $c_d=1$. Resulting Haigh diagram is showed in figure 4.39.

In order to study the fatigue behavior of the structure the load is considered pulsing from $\sigma_{min}=0$ and $\sigma_{max}=\sigma_{VM}$ obtained from static analyses, according to physiologic loads considerations given in the discussion of previous static results. This results in a fatigue ratio $R=0$.

The effective fatigue life of the devices is given in terms of number of cycle to failure N obtained by means of Wohler diagrams. Diagrams showed in figures 4.41 and 4.42 are related to a $\sigma_{max} = 753 \text{ MPa}$ and $\sigma_{max} = 75 \text{ MPa}$, which are the worst and better conditions respectively. The safety of the devices about the fatigue regime may be considered evaluating the trend of number of failure as a function of geometrical parameters of the clips (figures 4.43 and 4.44).

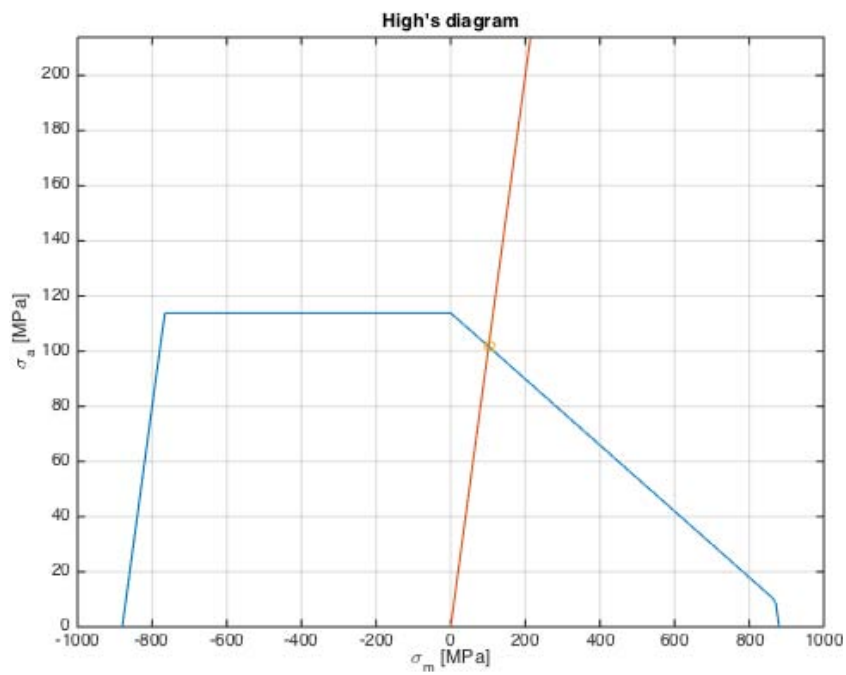


Figure 4.40. High diagram related to the material and functioning line according to the fatigue ratio.

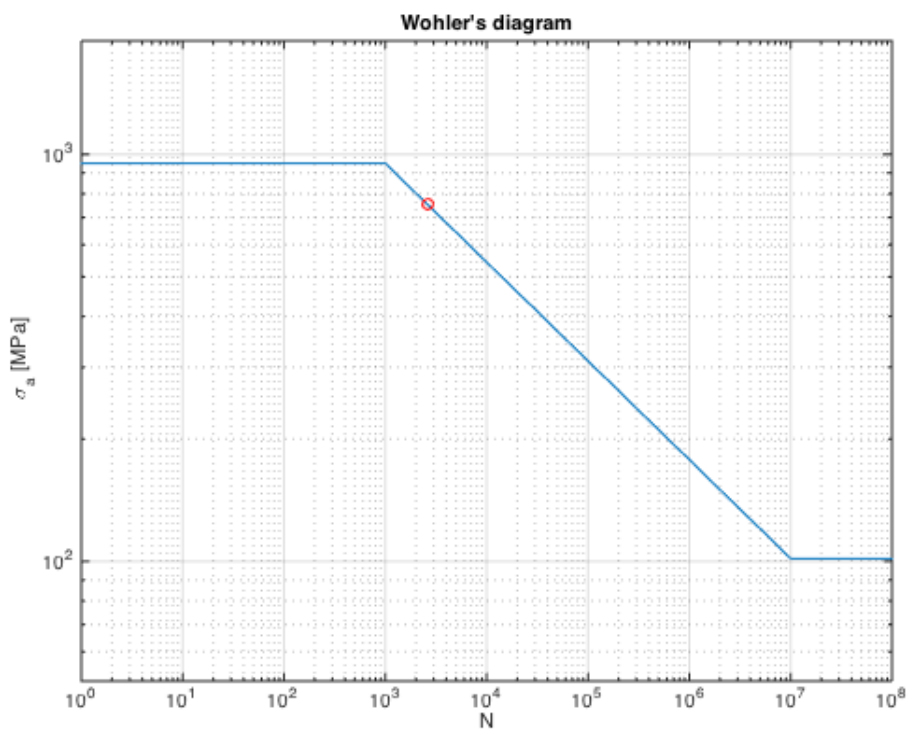


Figure 4.41. Wohler diagram of the material with $R=0$ related to $\sigma_{\max} = 753$ MPa (red).

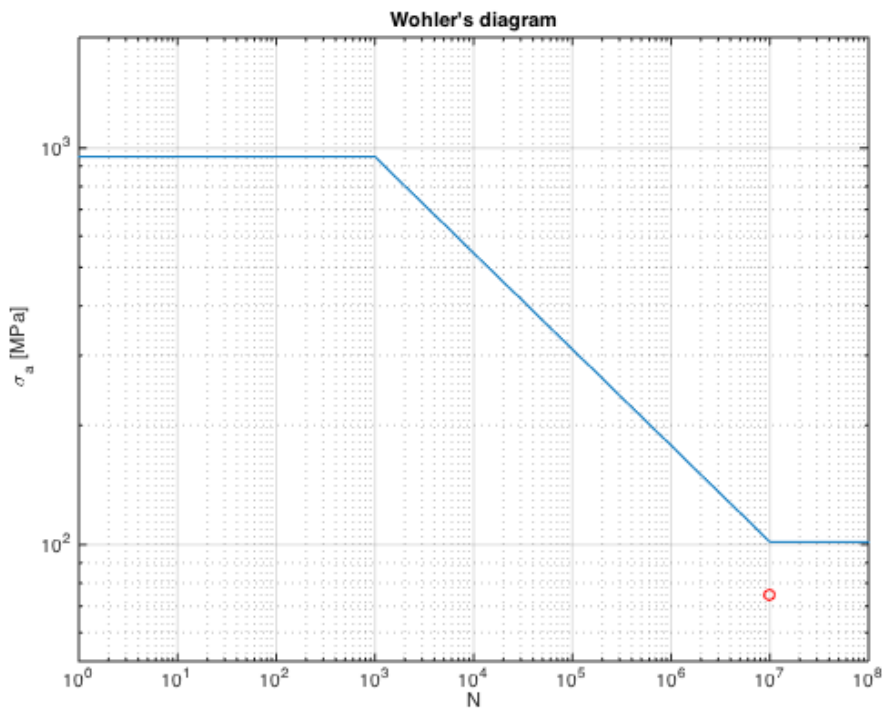


Figure 4.42. Wohler diagram of the material with $R=0$ related to $\sigma_{\max} = 75$ MPa (red) showing an infinite life of the structure.

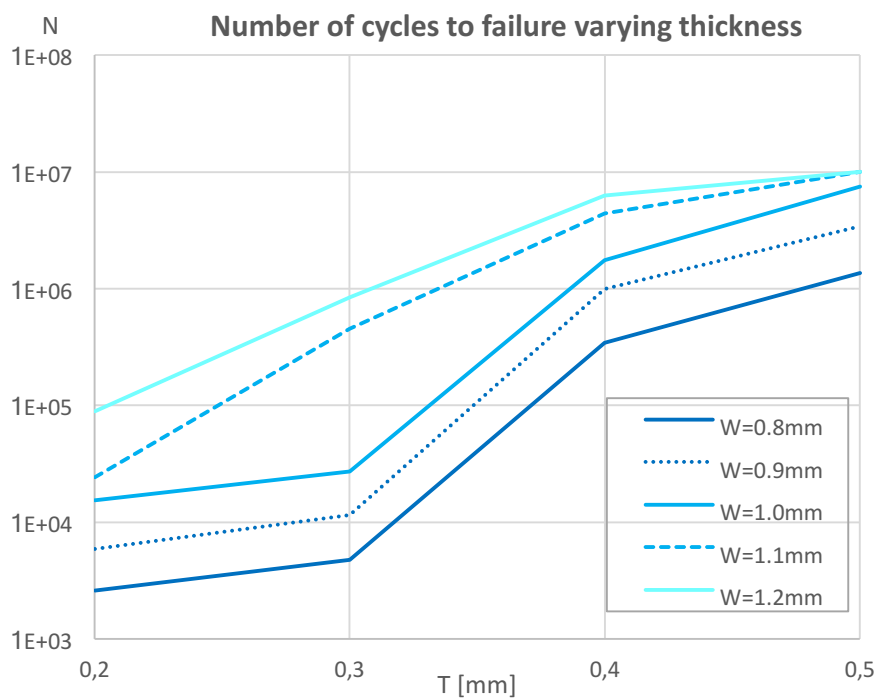


Figure 4.43. Trend of number of cycle to failure during 8N of reaction force RF, varying thickness (T) of the type A rocker.

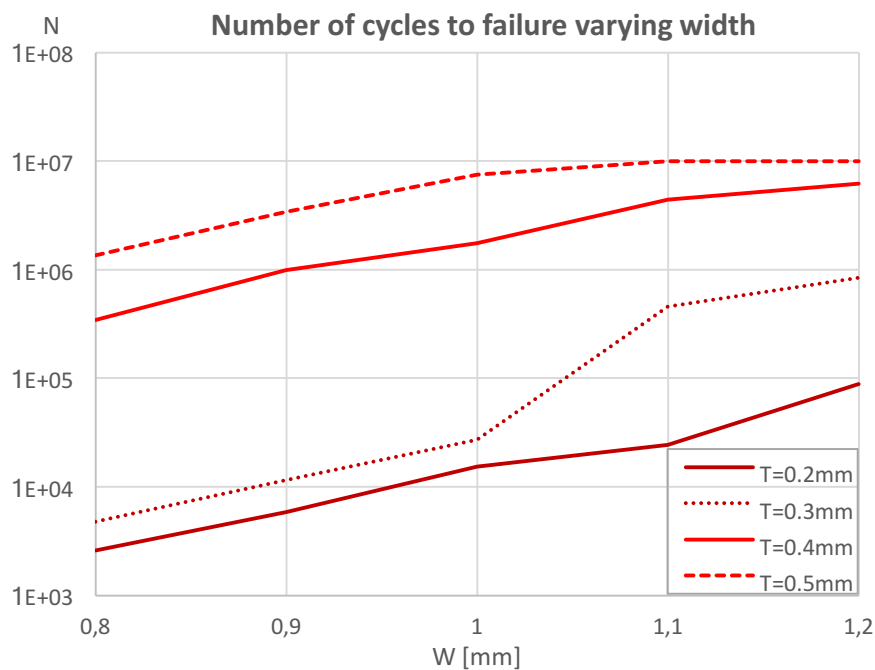


Figure 4.44. Trend of number of cycle to failure during 8N of reaction force R_F , varying width (W) of the type A rocker.

4.6 DISCUSSION

Previous numerical results on static loading (figures from 4.26 to 4.34) show the evidence that an overall augmentation of model dimensions lead to a significant reduction in terms of stress perceived. The curves in figure 4.35 show that Von Mises Stresses, as function of the rocker thickness, have an exponential trend approximatively. On the other hand, varying only the rocker width of the clip results in a quasi-linear trend (figure 4.36). Stress curves in both these final graphs are evaluated with a reaction force of 8N, that correspond to an internal stomach pressure of 7 KPa, 10KPa or 15 KPa with 8, 10 or 12 number of clips applied respectively to fix the implant [Gioela Pluchino]. As mentioned in chapter 1, pressure forces during the digestive phase are below 3.5 KPa even if during peristaltic contractions phase peaks up to 35-40 KPa occur in the pyloric antrum. Is important to notice that peaks of pressure are not a static condition and most of their energy is dissipated during the distension process of the stomach.

Therefore, an 8N reaction force to the stem may be considered a correct estimation of functioning loads involved to the clip structure.

Previous safety results lead to generally affirm that the novel structure proposed is safe, even if some further consideration must be done. In fact, from a static regime point of view the structure is considered safe due to the factor of safety higher than one during all the geometrical configurations of the models. However, from a dynamic regime of loads, the safety of the device is not obvious. Fatigue simulations show that, varying both the geometrical variables, the structure has huge differences in life estimation. Starting from 753MPa of load amplitude, the fatigue limit is observed at 2605 cycles. On the other hand, while geometrical parameters values raise close to the upper limits, an infinite fatigue life of the structure is observed. According to the curves slope trends in figures 4.43 and 4.44, the fatigue behavior depends more from the thickness parameter rather than width, in accordance with Von Mises stresses and static factor of safety trends, observed within the previous analyses.

CHAPTER 5

EXPERIMENTAL SET UP FOR THE ANALYSIS OF THE FUNCTIONALITY OF ARTIFICIAL URINARY SPHINCTERS

In general, looking at the action of natural urethral sphincter, a discrepancy can be found in comparison with the one induced by the different artificial sphincter cuffs. This aspect must be harvested in such investigations where mechanics is associated with surgery and material science. Attention is needed to the surgical practice, the specific conformation of the cuff and the characteristics of the cuff materials. The analysis must be performed considering the occlusive action of the cuff in composition with the pressure induced by bladder filling. Urethral pressure profile data can represent a valid reference term for functional evaluation. This entails a very difficult procedure but activity is already in progress both in experimental and numerical area. The result validation presents several difficulties for such a complex process of interaction between the artificial sphincter and the urethral duct. The computational biomechanics approach offers the possibility to investigate the problem by variation of basic parameters that influences the problem, leading to several set of results that can be evaluated by a sensitivity procedure. This action can be performed with reference to displacements, strain and stress field with an accurate and detailed data estimated at different points within urethral duct. The relevant potentiality of the numerical approach does not hide the fundamental relevance of mechanical testing. A new experimental setup is presented in this chapter, aiming to interpret the overall duct response during different inflation tests and under the action of different cuffs, leading to a direct

correlation with numerical results and to offer a valid contribute to a more complete reliability evaluation of numerical models.

5.1 EXPERIMENTAL TEST DESIGN

This work aim to obtain specific urethral pressure profile during inflation tests as a function of occluding pressure by means of a device that practically simulate the occlusion by the cuff of an artificial sphincter. Hence, during the inflation test the measure of three different quantities is required: the inflow and the outflow water pressure to obtain the pressure gap Δp of the urethra and the occluding pressure by the cuff designed.

In order to have a stable experimental workstation for urethral inflation tests, an experimental test bench is required (figure 5.1).

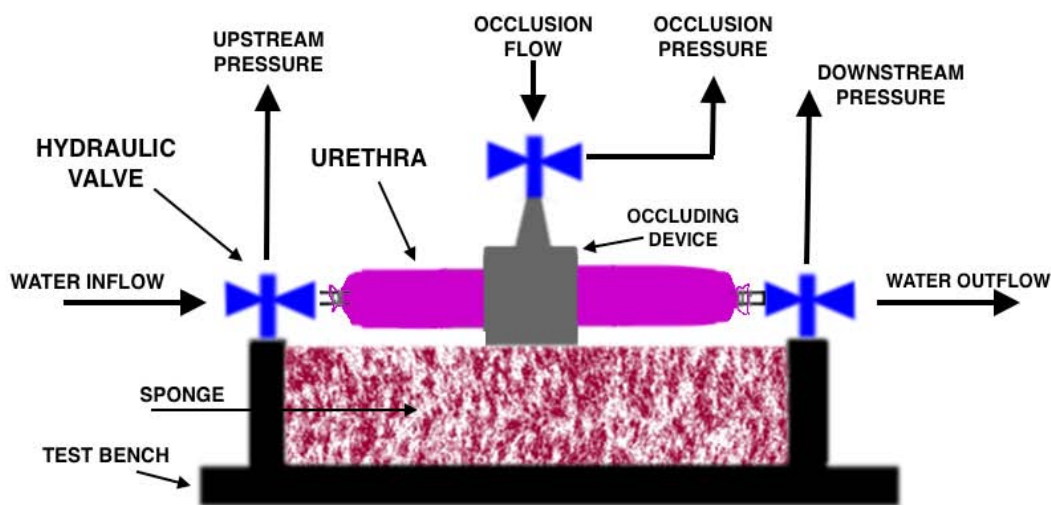


Figure 5.1. Overall scheme of the test bench setup for the investigation of urethral pressure profile as function of occlusion pressure.

The bench must be integrated with two hydraulic valve, one placed upstream and the other placed downstream, which allow to fix the two urethral extremities with an inflow and outflow hydraulic tubes. The upstream tube came from the peristaltic pump involved in the inflation tests and the downstream tube go to a reservoir that receive the water pumped. The two valves allow also to connect a

third tube by which is possible to measure the related pressure value of the water flow by means of suitable instrument.

A sponge is placed on the bench in order to regulate the thickness between the bench surface and the cuff of the artificial urinary sphincter (figure 5.1).

5.1 EXPERIMENTAL TEST BENCH

Figures from 5.2 to 5.4 show the test bench made for this purpose.

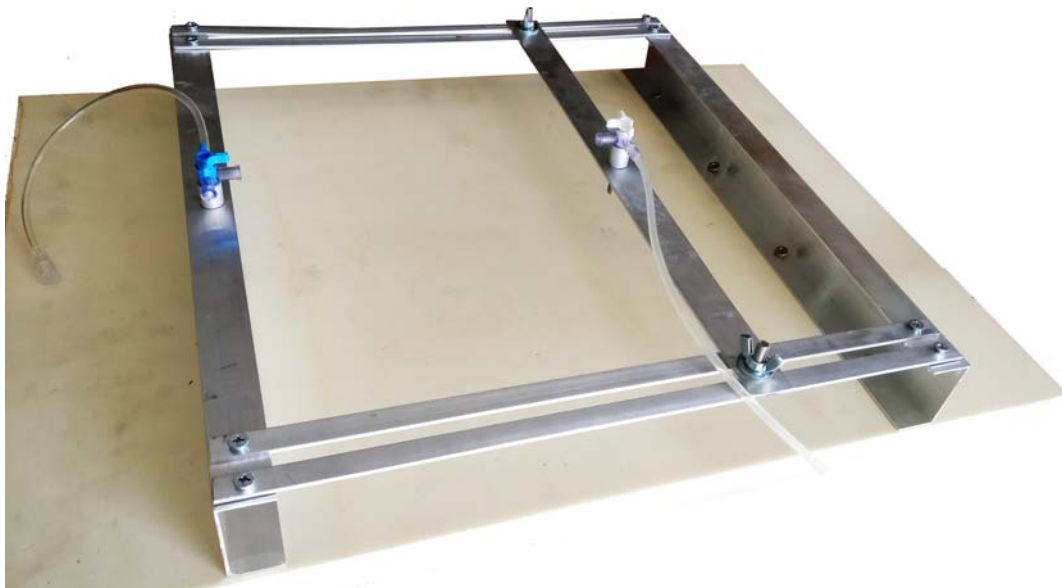


Figure 5.2. Lateral view of the designed test bench. The here reported one is without the sponge needed to improve the bench thickness in order to maintain the urethra supported on the same level of the valves.

On a wooden plate is fixed an aluminum frame composed by two fixed C-shaped bar on which are screwed two aluminum guides, from one bar to another. One hydraulic T-shape valve is fixed on one C-shaped bar. The other one is fixed to a plate bar which can slide towards the other valve in order to reduce the distance between the two valves. In fact, this bench is designed to be suitable for different specimens which may come from different animal species. Human urethrae may also have remarkable length difference (chapter 1). Once the desiderate length between the two valves is chosen, the mobile plate bar may be fixed to the guide by means of a wingnut positioned on both its extremities (figure 5.5).

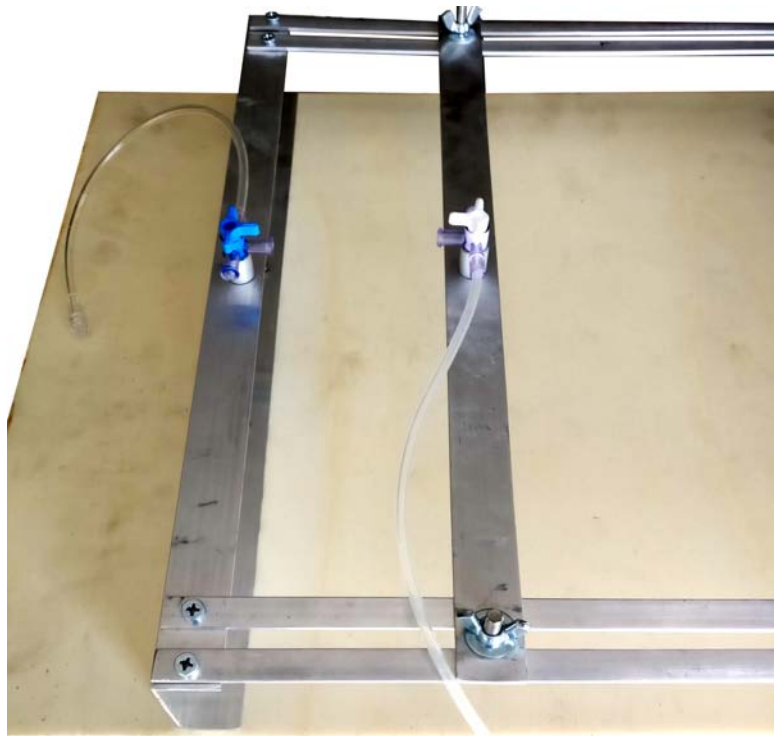


Figure 5.3. Lateral view of the test bench. The plate bar may slide on the guide to bring the mobile valve near the fixed one.

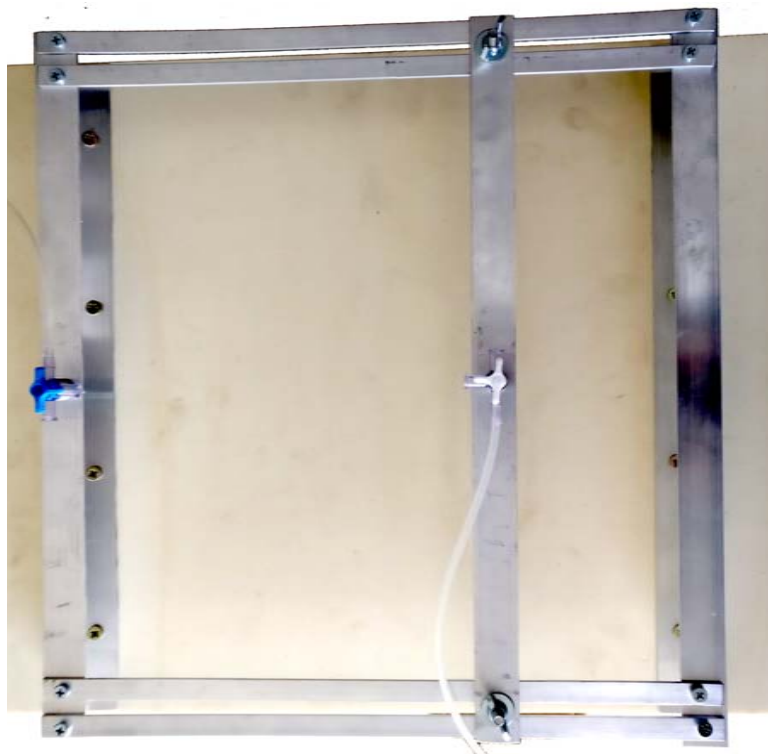


Figure 5.4. view of the bench from above.



Figure 5.5. The mobile bar of the bench may be fixed on the guides by means of a wingnut.

5.2 URETHRAL OCCLUSION DEVICE

A prototype of the cuff of an artificial urinary sphincter is made in order to restrict the urethral duct during a specific water flow imposed (figure 5.7). An overall scheme of the cuff realization is shown in figure 5.6. The device is made with an aluminum cylinder with a hydraulic connector passing through its wall. An elastomeric sleeve passing through the cylinder hole is folded at its extremities and fixed to the cylinder by means of elastic threads. Therefore, the inside sleeve and the cylinder form an inside chamber which may be inflated through the lateral connector. Its inflation pressure may occlude the duct of a urethra placed inside the device, as the cuff of common artificial urinary sphincters. In this way, it is possible to place another hydraulic valve directly before the device connector allowing both the inflation of the chamber and the occlusion pressure measure. This will lead to measure the pressure signals involved during the occlusion of the

urethral duct by the device designed while the urethra is inflated with an imposed water flow.

Devices of different sizes were made (15mm and 20mm of diameter and 30mm in length), according to different diameter of urethral specimens.

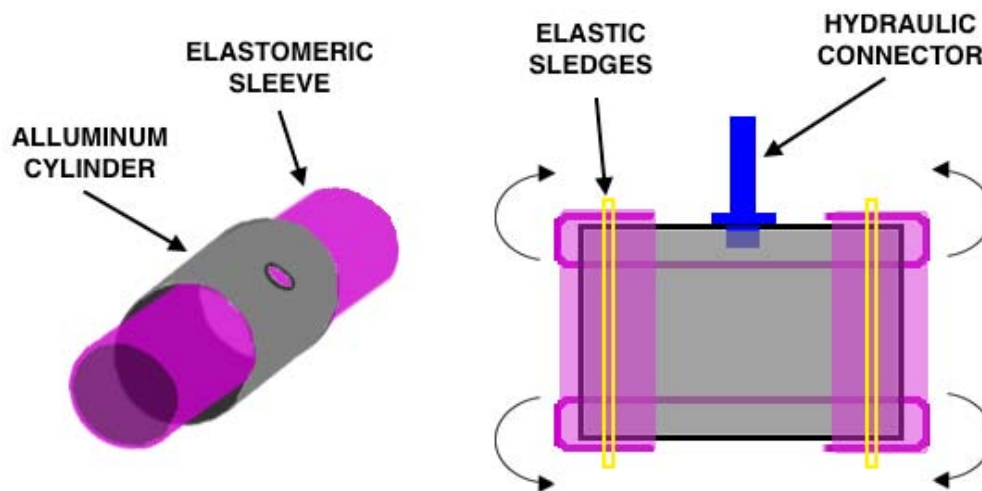


Figure 5.6. Scheme the occlusion cuff realization. The elastomeric sleeve is inserted into the cylinder (left); a suitable plastic hydraulic connector is placed to the cylinder wall through a hole drilled on the cylinder surface; sleeve extremities were fold on the external surface of the cylinder and fixed with suitable elastic sledge to form an internal chamber (right).



Figure 5.7. Artificial sphincter cuff prototypes.

5.3 DATA ACQUISITION SYSTEM

5.3.1 ARDUINO BASED SENSOR-INSTRUMENTATION

The experimental laboratory was already been equipped with an acquisition instrumentation self-made based on a microcontroller (Arduino MEGA 2560, Arduino LLC) interfaced with the PC. Such board was connected with two analog pressure sensors (142pc01d and 142pc05d Honeywell, USA) with a maximum range of measure of 1 psi and 5 psi respectively. Data acquisition rate was set to a 4 Hz sampling frequency.

ARDUINO MEGA is equipped with an 8-bit ATMEL mega2560 processor featured by 16 MHz internal clock and input analog ports connected with 8-bit DAC converter.

In order to improve instrumentation performance for further advanced applications, such as the precision and the accuracy of the measure, the possibility to improve data acquisition rate and relative calculation rate by the CPU, a novel acquisition system is designed based on an advanced microcontroller (Arduino M0 PRO, Arduino LLC) (figure 5.6). This latter is equipped by a 32-bit evolution of the previous CPU, with an internal clock of 48 MHz and 6 port directly connected with a 12-bit DAC converter according to improve the mentioned performance of the instrument. The board is connected with a breadboard (figure 5.6), which is supplied by a 5V of DC current line directly from the Arduino M0 PRO board, according to supplying the pressure sensor needed for the application. As mentioned in the experimental test design section of this chapter, inflation test data collection requires at least three pressure sensors. The novel acquisition system designed in this work is equipped with four different sensors. The first two sensors are a 1psi sensors (ABPDJTT001PGAA5, Honeywell, USA), the third is a 2psi sensor (ABPDANT160MGAA5, Honeywell, USA) while the third is a 5psi sensor (ABPDJTT005PGAA5, Honeywell, USA). Technical functioning data, packaging and pinouts of the sensors are reported in appendix A.3. Honeywell's sensors chosen are capable to functioning in both digital and analog mode (appendix A.3) and

analog functioning mode is chosen for this application. Thus, pins 3 of each sensor is connected to analog ports of Arduino M0 PRO board (A0÷A4) (figure 5.6). Default analog input full scale of the board is set to 3.3V. Therefore, AREF pin must be set to 5V, according to the complete range of the analog output of the sensors (appendix 5.3).

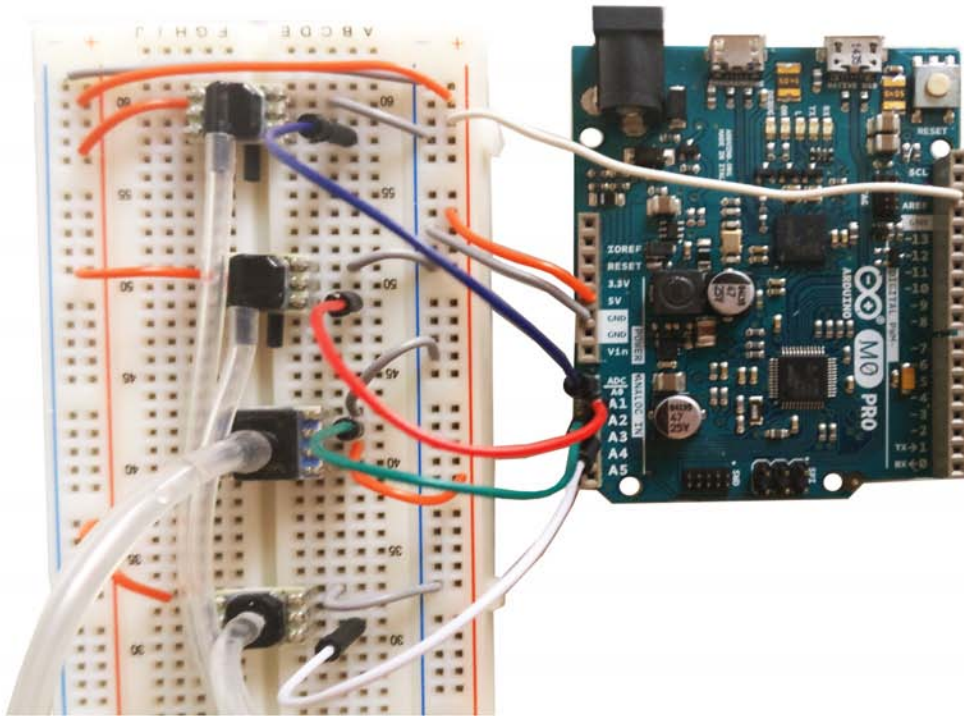


Figure 5.7. Arduino M0 PRO board set up and breadboard connections.

The board is supplied by the PC through a micro-USB cable through which pass the data. The device will be involved in water-based inflation tests where some experimental trouble may induce irreversible damages to the electronic circuit of the board. Hence, an almost waterproof plastic case is suitable to cover the board preventing any electric risk (figures 5.8 and 5.9). The frontal panel of the case is drilled and four holes are made allowing to connect the external environment with the pressure sensors by means of four rubber tubes. The upper surface of the case may be opened due to a cylindrical hinge placed on its side (figure 5.8). When it is closed, a little magnet led the case to remain closed despite some impact, in order to avoid electric risk.

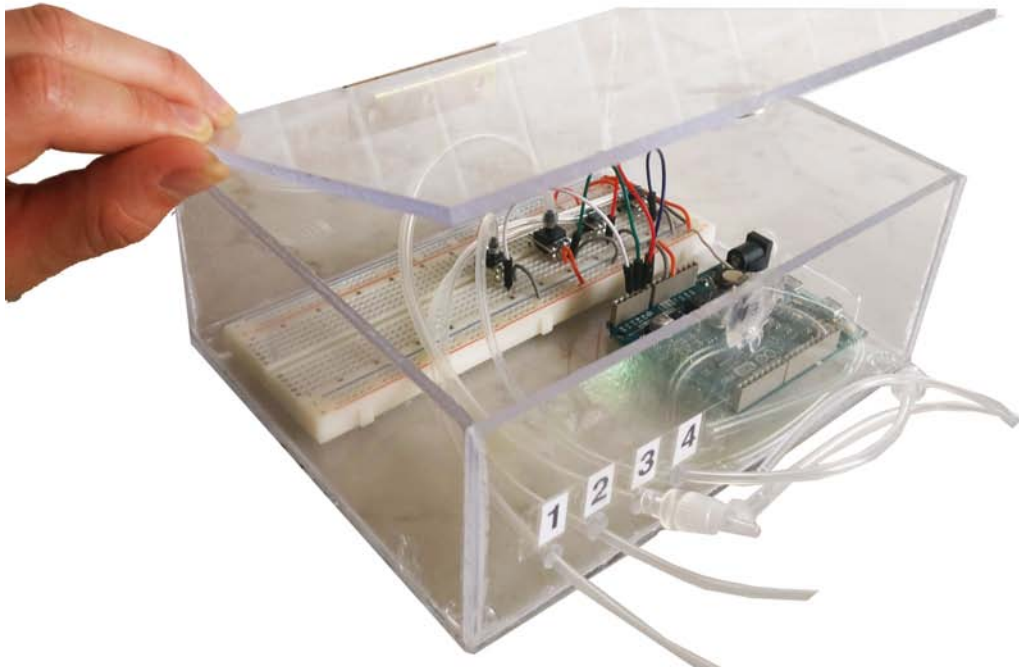


Figure 5.8. Perspective view of the data acquisition hardware designed.

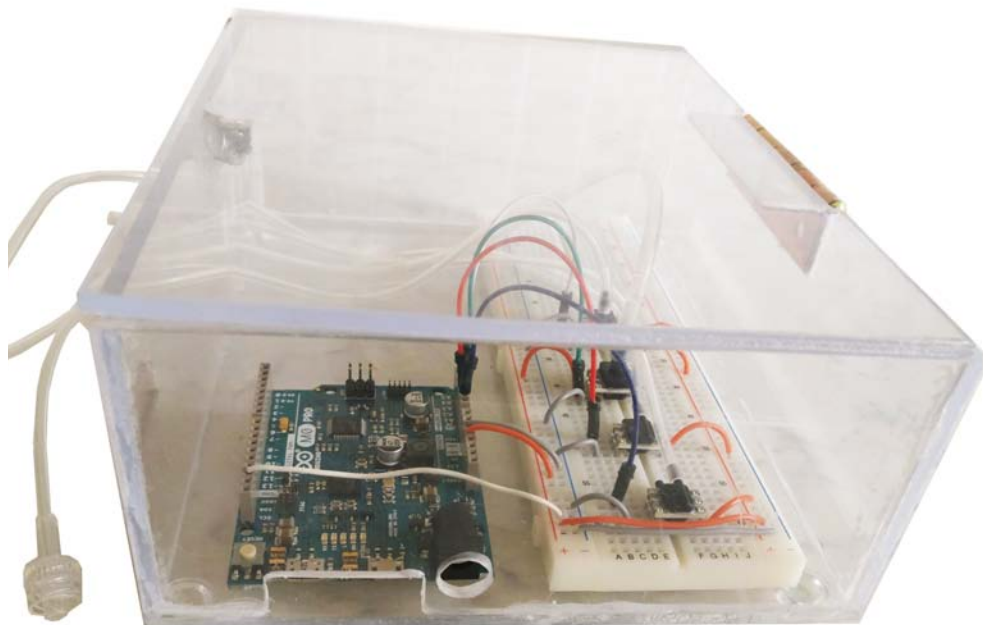


Figure 5.7. lateral view of the data acquisition hardware designed. Lateral surface is drilled allowing supply and USB connections of the board.

5.3.2 ARDUINOUI: LABVIEW-BASED USER INTERFACE

Pressure data acquired with Arduino board are sent to the PC by means of serial communication with a standard baud rate of 9600 bps and correspond to the digital code of the analogic value measured at the analog ports of the Arduino board (appendix 5.4 reports the Arduino software loaded on the board). All digital pressure codes are concatenated together with time value of the sample, forming a four-token string sent through the serial communication. The software involved to import in real time experimental data into the PC is LabVIEW-based (LabVIEW 2013, National Instruments) (appendix 5.5). Data are imported in LabVIEW runtime engine through serial communication and showed to a user interface called ArduinoUI as pressure-time signals. Digital data are converted in analog pressure signals by the software which create vectors of analogic values converted by means of an opportune matrix of calibration (appendix 5.5). ArduinoUI consists of three main panels (figure 5.10).

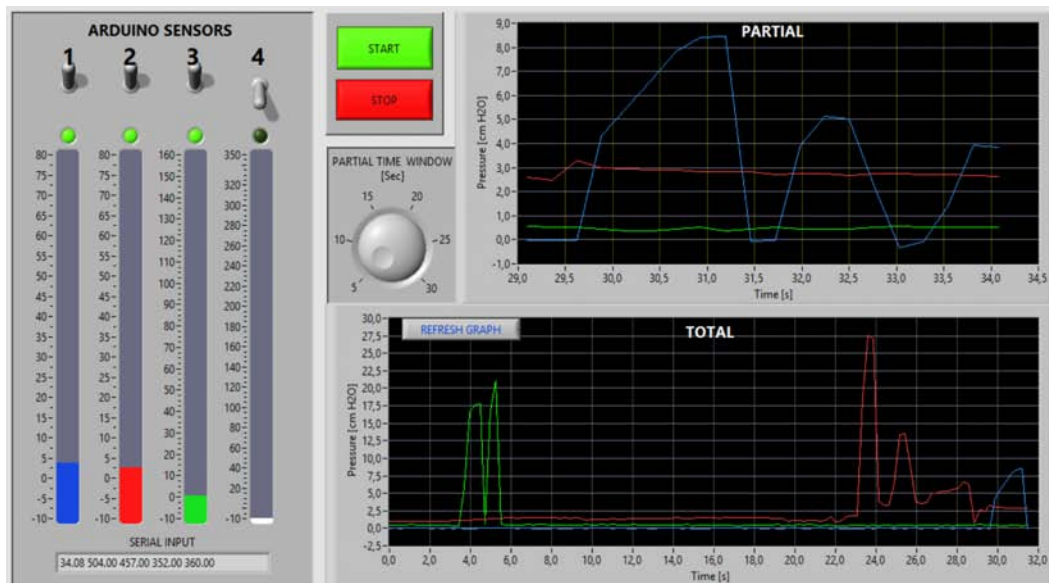


Figure 5.10. Total view of ArduinoUI. The interface is displaying pressure signals related to the first three sensors.

On the left of the interface is placed the sensor *control panel* (figure 5.11) which consists of an upper region formed by the sensor switches, a middle region formed by the indicators of the pressure measured on the relative sensor and a lower region which display the digital value obtained from the serial communication. Four led lights are related to each switch and turn on when the relative sensor is activated.

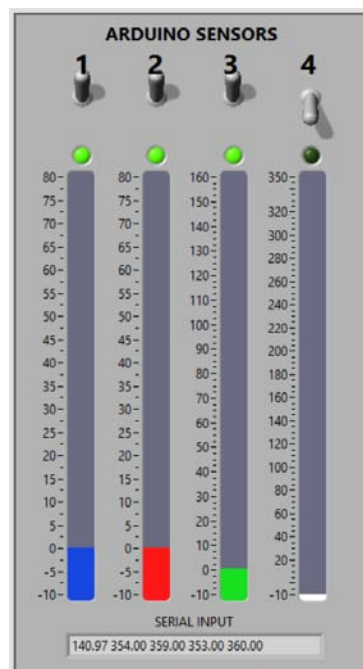


Figure 5.11. sensor control panel

The upper panel on the right side of the user interface consist of a two start and stop buttons, a graph called the *partial graph* and a control potentiometer called the partial time window controller (figure 5.12). Start and stop button control the begin and the end of the data acquisition process. The *partial graph* show all the pressure signals related to the switch activated at the *control panel*. The graph is called *partial* due to its restricted time window which width value is selected by the related potentiometer and range from 5 to 30 seconds. The lower panel placed on the right side of ArduinoUI consists of a larger graph, called the *total graph*. The *total graph* show all the history of the signals acquired until the zero time. The

graph is automatically update every 15 seconds but it could be manually updated in every time is needed by means of a button called *refresh graph* (figure 5.13).

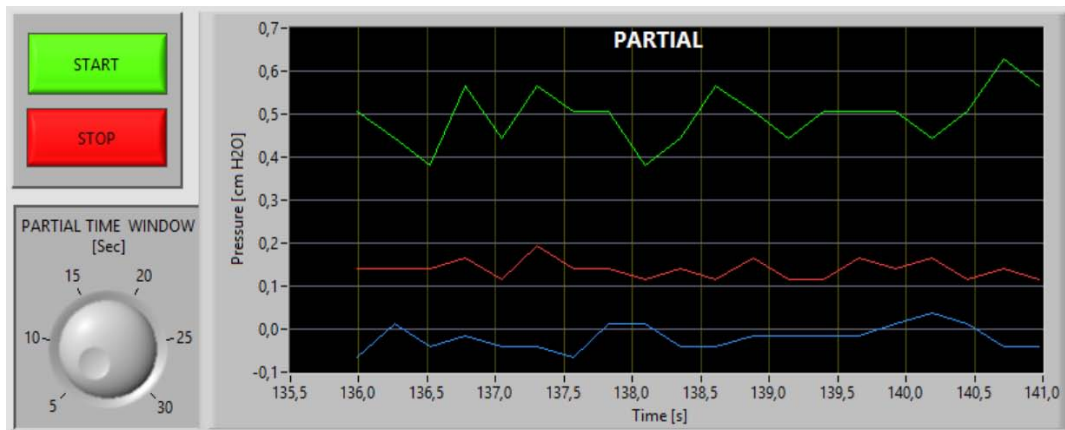


Figure 5.12. ArduinoUI partial panel and the start and stop button.

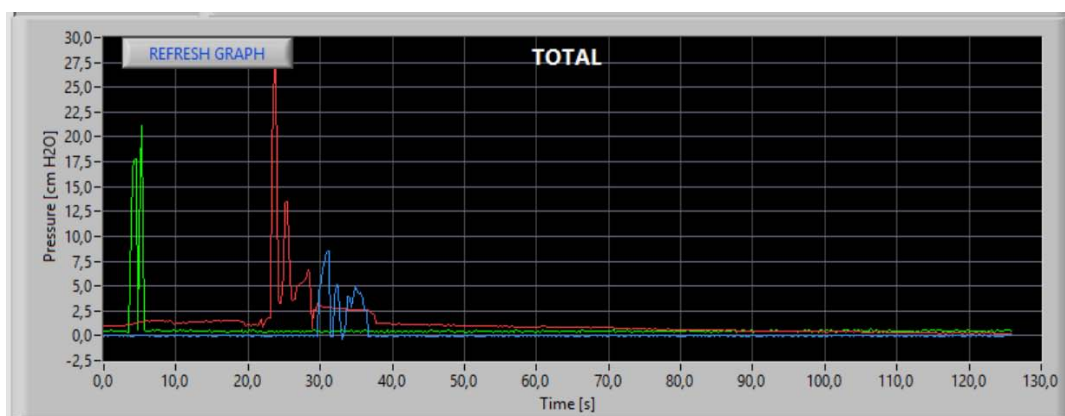


Figure 5.13. Total time graph of ArduinoUI displays all the signal history until zero time.

When the start button is activated the software control if any sensor is activated. If no switch is turned on ArduinoUI displays an error message which invite the user to activate at least one sensor. When, after the acquisition process the stop button is activated a message is displayed to the user (figure 5.14), which invites to a choice: SAVE (save data acquired into a text file), CALIBRATION (set the calibration matrix with new values related to the last acquisition) or EXIT (end the acquisition and discard last data acquired). During the data acquisition the software save data

automatically into a text file called *autosave*. This file is automatically placed into the ArduinoUI folder and file are auto-saved every 15 seconds.

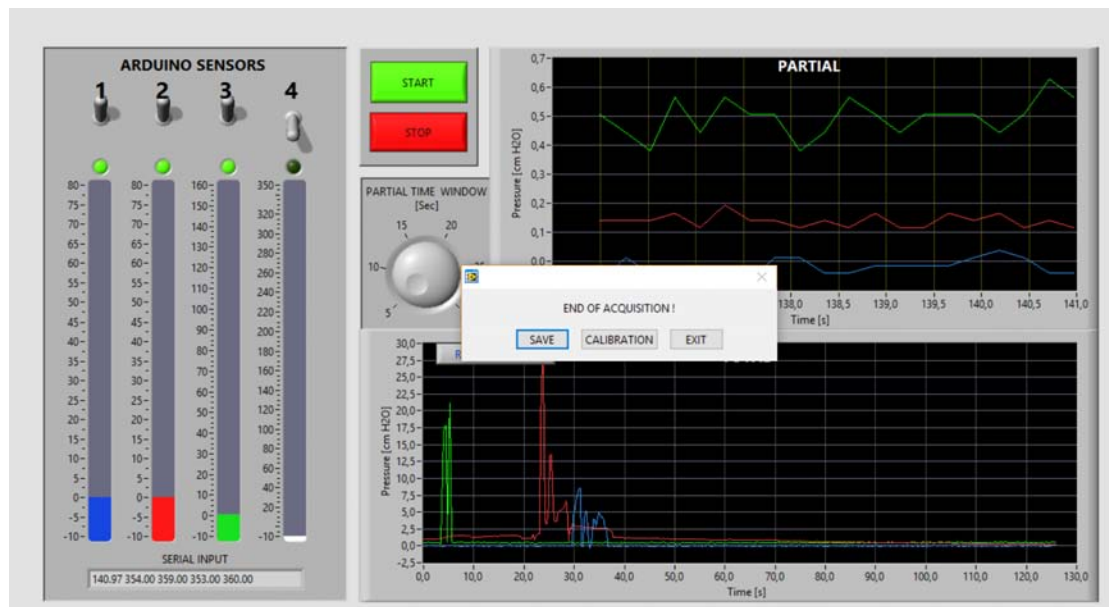


Figure 5.14. Message displayed after a data acquisition after the stop button is activated.

5.4 SET UP AND CALIBRATION

All the experimental setup required for the inflation tests is shown in figure 5.15. The green pump (VerderFlex Vantage 5000, Verder Ltd, UK) is a peristaltic pump which picks up the water from a reservoir and sends it to the test bench through a suitable rubber tube. With a LCD touch screen it is possible to set the water flow within a desirable value. The Arduino-based hardware is connected to the test bench by means of rubber tubes (figures 5.16). Figure 5.17 shows the setup testing with a rubber tube simulating the urethral duct and passing through the occlusion cuff designed. The hydraulic connector of the cuff leads to a T-shaped valve, which is connected to the acquisition system to measure the pressure signal and to a syringe, filled with water, involved to inflate the occluding cuff.

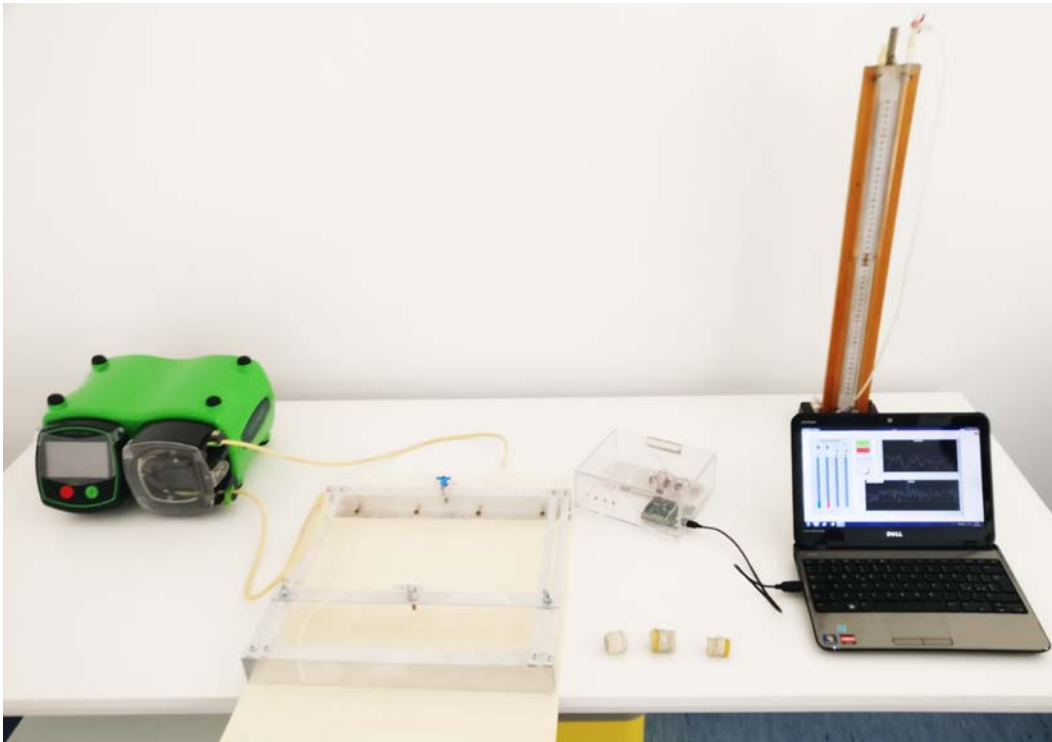


Figure 5.15. Experimental setup for the inflation tests.

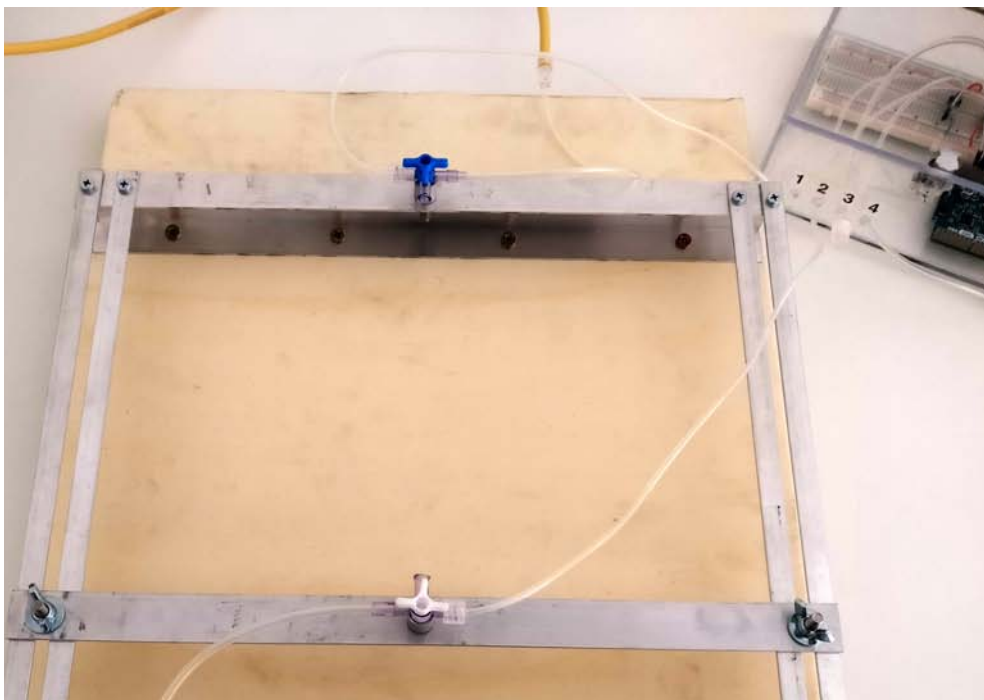


Figure 5.16. Sensing the test bench. Pressure sensors are connected to the valves on the test bench with rubber tubes.

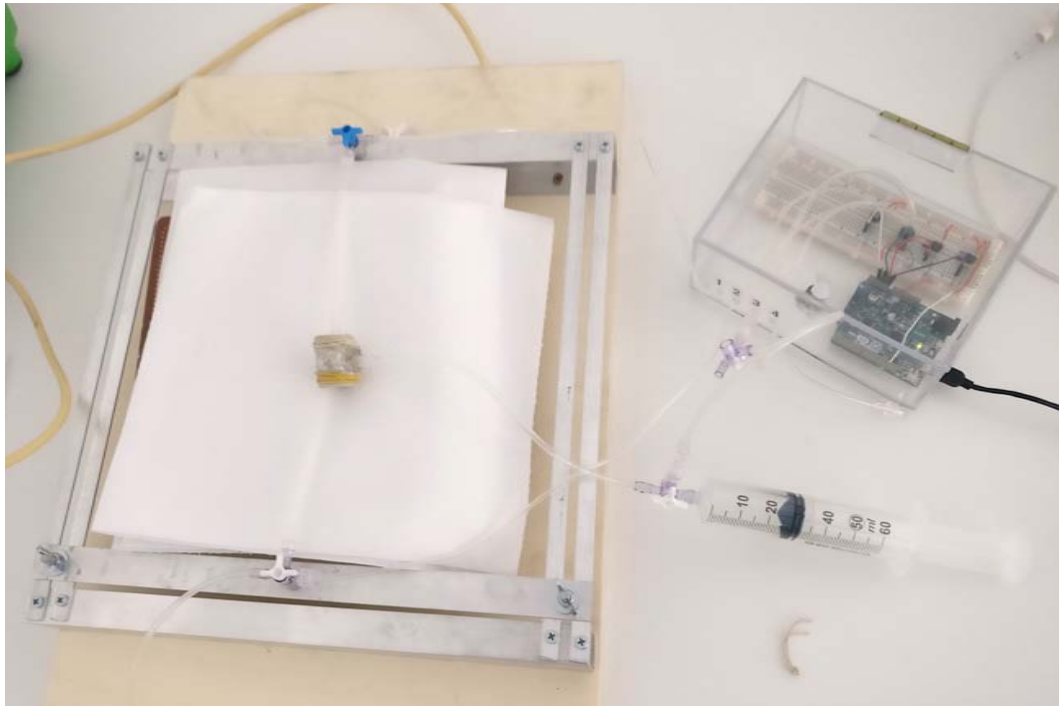


Figure 5.17. Occluding cuff set up. A syringe inflates the cuff and the acquisition hardware measure its pressure to measure the occluding pressure signal.

5.4.1 THE CALIBRATION PROCEDURE

The procedure of calibration requires a manual instrument to refer the measure. It is showed in figure 5.15, behind the PC. This procedure set the constant parameters of the calibration vector which transform the virtual digital pressure data into the real analog pressure data by means of a linearization by the instrument. This linear calibration of the instrument is possible due to the linear response of the sensors (appendix A.5).

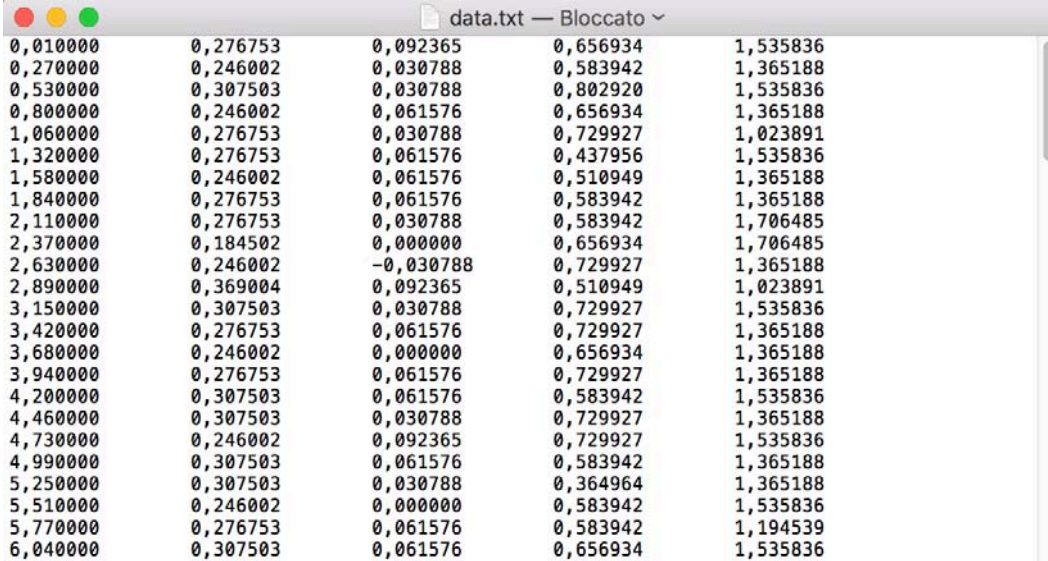
The first step of the calibration consists of an acquisition of 30s from all the sensors with an imposed pressure of 0 cmH₂O which allow to set the zero of the instrument. The last step consists of an acquisition of 30s from all the sensors with an imposed pressure of 50 cmH₂O. All the data acquired relative of each sensor and each calibration step are averaged forming the two calibration vectors, the zero vector $\{C_o\}$ and the slope vector $\{C_s\}$, saved to text files called Tara and Tara50 respectively whenever the user press the CALIBRATION button at the end of the acquisition. The software automatically creates the zero or the slope

calibration vectors according to the digital values acquired (appendix A.5). If some values do not conform to the calibration values required ArduinoUI displays an error message and invites the user to restart the calibration procedure. The software convert the string of digital data acquired into the string of analog data following this relation:

$$\{A\}_i = \{C_o\}_i + 50 \frac{\{D\}_i - \{C_o\}_i}{\{C_s\}_i - \{C_o\}_i}$$

where $\{D\}$ is the vector of the digital value obtained from the input string and $\{A\}$ is the vector of analog data in which $\{D\}$ is converted in in cmH₂O.

The text file of data saved during the autosave process or at the end of an acquisition is composed by a matrix of value. Each j th row of such matrix is composed by the vector $\{t_j \{A\}^T\}$, where t_j is the j th time value in which the j th sample of pressure is acquired by the hardware (figure 5.18).



Time (s)	Sensor 1	Sensor 2	Sensor 3	Sensor 4	Sensor 5
0,010000	0,276753	0,092365	0,656934	1,535836	1,365188
0,270000	0,246002	0,030788	0,583942	1,365188	1,535836
0,530000	0,307503	0,030788	0,802920	1,535836	1,365188
0,800000	0,246002	0,061576	0,656934	1,365188	1,023891
1,060000	0,276753	0,030788	0,729927	1,023891	1,535836
1,320000	0,276753	0,061576	0,437956	1,535836	1,365188
1,580000	0,246002	0,061576	0,510949	1,365188	1,365188
1,840000	0,276753	0,061576	0,583942	1,365188	1,706485
2,110000	0,276753	0,030788	0,583942	1,706485	1,706485
2,370000	0,184502	0,000000	0,656934	1,706485	1,365188
2,630000	0,246002	-0,030788	0,729927	1,365188	1,023891
2,890000	0,369004	0,092365	0,510949	1,023891	1,535836
3,150000	0,307503	0,030788	0,729927	1,535836	1,365188
3,420000	0,276753	0,061576	0,729927	1,365188	1,365188
3,680000	0,246002	0,000000	0,656934	1,365188	1,365188
3,940000	0,276753	0,061576	0,729927	1,365188	1,535836
4,200000	0,307503	0,061576	0,583942	1,535836	1,365188
4,460000	0,307503	0,030788	0,729927	1,365188	1,535836
4,730000	0,246002	0,092365	0,729927	1,535836	1,365188
4,990000	0,307503	0,061576	0,583942	1,365188	1,365188
5,250000	0,307503	0,030788	0,364964	1,365188	1,535836
5,510000	0,246002	0,000000	0,583942	1,535836	1,194539
5,770000	0,276753	0,061576	0,583942	1,194539	1,535836
6,040000	0,307503	0,061576	0,656934	1,535836	

Figure 5.18. Data text file created by the software. Each row consists of the time value and the analog value in measured at each sensor

CONCLUSIONS

The results presented in chapter 2 show the potentiality of experimental and computational biomechanics for the investigation of stomach functionality and the planning of bariatric surgery procedures and techniques. Experimental activities allow evaluating stomach pressure-volume behavior depending on surgical methods and parameters. The increased stomach stiffness after surgery confirms the clinical evidence that bariatric intervention reduces the stomach capacity. On the other side, computational methods make it possible to broaden experimental results to an extremely wider scenario, considering many different surgical procedures. Furthermore, computational models provide information that experimental methods cannot supply. In detail, the computational approach makes it possible to identify the stress and the strain fields in stomach tissues, whose distribution is strongly affected by the bariatric procedure. As an example, position and pre-tension value of the gastric band have a relevant impact on both the stomach capacity and the areas of gastric wall that are mainly stressed. Mechanical stimuli, as stress and strain, act on receptors that contribute to regulate the feeling of satiety. Considering the mechano-transduction capabilities and the locations of gastric receptors, it follows the relevance of methods that allow to evaluate the intensity and the conformation of stress and strain fields. The relevance of this topic is enforced by the recent trends in bariatric surgery, which aim not to restrict stomach capacity, but to induce satiety with small meals. A limitation of the computational models adopted to simulate the structural behaviour of the stomach is given by their isotropic formulation. In the first section of chapter 2, Zhao et al. activity showed a remarkable anisotropy of the stomach wall mechanical behaviour. Further numerical analyses with detailed

anisotropic constitutive formulation must be considered to have a better overall mechanical behaviour of the stomach structure.

The knowledge of the mechanical behaviour of the stomach and of the related mechanical transduction mechanism in all post-surgical conformations, lead to develop suitable innovative procedure in order to optimize the stomach filling sensation and the related filling of satiety. With the specific purpose of this work, concerning the specific gastric banding procedure, computational results from chapter 2 allow to plan an optimized band application in those position with a higher stress magnitude perceived from the structure, thus optimizing the feedback satiety stimuli. Considering also the magnitude of the forces, which develop inside the stomach during the digestion phase, computational tools allow to designing specific devices to give an endoscopic approach for the gastric banding creating an innovative solution of bariatric surgery. The coupling between materials and dimension of the devices is investigated and optimized by means of solid numerical models analyses. Devices must be safe, according with the theory of the mechanics of biomaterials. Numerical results from chapter 4 show that computational tools allow to compare different geometrical configurations of the models and choosing the optimal ones in terms of internal stress perceived. The conceived M2 clips model confirmed their better mechanical response due to the lower internal stresses. A limit of those results is based on the M2 model geometrical simplification, by which numerical analysis are processed considering the clip as a unique solid model, without considering the singular behaviour of each element acting against the other. To improve stress contour details and optimize design of devices a further multi-element FEM analysis must be done. These further investigations may also lead to an overall evaluation on the wear involved inside the hinge. Wear evaluations are necessary to confirm the total safety of the implant, according with the normative of all common prosthetic devices. From this latter point of view fatigue test results showed the possibility to have an optimal compromise between geometrical dimension in order to ensure the fatigue safety of the devices. Further data concerning the amplitude

and the frequency of the loads acting on the stomach wall are needed to improve the investigation on fatigue behavior of the clips. The mere hypothesis made on the sinusoidal shape of loads signal cannot represent the real conditions involving into the stomach, but is a suitable tool which allows to have an overall estimation on how the life of the structure may be affected varying geometrical parameters of the model. Furthermore, tests are made without considering the aggressive behavior of the gastric environment inside the stomach, subjected to gastric acids and other aggressive biological substances. Further specific investigation, aiming to an estimation of number of load cycles acting on the stomach wall during a patient lifetime, may lead to locate an opportune criterion able to distinguish between safe and unsafe clip structures in terms of fatigue life fixing a suitable safety limit to this specific application.

The first step to do in order to validate computational tool developed for the novel endoscopic bariatric technique will account for experimental surgery on animal models. The post-surgical configuration of the stomach will be defined by computational tools. The evolution of stomach configuration and animal parameters will be monitored after the surgical operation to evaluate the reliability of the computational prediction. The experimental activities will further allow to provide data about the reliability of endoscopic clips and bands, by the histological investigation of the tissues around the clips and the evaluation of the stomach conformation depending on clips distribution and band tension. Further experimental surgery will be developed to investigate remodeling phenomena within stomach tissues and to identify the stomach functionality depending on the stricture and its modifications in time. Such information will allow for the physiological and surgical validation of the procedures. The technical feasibility of the procedure will be assessed by acute animal models, while the postoperative safety of the procedure and the results in term of weight loss will be evaluated by survival animal models. Finally, surgical investigations will be developed on human cadavers. The implant will be applied to cadaver stomachs and tested by means of inflation tests in order to simulate physiological load condition of the stomach and

considering the number of cycles which will bring the prototype of the implant to failure.

Chapter 3 gave the basis for the mechanical description of the urethral mechanics by means of both experimental tests and computational analyses, confirming the potentialities of the coupling of both the approaches. Experimental tensile tests, on urethral specimens by Natali et al. (2016a) led to obtaining the stress-strain response of the urethral tissue allowing to assign a specific constitutive formulation and the identification of the constitutive parameters. On the other hand, computational tools given from Natali et al. (2016b and 2017), allowed to realize numerical models of the structure, which are validated by the previous experimental data. Such computational tools form the basis to investigate the urethral mechanical behaviour as internal stress profiles perceived, not only during the urethral lumen opening due to the micturition process, but also under an artificial sphincter occlusion.

Hyperelastic formulations allow interpreting some of the typical features of soft tissue mechanics, as almost incompressible behavior and non-linear elasticity. Biological tissues exhibit a more complex behavior and anisotropic conformation and time-dependent phenomena should be considered. Moderate anisotropy could just characterize the thin layer of dense connective tissue. Differently, time-dependent phenomena appear to be relevant and could significantly affect stress within urethral tissues during protracted occlusive actions. The evaluation of viscoelastic properties is extremely important for the description of the mechanical behaviour of urethral tissues and structure. At present, in computational modelling for urinary incontinence research, urethral tissues have frequently been simplified as linear elastic materials. Instead, the viscoelastic properties of the urethral tissues should be considered (Natali et al., 2016a). Moreover, uniaxial testing does not represent all loading conditions *in vivo*. For a more accurate mechanical evaluation, including an enhanced characterization of tissue anisotropy, biaxial tensile testing would be preferable, with loading being

applied to a sample along two perpendicular axes, preferably corresponding to longitudinal and circumferential directions.

The urethral occlusion by an artificial sphincter cuff is harvested by means of 2D and 3D computational models. The complexity of the geometrical conformation of the site is relevant and the 3D solid model definition entails attention and accuracy. In details, the conformation of lumen region is obtained by means of a detailed evaluation of the histo-morphometric data. In fact, this region represents the most sensitive portion of the model, in consideration of the occlusion process that takes place during the pressure action, determined by the artificial sphincter, through subsequent phases, up to the complete occlusion. Lateral portions of the cuff have a heavy interaction with the tissues and the specific deformational shape induced in the duct represents an important aspect of the analysis, in consideration of potential degenerative processes. Accuracy is required in defining the finite element mesh from the solid model acquired. The heavy non-linearity of the analysis, in terms of constitutive material characteristics, large deformation and contact phenomena, influences the discretization of the mesh and causes a relevant improvement in the degrees of freedom, primarily for getting to convergence in the iterative process and for an adequate accuracy of results. In particular, the characteristics of the dense connective tissue layer in the lumen region, that must undertake the occlusion process via a contact strategy with a high gradient in the final phase, influences the mesh requirements in this portion. Urethra occlusion is achieved in case of constant load along the overall length of the cuff, while marginal opening is present in border regions when a parabolic trend is assumed. The duct region in contact with borders of the cuff represents, in consideration of the sudden variation of deformational field, a potential source of problems in tissue mechanical response. In fact, this condition can produce tissues degradation, because of the permanence of a localized deformation that does not interpret properly the physiological action induced by the natural sphincter. This is evident in the case of constant load, while a better conformation is present in case of parabolic load. For a more direct interpretation of the

problem, results are mostly reported in terms of displacements and strains and allow for evaluation of the effects of occlusion process. The definition of a three-dimensional model entails a much larger effort but leads to a more reliable and complete set of results and offers the possibility of an accurate definition of the effects induced by different loading conditions.

As mentioned in chapter 5, a remarkable difference can be found in comparison with the action induced by the different artificial sphincter cuffs and physiological occlusion. To address this comparison and having a more in-depth knowing of the processes involved, an integration among mechanical, surgery and material science analyses is needed. The analysis must be performed considering the occlusive action of the cuff in composition with the pressure induced by bladder filling. Urethral pressure profile data can represent a valid reference term for functional evaluation.

This entails a very difficult procedure but activity is already in progress both in experimental and numerical area. The result validation presents several difficulties for such a complex process of interaction between the artificial sphincter and the urethral duct. The experimental setup realized in this work (chapter 5) is suitable to approach to the mentioned experimental analysis. The prototype of occlusion devices made in this work may be considered only as a basic occluding cuff. It is made without considering material and geometrical properties of common artificial sphincter cuffs. In fact, the purpose of the current experimental setup is to obtain pressure gap Δp of the urethra as function of occluding pressure, without considering friction phenomena or stress profiles. To improve reliability of tests outcomes common artificial sphincter cuffs must be used, according to simulate a real artificial occlusion and provide the validation of the computational models. To have a significant characterization of the hydraulic resistance of the urethral duct, inflation test must be performed with different water flows, imposed by a peristaltic pump. Due to the peristaltic mechanism of the pump, the water flow is affected by cyclic oscillating disturbing signals and results in a non-static condition. As a consequence, pressure signals are affected by the same oscillating disturbs

introduced by the system. To avoid these undesirable conditions a post-processing of data is required. As a first step, is possible to analyze the spectrum of all the signals obtaining the trend of the disturbing frequency a function of the flow pumped. Consequently, a suitable software filter must be introduced to the post-processing phase of the data in order to cut all the disturbing signals introduced by the pump. Furthermore, the water flow oscillations may result in a turbulent condition of the flow, augmenting the resistance of the hydraulic system and consequently of the urethral duct. A suitable damper system placed in the hydraulic branch upstream the urethra, such as a rubber balloon, could block those oscillations by means of a mechanical absorption according to the vibration mechanics theory. A flowmeter, coupled with the microcontroller, may reveal the effective flow passing through the urethra, showing discrepancies with the flow exiting from the pump and allowing to process data with a lower error. Further modifications will be evaluated to both the user interface and the microcontroller software, allowing the user to set the acquisition rate of data to a desirable value.

APPENDIX

A.1 PIG STOMACH HISTOLOGY

The stomach in the pig has a small non-glandular area adjacent to the cardiac valve. The cardiac region (figure A.1a) consists mainly of mucous secreting cells with some acid producing cells, this region is much larger in the pig than in the dog. The body of the stomach or fundus (figure A.1b) has upper tubular glands of mainly mucous neck cells and crypts which have acid secreting parietal or oxyntic cells and the enzyme producing chief or peptic cells with mucous and endocrine cells. The final area is the pyloric region (seen best in scan 14 where it merges into the duodenum) which is composed mainly of mucous neck cells (figure A.1c).

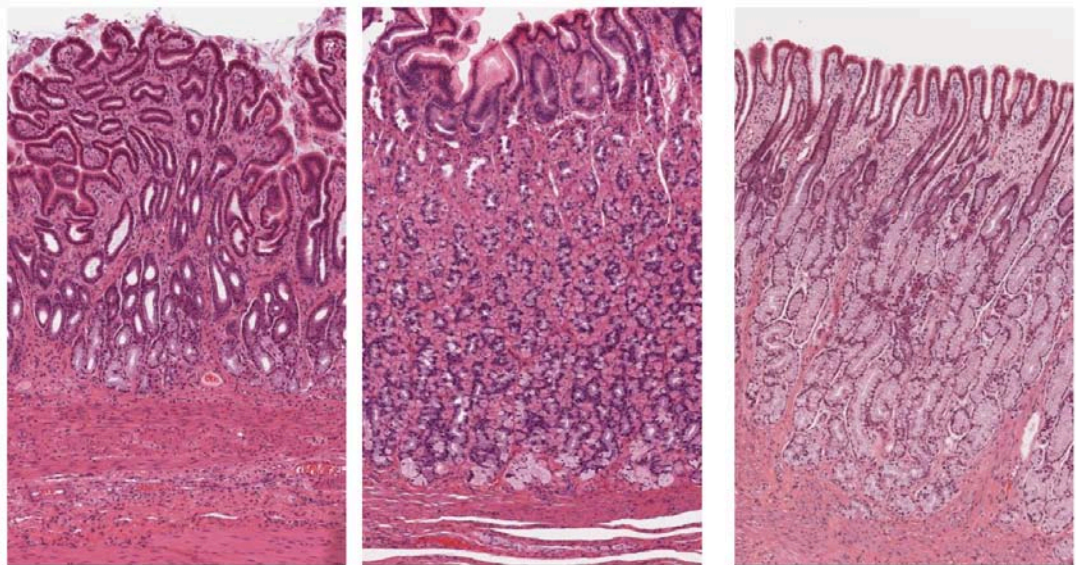


Figure A.1: Stomach mucosa and sub mucosa histology of the pig (10x EE). Cardiac stomach (a), fundic stomach (b) and and pyloric stomach (c).

A.2 HORSE URETHRA HISTOLOGY

Stallions and carnivores, in contrast with the fibroelastic penis of other mammals, have a musculocavernous penis, with larger septa in the cavernous and spongy regions and a greater amount of muscle fibres, with an overall conformation that is comparable to the human penis, with some approximation. Between these last two groups, also considering the availability of samples, the horse was assumed to represent a suitable model for *ex vivo* characterization.

The analysis of histological samples by Natali et al 2016 allowed evaluation of the structural components of the urethra and their distribution. Figure A.2 shows a histological view of a transverse section of the most proximal urethra. The trichrome staining makes it possible to identify the tissue conformation and the components (figure A.2a). A mucosal layer, surrounding the lumen of the urethra and the epithelium, was clearly identified as transitional epithelium (figure A.2b). Above the mucosa, there is a layer of dense connective tissue showing an arrangement of collagen fibrils (figure A.2c). Above the dense connective tissue, there was a loose tissue containing the corpora spongiosa, blood vessels and smooth muscle fibres (figure A.2a). The observation of muscular structures on subsequent transverse serial sections suggested the preferential alignment of muscle fibres along the urethra in a longitudinal direction. The orientation of muscular structures was confirmed by the histological analysis of longitudinal sections (figure A.3). The amount of smooth muscle fibres was very much larger in the proximal region of the urethra than in the distal portion (figure A.4). Image processing allowed quantitative identification of the muscle and collagen fibre content, which showed a linear decreasing and increasing trend, respectively, when moving from the proximal to the distal region of the urethra. A linear correlation between the percentage and position of each component ($r^2 > 0.8$) was found both for muscle (figure A.4a) and connective fibres (figure A.4b). The urethra section area (figure A.4c) and lumen perimeter (figure A.4d) showed a linear correlation with position ($r^2 > 0.7$). On the contrary, the lumen area varied

around the median value of 5.14 mm², being 3.61 and 5.71 mm² at the 25th and the 75th percentiles, respectively.

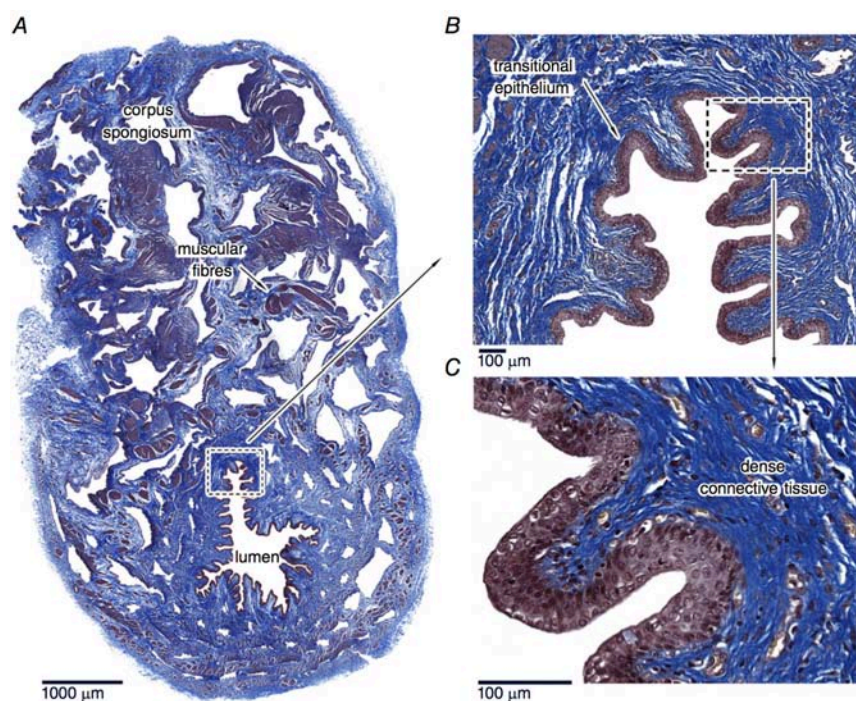


Figure A.2 Trichrome histological section of the proximal urethra General view of a transverse section of the urethra (A) and details (B and C) to show the conformation of the epithelium and connective tissues surrounding the lumen. The section was obtained 50 mm from the most proximal end of the urethra.

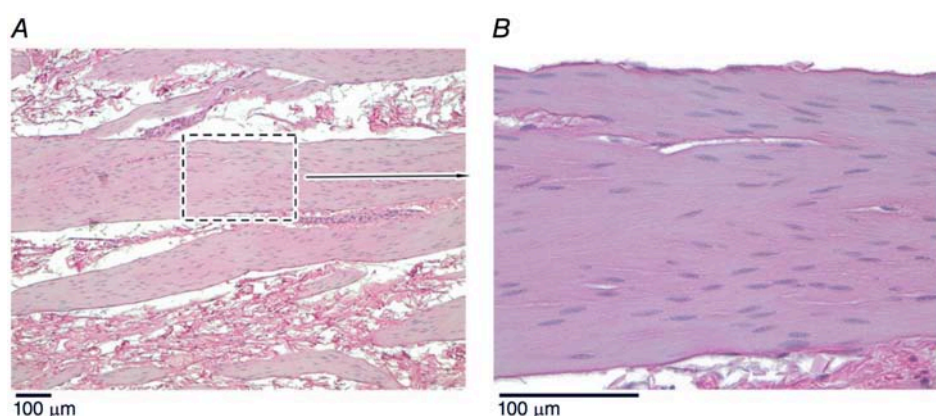


figure A.3. Histological section of the proximal urethra A, general view of muscle structures in a longitudinal section. B, detail to highlight the inner conformation of muscle components.

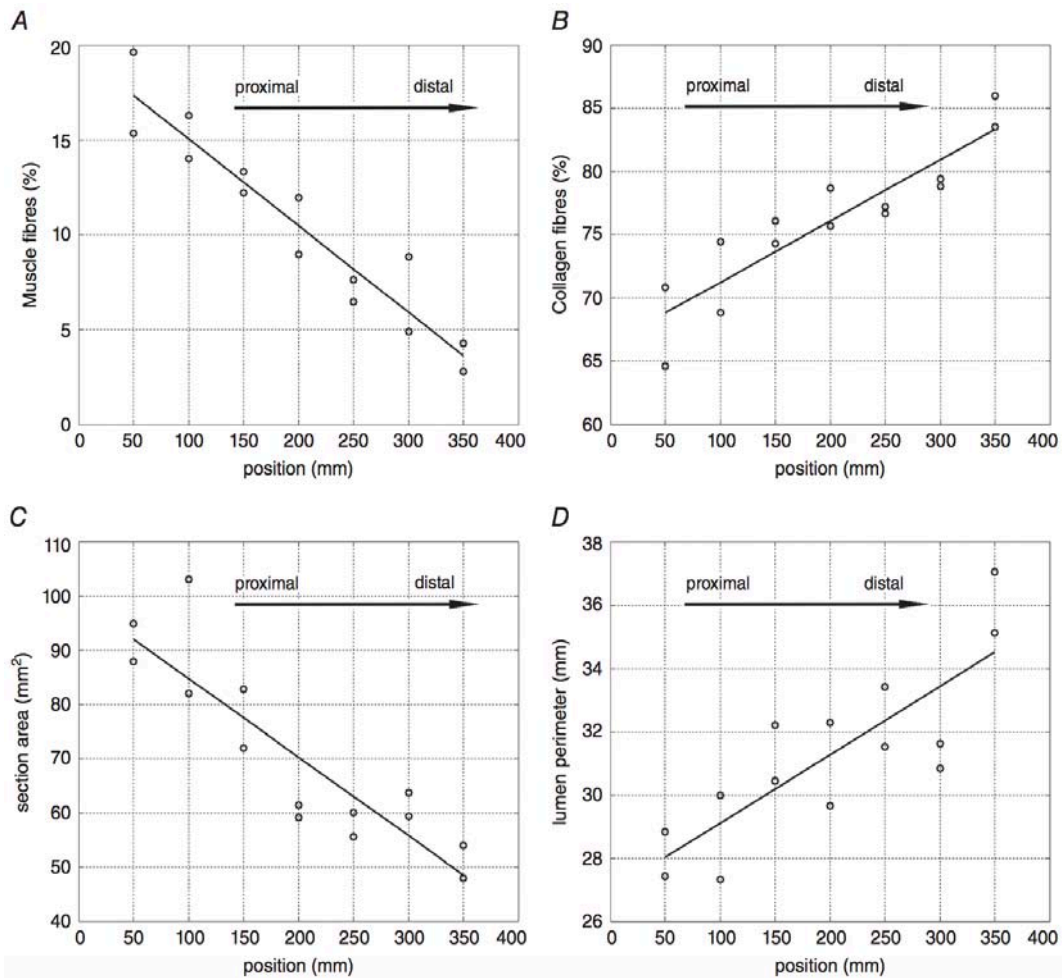


figure A.4 Quantitative analysis of histology of the urethra. Postprocessing of histological images shows the almost linear correlation between muscle content (A) or collagen content (B) and positioning. In addition, geometrical properties, such as the urethra section area (C) and the lumen perimeter (D), show good linear correlation with position. The experimental data at 50 mm from the most proximal end correspond to the histological section shown in Fig. 5. Measurement errors are $\pm 5\%$ of experimental values for muscle, collagen fibers and section area, ± 0.5 mm for lumen perimeter and ± 0.1 mm for position.

Regarding the morphology, in both human and equine penis, a transitional epithelium and a thin layer of dense connective tissue surround the lumen. Outside these layers, the urethra is composed of loose tissue containing the corpora spongiosa, blood vessels and smooth muscle fibres. Histological analysis of horse urethra showed different micro- and macrostructural conformations of the urethral section when moving from the proximal to the distal region. The area of the section progressively decreased. The area of the occluded lumen did not

change significantly, whereas the lumen perimeter progressively increased (figure A.4d). The amount of collagen fibres was relevant along the whole urethra, with a marginal decrease in the proximal region (figure A.4b). The amount of muscle fibres decreased from the proximal to the distal urethra (figure A.4a). Muscle fibres were preferentially oriented along the longitudinal direction. In the thin layer of dense connective tissue around the lumen, collagen was arranged along the lumen perimeter (figure A.4c).

A.3 TECHNICAL DATA OF THE PRESSURE SENSORS

Characteristic	Analog			Digital			Unit
	Min.	Typ.	Max.	Min.	Typ.	Max.	
Supply voltage (V_{supply}) ^{1,2,3}							
3.3 Vdc	3.0	3.3	3.6	3.0	3.3	3.6	Vdc
5.0 Vdc	4.75	5.0	5.25	4.75	5.0	5.25	
Supply current:							
3.3 Vdc	—	2.1	2.8	—	3.1	3.9	mA
5.0 Vdc	—	2.7	3.8	—	3.7	4.6	mA
sleep mode option	—	—	—	—	1	10	μA
Operating temperature range ⁴	-40 [-40]	—	85 [185]	-40 [-40]	—	85 [185]	°C [°F]
Compensated temperature range ⁵	0 [-32]	—	50 [122]	0 [-32]	—	50 [122]	°C [°F]
Temperature output option ⁶	—	—	—	—	1.5	—	°C
Startup time (power up to data ready)	—	—	5	—	—	3	ms
Response time	—	1	—	—	0.46	—	ms
Clipping limit:							
upper	—	—	97.5	—	—	—	%Vsupply
lower	2.5	—	—	—	—	—	
SPI/I ² C voltage level:							
low	—	—	—	—	—	20	%Vsupply
high	—	—	—	80	—	—	
Pull up on SDA/MISO, SCL/SCLK, SS	—	—	—	1	—	—	kOhm
Accuracy ⁷	—	—	±0.25	—	—	±0.25	%FSS BFSL ⁸
Output resolution	0.03	—	—	—	—	—	%FSS bits
	—	—	—	12	—	—	

¹Sensors are either 3.3 Vdc or 5.0 Vdc based on the catalog listing selected.

²Ratiometricity of the sensor (the ability of the device output to scale to the supply voltage) is achieved within the specified operating voltage.

³The sensor is not reverse polarity protected. Incorrect application of supply voltage or ground to the wrong pin may cause electrical failure.

⁴Operating temperature range: The temperature range over which the sensor will produce an output proportional to pressure.

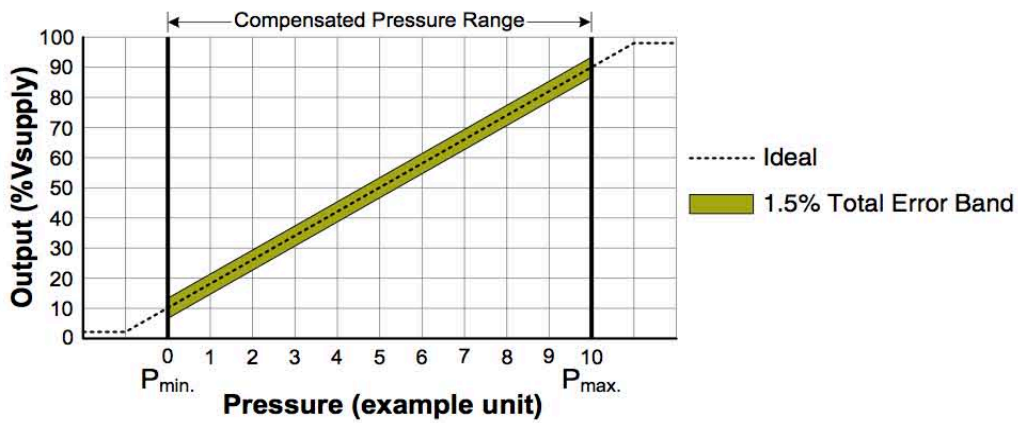
⁵Compensated temperature range: The temperature range over which the sensor will produce an output proportional to pressure within the specified performance limits.

⁶Temperature Output Option: Continuous operation in Sleep Mode only may provide different results.

⁷Accuracy: The maximum deviation in output from a Best Fit Straight Line (BFSL) fitted to the output measured over the pressure range at 25 °C [77 °F]. Includes all errors due to pressure non-linearity, pressure hysteresis, and non-repeatability.

⁸Full Scale Span (FSS): The algebraic difference between the output signal measured at the maximum (Pmax.) and minimum (Pmin.) limits of the pressure range. (See Figure 3 for ranges.)

Table A.1. Operating specifications of the sensors



$$\text{Output (V)} = \frac{0.8 \times V_{\text{supply}}}{P_{\text{max.}} - P_{\text{min.}}} \times (\text{Pressure}_{\text{applied}} - P_{\text{min.}}) + 0.10 \times V_{\text{supply}}$$

Figure A.5. Transfer function limits

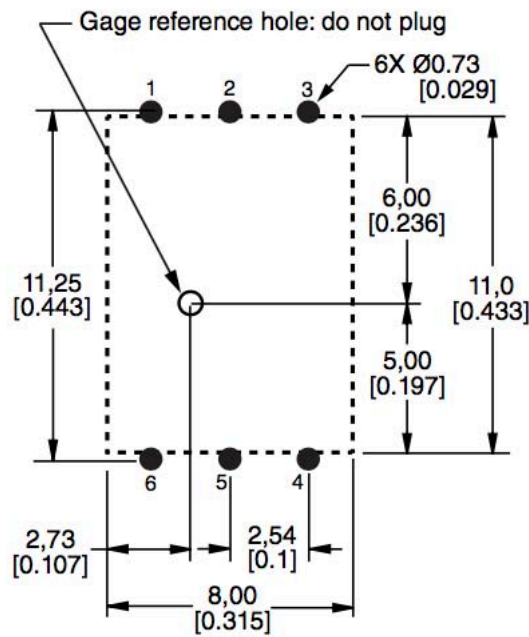


Figure A.6. PCB layout

Output Type	Pin 1	Pin 2	Pin 3	Pin 4	Pin 5	Pin 6
Digital (I ² C, SPI)	GND	V _{DD}	SS/INT	NC	SDA	SCL
Analog	GND	NC	V _{out}	NC	NC	V _{DD}

Figure A.7. Sensor pinout

DIP JJ: Dual radial barless ports, same side

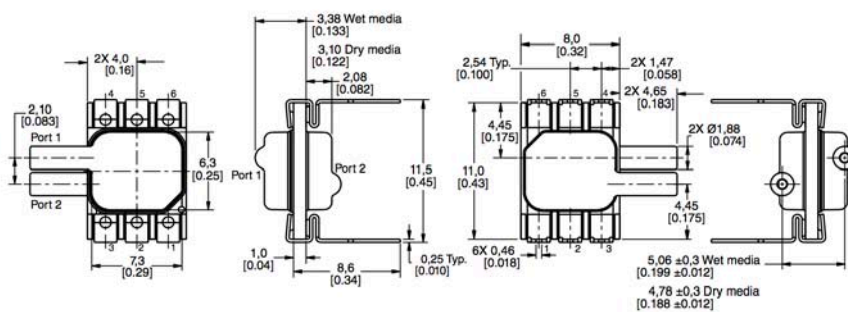


Figure A.8. Package and dimensional drawings of 1psi and 5psi sensors

DIP AN: Single axial barbed port

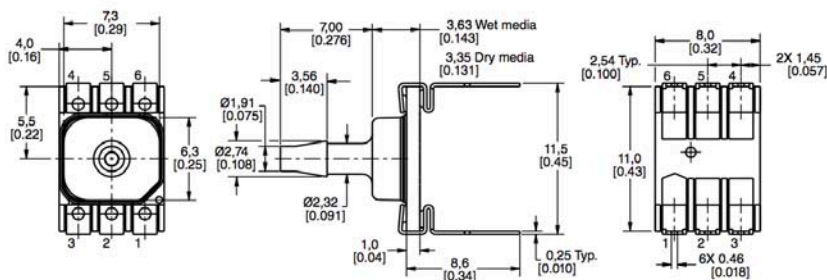


Figure A.9. Package and dimensional drawings of 3psi sensors

A.4 ARDUINO SOFTWARE

```
int sensorPin1=A0;
int sensorPin2=A1;
int sensorPin3=A2;
int sensorPin4=A3;
int reset=0;

float sensorValue1, sensorValue2, sensorValue3, sensorValue4;
double time, timediff=0;
int delayTime=250; //milliseconds to wait each cycle (4Hz of acquisition frequency
)

void setup() {
  SerialUSB.begin(9600);
  analogReadResolution(12);
}

void loop() {
  while(!SerialUSB){
    timediff=millis();
  }
  sensorValue1=(analogRead(sensorPin1));
  sensorValue2=(analogRead(sensorPin2));
  sensorValue3=(analogRead(sensorPin3));
  sensorValue4=(analogRead(sensorPin4));

  time= millis()-tempodiff;

  SerialUSB.println(String(time/1000.0) + " " + String(sensorValue1) + " " +
String(sensorValue2)+" " + String(sensorValue3) + " " + String(sensorValue4));

  delay(delayTime);
}
```


A.5 LABVIEW USER INTERFACE SOFTWARE

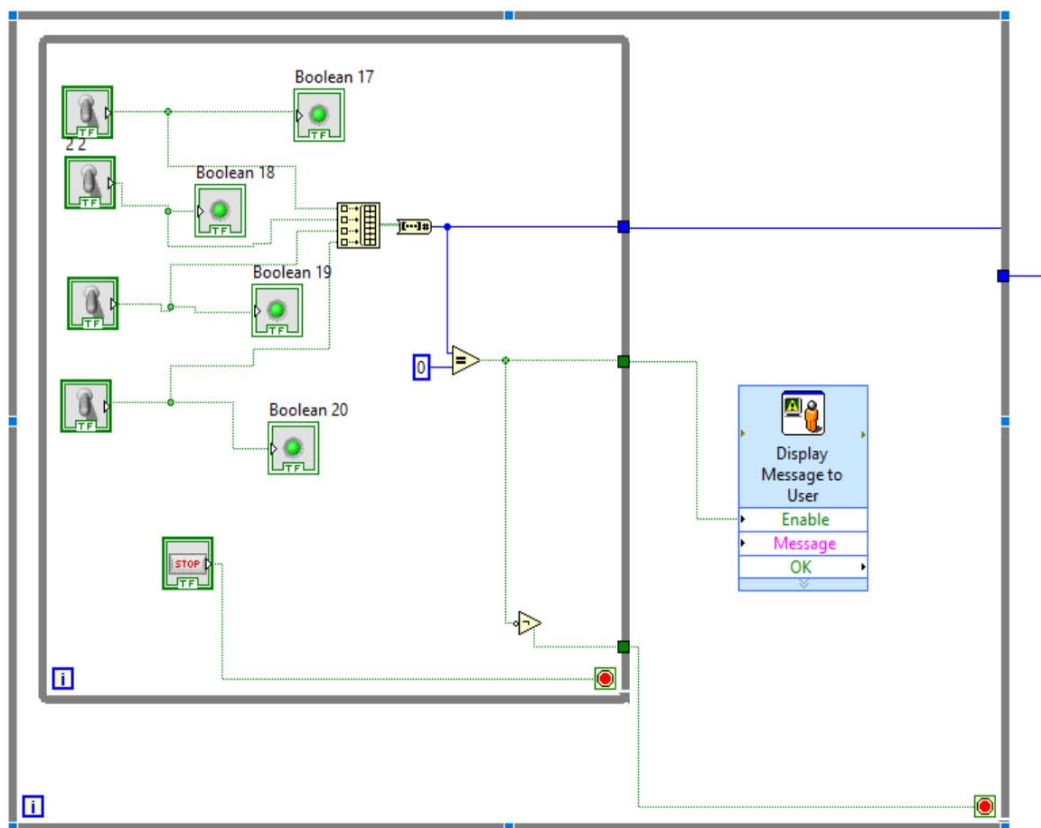


Figure A.10. First choice of the sensors by means of the 4 switches. If any switch is turned on a message is displayed to the user and the software don't pass to the next sequence.



Figure A.11. The serial communication is set on the COM5 USB port where the Arduino-based hardware is connected to the PC.

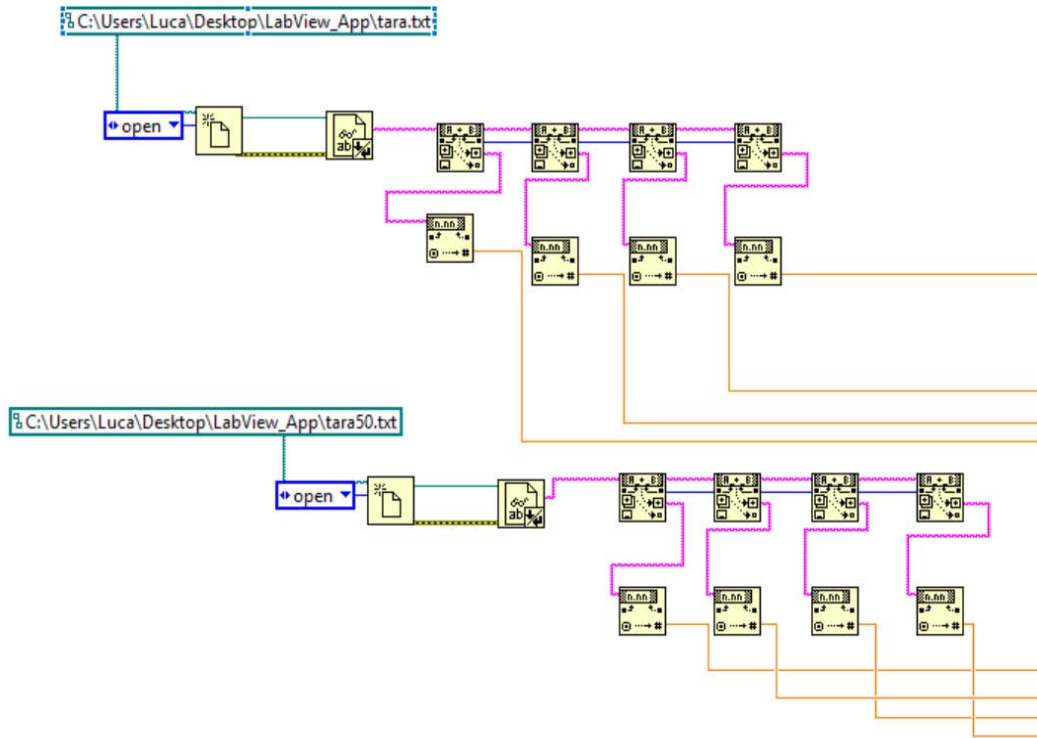


Figure A.12. Before every acquisition cycle the software open the text files where are saved the calibration parameters and convert the relative string tokens into their numerical value.

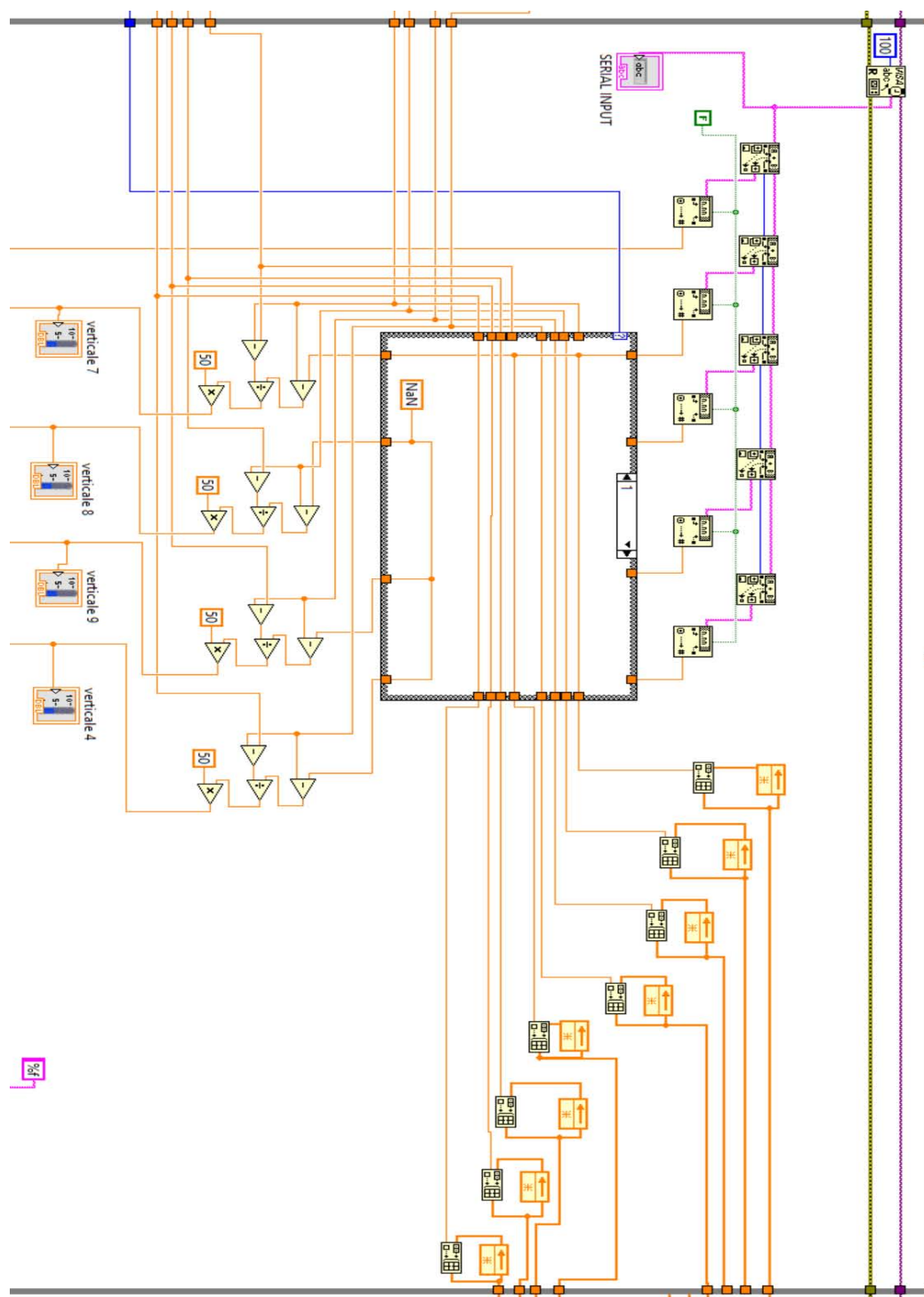


Figure A.13. From the serial port the string of samples received on each cycle of acquisition is separated in its tokens and the latter are converted in the corresponding analogic numerical value, using the calibration parameters. An oportune case structure creates the suitable connections according to which switches are turned on. Then analog values follow at the same time 2 different paths: one goes to the bottom of the structure to be visualized on the graph panels and one goes to the right of the structure to compose the data file or to form the novel calibration parameters.

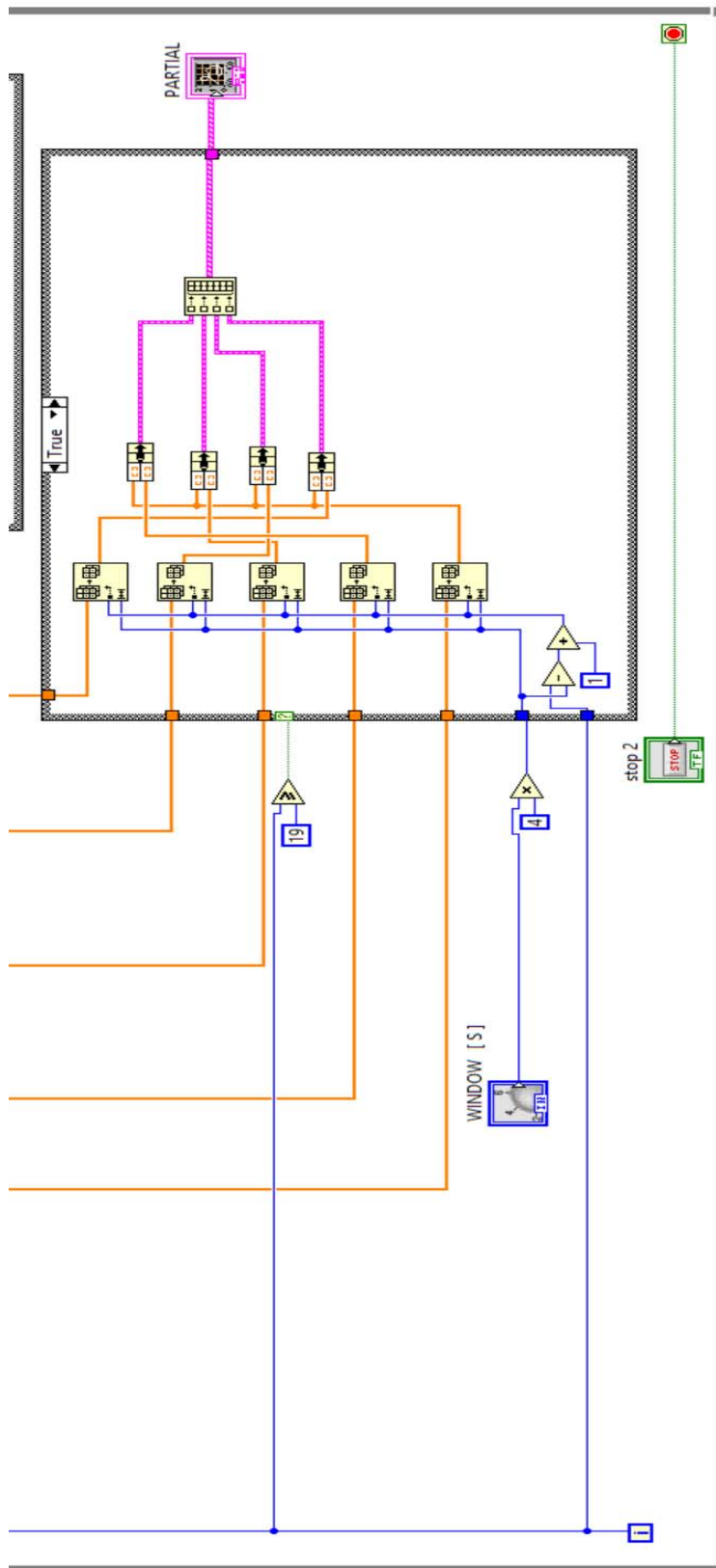


Figure A.14. At the bottom of the software structure, data were displayed on the partial graph according with the time window selected by means of the relative potentiometer.

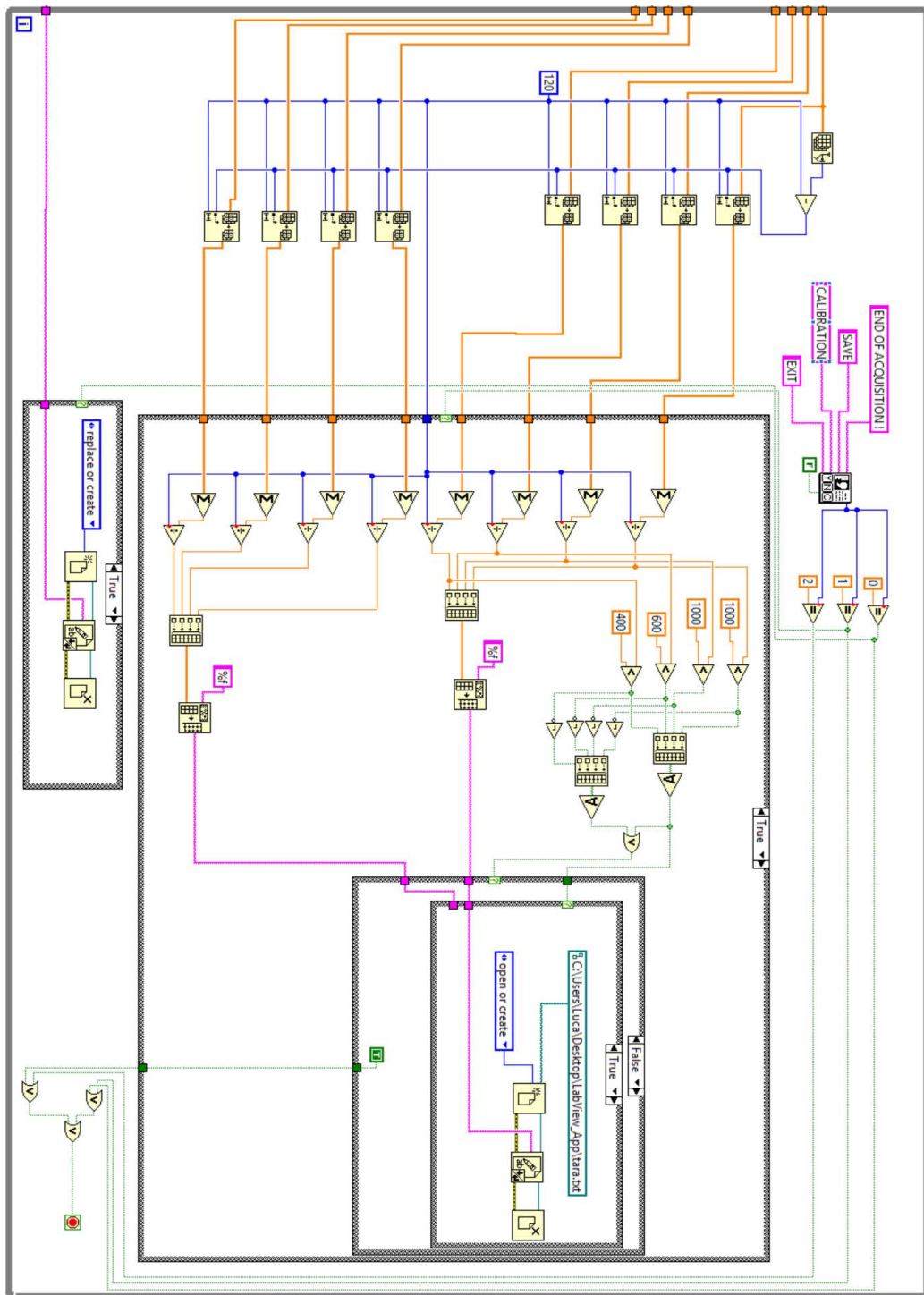


Figure A.15. When stop button is pressed a message is displayed to make a choice: SAVE, CALIBRATION, EXIT. Pressing SAVE button a text file is created where is inserted the matrix of all the values collected. Pressing CALIBRATION all the data were averaged before and then they are saved on the corresponding calibration vectors due to a comparison of their value. If EXIT is pressed, the software avoid this first two paths and stop the software directly without doing anything.

REFERENCES

Amerongen H.M., *Anatomy and Histology of the Digestive Tract*, Elsevier (2010)

Andretto S., Analisi del comportamento meccanico dei tessuti e della conformazione meccanica dell'uretra maschile, Tesi di laurea Magistrale in Bioingegneria, Università degli Studi di Padova, 2013.

ASGE (American Society for Gastrointestinal Endoscopy), *Endoscopic bariatric therapies*, GASTROINTESTINAL ENDOSCOPY, Volume 81, No. 5 (2015)

Bellmann S., Lelieveld J., Gorissen T., Minekus M., Havenaar R., *Development of an advanced in vitro model of the stomach and its evaluation versus human gastric physiology*, Food Research International 88 (2016) 191–198

Booth H., Khan O., Prevost A.T., Reddy M., Charlton J., Gulliford M.C., *Impact of bariatric surgery on clinical depression. Interrupted time series study with matched controls*, Journal of Affective Disorders 174 (2015) 644–649

Brandes S.B., Morey A.F., *Advanced male urethral and genital reconstructive surgery*, Humana Press (Springer Science) (2014)

Carniel E.L., Frigo A., Rubini A., Natali A.N., *Analysis of the biomechanical behaviour of gastrointestinal regions adopting an experimental and computational approach*. Computer methods and programs in biomedicine 113 (2014) 338–345.

Carniel E.L., Polese L., Foletto M., Rubini A., BIO-OBESSE: biomechanical optimization of bariatric surgery procedures and design of devices for endoscopic approach. Research proposal; Centre for Mechanics of biological materials, University of Padova, (2016)

Carniel E.L., Frigo A., Fontanella C.G., De Benedictis G.M., Rubini A., Barp L., Pluchino G., Sabbadini B., Polese L., *A biomechanical approach to the analysis of methods and procedures of bariatric surgery*. J. Biomech. (2017).

Chang A.R., Grams M.E., Navaneethan S.D., *Bariatric Surgery and Kidney-Related Outcomes*, Kidney International Reports, Elsevier (2017) .

DeLancey J., Gosling J., Gross anatomy and cell biology of the lower urinary tract, Incontinence, Health Publications, 17-82, 2002.

References

Flegal K.M., Carroll M.D., Kit B.K., Ogden C.L., *Prevalence of Obesity and Trends in the Distribution of Body Mass Index Among US Adults, 1999-2010*. JAMA. 2012; 307(5):491-497

Griebing T.L., *Geriatric Urology*, Springer Science 2014

Holtmann G., Talley N.J., *The stomach-brain axis*, Best Practice & Research Clinical Gastroenterology 28 (2014) 967-979

Hellis H., *Anatomy of the stomach*, Surgery 29:11, Elsevier (2011)

Houston D.K., Ding J., Nicklas B. J., Harris T.B., Lee J.S., Nevitt M.C., Rubin S.M., Tylavsky F.A., Kritchevsky S.B., *Overweight and Obesity Over the Adult Life Course and Incident Mobility Limitation in Older Adults*, Am J Epidemiol 2009;169:927–936

Jung U.J., Choi M.S., *Obesity and Its Metabolic Complications: The Role of Adipokines and the Relationship between Obesity, Inflammation, Insulin Resistance, Dyslipidemia and Nonalcoholic Fatty Liver Disease*, Int. J. Mol. Sci. 2014, 15, 6184-6223;

Knai , Suhrcke M., Lobstein T., *Obesity in Eastern Europe: An overview of its health and economic implications*, Economics and Human Biology 5 (2007) 392–408

Koraitim M.M., *The Male Urethral Sphincter Complex Revisited: An Anatomical Concept and its Physiological Correlate*, The journal of urology, Vol. 179, 1683-1689 (2008)

Mahadevan V., *Anatomy of the lower urinary tract*, Surgery 34:7, Elsevier (2016)

Natali A.N., Carniel E.L., Frigo A., Pavan P.G., Todros S., Pachera P., Fontanella C.G., Rubini A., Cavicchioli L., Avital Y., De Benedictis G. M., *Experimental investigation of the biomechanics of urethral tissues and structures*, *Experimental Physiology* 000.0 (2016a) pp 1–16 .

Natali A.N., Carniel E.L., Fontanella C.G., Todros S., De Benedictis G. M., Cerruto M.A., Artibani W, *Mechanics of the urethral duct: tissue constitutive formulation and structural modeling for the investigation of lumen occlusion*, *Biomechanics Modeling in Mechanobiology* (2016b) 16:439–447

Natali A.N., Carniel E.L., Fontanella C.G., Todros S., De Benedictis G. M., Cerruto M.A., Artibani W., *Urethral lumen occlusion by artificial sphincteric devices: a computational biomechanics approach*, *Biomechanics and Modeling in Mechanobiology*, (2017)

- Ovalle W.K., Nahirney P.C., *Netter's essentials histology*, 2nd ed, Elsevier 2013
- Owers C.E., Ackroyd R., *Bariatric surgery*, SURGERY 32:11, Elsevier (2014)
- Peruzzi G, *Vortici e colori: alle origini dell'opera di James Clerk Maxwell*, Edizioni Dedalo 2010
- Pluchino G., *Endoscopic technique for gastric banding in bariatric surgery: computational methods for the analysis of mechanical reliability*. Dissertation of master degree in Bioengineering, University of Padova, 2017
- Reeves F., Everaerts W., Murphy D.G., Costello A., *Surgical anatomy of the prostate*, Surgery 6, Prostate Cancer, Elsevier (2016)
- Richardson M.L., Sokol E.R. *A cost-effectiveness analysis of conservative versus surgical management for the initial treatment of stress urinary incontinence*. Am J Obstet Gynecol (2014); 211:565.e1-6.
- Subak L.L., Goode P.S., Brubaker L., Kusek J.W., Schembri M., Lukacz E.S., Kraus S.R., Chai T.C., Norton P., Tennstedt S.L., *Urinary incontinence management costs are reduced following Burch or sling surgery for stress incontinence*, Am J Obstet Gynecol (2014); 211:17, e1-7
- Swindle M.M., Makin A., [Herron](#) A.J., [Clubb](#) F.J., [Frazier](#) K.S., *Swine as Models in Biomedical Research and Toxicology Testing*, Veterinary Pathology (2012) 49(2) 344-356
- Ussain U., Kearney R., *Surgical management of stress urinary incontinence* , Obstetrics, gynaecology and reproductive medicine 23:4 , Elsevier 2013
- WHO (World Health Organization), Consultation on Obesity (2000, Geneva, Switzerland), *Obesity: preventing and managing the global epidemic*. (WHO technical report series; 894)
- Zhao J., Liao D., Chen P., Kunwald P., Gregersen G., *Stomach stress and strain depend on location, direction and the layered structure*. Journal of Biomechanics 41 (2008) 3441–3447

References

WEB SITES CONSULTED:

- www.en.wikipedia.org/wiki/Small_intestine

- www.iuga.org/resource/resmgr/Brochures/eng_mus.pdf

(International Urogynecological Association (IUGA), Mid-urethral slings procedure for stress incontinence. A guidance for women, 2011)

- www.matweb.com

- www.minipigs.dk/fileadmin/filer/Education_package/Histology_of_the_Gottingen_minipig.pdf

(Roger Burnet, *Notes on the histology of the göttingen minipig to accompany the dvd set*)